THE UNIVERSITY OF QUEENSLAND

AUSTRALIA

Enhancement of the performance of rechargeable batteries by proposing new materials

Amir H. Farokh Niaei

BSc and MSc of Chemical Engineering

A thesis submitted for the degree of Doctor of Philosophy at

The University of Queensland in 2018

Australian Institute of Bioengineering and Nanotechnology (AIBN)

Centre for Theoretical and Computational Molecular Science (CTCMS)

Abstract

Nowadays, rechargeable batteries are widely used for many different purposes and they are among the main clean energy storage systems that are readily available. Electrical energy is stored in the battery through oxidation and reduction and via a charge transfer agent that moves between the cathode and anode. Rechargeable batteries commonly use the alkali metal, lithium (Li) as the charge transfer agent. The capacity of the anode material and selection of a charge transfer agent that is easily adsorbed by the anode material are two important factors when designing rechargeable batteries. In this PhD thesis, we propose several types of carbonaceous materials that could be potentially used as an anode in rechargeable batteries. These materials are derivatives of graphene: graphdiyne (GDY), hydrogenated defective graphene (H-DG), edge-functionalised graphene nanoribbons (F-GNRs), and doped graphene. In addition, we select the charge transfer agents, sodium (Na) and calcium (Ca) on several materials, and we also consider the use of potassium (K).

The first material, GDY, adsorbed Na atoms with a binding energy appropriate for battery applications. Adsorption occurs on the 6-membered ring and the pores, with an empirical formula of $NaC_{2.57}$, which is equivalent to an electrical capacity of 497 mA h g^{-1}. If expansion is allowed for the bulk layered GDY, this loading will occur on each layer of bulk GDY, with an expansion of 28% of the interlayer spacing compared with the unloaded material. Furthermore, the bulk layered GDY in an AB-2 stacking has a barrier of energy against Na movement, parallel to the layers of 0.84 eV and as low as 0.12 eV for vertical movement within a slit pore. These values were even lower for the bulk material with AB-3 stacking.

A hydrogenated mono-vacancy repeated four times within a graphene sheet supercell with 68 carbon atoms, 4(H1-MVG), has been considered as another suitable material for the NIB and CIBs. It also provided a model hydrogenated graphene that could be compared with graphene. Compared with graphene, this material strengthened the binding of Na by an energy of 0.72 eV. A similar strengthening occurred for Ca binding. This material can bind up to 16 Na and 14 Ca atoms per 4(H1-MVG) supercell on a single layer. Although the bulk layered 4(H1-MVG) did not strongly bind Na within the layers, Ca effectively intercalated within the layers, with binding energies varying between -2.05 to -2.79 eV, which is strong in comparison with Ca binding to graphene (-0.82 eV). Finally, we found that up to 16 Ca atoms could intercalate

within the bulk layered material, which is equivalent to an electrical capacity of 591.2 m A h g^{-1} and results in 29.3% for the interlayer expansion.

Edge-functionalised graphene nanoribbons have been proposed as the third material for NIBs and CIBs. Nanoribbons with zigzag and armchair edges are functionalised with the selected oxygen-containing functional groups hydroxyl (HO-), carbonyl (O=), and carboxyl (HOOC-). These groups are found abundantly in reduced graphene oxide (r-GO), and we intended to simulate the strength of Na and Ca adsorption over these groups. According to the results, the hydrogen passivated and edge-functionalised ribbons improved the binding of Na and Ca by about 1.1 to 1.9 eV compared with the bindings over the graphene sheet, respectively. This improvement is due to electronic structure of the nanoribbons as well as the direct interaction with the oxygen functional groups. The improvement in binding compared with graphene was more significant over the edge of the ribbons with carbonyl and carboxyl groups. In addition, each carbonyl and carboxyl group could bind as many as five Na or Ca adatoms around it.

DFT calculations for the binding of Na atoms to the nitrogen-doped graphene (graphitic N) and nitrogen-containing functional groups within the graphene sheet showed that pyridinic N, amine and amide groups bound Na more strongly than the Na cohesive energy. We also carried out DFT calculations to determine the binding of Na, Ca and K over the oxygen groups found in the basal plane of the r-GO sheet. When considering Ca adsorption over the hydroxyl group, the Ca bound to the OH group in all cases due to the high charge of Ca as a multivalent metal. However, K did not form KOH, except in one case. Therefore, K is a better choice than Na and Ca in binding over the oxygen groups in the r-GO. Finally, we considered the binding of K over HO-, O-, and HOOC- groups at the edge of GNRs. We found that HO- and O-GNRs bound K with energies that are suitable for use in rechargeable batteries. We completed this study to investigate the effect of oxygen groups found in the cellulose derivative material applicable in potassium ion batteries.

Declaration by author

This thesis is composed of my original work, and contains no material previously published or written by another person except where due reference has been made in the text. I have clearly stated the contribution by others to jointly-authored works that I have included in my thesis.

I have clearly stated the contribution of others to my thesis as a whole, including statistical assistance, survey design, data analysis, significant technical procedures, professional editorial advice, financial support and any other original research work used or reported in my thesis. The content of my thesis is the result of work I have carried out since the commencement of my higher degree by research candidature and does not include a substantial part of work that has been submitted to qualify for the award of any other degree or diploma in any university or other tertiary institution. I have clearly stated which parts of my thesis, if any, have been submitted to qualify for another award.

I acknowledge that an electronic copy of my thesis must be lodged with the University Library and, subject to the policy and procedures of The University of Queensland, the thesis be made available for research and study in accordance with the Copyright Act 1968 unless a period of embargo has been approved by the Dean of the Graduate School.

I acknowledge that copyright of all material contained in my thesis resides with the copyright holder(s) of that material. Where appropriate I have obtained copyright permission from the copyright holder to reproduce material in this thesis and have sought permission from co-authors for any jointly authored works included in the thesis.

Amir H. Farokh Niaei

[Oct 2018]

Publications included in this thesis

1- Farokh Niaei AH, Hussain T, Hankel M, Searles DJ. Sodium-intercalated bulk graphdiyne as an anode material for rechargeable batteries. J Power Sources 2017; 343: 354-63 (incorporated as Chapter 4).

2- Farokh Niaei AH, Hussain T, Hankel M, Searles DJ. Hydrogenated defective graphene as an anode material for sodium and calcium ion batteries: A density functional theory study. Carbon 2018; 136: 73-84 (incorporated as Chapter 5).

3- Farokh Niaei AH, Roman T, Hussain T, Searles DJ. Computational Study on the Adsorption of Sodium and Calcium on Edge-Functionalized Graphene Nanoribbons. J Phys Chem C 2019; 123: 14895-908 (incorporated as Chapter 6).

Other publications during candidature

Peer-reviewed papers:

1- Gaddam RR, Farokh Niaei AH, Hankel M, Searles DJ, Nanjundan AK, Zhao XS. Capacitance-enhanced sodium-ion storage in nitrogen-rich hard carbon. J Mater Chem A 2017; 5: 22186-97.

Conference Abstracts:

1- Farokh Niaei AH, Hussain T, Hankel M, Searles DJ. Enhancement of the Performance of Rechargeable Batteries by Proposing New Materials. The 8th International Symposium on Nano & Supramolecular Chemistry (ISNSG 8). 13-16 Jul 2016, Brisbane Australia.

2- Farokh Niaei AH, Hussain T, Hankel M, Searles DJ. Hydrogenated defective graphene as anode material for sodium and calcium ion rechargeable batteries. The 9th International Conference on Materials for Advanced Technologies (ICMAT 2017), Singapore 18-23 Jun 2017.

3- Farokh Niaei AH, Hussain T, Hankel M, Searles DJ. Hydrogenated carbon nanoribbons for sodium and calcium ion batteries. 2017 International Symposium on Energy Conversion and Storage Materials (ISEC 2017), Brisbane Australia, 31st July – 3rd Aug 2017.

4- Farokh Niaei AH, Hussain T, Hankel M, Searles DJ. Hydrogenated defective graphene and carbon nanoribbons for sodium and calcium ion batteries. 2017 International Conference on BioNano Innovation (ICBNI 2017), Brisbane Australia, 24-27 Sep 2017.

5- Farokh Niaei AH, Roman T, Searles DJ. Adsorption of sodium, potassium and calcium over oxygen functional groups in reduced graphene oxide. 2018 International Symposium on Advanced Materials and Sustainable Technologies (AMST 2018), Brisbane, Australia, 22-25 Jul 2018.

Conference abstracts for presentations by my supervisor (Debra Bernhardt) that included research from this thesis:

1- Farokh Niaei AH, Hussain T, Hankel M, Ye D, Wang L, Searles DJ. *Computational Studies on Materials for Lithium and Sodium Ion Batteries*. Oral presentation, International Conference on Computational Physics, University of Macao, Macao, 16th - 20th Jan 2017.

2- Fischer JMTA, Su Y, Farokh Niaei AH, Hankel M, Wang L, Reid JC and Searles DJ. *Application of molecular computation to improve energy nanotechnology*. Oral presentation, International Symposium on Energy Conversion and Storage Materials (ISEC 2017), Brisbane, Australia, 31st July – 3rd Aug 2017.

3- Fischer JMTA, Su Y, Farokh Niaei AH, Hankel M, Hussain T, Reid JC, and Searles DJ. *Application of Molecular Computation in Materials Research.* Invited speaker, Frontiers of Materials Research, QUT, Brisbane, Australia, 19th October 2017.

4- Baktash A, Farokh Niaei AH, Hankel M, Reid JC, and Searles DJ. *Computational Studies of Ion Mobility in Battery Materials.* Plenary lecture, the 3rd International Symposium on Renewable Energy Technologies, Griffith University, Gold Coast, Australia, 19th -22nd Jul 2018.

5- Hunter MA, Fischer JMTA, Farokh Niaei AH, Baktash A, Reid JC, Hankel M, and Searles DJ. *Application of molecular computation in materials research for sustainable technologies* Plenary lecture, International Symposium on Advanced Materials & Sustainable Technologies (AMST 2018), QUT, Brisbane, Australia, 22nd -25th Jul 2018.

Contributions by others to the thesis

Prof. Debra Bernhardt has been the main supervisor of all projects during my candidature over the past 3.5 years. She made the primary contributions to the projects, provided theoretical advice, paper reviews and corrections. Marlies Hankel was the associate advisor of my projects in the first 17 months of my candidature (Apr 2015 to Sep 2016), while Tanveer Hussain was the second associate advisor of my projects for about 2.5 years of my candidature (Apr 2015 to Oct 2017), and Tanglaw Roman has been the third associate advisor of my last project (graphene nanoribbons) since Nov 2017. These people were within the CTCMS group as theoretical advisors to my projects during the above-mentioned times. I have also worked with an experimental group in the school of Chemical Engineering of the University of Queensland for sodium and potassium ion batteries (discussed in Chapter 7). Rohit Gaddam was the PhD student who carried out the experiments for the anode materials. Ashok Kumar was the associate advisor and George Zhao was the main supervisor of those experimental projects. Moreover, Danni Allison from Smart Editing Services 360 reviewed and edited my

thesis (Chapters 1, 2, 3, 7 and 8) for word, punctuation, spelling, and grammar corrections only.

Statement of parts of the thesis submitted to qualify for the award of another degree

No works submitted towards another degree have been included in this thesis

Research Involving Human or Animal Subjects

No animal or human subjects were involved in this research

Acknowledgements

I acknowledge the help, assistance and scientific advice of Prof. Debra Bernhardt, the supervisor of the centre of the computational and molecular sciences (CTCMS, Australian Institute of Bioengineering and Nanotechnology, AIBN) and the School of Chemistry and Molecular Biosciences (SCMB) during the past three and half years of my PhD study. I also appreciate the help and assistance of Dr. Marlies Hankel, Dr. Tanveer Hussain and Dr. Tanglaw Roman during my candidature for their technical and theoretical advice.

I appreciate the cooperation of the experimental group in the Chemical Engineering Department, Mr. Rohit Gaddam, Dr. Ashok Kumar and Prof. George Zhao for their experimental tests.

I appreciate the assistance of AIBN admin staff (HDR, finance and reception) and the IT help desk who helped me with the computer affairs administration.

I also appreciate the editing services of Dr. Danni Allison (Smart Editing Services 360) for English lexicon, syntax, punctuation, spelling, and grammar corrections in my thesis.

Financial support

This research was supported by an Australian Government Research Training Program (RTP) Scholarship.

Keywords

Sodium-ion batteries, calcium-ion batteries, potassium-ion batteries, rechargeable batteries, DFT calculations, graphene, hydrogenated defective graphene, graphene nanoribbons, reduced graphene oxide

Australian and New Zealand Standard Research Classifications (ANZSRC)

ANZSRC code: 020403 Condensed matter modelling and density functional theory (60%)
ANZSRC code: 020404 Electronic and magnetic properties of condensed matter; superconductivity (10%)
ANZSRC code: 030602 Chemical Thermodynamics and Energetics (30%)

Fields of Research (FoR) Classification

FoR code: 0204 Condensed matter physics (40%)

FoR code: 0306 Physical chemistry (incl. Structural) (30%)

FoR code: 0307 Theoretical and computational chemistry (30%)

To my beloved parents

Table of Contents

List of Figures

List of Tables

List of abbreviations, letters and symbols

Abbreviations	
4(H1-MVG)	Material studied in chapter 5, with 4 repeated H1-MVG in the supercell
24VG	Vacancy in graphene sheet with 24 carbon atoms extracted
AA	Type of stacking for the layers (graphene based) where the sheets are directly over each other
AB	Type of stacking for the layers (graphene based) where the sheets are shifted with respect to each other
BZ	Brillouin zone
CDD	Charge density difference
CIB	Calcium ion battery
CPU	Central processing unit
DFT	Density functional theory
DOS	Density of states
DV	Di-vacancy
F-GNR	Edge-functionalised graphene nanoribbons
G	Graphene
GGA	Generalised gradient approximation method
GY	Graphyne
GDY	Graphdiyne
GKZ	Gaddam Kumar Zhao
GNR	Graphene nanoribbon
GO	Graphene oxide
H-DG	Hydrogenated defective graphene
H1-MVG	Mono-vacancy with 1 hydrogen bound to the under-coordinated carbon atom
H12-24VG	24 vacancy with 12 hydrogen bound to the 12 under-coordinated carbon atoms
HF	Hartree-Fock method
IBZ	Irreversible Brillouin zone
KS	Kohn Sham
LDA	Local Density Approximation
LIB	Lithium ion battery
MEP	Minimum energy pathway
MV	Mono-vacancy
NEB	Nudged elastic band method
NIB	Sodium ion battery
NS	Not stable (site)
PAW	Projector augmented-wave
PBE	Perdew-Burke-Ernzerhof (for GGA method)
PBC	Periodic boundary condition
PDOS	Partial density of states
QV	Quad-vacancy
r-GO	Reduced graphene oxide
SCF	Self-consistent field
TDOS	Total density of states
TS	Transition state
TV	Tri vacancy
USSP	Ultra-soft pseudopotential
VASP	Vienna Ab initio Simulation Package
vdW	van der Waals forces
Letters	

A, B	Coefficients appearing in the wave equation
c_{k+G}	Fourier series coefficients for the Bloch wave function
d	Interlayer distance between the layers
E	Energy, eV
E_0	Ground state energy of the system obtained from SCF cycles
E_b	Binding energy (eV)
E_c	Energy due to correlation (interaction between opposite spin electrons)
E_{coh}	Cohesive energy of metals (eV)
E_{kin}	Kinetic energy (eV)
E_{min}	Ground state energy of the system obtained from ionic minimisation cycles
En	Cut-off energy in POTCAR files
E_x	Energy due to exchange (interaction between the same spin electrons)
E_{xc}	Energy of exchange – correlation
$\hat{E}_{kin}$	Kinetic energy operator
F	Faraday's constant = 9.648×10^4 C mol^{-1}
$\mathbf{G}$	Reciprocal space lattice vector
$\hat{H}$	Hamiltonian operator
k	Wave vector in reciprocal space
k_B	Boltzmann constant = 1.381×10^{-23} m^2 kg s^{-2} K^{-1}
m	Mass
M	Metal
n	Number of atoms
n_e	Number of valence electrons
N_e, N_A	Number of electrons and nuclei
$\hat{p}_x$	Momentum operator in x direction
$\mathbf{r}$	Coordinates (positions) of electrons
$\mathbf{R}$	Coordinates (positions) of nuclei
t	Time
T	Temperature
$u_k(\boldsymbol{r})$	Periodic function
U	Potential energy
$\hat{U}$	Potential energy operator
x, y, z	Axis labels in Cartesian coordinators
Greek letters and special characters	
Δ	Difference
∇	Gradient
∞	Infinity
Φ	Electrostatic charge potential
$\boldsymbol{\Psi}$	Wavefunction (time-dependant)
ε_{xc}	Exchange correlation energy per electron
ϵ_0	Electric permittivity of free space (vacuum) = 8.854×10^{-12} C^2 N^{-1} m^{-2}
$\hbar$	Planck constant (6.62×10^{-34} J s)
ρ	Density
χ	Plane wave symbol ($e^{ik.r}$)
ψ	Wavefunction (time-independent)
μ_B	Magnetic moment (Debye)
Subscript	
0	Ground state
A	Nuclei
ad	Adsorption
b	Binding
c	Correlation

coh	Representing cohesive energy
cut	Representing cut-off energy
e	Electrons, or charge of electrons
ext	External
f	Fermi level
f	Formation
G	Reciprocal space lattice vector
H	Hartree
i, j	Enumerator
i	Unit imaginary number
int	Interaction energy
k	Wave vector in reciprocal space
kin	Kinetic
KS	Kohn Sham
M	Metal
n	Number of atoms
S	Substrate
x	Exchange
xc	Exchange-correlation
Superscript	
non-int	Non interacting

Chapter 1

Introduction

Rechargeable batteries are among the main instruments used for electrical energy storage in many modern devices, including mobile phones, laptop computers, electrical toothbrushes, cars, and heart pacemakers. Furthermore, rechargeable batteries function as a medium for clean energy storage and as a receptacle for the later release of that energy, which renders them highly convenient for both large and small applications. Rechargeable batteries can be charged and discharged many times, though this process has a limit, known as maximum 'cycling' of the cell. Their rechargeability is the main advantage of these over single-use batteries, which renders them favourable for many users, both economically and operationally [1, 2]. One of the key specifications of rechargeable batteries is the discharge time: The longer, the better. Discharge time is directly related to several factors, including electrical capacity of the anode material, type of electrolyte, diffusion coefficient of the mobile ions, cathode type, and rate of reaction, etc. Higher electrical capacity can be attained through a higher number of charge transfer agents (like lithium, sodium or calcium) that are adsorbed over a specified area of anode material. So far, many rechargeable battery types have been used, such as lead-acid, nickel cadmium, nickel metal hydride, lithium-sulphur and lithium ion batteries [3, 4].

However, lithium ion batteries (LIBs) have attracted greater interest and higher usage since their invention in the 1990s [3], which is mainly due to their relatively high gravimetric and volumetric energy, high power density, long life cycle and low self-discharge properties [5]. On the other hand, owing to the fact that lithium has limited natural reserves and is expensive to produce, research on new charge transfer agents, like sodium (Na) and calcium (Ca), has become increasingly widespread [6]. These metals are abundant in nature and cheap to produce; however, the usual carbonaceous materials do not adsorb these metals adequately. Graphene has been used for many years as the primary two-dimensional (2D) carbonaceous material—it has been used as an anode material for lithium ion batteries, with a theoretical capacity of 372 mA h g^{-1}. One of the reasons for its use is that graphene has high flexibility, good electrical conductivity, large surface area, and high values of charge mobility in lithium ion batteries [5]. However, it is not a suitable anode for Na and Ca metal ions, mainly due to its low binding energy values [7]. Therefore, the search for new materials with higher capacities, and higher discharge time as a result, is still ongoing [6, 8]. Considering all these issues, in selection of new materials for rechargeable metal ion batteries a number of matters need to be considered:

1- Open cell voltage,

2- Electrical capacity,

3- Charge and discharge times,

4- Durability and stability,

5- Safety, and

6- Sustainability.

In this PhD thesis, we search for new carbonaceous materials that maximise the adsorption of Na and Ca ions, which are likely to constitute the next generation of charge transfer agents. These materials are graphdiyne (GDY), defective and hydrogenated defective graphene (H-DG), graphene nanoribbons with different oxygen functional groups at their edge (F-GNR), along with oxygen functional groups on the basal plane of graphene sheet to simulate the structure of reduced graphene oxide (r-GO). In addition, barriers of energy against the movement of metal ions, expansion of the layers as a result metal ions' intercalation, the possibility of metal sheet formation over the substrate, adsorption of potassium (K) on the

oxygen functional groups, and the effects of different oxygen functional groups in F-GNRs on the physical properties of ribbons, such as magnetic states and density of states, are presented.

1.1 Background

1.1.1 Chemical mechanism of rechargeable batteries

Rechargeable batteries have three major components: cathode, anode, and electrolyte. Figure 1.1 depicts a schematic of a typical lithium ion battery. One of the main mechanisms in these types of cells is the movement of lithium ions between the anode and cathode during charge and discharge cycles. During discharge, Li ions migrate from the anode to the cathode through the electrolyte [2]. Graphite has been widely used for LIBs as anode materials, where each Li is adsorbed by 6 C atoms (LiC_6 represents the empirical formula) [5, 9], with a typical arrangement shown in Fig. 1.2. As shown in the figure, on top of the hexagonal ring is established to be the most favourable site for Li binding, as confirmed by Chan et al. [10].

The following reactions occur during the charge-discharge for a typical LIB that uses graphite and $LiCoO_2$ [2, 5]:

Graphite: $$Li_x\ C_6 \rightleftharpoons xLi^+ + xe^- + C_6 \quad (1.1)$$

$LiCoO_2$: $$xLi^+ + xe^- + xCoO_2 \rightleftharpoons xLiCoO_2 \quad (1.2)$$

Li^+ moves between the anode and cathode through the electrolyte, which acts as an intermediate medium. Following that, Li diffuses within the porous media of the electrodes. Electrons, on the other hand, travel through the external circuit, providing electrical energy. The forward reactions (oxidation of Li to Li^+ and reduction of Co(IV) to Co(III)) occurs during discharge and the reverse reactions occur during charging. The charging process is driven by an external electrical power and results in intercalation of the Li in the graphite.

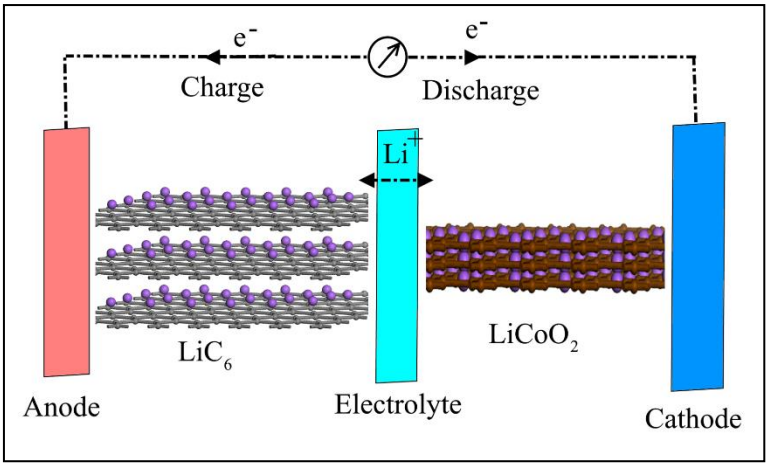

Fig. 1.1. A schematic diagram of a lithium ion battery (LIB)

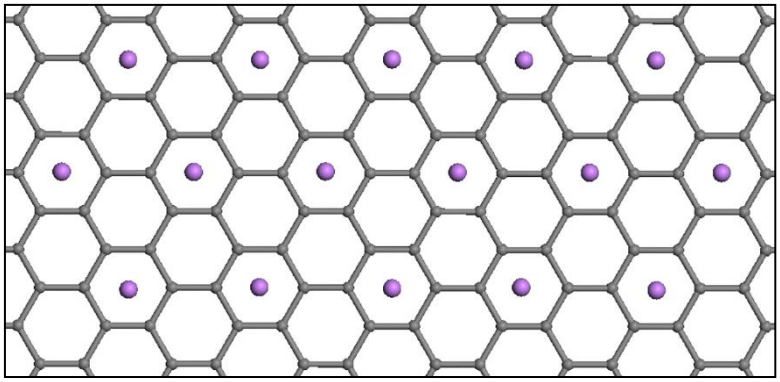

Fig. 1.2. Li atom adsorption over graphene with the empirical formula of LiC_6

1.1.2 Problems of lithium in battery technologies

As already mentioned, Li is light and small, which renders it very suitable for rechargeable batteries [5]. However, it is rare in nature, which makes it expensive to produce [6, 11]. Moreover, LIBs are normally categorised as dangerous goods in cargo freights because short circuits may occur due to dendrite formation of Li, which can cause afire [12-14]. For example, Barai et al. [12] conducted an experiment with a cell made of graphite/$LiFePO_4$. They observed sudden sparks, fumes, and fire for voltages higher than 2.3 V. They also investigated the problem of short-circuiting because of dendrite formation under different conditions for LIBs. Therefore, they suggested a protocol for removing 99.1% of the total stored energy for long-haul transportation of LIBs [12].

1.1.3 Na and Ca cations, advantages and disadvantages

For the first time ever, in 2000 Stevens and Dahn [15, 16] inserted sodium into disordered hard carbon materials for sodium ion batteries (NIBs), producing an electrode with a reversible capacity of 300 mA h g^{-1}. The experiments showed an increase in interlayer spacing of the layered material as well. Since then, a large number of theoretical and experimental studies have been conducted for NIBs for better materials and performance [6, 8, 11, 17-19], although we do a thorough review on different features of NIBs and calcium ion batteries (CIBs) in Chapter 2. The reason for the selection of Na as an alternative to Li is the greater abundance of sodium in nature, and consequently, it's less expensive to produce. Therefore, NIBs are more economical for end-users [6]. The same things hold for Ca; it is abundant in nature, and even more so than Na. Furthermore, it has a negative-two charge [20-22]. Therefore, the electrical capacity of calcium ion batteries (CIBs) is theoretically higher than NIBs, which have the same number of ions adsorbed on anode material, because Ca is multi-valent, without having double the mass. This is considered an advantage of Ca over Na. However, calcium ion batteries are very difficult to produce because the materials of the anode, cathode and electrolyte should be carefully selected to avoid electrode instability, chemical decomposition and Ca electroplating [19, 21, 23].

The main challenge of Na and Ca is their incompatibility with graphite, which has been traditionally used for commercial LIBs [5, 9, 24]; this is mainly due to the small interlayer distance of graphite (3.35 Å) for such large alkali Na and alkaline earth Ca adatoms to intercalate [15, 25]. Moreover, Na and Ca are not capable of strongly binding with the graphene sheet [7]. For example, binding energies (E_b) of -0.462 and -0.632 eV were reported by Chan et al. [10] for Na and Ca binding over a hexagonal ring of graphene, respectively. These values are not strong enough because they are higher than the corresponding cohesive energies of Na and Ca in their bulk structures, at -1.113 and -1.840 eV, respectively [10]. Consequently, clusters of metal atoms may form above the substrate. In contrast, Li can bind strongly to the graphene sheet and intercalate into the graphite layers to form LiC_6 [9]; this is why graphite has been used as an anode material in commercial LIBs since 1990 [3].

1.2 Scope of our work: proposing suitable materials for Na and Ca

The limitations and obstacles of Na and Ca were discussed in sec. 1.1.3, although we note that many carbonaceous and non-carbonaceous types of materials have been proposed for anodes

of NIBs so far [6, 8, 11, 17-19]. However, achieving a high electrical capacity (i.e. more than 372 mA h g^{-1} for Li on graphite [5]) has been challenging due to the large size of Na atoms. In addition, only a few materials have been proposed for CIBs [26]. These findings constitute motivation for us to search for new materials for NIB and CIB. Due to the afore-mentioned benefits of graphene-based materials for LIBs, we are mainly focused on these types of materials to render them suitable for the binding of Na and Ca, intercalation, and convenient movement. Based on our literature review, there are four main methods that show promise in their ability to achieve this purpose. They are summarised, as follows:

7- Creation of large regular geometrical pores, created by carbon chains, like graphyne and graphdiyne [27-29].

8- Creation of defects on the graphene sheet, like mono-vacancies or di-vacancies [30-34].

9- Add chemical functional groups, such as hydroxyl or carbonyl, to the base or edge of graphene sheets or graphene nanoribbons (GNRs) [35-37].

10- Doping of new atoms, such as nitrogen, in the carbon sheet [38-41].

In the current thesis, we search for new materials produced by the first three methods. Fig. 1.3 depicts our proposed materials in this thesis: Graphdiyne (GDY, Fig. 1.3a), hydrogenated defective graphene (Fig. 1.3b), and oxygen functional groups at the edges of GNRs (Fig. 1.3c). We thoroughly investigate these proposed materials in conjunction with Na and Ca adsorption.

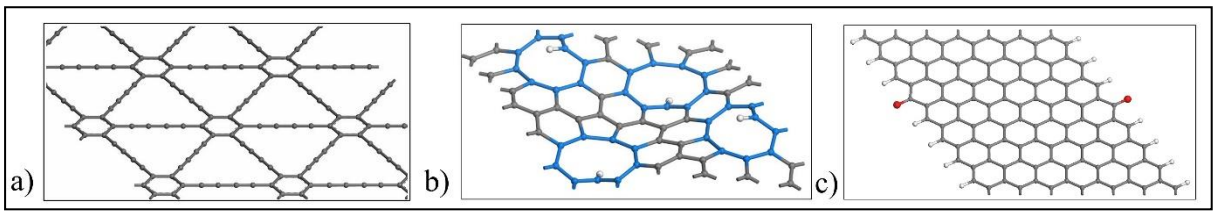

Fig. 1.3. A typical view of a) Graphdiyne (GDY), b) hydrogenated mono-vacancy graphene sheet, c) zigzag graphene nanoribbons with hydrogen and oxygen atoms at the edge

1.3 Thesis content

The current thesis first presents a literature review and provides a background of the proposed materials, followed by a methodology. Then, it considers the major results of Na and Ca adsorption on the three proposed materials of GDY, defective and hydrogenated defective

graphene (H-DG), graphene nanoribbons with oxygen functional groups at the edges (F-GNR), and finally oxygen functional groups in the basal plane of graphene sheet as a case study.

In Chapter 2, we present a thorough literature review of LIBs, NIBs, CIBs, and potassium ion batteries (KIBs). This is followed by the history of GDY, defective graphene and hydrogenated defective graphene, GNRs, and finally, r-GO, with focus on the effect of oxygen functional groups in adsorbing alkali metals for battery purposes.

In Chapter 3, we present an extensive review on the methodology that we have used in this project, Density Functional Theory (DFT) which is one of the methods used for first-principles calculations in quantum chemistry. The calculation package that we have used for this study is the Vienna Ab initio Simulation Package (VASP) [42]. We provide a brief introduction to it, with a summary of input files and parameters in the Appendices 2A and 2C.

In Chapter 4, we present the results and analyses of the first topic mentioned in sec. 1.2, which is the adsorption of Na on graphdiyne (GDY). It presents the results of adsorption of Na over the pores and rings of GDY in both single layer and bulk layers. The results indicate that 7 Na atoms can bind with a single layer of GDY in a unit cell as well as bulk layers (with empirical formula of $NaC_{2.57}$), provided that the layers are allowed to expand. Therefore, expansion naturally occurs because of Na intercalation to the layers [28]. We also present the result of energy barrier calculation against Na movement in different directions in single layer and bulk layers of GDY.

In Chapter 5, we investigate the second topic, the adsorption of Na over hydrogenated defective graphene with mono-vacancies. Based on the good performance of hydrogen containing carbonaceous materials in adsorbing alkali metals, like Li [43] or Na [16, 44], we investigate the adsorption of Na and Ca on the proposed hydrogenated graphene sheet with a number of mono-vacancies. Having had an apical C-H bond in the vacancy of the substrate (hydrogenated defective graphene) [45], this material showed very good performance in adsorbing Na and Ca over a single layer. However, Ca showed a better performance in intercalation within bulk layers, with some side expansion. Indeed, this is due to the apical C-H bonds in the graphene plane that caused expansion.

In Chapter 6, we present the results of Na and Ca adsorption over the rings and specifically functionalised edge of the graphene nanoribbons (GNRs) [46]. We considered the two major types of GNRs: zigzag and armchair. These GNRs were functionalised at the edge with oxygen-containing functional groups of HO- (hydroxyl), O- (carbonyl), and HOOC- (carboxyl), and

we measured the E_b values of Na and Ca binding over and in front of these groups. This was done with a single atom as well as a number of atoms in various spots. The results indicated that carbonyl and carboxyl groups showed the strongest binding with Na and Ca. This finding suggests that these chemical functional groups on the edge of the GNRs enhance the binding of Na and Ca atoms, which is applicable in rechargeable batteries.

In Chapter 7, we first present the results of our collaborative work with an experimental group in the School of Chemical Engineering at The University of Queensland, which pertains to the adsorption of Na over nitrogen-containing functional groups available in the nitrogen-rich hard carbon or *N*-HCS [39]. According to the results, Na showed strong binding to the amide and pyridine groups in the graphene sheet. Second, we present the result of Na, K and Ca binding to the oxygen-containing functional groups available in the basal plane of r-GO. We mainly did this part to evaluate the performance of r-GO acting as anode, as reported in previous work [47, 48]. Finally, we present the results of adsorption of K over the oxygen functional groups at the edge of GNRs, similar to what we did in Chapter 6. We conducted this study to analyse the performance of K adatoms over cellulose based material as anode of KIB. According to the results, K showed strong binding over oxygen groups, both on the base and the edge of GNRs.

In Chapter 8, we summarise and bundle the notable results of all previous chapters (4 to 7) and provide advice to the experimental researchers in this field. We also propose some areas in the same field for theoretical study to search for new materials for rechargeable batteries.

Chapter 2

Literature Review

In this chapter, we review the literature related to the proposed materials for rechargeable batteries. In section 2.1, we do a general review of the prominent anode materials for LIBs. Some of the materials are commercially used in batteries, especially carbonaceous materials used in LIBs. Therefore, we review the properties of the metal atoms that are applicable in our project (Na, K and Ca), and then briefly review recent advancements in materials for NIB, KIB, and CIBs. In sections 2.2 to 2.4, we specifically review the literature regarding the materials in our project, namely, graphdiyne (sec. 2.2), defective graphene (sec. 2.3), hydrogenated defective graphene (sec. 2.4), reduced graphene oxide (r-GO) and graphene nanoribbons (GNRs), with oxygen functional groups at the edge (F-GNRs, sec. 2.5).

In this thesis, we only focus on anode materials, although the choice of cathode and electrolyte are also crucial for the performance of a rechargeable battery. For the cathode, materials such as $LiCoO_2$, $LiMn_2O_4$ and $LiFePO_4$ are commonly used [5]. A comprehensive list of proposed cathode materials can be found in the review papers [17, 49-52].

In terms of electrolytes, there are a variety of electrolytes that exist in solid or liquid states that are capable of transporting ions; this, in turn, affects the time of charge and discharge. For solid

state batteries, solid electrolytes are more efficient, safer against leakage, less flammable, and provide a better lifetime [24]. Lithium-based polymeric solid-state electrolytes, such as LiPON, $LIBO_2$ and LiPON), fall under this category.

2.1 Anode materials for metal ion rechargeable batteries

2.1.1 Carbonaceous anode materials for lithium ion batteries (LIB)

As discussed in Chapter 1, LIBs are widely used as rechargeable batteries. A comprehensive review of LIBs and their different components (anode, cathode, charge transfer ions, and electrolyte) can be found in many review papers and books (see, for example, [5, 9, 24, 46, 53, 54]). Graphite has been the most common carbonaceous material used as an anode of LIBs where the theoretical capacity is one Li for every 6 C atoms, giving an empirical formula of LiC_6 [5, 9], and corresponding to a specific capacity of 339 mA h g^{-1}. For a carbon electrode of a metal ion battery, the capacity in mA h g^{-1} can be determined using the following equation:

$$C_E\ (mA\ h\ g^{-1}) = \frac{n_e\ n_M\ F}{3.6(n_M m_M + n_C m_C)} \qquad (2.1)$$

where m_M and m_C are the atomic masses of the metal (M) and carbon (C) atoms; n_M and n_C are the number of metal and carbon atoms in the empirical formula and F is Faraday's constant, equal to 9.648×10^4 C mol^{-1}. The value of n_e is given by the valency of the metal atoms (e.g., 1 for Li, Na, K, and 2 for Ca). Note that the capacity is often calculated with the mass of the metal atoms excluded from the denominator of (2.1), in which case a capacity of 372 mA h g^{-1} will be obtained for LiC_6 [5, 9]. Due to these two different definitions of capacity, care must be taken when comparing the capacities stated in different references. In this thesis, we will use the Eq. 2.1, unless otherwise specified.

Generally, we can categorise the proposed anode materials for LIBs into two major groups: carbonaceous and non-carbonaceous materials. In addition to graphite, the carbonaceous materials include graphyne and graphdiyne [27, 29, 55], defective graphene [32, 34], reduced graphene oxides [36, 56-58], nitrogen doped/containing carbon [38, 59], and many others [60, 61]. The non-carbonaceous materials include metal oxides (MO_x), phosphides (MP_x), metal nitrides (MN_x), metal sulphides (MS_x), and titanium oxides (TiO_2) [5, 17].

The interaction between the metal adatoms and substrate should be physisorption, because chemisorption renders the desorption of adatoms more difficult during discharge. The

boundary between physisorption and chemisorption has been approximated as 2 eV atom^{-1} [62]. Nonetheless, the binding or adsorption energy is dependent on the type of anode material and charge transfer ions in the battery. We define the binding energy as:

$$E_b = \frac{E_{subs.Mn} - E_{subs} - E_M}{n} \tag{2.2}$$

Where E_{subs}, E_M and $E_{subs.Mn}$ are the total energy values of the substrate as a standalone 2D sheet (graphene in this case), energy of metal as an isolated atom in gas phase, and energy of the adsorbed substrate with n metal cations, respectively.

For adsorption of Li on graphene, Garay-Tapia et al. [63] obtained a binding energy of -1.29 eV (equivalent to -29.7 kcal mol^{-1}). In a similar way, Chan et al. [10] found a binding energy of -1.096 eV (equivalent to -25.27 kcal mol^{-1})[1]. Finally, Liu et al. [7] found a binding energy[2] of -1.3 eV. These values were calculated by DFT using the VASP package, with similar methodologies, such as projector augmented wave (PAW) and generalised gradient approximation (GGA), with Perdew− Burke−Ernzerhof (PBE) methods[3]. We should note that there were some differences in their calculation methods that resulted in different values of binding. These are different supercell sizes: 4×4×1 rings, selected by Garay-Tapia et al. [63], 6×6×1 by Liu et al. [7] and Chan et al. [10]; different *k*-points: 3×3×1, selected by Garay-Tapia, 15×15×7 by Liu et al. [7] and 9×9×1 by Chan et al. [10] and different energy E_{cut} values, ranging from 400 eV to 550 eV. Moreover, only Liu et al. used van dev Waals' correction of DFT-D3 [64]. We conducted a test to observe the effects of these parameters and found that with a supercell size of 6×6×1 rings, DFT-D3, *k*-points 3×3×1, and $E_{cut\text{-}max}$ 700 eV; we achieved -1.33 eV for this binding, which agrees with Liu et al.'s value of -1.3 eV.

2.1.2 Comparison of properties of Li, Na, K and Ca

Some properties of Li, Na, K and Ca that are likely to influence adsorption or intercalation in carbon materials are presented in Table 2.1. These are atomic mass, atomic radii, redox potentials [2], 3D crystal structure, cohesive energy according to the 3D crystal structure [65],

[1] We note that Chan et al. [25] in their table reported the binding energy values as positive, which seems inconsistent with their definition and also Eq. 2.2.
[2] We estimated this value from the graphs provided in the paper [7].
[3] These methods are discussed in Chapter 3, sec. 3.3.3

and also binding energy (E_b) on a graphene sheet (based on our computations and other references). The most notable differences between the atoms are their mass, size and binding energies with graphene, compared with their cohesive energies. The atomic mass of lithium is much lower than that of the other metal atoms, which is an important consideration in material selection for portable applications. However, disadvantages, such as cost and safety, render other metal atoms worthy of consideration. According to the Table 2.1, Li has the smallest atomic radius, which makes it suitable for intercalation and diffusion within bulk materials. The Na, K, and Ca atoms are about 22%, 49% and 30% (respectively) larger than Li in radius. More notably, Na, K and Ca cations are 34%, 82%, and 32% larger in radius, respectively, compared with Li cations. Therefore, atomic size is one of the underlying reasons for difficult or impossible adsorption/intercalation of Na and Ca into graphite-based materials that have been observed in the past [7, 16, 25, 66]. One of the aims of this thesis is to consider carbonaceous materials that have larger pore sizes, which will reduce the expansion of the materials required for intercalation.

Table 2.1. Physical properties and binding energy of Li, Na, K and Ca over graphene sheet

Atoms / Properties	**Li**	**Na**	**K**	**Ca**	**Ref.**
Atomic mass	6.941	22.99	39.10	40.08	[67]
Atomic radii, Å	152	186	227	197	[2, 67]
Ionic radii, Å	76	102	138	100	[67]
Redox potential, V	Li^+ / Li: -3.04	Na^+ / Na: -2.71	K^+ / K: -2.94	Ca^{2+} / Ca: -2.87	[67]
3D crystal structure	bcc	bcc	bcc	fcc	[65]
Cohesive energy, eV	-1.63	-1.113	-0.934	-1.84	[65]
***E_b* on graphene, eV**	-1.096	-0.462	-0.802	-0.632	[10]
	-1.3	-0.7	-1.1	-0.5	[7][4]
	-1.33	-0.763	-1.261	-0.817	Our computations
Stoichiometry formula over graphene sheet	LiC_6	No binding	KC_8	No binding	[5, 68]

[4] We estimated these values from the graphs provided in the paper [7].

Another noticeable point in Table 2.1 is that, in most cases, our computed values for E_b of Li, Na and K over graphene (-1.33 eV) are most consistent with Liu et al.'s value (-1.3 eV). This result can be attributed to the fact that we have used similar parameters in most cases, except different *k*-points (3×3×1) and E_{cut} values (700 eV)[5], which caused some differences for the binding of Ca over the hexagonal ring. However, our complementary calculations indicated that the variation of *k*-points from 3×3×1 to 11×11×1 did not cause such effects.

As depicted in Table 2.1, most of the binding energies are weaker than their corresponding cohesive binding energies; this means they might create metal clusters over the substrate [69]. The only exception is K, which is capable of binding with graphene more strongly than its cohesive energy (based on our computed and Liu et al.'s E_b); this renders it interesting for using in an anode material despite its larger size compared with Na and Ca.

Liu et al. [7] did a thorough investigation of the reasons for the trends in binding energies. They did their analysis by breaking the E_b into the two following terms:

$$E_b = E_{ionisation} + E_{coupling} \tag{2.3}$$

The binding energy gives the change in energy when a metal atom comes from a vacuum to the binding site over the substrate. This process first involves the ionisation of a metal atom by taking its electron at the valence band and becoming a cation, with energy $E_{ionisation}$. This step is energy demanding, although with a decreasing trend (in absolute value) via increasing the alkali metal atomic number. Following ionisation, coupling of the cation to the substrate (negatively charged) occurs, which is an energetically favourable process with energy, $E_{coupling}$. The summation of these two terms determines whether or not the binding is favourable (energy releasing). Nonetheless, these two terms had different values for alkali and alkaline earth metals. Specifically, Na and Mg posed the lowest magnitude E_b on graphene of all the elements considered: -0.7 eV for Na and -0.1 eV for Mg. Consequently, this led to weak binding on graphene. As can be seen in Table 2.1, the binding for Ca is also low, cited as -0.5 eV by Liu et al. [7]. Therefore, it is one of our main aims of this thesis to seek new materials that increase the binding between Na/Ca and carbonaceous materials.

[5] We present our selected parameters in Chapter 3, sections 3.3 and 3.4, along with a summary of these parameters in Appendix 2C.

Another major aim of this thesis is to examine how the binding energy of these atoms can be enhanced by modifying the structure of carbonaceous materials, such as the addition of new functional groups or adatoms (like hydrogen).

According to Table 2.1, K has the largest atomic and ionic radii amongst all presented metals: it is 49% and 82% larger than Li in terms of atomic and ionic radii, respectively. However, based on the literature [7, 70], the binding energy of K over graphene ring is strong in comparison with the cohesive energy value. Therefore, theoretically, there should not be any problem binding a group of K cations on a graphene sheet and graphene derivatives. We review this issue further in relation to the literature in sec. 2.1.3.4.

2.1.3 Carbonaceous anode materials for post-lithium ion batteries

2.1.3.1. Materials proposed and used in sodium ion batteries (NIB)

Reviews of the proposed anode materials for NIBs can be found in several review papers [6, 8, 11, 17, 18]. In summary, we categorise all proposed materials for NIBs (either theoretical or experimental) in Table 2.2.

Table 2.2. The major categories of materials proposed for NIBs

Major groups	**Material Type**	**Example**	**Reference**
Carbonaceous Materials	Hard / disordered carbon	Stacked rumpled graphenic sheets	[15, 16, 19, 71]
	Defective graphene	Mono-vacancy, multi vacancies	[32-34, 69, 72, 73]
	Hydrogenated graphene	Hydrogen-enriched porous carbon nanosheets (H-PCNs)	[44, 74-76]
	Large pore materials	Graphyne and graphdiyne	[28, 77, 78]
	Reduced graphene oxide (r-GO)	r-GO composites	[47, 48, 56, 79-82]
	Nitrogen doped/containing materials	Nitrogen-rich hard carbon (*N*-HCS)	[39, 41, 83, 84]
Non-carbonaceous Materials	Metal Oxide (MO_x)	P2-$Na_{2/3}[Fe_{1/2}Mn_{1/2}]O_2$	[85-87]
	Metal chalcogenides (MX_n)	MoS_2	[88-91]
	MXenes	Transition metal carbides, nitrides or carbonitrides	[92]
	Metal sulphides (MS_x)	Ni_3S_2	[93, 94]

We have presented an overview of some selected anode materials for NIBs in recent years in Table 1A.1 (Appendix 1). As seen in Table 1A.1, the materials are quite diverse, and the variation of electrical capacities (mA h g^{-1}) is large, ranging from 60 to 1890 mA h g^{-1}. This large range can be attributed to many different factors; among the most significant is the type of substrate (anode material), or in other words, chemical composition to accept Na cations.

In the following section, we discuss some specific examples of carbonaceous materials that were proposed for NIBs. We have indicated that two major categories of the materials are carbonaceous and non-carbonaceous; however, in this thesis, we only focus on the carbonaceous material based on the graphene sheet because graphite has been widely used as a common anode of LIBs, and we are eager to see whether we can make it compatible with Na and Ca as well.

2.1.3.2. Carbonaceous anode materials proposed for NIBs

In 2000, Stevens and Dahn [15] published the first paper on a NIB. The electrode was formed using hard carbon, obtained from a glucose precursor. They achieved a reversible capacity of 300 mA h g^{-1} [6]. Following this work, in 2001 [16] they found that the main mechanism of Li and Na insertion into the carbonaceous materials are the same (with the exception of graphitic carbon), and both alkali metal atoms caused expansion of the interlayer spacing due to intercalation.

To resolve the problem of Na intercalation into the graphite-based materials, Cao et al. [25] found that the minimum required interlayer distance of any carbonaceous material must be 3.70 Å for Na to intercalate easily, i.e., with a maximum energy barrier of 0.053 eV. They proposed that hollow carbon nano-wires (HCNW), with an interlayer separation of 3.70 Å, would be suitable for Na intercalation. They found that the interlayer distance of HCNWs rose to 4.5 Å as a result of Na intercalation.

Stevens and Dahn [16] found that hydrogen-containing carbon atoms have a higher tendency to adsorb both Li and Na following re-hybridisation of the carbon atom. Similar conclusions were previously found by Dahn et al. in 1996 for LIBs with hydrogenated carbon materials as

[6] With inclusion of mass of Na into the capacity equation (Eq. 2.1), this value became 239 mA h g^{-1}.

an anode [43]. In 2016, Yoon et al. [44] showed that there is a high tendency for Na atoms to bind around hydrogen-terminated groups in porous carbon nanosheets produced by modified Hummers method[7] [95, 96].

Another approach to enhance the binding of Na to carbonaceous materials is to consider materials doped with other elements or with vacancies. In 2017, Dobrota et al. [82] published a DFT study on the interaction of Na with boron (B), nitrogen (N), phosphorous (P), sulphur (S), doped graphene, oxidised dope graphene, and graphene with a vacancy. Since a hydroxyl group on a graphitic carbon can lead to NaOH formation, they found that the hydroxyl group improves the dopant binding with Na. For example, they found that while B-doped graphene ($C_{23}B$) had an E_b of -2.05 eV, the addition of 1 or 2 hydroxyl groups (associated with B dopant and the nearby carbon atoms) strengthened the E_b to -2.36 and -2.57 eV, respectively. These calculations were carried out for 1 Na atom using DFT, (Perdew-Burke-Ernzerhof) PBE and the DFT-D2 approximation for the van der Waals (vdW) model[8] [82]. In general, they found that oxidising the materials with dopants (B, N, S and P) could strengthen the E_b of Na.

In this thesis, we focus on a number of specific carbonaceous materials to examine whether these materials can be enhanced for potential use in NIBs. We review the literature of these carbonaceous materials for NIBs in the next sections (sections 2.2, 2.3, 2.4 and 2.5). In summary, these carbonaceous materials are GDY (sec. 2.2), defective graphene, hydrogenated defective graphene (sections 2.3 and 2.4), reduced graphene oxide (r-GO), and edge-functionalised graphene nanoribbons (sec. 2.5).

2.1.3.3. Materials used in calcium ion batteries (CIB)

Many researchers have also considered calcium (Ca) in recent years as an alternative to Li [20-22], although there are fewer experiments and published papers than for Na; among the reasons for this is the larger ionic radius of Ca (99 vs 76 of Li^+, according to Table 2.1), which renders it difficult to diffuse within the host material because it requires more interlayer distances between the host material's layers. This can lead to some irreversibility in the battery's performance [23, 26, 97]. Nonetheless, calcium as a multivalent alkaline earth metal, is capable of transferring two charges of electrons ($2e^-$) to the anode material rather than one charge of alkali metals, such as Li, Na, or K. Consequently, the electrical capacity of a CIB is slightly

[7] Hummers' method is a chemical process to synthesise graphite oxide through the addition of $KMnO_4$ to a solution of graphite, $NaNO_3$, and H_2SO_4 [95, 96].
[8] For definition of PBE, DFT, and the D2 vdW model, refer to Chapter 3, sections 3.3.3 and 3.3.5.

less theoretically than twice that of NIB, assuming the same number of cations are bound to the substrate.

According to the results of Liu et al. [7], the E_b (Eq. 2.2) of Ca over a mono-vacancy (MV), di-vacancy (DV), and Stone-Wales (SW), defects in graphene are considerably stronger than the corresponding binding energies of Na. More precisely, E_b for Ca is -3.1 eV over MV, -2.6 eV over DV, and -1.5 eV over SW, whereas the corresponding values for Na are -1.8, -1.9, and -1.1 eV, respectively. The stronger binding energies over these defects and vacancies indicate another advantage of Ca over alkaline metals, such as Li, Na, or K. Nonetheless, the binding of Na over graphene sheet is stronger than that of Ca, -0.70 versus -0.5 eV, respectively [7].

There are few experimental publications on CIBs. Among these published papers, Lipson et al. [20] proposed a CIB, working with Ca/Ca^{2+}, $Na_xMnFe(CN)_6$ (dehydrated form of Prussian blue) as the cathode, and tin (Sn) as the anode, which yielded a reversible capacity of 80 mA h g^{-1} [9], and potential of 2.6 V. However, they reported that the capacity drops by up to 50% after 35 cycles. There are also some other materials suggested for CIBs [21-23, 98, 99]. For example, Tojo et al. [22] used Ca/Ca^{2+} with dehydrated Prussian blue ($K_xNiFe(CN)_6$) as the cathode. The battery yielded an electrical capacity of approximately 50 mA h g^{-1} [10], with a Columbic efficiency of about 92%. The Columbic efficiency is defined as the ratio of the charge removed from a battery during discharge, $Q_{discharge}$, to the charge that needs to be transferred to the battery to restore it to its original charged state, Q_{charge} [100, 101]:

$$\eta = \frac{Q_{discharge}}{Q_{charge}} \times 100\% \qquad (2.4)$$

Mortazavi et al. [99] used DFT to study the applicability of borophene for CIBs and other types of batteries with different transfer agents (Li, Na, Mg). According to the results, Ca showed a strong E_b of 4.03 eV[11] over borophene, which was stronger than Mg, Na, or Li's binding. However, the substrate structure (borophene) was highly deformed (or distorted), observable from a side view, due to Ca intercalation. Generally, the materials of the anode, cathode and electrolyte of the CIB should be carefully selected to avoid electrode instability and Ca electroplating [19, 21, 23].

[9] With inclusion of mass of Ca into the capacity equation (Eq. 2.1), this value became 71 mA h g^{-1}
[10] With inclusion of mass of Ca into the capacity equation (Eq. 2.1), this value became 47 mA h g^{-1}
[11] Obtained with Eq. 2.2; however, with a negative sign multiplied to the right side of this equation

2.1.3.4. Graphite and potassium ion batteries (KIB)

In 2015, Jian et al. [102] did an experimental test of KIB, using graphite as the anode. After they achieved a maximum reversible capacity of 273 mA h g^{-1}, they verified the formation of KC_8, KC_{24} and KC_{36} by using ex situ X-ray diffraction (XRD) methods. Similarly, Komaba et al. [103] tested a KIB with graphite as the anode material. They achieved a reversible capacity of 244 mA h g^{-1} for the KC_8 formation. However, we should note that none of these values are consistent with KC_8 by using Eq. 2.1. If we use this equation, we achieve a capacity of 198.3 mA h g^{-1} for KC_8.

Luo et al. in 2015 [68] conducted experiments for adsorption and intercalation of K into graphite and reduced graphene oxide (r-GO). Based on the experimental results, K intercalated into graphite in three consecutive stages: $KC_{24} \rightarrow KC_{16} \rightarrow KC_8$. XRD patterns, ex situ optical images, as well as the changed colour of the intercalated graphite, verified the actual intercalation of K into graphite. Moreover, XRD measurements showed an interlayer distance of 5.35 Å for KC_8. This is 59.7% more than graphite interlayer spacing. Finally, the battery posed a reversible capacity of 207 mA h g^{-1} [12], which was an acceptable capacity for a rechargeable battery [68]. Indeed, this result is in contrast with Na and Ca performances that could not intercalate into graphite bulk materials.

Xu et al. [70] did a theoretical DFT study using the CASTEP code, DFT-D2 for vdW corrections, PBE, GGA, USPP for pseudopotentials, and *k*-points at 7×7×4 using the Monkhorst-Pack method [13]. They reported a value of -1.54 eV for the binding energy of the KC_8 structure, but noted that they used a different definition of binding energy to that in Eq. 2.2, referring to average energy of a K atom in the bulk rather than an isolated K atom[14]. They reported -0.51 eV for this $E_{b,}$ without including the vdW corrections. They also examined other configurations, such as KC_6; however, they found a positive value for binding energy, which showed the adsorption was thermodynamically unstable for this conformation. They concluded that the values that included vdW corrections were more accurate and consistent with

[12] As we said, this value is not consistent with KC_8 formation using Eq. 2.1. If we use this equation, we achieve a capacity of 198.3 mA h g^{-1}.
[13] These methods are discussed in Chapter 3, sec. 3.3.
[14] To obtain their reported value of the binding energy that used bulk value for E_K, we need to add the E_{coh} of K (reported in Table 2.1) to the binding energy, given by our definition in Eq. 2.2. For example, the reported value of -1.54 eV becomes -2.47 eV, using the definition in Eq. 2.2.

experimental data. Overall, they concluded that K was capable of intercalating into graphite layers.

2.2 Graphdiyne (GDY)

2.2.1 Structure and properties of GDY

Chapter 4 of this thesis considers the applicability of graphdiyne (GDY) as an anode material for NIBs. In this section, we will review this material and discuss why it is of interest for this application. Following synthesis of graphene in 2004 [104] and graphyne [105], graphdiyne [106] (graph derived from graphene, where di means 2, and yne represents a triple bond) is another specific carbon allotrope. Indeed, there can be a different number of carbon atoms between the two rings in these types of carbon allotropes. Therefore, depending on the number of repeated acetylene (triple) bond in the chain, prefixes of di (2), tri (3), quad (4), etc. are added after 'graph'. For example, graphyne has only two carbon atoms (with one triple bond between them), between the two rings [55]. In GDY, the interconnection between the benzene ring is provided by 4 carbon atoms with two single and two triple (acetylene) bonds between them: $-\mathrm{C}\equiv\mathrm{C}-\mathrm{C}\equiv\mathrm{C}-$. A schematic view of the GDY network can be seen in Fig. 2.1.

There are different ways to synthesise GDY, like the cross-coupling reaction using hexaethynylbenzene [107], acetylene coupling reactions [108], or bottom-up synthesis of the nanosheets [109]. The special configuration of GDY provides large pores in the carbon network, which is potentially suitable for large atoms like Na to either diffuse throughout the layers (in-plane) or over the layers between them (out-plane). We calculated the GDY's pore area at 36 $Å^2$, which is ~5.5 times larger than that of hexagonal rings in graphene (~6.5 $Å^2$). This fact suggests that Na atoms are capable of settling in the pore area, and testing this was the main aim of the first topic of this thesis. A full description of GDY, and the structure and properties, can be found in several review papers [46, 55, 110-115]. Peng et al. [115] listed different synthesis methods as well as applications of graphyne, such as nanofillers, transistors, sensors, semi-conductors, anisotropic conductors, transistors, sensors, or field effect transistors (FETs). Furthermore, theoretically, GDY has been proposed for anode of rechargeable batteries [27, 28, 77, 116], experimentally [38, 78], and in our work, which is presented in Chapter 4 [52].

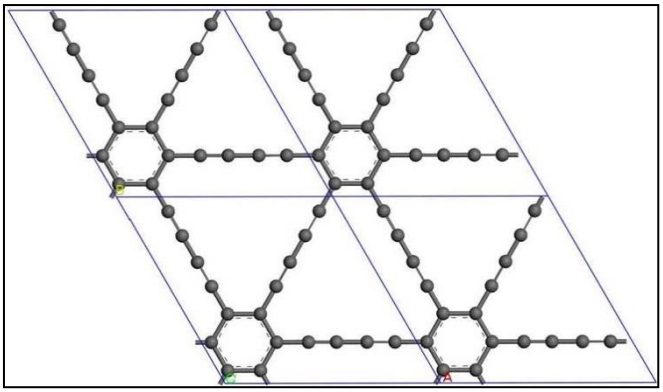

Fig. 2.1. Schematic view of GDY (prepared by Material Studio software)

2.2.2 Theoretical studies on GDY as a promising anode material

Sun and Searles [27] carried out the first theoretical study to investigate the use of GDY as an anode material for LIBs. They showed the maximum adsorption capacity of GDY was LiC_3, which is higher than the capacity of graphyne reported at LiC_4 and graphite with LiC_6 (equivalent to 339 mA h g^{-1}) [5, 27, 117]. Moreover, they indicated that the corner of the GDY's triangular pore was the most favourable place for Li to bind. They also showed that the energy barriers for diffusion of Li within the triangular pore (corner to corner or in-plane), from one pore to the adjacent pore and from one side of the pore to the other side (through the pore, or out-plane) were 0.18, 0.70, and 0.27 eV, respectively; this finding suggests that the cases with less barrier energies (first and third cases) were more likely to occur.

Zhang et al. [116] did similar work for adsorption of Li on GDY. They found the same arrangement of LiC_3 for the GDY single layer and LiC_6 for double layers. They proposed a triangular arrangement of three Li atoms on the three corners of triangular pore; it can occur on both sides of the GDY single layer and double layers, with average binding energy of 1.60 and 2.19 eV Li^{-1}, respectively. Moreover, they evaluated the energy barriers for Li diffusion from one corner of the triangular pore to the hexagonal ring, from one pore to adjacent pore (in-plane) and from one side of the layer to the other side (out-plane) at 0.72, 0.52, and 0.07 eV, respectively.

Xu et al. [77] proposed GDY as a suitable anode material for NIBs. Using a similar methodology to Zhang, et al. [116], they concluded that the arrangement of 6 Na atoms on the corners of a pore in a single layer is the most stable arrangement (NaC_3). Likewise, 6 Na atoms could be placed on top and in the middle of GDY double layers (NaC_6) as a more favourable arrangement. Moreover, having used the same transition pathways as Zhang et al. [116], they

indicated that barriers of energy are 1.09, 0.64, and 4.5 eV, respectively. The last value is for out-plane movement of Na located in the corner of the pore, which renders the movement impossible because of the high barrier.

For a more realistic approach towards the applicability of GDY for metal adatoms intercalations, it is very useful to study the stacked layers of GDY. For this purpose, Luo et al. [118] proposed a four stacking configuration of GDY bulk layers and found that the two configurations of AB stacking (AB-3 and AB-2) were the most stable stacking formation in terms of energy; these are convertible to each other, with a barrier of 1.5 meV $atom^{-1}$. They also measured the AB stacking inter-layer distance at 3.20 Å [118]. We used both AB-2 and AB-3 stacking types of Luo [118] for our GDY bulk computations in Chapter 4 [28].

Zheng et al. [119] did the same study for GDY stacking configurations and suggested that AB(β1) and AB(β2) stacking types in double layer configuration were the most stable configurations. The corresponding interlayer distances of the two mentioned configurations were 3.42 and 3.40 Å, respectively.

We extensively study the intercalation of Na adatoms within AB-2 and AB-3 stacked layers in Chapter 4, and in sections 4.4.2 to 4.4.4.

2.2.3 Experimental tests of GDY as an anode material

Huang et al. [29] experimentally tested GDY as anode of LIB for the first time. The experiment showed a maximum reversible capacity of 520 mA h g^{-1} after 500 cycles at 500 mA g^{-1}. The battery's capacity was recorded at 420 mA h g^{-1} [15] after 1000 cycles at a higher current density of 2 A g^{-1}. They measured the interlayer distance of the GDY at 3.7 Å by using a scanning electron microscope (SEM) and transmission electron microscope (TEM) [29]. Additionally, Zhang et al. [78] tested GDY as anode for NIBs. They obtained a reversible capacity of 261 mA h g^{-1} after 300 cycles at a current density of 50 mA g^{-1}. At a high current density of 100 mA g^{-1}, the electrode delivered a moderate specific capacity of 211 mA h g^{-1} [16] after 1000 cycles, with a capacity retention of 98.2% [78]. After comparing the capacities of the two recent experiments for LIB and NIB with GDY as anode, we found that the LIB posed a higher

[15] With inclusion of mass of Ca into the capacity equation (Eq. 2.1), these values became 458 and 379 mA h g^{-1}, respectively.
[16] With inclusion of mass of Ca into the capacity equation (Eq. 2.1), these values became 213 and 179 mA h g^{-1}, respectively.

capacity of 420 mA h g^{-1} against 211 mA h g^{-1} for NIB. Nevertheless, they were measured at different current densities (2 against 0.1 A g^{-1}), and also, other different experimental conditions. The same group (Zhang et al.) did similar testing of nitrogen doped GDY for LIBs [38]. They concluded that N atom insertion (by using NH_3) could create heteroatomic defects and electrochemical active sites; this resulted in enhanced electrochemical performance. The doping of nitrogen could be theoretically done in three different configurations of graphitic, pyrrolic, and pyridinc for C-N bonds. Details of these bonds can be found in other references [39, 120]. According to the results of energy-dispersive X-ray (EDX) and X-ray photoelectron spectroscopy (XPS), Zhang et al. found that N/C ratio varied from 11.1% to 13.5% in their prepared films [38].

2.3 Defects and vacancies in graphene

2.3.1 Structure, properties and synthesis of defects and vacancies

Typical defects and vacancies in graphene sheets are Stone-Wales (SW) defects, mono-vacancies (MV) and di-vacancies (DV) [30]. In addition, there are larger vacancies, such as tri-vacancies (TV) and quad-vacancies (QV). Fig 2.2 shows a schematic view of the SW, MV, DV, TV, and QV in a graphene sheet.

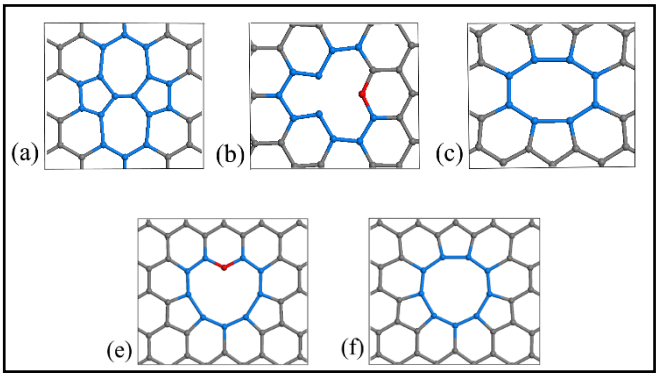

Fig. 2.2. Schematic views of the a) SW, b) MV, c) DV, d) TV, and e) QV. The blue coloured atoms indicate those carbon atoms surrounding the defect or vacancies, and red coloured carbon atoms indicates carbon atoms with dangling bond (or under-coordinated atom).

Much work has been published on defective graphene, conditions that result in formation of vacancies, and experimental methods to create them [30, 31, 121-125]. Since we will propose a material based on the vacancy containing graphene in Chapter 5, we will review some of this work here.

Hahn and Kang [121] produced vacancies in graphene layers by bombarding it with Ar^+ ions, with energies of 40 to 80 eV. In addition to the vacancies, some protrusions appeared after ion radiation, with average diameters between 6.3 and 13.1 Å. They also found that high-energy radiation (more than 1,000 eV) can destroy the graphene surface, which is problematic in defect creation. Moreover, low energy beams (less than 100 eV) remove only a few carbon atoms from the layer, leading to MV or DV.

Hashimoto et al. [31] published high resolution TEM images of defective graphene layers and carbon nanotubes. The creation of defects was experimentally proven, showing that electron bombardment of nanotubes led to creation of nonuniform single walled carbon nanotube (SWNT) [31], and both semiconducting and metallic nanotubes were produced. The same method produced a pentagon-heptagon defect in the carbon nanotubes [31]. They also showed that the existence of defects, vacancies (such as MV or DV), and carbon adatoms on the graphene layers (created by electron irradiation), can be numerous and stable at ambient conditions.

Clarsson and Scheffler [122] deployed a DFT study for computations on the MV, DV, TV and QV. Vacancies with an odd number of carbons removed have one dangling bond on a carbon atom (Fig. 2.2b and e). However, vacancies with even numbers of missing carbons do not have a dangling carbon atom and form a ring or eclipse configuration (Fig. 2.2c and f). Moreover, they found that the bond length around the vacancy could be higher than the normal C-C bond. They varied between 1.42 to 1.8 Å, with the longest bond being about 30% higher than the normal bond length in graphene [122]. Therefore, the carbon atom is quite vulnerable and chemically reactive to the reacting agents, such as H- or HO- groups. In this case, the benefits of defects for adsorbing metal cations may disappear. According to our computations (in Chapter 5), the C-C bond lengths (Fig. 2.2c) are 1.44, 1.47, and 1.72 Å for the non-equivalent C around the ellipse, which is consistent with the results of Clarsson. In addition to this, we show in Chapter 5 that DV is not suitable as an anode material due to the high difference in binding energies of Na at the difference sites of this material.

Banhart et al. [30] carried out an experimental study of the types of defects and vacancies in graphene sheets. In addition to the single-walled defects in graphene sheets, they depicted the TEM and scanning tunnelling microscope (STM) images of a MV (which underwent Jahn-

Teller distortion) and DVs in a number of arrangements[17]. However, the DV was found to be more favourable and thermodynamically stable than MV, with its formation energy equal to the MV's creation, which is about 8 eV. These formation energies become 4 eV $atom^{-1}$ in DV creation and 8 eV $atom^{-1}$ in MV creation. Therefore, DV was found to be more favourable [30]. In contrast, the energy barrier for migration of a DV to the adjacent layer (which can occur in graphene sheets) is much higher than that of a MV—7 eV vs. 1.2-1.4 eV [30]. According to Banhart et al., MV and DV are the most likely vacancies to form (following radiation of low energy beams) due to their relative low formation energies.

Some chemical methods also produce defects in graphene. For example, some highly disordered defects may be observed in reduced graphene oxide [47, 48, 126] and very large defects might be created after the annealing process (thermal heating from 1000 to 1500 K) of graphene oxide (GO) [127]. It has been found that a combination of defects with carbonyl group (-C=O) on the graphene plane and oxygenated groups (hydroxyl, carboxyl, and carbonyl) on the edges can act as highly active sites for catalytic reactions [128].

2.3.2 Defective graphene as an anode material

Datta et al. [32] used DFT to investigate the adsorption of Na and Ca adatoms on the defective graphene sheets with different concentrations of vacancies. After considering SW and DV types of defect, they found a maximum electrical capacity of 1450 mA h g^{-1} and 2900 mA h g^{-1} for Na and Ca adsorption over a graphene sheet with DV at a rate of 25%. This structure had 4 DV in a supercell, with a size of 4×4 hexagonal rings, including 24 carbon atoms. The empirical formula for Na and Ca intercalation became $NaC_{1.54}$ and $CaC_{1.54}$, respectively. Therefore, each DV had almost 4 Na atoms bound near it. First, their formulation for capacity did not include the atomic weight of Na or Ca, in contrast with our formulation (Eq. 2.1). Using Eq. 2.1, we found 646 for $NaC_{1.54}$ and 917.1 mA h g^{-1} for $CaC_{1.54}$, respectively. Second, the high number of metal cations over the substrate, as they proposed, might be expected to cause metal sheet formation, which is a hazard to the battery performance. We discuss these two issues more in Chapter 5, sec. 5.4.5.

Tsai et al. [33] studied Li and Na intercalation into disordered carbon sheets derived from graphite. First, they found that the selection of optPBE for van der Waals' (vdW)[18] correction

[17] Different arrangement of 1, 3 and 4 DVs in the vicinity of each other [30].
[18] We discuss the vdW forces in Chapter 3, sec. 3.3.5.

posed the highest compatibility with experimental data of graphene in terms of carbon-carbon bond length, interlayer distance, and also binding energy of Li over hexagonal rings [33] . They also indicated that creation of vacancies improved the potential adsorption of Na over the disordered carbon, and by increasing the interlayer distance of disordered graphene layers that contained MV or DV, the Na binding strengthened considerably [33]. They also considered the possibility of Na intercalation between the graphene layers at a distance of 4.5 Å, when one layer has a DV. This led to a configuration of NaC_8 for the layer, without any defects. In Chapter 5, we carry out a systematic study of this type of system, showing the performance of a variety of vacancies independently.

Yang et al. [73] conducted a DFT study for adsorption and intercalation of Na in the bilayer of pure graphene, and also one layer, with one MV in both AA and AB stacking types. They found that despite the weak interaction between Na and bilayers of graphene (known before), there was a high tendency for Na to intercalate into bilayers containing MV. The stacking of the bilayers was AA, and the achieved stoichiometry was $Na_6C_{35,}$ equivalent to the capacity of 382.5 mA h g^{-1}, which does not include the mass of Na. Applying Eq. 2.1, we found this capacity to be 288.0 mA h g^{-1}.

In 2016, Er et al. [34] considered the adsorption of magnesium (Mg) on graphene with a high concentration of DVs (25% defect rate, equivalent to 24 carbon atoms in a supercell of 4×4 hexagonal rings), cyclic network with C_3 / C_{12} carbon rings (which consists of 12-carbon rings in horizontal rows and a small 3-carbon ring in-between) and octagonal network with C_4 / C_8 rings (8-carbon rings in horizontal rows and a medium size 4-carbon ring in-between). The result showed a high amount of Mg adsorption could occur on the structurally defective graphene, indicating its high capability in adsorbing metal adatoms.

In 2017, Liang et al. [69] used DFT to study the possibility of Na cluster formation over pristine graphene and also DV in graphene sheet. They showed that Na ions and clusters could be stored effectively on graphene with a DV. Moreover, they found that the adsorption energy of small Na clusters near a DV decreases with increasing cluster size. We review this result further in Chapter 5, sec. 5.4.5, in relation to the Na metal formation.

2.4 Hydrogenated defective graphene (H-DG)

2.4.1 Structures, properties and theoretical background

Following the synthesis of graphene, many researchers considered doping of adatoms (like B, N or S) or chemical functionalisation with H, HO-, O=, and HOOC- groups [111, 114, 129]. For example, Casartelli et al. [45, 130] investigated hydrogenated MVs in graphene. They considered 1 to 6 H atoms (ultimately, 2 H for each C) for the three carbon atoms around the vacancy. They found that the energy of formation of materials with increasing numbers of hydrogen atoms became less exothermic. For example, adding the first H atom to the dangling bond on the carbon atom was extremely exothermic at -4.24 eV; however, it decreased to -1.21 eV for the last of the six H atoms added to the vacancy, with having 5 H adatoms [45]. Figure 2.3 a and b show a schematic view of the MV with 1 and 2 H atoms, named H1-MVG and H2-MVG, respectively:

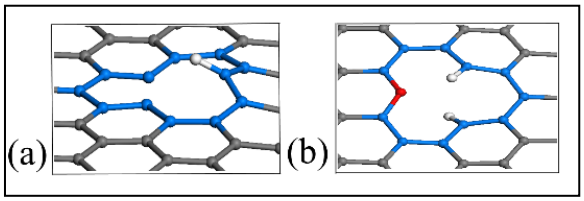

Fig. 2.3. Depiction of the optimised structure of a) H1-MVG with one apical carbon atom (1 C-H bond with length of 1.077 Å), b) H2-MVG with two apical carbon atoms (2 C-H bonds with length of 1.080 and 1.089 Å). Red colour indicates carbon atom with dangling bond on it (or under-coordinated carbon atom).

According to the Casartelli's result [130], the creation of a C-H bond on the MV, changes the bonding in such a way that the C-H bond is out of the plane of the carbon material, which is technically named an 'apical carbon atom', as shown in Fig. 2.3a. Indeed, the carbon atom lies 0.694 Å above the graphene plane in H1-MVG (Fig. 2.3a) [130]. Our result shows a similar value of 0.748 Å for this apical carbon atom. H2-MVG (Fig. 2.3b) has C-H bonds in two different directions; one is above the carbon plane and the other is below it. Casartelli called this the '*anti*' structure [45]. For a MV in a graphene sheet, a planar sheet (Fig 2.2b) is the most stable structure due to the triplet hybridisation of the under-coordinated carbon atom [130] and a non-planar sheet (with swelled dangling carbon), whereby singlet hybridisation for the carbon atom was found to be less stable. The difference in energy between these two structures (planar and non-planar) is about 0.18 eV [130]. Matsutsu et al. [131] found a similar result and explained that the planar structure is the most stable structure due to the sp^2 hybridisation of all the C carbon atoms around the vacancy.

Casartelli's result is of importance, because it indicates that hydrogenated graphene (H1-MVG) has a C-H bond that points out of the plane of the carbon sheet. This finding suggests it could be a potential alternative for a graphene sheet, since graphene could not bind with Na and Ca strongly, as discussed in sec. 2.1.2. It was found that Na or Ca binds more strongly to H1-MVG, and in addition, the apical bond would be likely to cause an increase in the interlayer spacing of H1-MVG bulk materials, accordingly. We consider this issue in Chapter 5.

Ricco et al. [132] showed that a muon can turn a C-H bond in a MV to CH-Mu (analogues to CH_2), which is chemically stable up to 1200 K. In summary, they proposed that sp^2 carbon atom in a MV has a high tendency to trap muonium or hydrogen. This theoretical study can be applicable in experimental synthesis methods of hydrogenated graphene with MV, starting from the hydroxyl group on a graphitic carbon that vastly exists in graphene oxide. For this purpose, they proposed a process for hydrogenation of MV, starting with the graphene sheet, which has a –OH group bound to one of the carbons. Following the thermal exfoliation process, a CO molecule is formed and then released. The remaining H atom attacks the highly active carbon atom in MV, and then a C-H bond forms (or H1-MVG, shown in Fig 2.3 and further specified in Chapter 5, sec. 5.4.1) [132].

Pontiroli et al. [133] studied a hydrogen atom's motion over defective graphene (or reduced graphene) obtained from the exfoliation of graphene oxide. They showed that the vacancies in defective graphene had a strong tendency to dissociate the H_2 molecule to form a C-H covalent bond, with only a 30 meV energy barrier against H atom motion. They also indicated that the zigzag edge on the reduced graphene could easily adsorb the H atom, with a low energy barrier. These results show the high chemical reactivity of non-graphitic carbons in basal vacancies and edges of the graphene sheet. Therefore, these results can lead to practical pathways toward the experimental synthesis of hydrogenated graphene.

2.4.2 Experimental tests of H-DG as an anode material

The first experimental test of hydrogenated graphitic material as an anode material was in 1995 when Dahn et al. [43] did the first tests for LIBs. They found that Li and Na had a high tendency to bind around H sites in hydrogenated carbonaceous material. They prepared this material by heating up organic precursors to 700 -1000 °C. When the precursors were heated to 1000 °C,

the maximum capacity of 300 mA h g^{-1} [19] was achievable, equivalent to each Li bound to each H atom. Following that, in 2001 Stevens and Dahn [16] synthesised a range of soft and hard disordered carbon materials that contained a significant amount of hydrogenated carbons. They showed that the main mechanisms of adsorption of Na and Li around non-graphitic carbons are the same. They also showed that most Li and Na adsorption occurs around hydrogen terminated groups. Finally, the insertion of adatoms within the layers caused expansion of the layers [16].

Chen et al. [75] proposed a method for synthesis of hydrogenated graphene by radiating the aqueous solution of graphene oxide (GO), prepared by the modified Hummers method with gamma rays. The H/C ratio of the product (HHG) was found to be between 0.35 and 0.76 (1.31 to 5.2 % wt). A reversible capacity of 670 mA h g^{-1}, with a current below 0.8 A g^{-1} and 490 mA h g^{-1} [20] at 1.0 A g^{-1}, was found in LIBs. They indicated that this high capacity could be related to the highly disordered structure of HHG, which contained many single sheets. The Li was able to diffuse and then bind to the defects and edges.

In 2015, Pramudita et al. [74] tested a sample of hydrogenated graphene (H-TEGO), with about 0.69 wt % of H as an electrode in LIB and NIBs. This sample showed a reversible capacity of 488 mA h g^{-1} for the LIB after 50 cycles, and 491 mA h g^{-1} [21] for the NIB after 20 cycles. It was suggested that the reversible capacity was enhanced due to the existence of hydrogen groups in their samples.

In 2016, Yoon et al. [44] proposed a new route to fabricate hydrogen-enriched porous carbon nanosheets (H-PCNs) suitable for anode of NIBs, in a process that used supercritical alcohol. The method first comprised oxidation of graphite through modified Hummers method, using H_2SO_4 and $KMnO_4$ as oxidisers. This step exfoliates the graphite layers, created defects, and added oxygen functional groups to the basal carbon atoms. The H/C ration in the H-PCN product was 2.3, with electrical capacity of 300 mA h g^{-1} [22] at 50 mA g^{-1}, and cycling stability of 2000 at 1-5 Ag^{-1}. They suggested that this remarkable capacity was attributed to the high number of hydrogen terminated groups and large number of defects on the sheets. They finally

[19] With inclusion of mass of Li into the capacity equation (Eq. 2.1), this value became 278 mA h g^{-1}.
[20] With inclusion of mass of Li into the capacity equation (Eq. 2.1), these values became 571 and 435 mA h g^{-1}, respectively.
[21] With inclusion of mass of Li and Na into the capacity equation (Eq. 2.1), these values became 433 and 345 mA h g^{-1}, respectively.
[22] With inclusion of mass of Na into the capacity equation (Eq. 2.1), this value became 239 mA h g^{-1}.

showed a large interlayer spacing of 3.80 Å of the material because of the high number of Na insertion.

Considering the above-mentioned experimental tests on the hydrogenated graphene materials, we were interested in determining what properties of the hydrogenated graphene rendered it a suitable material for NIB and whether it might be suitable for a CIB. Chapter 5 of this thesis explains how hydrogenation could improve the Na and Ca binding to the substrate material.

2.5 Reduced graphene oxide (r-GO) and graphene nanoribbons (GNRs)

In this section, we review the work on oxygen functional groups in graphene oxide (GO) and reduced graphene oxide (r-GO). These groups are the groups that are located on the basal plane and at the edge of graphene-based sheet or large vacancies. To simulate the effect of metal adsorption over those groups at the edge, in the next sections we review the graphene nanoribbons that have oxygen functional groups at the edge. These are related to the topics of functionalised graphene nanoribbons (F-GNRs, Chapters 6) and r-GO (Chapter 7), respectively.

2.5.1 An overview of graphene oxide (GO) and r-GO with their applications as anode materials

Yoon et al. [44] synthesised graphene oxide through modified Hummers' method [95, 96], which was used as an intermediate material to produce the final product (the hydrogenated graphene sheet). However, this material is also the main precursor in the synthesis of r-GO, with many important applications. We show a schematic view of these two materials (GO and r-GO) in Fig. 2.4.

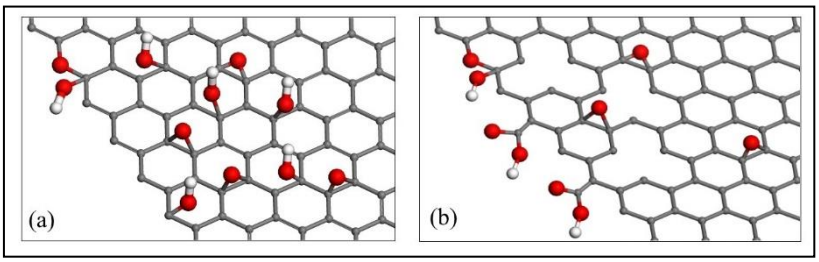

Fig. 2.4. Schematic view of a) GO with plenty of hydroxyl and epoxy groups on the base, and b) r-GO with some defects and basal epoxy groups, and ether and carboxyl groups at the edge

As seen in the two figures, the GO has many oxygen groups over the graphene sheet. In fact, GO refers to a graphene-based sheet with a variety of oxygen-containing functional groups on the basal plane or at the edge. One of the structural models is Lerf-Klinowski's model, developed in 1998 [134]. Based on this model, GO contains epoxy and hydroxyl throughout the entire basal plane or the edge, and carboxyl group at the edge [46]. Following the reduction process of GO, the r-GO produced has many vacancies in the sheet, along with fewer oxygen functional groups in the sheet because they have already been removed by reduction agents. Additionally, some of them have already migrated toward the edge of the sheets [37]. Gao et al. [135] and other researchers [46, 136-138] investigated the properties and structure of GO by using NMR or TEM spectroscopy. Gao found that epoxide and hydroxyl are the most abundant groups found in the GO. However, by applying reduction methods for deoxygenation (with $NaBH_4$) of GO, dehydration (with H_2SO_4) and then the annealing process (from 700-1500 °C), plenty of oxygen containing groups are detached from the base [135]. Following the annealing process, many defects with different sizes are created [127]. They might be small, medium or large, with or without oxygen groups that may cause many distortional effects on the sheet. The material obtained is r-GO, as shown in Fig. 2.4b. It has wide applications in battery materials, such as LIBs [139] and NIBs [47, 48], because it has basal defects with possible hydroxyl groups on top [46], some occasional epoxy on the basal plane, and carbonyl, ether, and carboxyl on the edge [36, 37, 140]. Uthaisar et al. showed that during a mild annealing process, many oxygen containing groups migrate from the base toward the edge [37]. The obtained r-GO, with lots of groups at the edge, is a very useful material for anode of LIBs because they create a strong binding for metal adatom [37, 140].

It has been found that GO with many OH groups on the basal plane is not a suitable material for NIBs. They lead to steric effects and can easily react with Na to form NaOH [82, 141]. We will show the related calculations and results in Chapter 7.

As a test to see the performance of Na on r-GO, Wang et al. [47] demonstrated that the r-GO treated at 450 °C had a good electrochemical capacity for NIBs of 174.3 mA h g^{-1} [23] at 40 mA g^{-1}. They suggested the achieved capacity was related to high electrical conductivity, large

[23] With inclusion of mass of Na into the capacity equation (Eq. 2.1), this value became 151.6 mA h g^{-1}.

interlayer distance with disordered structures of the sample, and more importantly, the effect of oxygen terminating groups (mainly carbonyl and hydroxyl) to bind Na cations.

Lamuel and Singh [56] studied the effect of thermal annealing temperature on r-GO and its Li and Na adsorbing strength. In summary, they observed a maximum Li capacity of 325 mA h g^{-1} for the specimen annealed at 900 °C. However, they observed that Na had a maximum capacity of 140 mA h g^{-1} [24] at 500 °C. They justified that high Na uptake could be related to the increased interlayer spacing (3.65 Å), large number of defects, and large surface area because of chemical oxidation, along with annealing effects. We present the calculations of Na, K, and Ca binding on oxygen containing groups that are available in r-GO in Chapter 7, sec. 7.3.

2.5.2 Structure and properties of graphene nanoribbons (GNRs)

Following invention of graphene as an important 2D carbonaceous material, study on graphene nanoribbons (GNRs) has significantly increased [46]. Studies on the chemistry of GNRs have mainly looked at edge chemistry and morphology of the ribbons, some of which are functionalised on the edge. Since 1996, there have been many publications about the ribbons [142]. A complete review can be found in Müllen and Feng [46]. GNRs have various applications, including functioning as catalysts for chemical reactions [143-145], adsorption and dissociation of H_2 [133, 146, 147], providing materials with desirable electronic and optical properties through band gap tuning [148-151], and in energy storage, such as materials for rechargeable batteries [36, 140, 152-154]. Fig. 2.5 depicts a schematic view of a GNR with a zigzag edge (a) and armchair edge (b), both with hydrogen atoms at the edge.

The nomenclature for identifying the nanoribbons and the supercell used in simulations is given in Fig. 2.5. The width of the ribbon is counted by horizontal numbers from 1 to 6 in the 6-member rings. In addition, the size of the supercell along the length of the ribbon is shown by the vertical numbers from 1 to 8 [155]. The ribbons in the supercells are referred to as 8×6 zigzag or armchair graphene nanoribbons, abbreviated to ZGNR or AGNR, respectively. We further discuss these structures and their physical properties in Chapter 6, sections 6.3.1 and 6.3.5.

[24] With inclusion of mass of Li and Na into the capacity equation (Eq. 2.1), these values became 300 and 125 mA h g^{-1}, respectively.

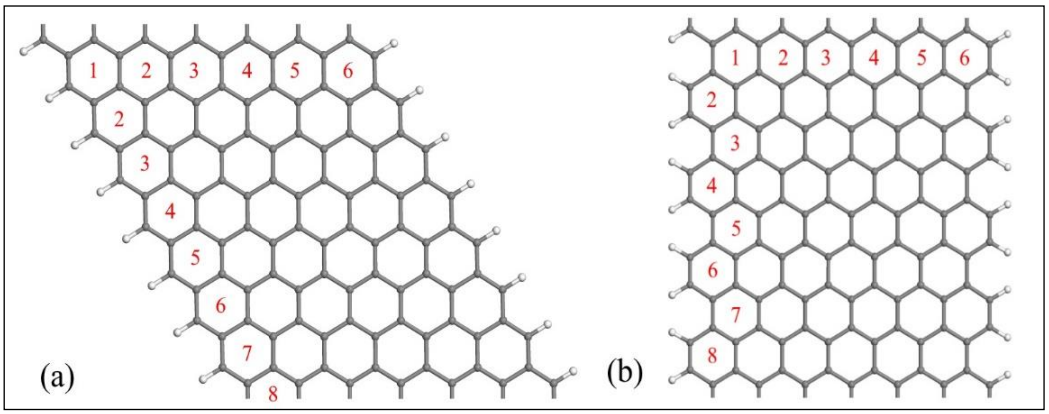

Fig. 2.5. Schematic view of graphene nanoribbons with a) zigzag edge and b) armchair edge

2.5.3 Functionalised graphene nanoribbons (F-GNR) as anode materials

In 2009, Uthaisar et al. studied the effect of hydrogenated edge of zigzag and armchair GNRs in binding Li adatoms [152]. They found that the zigzag edge adsorbs Li adatoms more strongly than the armchair edge. They also studied the effect of oxygen terminating groups on the basal plane and on the edge of r-GO and GNR [37, 140]. They found that ketone groups at the edge, compared with other groups (like hydroxyl, ether and carboxyl), had the greatest uptake of Li atoms [37, 140]. Nevertheless, in some cases when carboxyl groups existed at the edge, covalent bonding could form. Consequently, irreversibility and capacity reduction of the electrode occurs [140]. In addition, via mild heating of GO during the annealing process (best at 250 °C), the amount of oxygen containing groups on the plane, such as epoxide and hydroxyl, decreases. At the same time, these groups become more populated at the defect and edge sites [37, 56]. This has an important role in the development of new carbonaceous materials for LIBs.

Vargas et al. [156] also investigated the effect of oxygen containing groups in graphene nanosheets (GNS). They found that the mild, thermally treated graphene oxide (at 300 °C) had the highest proportion of oxygen containing groups (22.6%). These groups were mainly responsible for maximising Li ion uptake and posed an approximate capacity of 500 mA h g^{-1} [25] after 100 cycles at 149 mA g^{-1}. Moreover, this GNS posed the highest interlayer distance of 3.64 Å amongst the other GNSs obtained from other treating methods. Similar observations

[25] With inclusion of mass of Li into the capacity equation (Eq. 2.1), this value became 443 mA h g^{-1}.

(best electrochemical performance of GNS treated at 300 °C) and also increased interlayer spacing of GNS, have been observed by the other researchers [157, 158].

Xiao et al. [153] found that GNRs synthesised by the controlled unzipping of carbon nanotubes (CNTs) are superior to GNS in terms of Li uptake and Li diffusion rate. They showed that the created defects, surface area of the unzipped CNT, and presence of oxygen functional groups, played an important role in Li ions' uptake capacity. However, much of the Li binding to oxygen in GNRs was found to be irreversible [153].

Recently, Lin et al. [36] performed a DFT study on GNRs with oxygen terminating groups, like carbonyl (O=) and ether (-C-O-C-). They found that a strong adsorption of Li occurs around oxygen terminating groups at the edge, and mainly ketone groups. For ketone groups (carbonyl, C=O) the Li/C ratio was found to be 1.0, and for ketone-ether (pyrone) this ratio was found to be 0.5. Nonetheless, they found that Li uptake can be greater around epoxy and hydroxyl groups on the graphitic carbon. In those cases, the Li/C ratio was about 3 to 4, respectively [36].

We would generally expect that similar behaviour would be observed for other alkali and alkaline earth metals, so it makes sense to study the effect of other metals in greater detail. We present the results of Na and Ca binding over the hydrogen and oxygen functional groups of GNRs (or F-GNRs) in Chapter 6. We also present the results of physical properties of F-GNRs in terms of magnetic state, electrostatic charge distribution, and density of states (DOS).

Chapter 3

Methodology

In this chapter, we describe the theoretical bases of the methodology we have used in our project, the electronic *Density Functional Theory* (DFT). This method is a first-principles method that uses quantum mechanics. In this work, we use this method to find properties of materials, including the optimised structure, and its associated energy, transition states, electronic structures and charge distributions for a system. This technique has been widely used since the 1990s, and nowadays it accounts for more than 80% of computations in the field of computational chemistry; these are commonly intended for material design and transition states in chemical reactions [159]. In this chapter, we first present a brief description of the theory of intermolecular forces. Then, we briefly review mathematical operators in quantum mechanics, Schrödinger wave equations, Hohenberg-Kohn, and Kohn-Sham theories, as the bases of DFT. We follow with solid structure modelling, *k*-points sampling, plane-wave basis sets, densities of states, and transition states theories. Finally, we present the parameters of VASP package [42] that we used in our DFT computations.

3.1 Intermolecular forces

3.1.1 Introduction to the types of intermolecular or interatomic forces

Intermolecular or interatomic forces affect the physical and chemical properties of substances. They are also responsible for the state of matter, namely, solid, liquid and gas, at a given state point. These forces exist between each of two atoms or molecules. They can be categorised into the following groups [2, 160]:

1. **London dispersion forces (or van der Waals):** These occur between molecules when a fluctuation in the electron cloud around one molecule induces an instantaneous electric dipole moment on the neighbouring molecule. Therefore, a temporary attraction occurs between the molecules; these occur between all sorts of atoms and molecules. For example, they occur between a pair of CH_4 molecules that are non-polar. Moreover, the forces often become larger in magnitude when the molecule becomes larger. The energy of dispersion forces varies between approximately 0.1 and 5 kJ mol^{-1}.
2. **Dipole-dipole forces:** These occur between two polar molecules with permanent dipoles, when the positive end of a polar molecule attracts the negative end of a neighbouring molecule; this is mainly due to Coulombic forces between two particles. The energy of dipole-dipole forces varies between approximately 5 and 20 kJ mol^{-1}. For example, it occurs between CO and NH_3 molecules.
3. **Dipole induced-dipole forces:** These occur between a polar molecule and a non-polar molecule when the negative end of the polar molecule induces a dipole in a non-polar neighbouring molecule and makes it temporarily polar. For example, this occurs between acetone (H_3C-CO-CH_3) and CH_4 molecules.
4. **Hydrogen bonding forces:** In a dipole-dipole type bonding, if a molecule contains a hydrogen atom, then hydrogen bonding occurs between the H atom and highly electronegative atoms, like N, O, and F. The energy of a hydrogen bond varies from approximately 5 to 50 kJ mol^{-1}, which is generally higher than the intermolecular forces discussed above. For example, this occurs in H_2O, NH_3, HNO_3 and HF. Due to these forces, the boiling point of these compounds is higher than substances of similar size but without hydrogen bonding (H_2O has a boiling point of 100 °C but SO_2 has a boiling point of -10°C).

Intramolecular forces, existing between atoms within a molecular material, can also be categorised into the four following groups [2, 160]:

1. **Ionic forces (or ionic bonds):** These occur between atoms with low electronegativity (metals) and high electronegativity (non-metals) as a strong electrostatic force. An example of a substance with ionic forces is NaCl solid, which has a strong ionic interaction of 769 kJ mol^{-1} between Na and Cl [2]. This leads to the 3D structure of NaCl.

2. **Covalent bonds:** These occur between non-metal atoms when they share a pair of valence electrons. For example, this occurs in allotropes of carbons (diamond, graphite), O_2, and N_2. The bonding energy is normally very high, like 345 kJ mol^{-1} for a C-C single bond.

3. **Coordinate covalent bonds:** These occur when one atom donates a pair of electrons as shared electrons to the other atom. They are similar to a covalent type bond; however, the pair of electrons is supplied by one atom. For example, a metal complex, such as $[Cu(H_2O)_6]^{2+}$, has coordinate bonds from the metal to the water ligands.

4. **Metallic bonds:** These occur between metal atoms when their valence electrons are delocalised across the crystal structure. It is a kind of chemical bond that leads to the crystal structures of metals, such as the body centred cubic (bcc) structure for sodium. We investigate this bonding more in Chapter 5, sec. 5.4.5.

As discussed in section 2.1.1, the adsorption of atoms on a surface can be categorised into physisorption and chemisorption based on the binding strength; however, there is not a clear distinction between these two terms and often the adsorption is described as ‘strong physisorption’ or ‘weak chemisorption’.

3.1.2 Attractive forces

Generally when two particles are in proximity of each other, they experience forces that can be attraction forces, which cause particles to move towards each other, or repulsion forces, which cause them to move away from each other [161]. When the particles are at their optimal distance, there will be no forces between the two particles to move them. Based on the definitions of sec. 3.1, these forces can be categorised as [161]:

- **Electrostatic forces:** Between charged particles (ions) and permanent dipoles, quadrupoles and higher.
- **Induction forces:** Between a permanent dipole and an induced dipole.
- **Dispersion forces:** Between non-polar particles.
- **Specific forces:** Leads to association or solvation, such as hydrogen bonding or charge transfer complexes.

All types of particles have both kinetic energy (E_{kin}) and potential energy (U). Kinetic energy appears due to the particles' translation, vibration or rotation with respect to a fixed frame, and also, its average is proportional to the temperature. Potential energy of the particles (which are not subject to an external field) appear because of their positions relative to each other.

3.2 A brief introduction to quantum wave mechanics

In this section, we briefly review the basics of wave mechanics: The Schrödinger wave equation is proposed as the primary basis of quantum mechanics and DFT. Since the Hamiltonian is the main operator that appears in the Schrödinger wave equation, we review this operator in the following section.

3.2.1 Hamiltonian operator for many-particle systems

In quantum mechanics, the Hamiltonian ($\hat{H}$) is an operator that describes the total energy of a system while it evolves over time. It appears in the Schrödinger wave equations, and can be written as the sum of the kinetic energy operator ($\hat{E}_{kin}$) and potential energy operator ($\hat{U}$) of the system, which depends on the coordinates of the system:

$$\hat{H}=\hat{E}_{kin}+\hat{U} \tag{3.1}$$

For many particles (i=1, 2, 3, …, N), the equation takes the following form:

$$\hat{H}=\sum_{i=1}^{N}\hat{E}_{kin,i}+\hat{U} \tag{3.2}$$

where N is the number of particles. In quantum mechanics, the $\hat{H}$ operator takes the following form [162]:

$$\hat{H} = \frac{-\hbar^2}{2m}\nabla^2 + U(\mathbf{r}) \tag{3.3}$$

where $U(\mathbf{r})$ is the potential energy of the system based on the positions of all the particles in the system ($\mathbf{r}$), and $\hbar = h/2\pi$ (h is Planck constant). ∇ is the gradient and ∇^2 is the Laplacian, defined by the following equation in the Cartesian coordinates:

$$\nabla^2 = \partial^2/\partial x^2 + \partial^2/\partial y^2 + \partial^2/\partial z^2 \tag{3.4}$$

The equivalent quantum mechanical operator for classical kinetic energy can be obtained from definition of the momentum operator in a specific axis, like x , $\hat{p}_x$, which maps or projects momentum [162, 163]:

$$\hat{p}_x = \frac{\hbar}{i}\frac{\partial}{\partial x} \tag{3.5}$$

where i is the unit imaginary number $(= \sqrt{-1})$. This can be used to obtain the kinetic energy operator, stated above. Having defined the required operator that appears in quantum wave mechanics, we discuss the Schrödinger wave equations in the next section.

3.2.2 Schrödinger wave equations

At the beginning of the 20th Century, scientists were trying to determine properties of atoms and molecules, such as the exact locations of electron orbitals, electron momenta, energy states, and the frequency of the emitted beams from the atoms due to energy adsorption and release. Following early work by Heisenberg, Born and Jordan, in 1925 Schrödinger developed wave mechanics that was quite different from classical mechanics. In this theory, he formulated the wave behaviour of matter and the non-relativistic Schrödinger equation as an approach to the generalised theory of de Broglie and Bohm's theory based on *wave-particle duality* [164, 165]. The new theory could give a full description of a system and its time evolution. It considered the wave mechanics of atomic and subatomic particles (such as electron, nucleus, protons, …). However, in quantum mechanics, those particles are not considered to be classical particles, as described by Newtonian mechanics. Rather, they are considered as oscillating waves that exhibit both wave and particle behaviour. Schrödinger used the Hamiltonian operator to

combine the wave behaviour of the matter with the de Broglie equation to generate a mathematical model for finding the optimal distribution of electrons in an atom.

The following equation is the general *time-dependent* form of the Schrödinger equation [162, 166]:

$$E\,\mathbf{\Psi}(\mathbf{r},t) = i\hbar\frac{\partial}{\partial t}\mathbf{\Psi}(\mathbf{r},t) = \hat{H}\,\mathbf{\Psi}(\mathbf{r},t) \tag{3.6}$$

where $\mathbf{\Psi}(\mathbf{r},t)$ is the *wavefunction* of the quantum system, which is a function of the positions of all the particles ($\mathbf{r}$) and time (t). $\hat{H}$ is the Hamiltonian operator defined by Eq. 3.3. To obtain the time independent form of Schrödinger's equation, we assume that the wavefunction can be expressed as a product of two functions of the positions and the time. Therefore, $\mathbf{\Psi}(\mathbf{r},t)$ can split to:

$$\mathbf{\Psi}(\mathbf{r},t) = \psi(\mathbf{r})e^{-iEt/\hbar} \tag{3.7}$$

In the above equation, the new wavefunction, $\psi(\mathbf{r})$, does not have time dependence. Substitution of Eq. 3.7 to Eq. 3.6 and separating the time-independent part, leads to the general form of time-independent Schrödinger equation [162]:

$$E\psi(\mathbf{r}) = \hat{H}\psi(\mathbf{r}) = \left[-\frac{\hbar^2}{2m}\nabla^2 + \hat{U}(\mathbf{r})\right]\psi(\mathbf{r}) \tag{3.8}$$

The above equation states that when the system is time independent, the operator, $\hat{H}$, acts directly on the wave function to give scalar multiples of the wavefunction. Then, Eq. 3.8 is an *eigenvalue equation* [26].

3.2.3 Wavefunctions for a system of electrons and nuclei

The time independent Schrodinger wave equation (Eq. 3.8) for a system of electrons and nucleus can be written as follows:

[26] If L is a linear operator on a function space, then f is an eigenfunction of L and λ is the associated eigenvalue whenever $\hat{L}f = \lambda f$. Furthermore, this expression is called an eigenvalue equation.

$$\hat{H}(\mathbf{r},\mathbf{R})\,\psi(\mathbf{r},\mathbf{R})=E\,\psi(\mathbf{r},\mathbf{R}) \tag{3.9}$$

where **r** and **R** indicate the electronic coordinates of electrons and nuclei in the atomic systems, respectively[27]. Comparing with Eq. 3.8, we can write the following equation that describes the Hamiltonian for a set of atoms consisting of N_e electrons and N_n nuclei [165, 167]:

$$\hat{H}=-\sum_{i=1}^{N_e}\frac{\hbar^2}{2m_e}\nabla_i^2-\sum_{A=1}^{N_n}\frac{\hbar^2}{2m_A}\nabla_A^2-\sum_{i=1}^{N_e}\sum_{A=1}^{N_n}\frac{Z_A e^2}{4\pi\epsilon_0|\mathbf{R}_A-\mathbf{r}_i|}+\sum_{i=1}^{N_e}\sum_{j>i}^{N_e}\frac{e^2}{4\pi\epsilon_0|\mathbf{r}_i-\mathbf{r}_j|}+\sum_{A=1}^{N_n}\sum_{B=1}^{N_n}\frac{Z_A Z_B e^2}{4\pi\epsilon_0|\mathbf{R}_A-\mathbf{R}_B|} \tag{3.10}$$

Here *i* and *j* count the number of electrons, *A* and *B* count the number of nuclei, Z_A is the charge of nucleus, and A, **r** and **R** are the coordinates of electrons and nuclei, respectively. The first two terms are the kinetic energy operators for the electrons and nuclei. The last three terms are the Coulombic potentials between each pair of electron-nucleus, electron-electron and nucleus-nucleus, respectively. According to the Born-Oppenheimer approximation [168], the wavefunction of a molecule is divided into wavefunctions of electrons and nuclei [165, 167]. In this approximation, the nuclei are considered frozen relative to the electron positions. Therefore, the kinetic energy of the nuclei is zero, and inter-nuclei potential energy can be considered constant in Eq. 3.10 [167]. As a result, the wave equation of Eq. 3.9 can be separated into a nuclear and electronic equation. This leads to the following equation, which is called the *time-independent electronic wave equation*:

$$\hat{H}_{el}(\mathbf{r};\mathbf{R})\,\psi(\mathbf{r})=E_{el}\,\psi(\mathbf{r}) \tag{3.11}$$

The above equation incorporates the electron–electron interaction (collection of electrons) as well as electron–nucleus interaction (collection of electrons and collection of nuclei) depending on the coordinates of the electrons and nuclei (**r** and fixed positions **R**). Based on the Born-Oppenheimer approximation, the electronic Hamiltonian is the sum of the kinetic energy

[27] Note that in the previous sections, **r** was used to represent the positions of all the particles in the system. In the next sections, it will refer to the positions of the electrons only or the position in space, depending on the context.

operator of the electrons and potential energy of electron-nuclei and electron-electron interactions only. Therefore, we have the following equation [167, 169]:

$$\hat{H}_{el}=-\sum_{i=1}^{N_e}\frac{\hbar^2}{2m}\nabla_i^2-\sum_{i=1}^{N_e}\sum_{A=1}^{N_n}\frac{Z_A e^2}{4\pi\epsilon_0|\mathbf{R}_A-\mathbf{r}_i|}+\sum_{i=1}^{N_e}\sum_{j>i}^{N_e}\frac{e^2}{4\pi\epsilon_0|\mathbf{r}_i-\mathbf{r}_j|} \tag{3.12}$$

In order, the three terms in the above equation are kinetic energy operator for the electrons, potential energy between electron and collection of nuclei, and potential energy between all electrons. Eq. 3.12 is considered as an underlying equation for deriving the single electron model of Hartree-Fock and Kohn-Sham methods and we review them in sec. 3.2.4 and 3.3.2.

3.2.4 Hartree-Fock (HF) method

In 1930, Hartree and Fock developed the HF method based on the single electron model and mean-field concept [165]. This method was considered the early first-principles method for calculating the ground state energy (E_0) of the systems. The HF method works directly with the wavefunctions of electrons, which depends on the coordinates of all the electrons in the system and scales with the number of electrons or basis sets to some power (depending on the type of calculation and formally N_e^4 [170]). To understand the single-electron model, we briefly describe the Hartree method developed in 1928 for the single-electron model. In this model, a single electron is considered a single entity; however, repulsion forces exist between this electron and an average force coming from the collection of other electrons in a mean-field. So, there is one electron and a collection of other electrons in the mean-field. A system consisting of N_e electrons for several atoms (or many-body system) can be converted to a set of N_e 1-electron equations, summarised in a *Slater determinant*. The following equation is the Slater determinant for an N_e electron system (without the inclusion of the electron spin). This is used in the HF method for the wavefunction of single electrons [159, 165]:

$$\psi(r_1, r_2, \ldots, r_N)=\frac{1}{\sqrt{N_e!}}\begin{vmatrix}\psi_1(r_1) & \cdots & \psi_{N_e}(r_1)\\ \vdots & \ddots & \vdots\\ \psi_1(r_N) & \cdots & \psi_{N_e}(r_N)\end{vmatrix} \tag{3.13}$$

The above equation constitutes the separation of the primary wavefunction for all the electrons to the wavefunction of each electron, ψ_i. Hartree presented the self-consistent field (SCF) method to solve the wave equation for each single electron.

3.3 Density Functional Theory (DFT)

Quantum mechanics forms the basis of first-principles methods, including DFT calculations. Material scientists and computational chemists can use this method for simulating the interaction between materials' particles, atoms and molecules to find the ground state energy of material, binding energy of adsorbent and the optimised structures of atoms and molecules. DFT is generally a more efficient method than wavefunction methods as it scales with the physical size of a system rather than the number of electrons. DFT is currently feasible when the number of atoms in the primary cell are less than approximately 1000 atoms [165] (or for periodic systems, 1000 atoms in a unit cell). For more than this number, the distance and the size of the system become too large for standard computer infrastructures. In this case, force field methods might be more applicable [161].

3.3.1 The concept of electron density

Standard DFT calculations determine the ground state energy of the electronic system (E_0) based on electron density ($\rho(\mathbf{r})$) of the system. Therefore, $\rho(\mathbf{r})$ is central to the DFT method. The $\rho(\mathbf{r})$ is defined as the number of electrons (N_e) per unit volume at position $\mathbf{r}$ of the electron cloud. Therefore, the integral of electron density over all the positions equals N_e [165]:

$$\int \rho(\mathbf{r}) d\mathbf{r} = N_e \tag{3.14}$$

In contrast to Hartree Fock (HF) method that treats wavefunctions to calculate E_0, the DFT method treats $\rho(\mathbf{r})$ obtained directly from wavefunctions to calculate E_0. If the wavefunction is considered a product of 1-electron wavefunctions, the following equation describes $\rho(\mathbf{r})$ in terms of wavefunction [167, 171]:

$$\rho(\mathbf{r}) = \sum_{i=1}^{N_e} \left|\psi_i(\mathbf{r})\right|^2 = \sum_{i=1}^{N_e} \psi_i^*(\mathbf{r})\, \psi_i(\mathbf{r}) \tag{3.15}$$

The above equation is important because it relates the electronic wavefunctions of the system to the electron density of the system.

The probability of the existence of an electron in a specified volume (V) about $\mathbf{r}$ in the space, $P(\mathbf{r})$ is:

$$P(\mathbf{r}) = \frac{1}{N_e} \int_V \rho(\mathbf{r}) d\mathbf{r} \tag{3.16}$$

The product $\psi_i^*(\mathbf{r})\psi_i(\mathbf{r})$ is a probability density, so the integral of probability over all space must be 1:

$$\int_{-\infty}^{+\infty} \psi_i^*(\mathbf{r})\psi_i(\mathbf{r}) d\mathbf{r} = 1 \tag{3.17}$$

where $\psi_i^*(\mathbf{r})$ is the conjugate wavefunction [162]. The above equation (Eq. 3.17) states the *normalised* condition of the wavefunction, $\psi_i(\mathbf{r})$. The complete set of wave functions are also defined to be *orthogonal*; that is, for wave functions, ψ_i and ψ_j, the following integral holds [165]:

$$\int \psi_i(\mathbf{r})\, \psi_j(\mathbf{r})\, d\mathbf{r} = 0 \tag{3.18}$$

The above two equations (3.17 and 18) constitute two important constraints for giving a unique solution for wavefunction rather than many similar functions.

3.3.2 Single-electron model and Kohn-Sham equation

To improve the efficiency of first-principles methodologies for larger systems that consist of many atoms, predicting properties of molecules and condensed matter systems, Hohenberg and Kohn (1964) [172], and then Kohn and Sham (1965) [173], developed the DFT method. This method considered the electron density of the system to calculate the ground state energy of a system, E_0. This method also accounts for the electron's exchange and correlation [165].

The first Hohenberg and Kohn theorem (1964) [172] stated that E_0 is a unique functional of the $\rho(\mathbf{r})$ of the system, so $E_0 = E[\rho(\mathbf{r})]$, although the exact form of the functional is not known [62, 167, 169]. Their second theorem found that to determine the E_0 of the system, the $\rho(\mathbf{r})$ can be treated mathematically and optimised variationally rather than wavefunction ($\psi_i(\mathbf{r})$), as is done in the HF method. Based on these theorems and using the single-electron model of Hartree in 1961 (discussed in sec. 3.2.4), in 1965 Kohn and Sham [173] developed an approach to obtain the density and energies using DFT. They assumed that the density of a many-electron system can be taken to be equal to that of a set of noninteracting electrons (a system that is solvable). However, the Hamiltonian for the noninteracting electrons needs to be corrected to find the correct energies. The Kohn-Sham (KS) Hamiltonian takes the following form [165, 173]:

$$\hat{H}_{KS}=\hat{E}_{kin}^{non\text{-}int}+\hat{U}_{ext}+\hat{U}_{H}+\hat{U}_{xc} \tag{3.19}$$

where $\hat{E}_{kin}^{non\text{-}int}$ is the kinetic energy operator and the superscript, *non-int*, indicates the kinetic energy for the system with non-interacting electrons. $\hat{U}_{ext}$ is external energy operator or the interaction between the electron and collections of nuclei. $\hat{U}_{H}$ is the classical potential energy operator impacting each of the electrons in the mean field approximation. The last term, $\hat{U}_{xc}$, is the exchange–correlation energy operator, which is the correction term due to non-interacting electrons in the system. This is approximated by some methods (or functional) and is discussed in sec.3.3.3.

Based on the Hamiltonian of Eq. 3.19, the Kohn Sham wavefunction is obtained by solving [171]:

$$\hat{H}_{KS}\psi(\mathbf{r})=E\,\psi(\mathbf{r}) \tag{3.20}$$

Where $\psi(\mathbf{r})$ is the KS single-electron wavefunction, which is a function of position, **r**. The KS energy functional can be written as [171]:

$$E[\rho(\mathbf{r})]=E_{kin}[\rho(\mathbf{r})]+E_{ext}[\rho(\mathbf{r})]+E_{H}[\rho(\mathbf{r})]+E_{xc}[\rho(\mathbf{r})] \tag{3.21}$$

$E_{kin}[\rho(\mathbf{r})]$ can be expressed as follows [171]:

$$E_{kin}[\rho(\mathbf{r})] = -\frac{\hbar^2}{2m}\sum_{i=1}^{N_e}\int \psi_i^*(\mathbf{r})\,\nabla^2\,\psi_i(\mathbf{r})d\mathbf{r} \tag{3.22}$$

The second term, $E_{ext}[\rho(\mathbf{r})]$, describes the energy of interaction between the electron clouds and the collection of nuclei:

$$E_{ext}[\rho(\mathbf{r})]=-\frac{e^2}{4\pi\epsilon_0}\sum_{A=1}^{N_n}\int \rho(\mathbf{r})\frac{Z_A}{|\mathbf{R}_A-\mathbf{r}|}\,d\mathbf{r} \tag{3.23}$$

The following equation describes the Hartree energy or the Coulombic interactions between electrons [171]:

$$E_H[\rho(\mathbf{r})] = \frac{e^2}{2}\int\int \frac{\rho(\mathbf{r})\rho(\mathbf{r}')}{|\mathbf{r}-\mathbf{r}'|}\, d\mathbf{r}\, d\mathbf{r}' \qquad (3.24)$$

where the **r** and **r′** indicate the positions of the electrons. The exact form of the exchange-correlation functional is not known. Some of the common approximations are discussed in the next section.

After selection of the exchange-correlation functional, Eq. 3.21 can be solved for a set of single electrons and the KS wavefunctions can be found. Then, by using Eq. 3.15, the $\rho(\mathbf{r})$ is found. These calculations can be done in a loop, called energy minimisation or self-consistent field (SCF, which is further discussed in sec. 3.3.4). This loop eventually provides the converged value of $\rho(\mathbf{r})$, and by using Eq. 3.21, that, in turn, gives E_0. Kohn and Sham's findings in 1965 rendered DFT suitable for systems that consist of a much larger number of electrons than could be done with the same accuracy using wavefunction theory. The new DFT method often provided better results than the HF method (which was highly suitable for several tens of atoms) [165].

3.3.3 Exchange-correlation (xc) functionals

The exact exchange-correlation functional (appearing in Eq. 3.19) is not known, but it is necessary to approximate it well to obtain accurate results. It can be considered to consist of two terms:

$$E_{xc} = E_x + E_c \qquad (3.25)$$

where exchange energy or E_x represents the contribution due to the exchange of electrons, and correlation energy, or E_c, represents the remaining terms due to correlation. These two terms are normally negative to correct the overestimation of Hartree energy, and the magnitude of E_c is much less than the magnitude of E_x [165]. To avoid solving very sophisticated wave equations to approximate these terms, Kohn-Sham proposed approximating them using the *local density approximation* (LDA) [173, 174]. In this method, the E_{xc} functional only depends on the local density of the electrons. One example that allows the exchange energy to be determined analytically assumes that the exchange-correlation is the same as that of

homogeneous electron gas [28]. Nevertheless, the result of this functional is not usually accurate [169].

There are some other xc functionals that are more accurate, such as generalised gradient approximation (GGA), developed in the 1980s and 1990s [175, 176]. This method used the local gradient of electron density ($\nabla\rho(\boldsymbol{r})$) in addition to local electron density. Therefore, it was more accurate than LDA [165]. Depending on the gradient calculation method, there is a variety of GGA functionals. These functionals include PW91, 92 [176], PBE [177], AM05 [178], and revised PBE for solids (PS) [179] functionals. In addition, *hybrid functionals*, based on GGA methods and other parameters, such as higher-order density gradient or mixing a certain amount of non-local HF exchange energy, render them more accurate in predicting the xc potentials, but more computationally expensive. Some examples of hybrid functionals are B3LYP [180], PBE0, and HSE (Heyd, Scuseria and Ernzerhof) [165]. They are often used for accurate density of states (DOS) or electronic band structure calculations.

Perdew and Schmidt in 2001 [181], presented the 'Jacob's ladder' for approximating the exchange-correlation energy as a function of electron density. In summary, they described the E_{xc} in the following equation:

$$E_{xc}[\rho\uparrow,\rho\downarrow]=\int \rho(\mathbf{r})\varepsilon_{xc}([\rho\uparrow,\rho\downarrow];\mathbf{r})\, d\mathbf{r} \tag{3.26}$$

$$\rho(\mathbf{r})=\rho\uparrow(\mathbf{r})+\rho\downarrow(\mathbf{r}) \tag{3.27}$$

Where $\rho(\mathbf{r})\varepsilon_{xc}$ is exchange-correlation energy density, and ε_{xc} is the exchange-correlation energy per electron. The signs ↑ and ↓ refer to the two spin states of the electrons. According to the Eq. 3.27, $\rho(\mathbf{r})$ is the summation of electron density of the two opposite spin states. Depending on the theory used to construct the $\varepsilon_{xc}([\rho\uparrow,\rho\downarrow];\mathbf{r})$, Perdew and Schmidt attributed different levels to the imagined ladder with the name of those theories. At the lowest level of the ladder, local density approximation (LDA) as the simplest theory exists. At the next level, the gradient of the densities, $\nabla\rho\uparrow(\mathbf{r})$ and $\nabla\rho\downarrow(\mathbf{r})$ are added to provide more accuracy. At the next higher level, the Kohn-Sham-DFT orbitals are added which give the meta-generalized

[28] Jellium or homogenous electron gas (HEG) is a quantum mechanical model of interacting electrons in a solid where the positive charges are uniformly distributed in space, so the electron density becomes uniform throughout the space.

gradient approximation. Therefore, the higher levels give more accurate results, although more complex and time-demanding to calculate. In summary the levels of the Jacob's ladder (from lower to the higher) are [181]:

1- Local spin density approximation (LDA),
2- Generalized gradient approximation (GGA),
3- Meta-generalized gradient approximation (MGGA),
4- Exact exchange and compatible correlation,
5- Exact exchange and exact partial correlation,

As mentioned above, the methods have different levels of complexity and accuracy for the calculations of different electronic properties. For example, for band gap calculations [29] both LDA and GGA-PBE underestimate the band gap. Therefore, more complex functionals such as hybrid functionals (e.g. HSE06) or green-functions-based (GW) methods are required [182] [30]. However, these functionals are complicated and can be very time-demanding in calculations. Therefore, we always used GGA-PBE functionals in our projects due to their suitable accuracy and computational feasibility. We used these functionals as implemented in the VASP package, ver. 5.3.5 and 5.4.4. Moreover, we used the same functionals (PBE) for the outer atomic orbitals by using the default tag of GGA in VASP [42].

3.3.4 Iterative cycles of DFT in a flow chart

In this part, we give a brief description of the DFT calculation cycles and also present them in a flow chart. Additionally, we discuss how various parameters are set in VASP. DFT has two main iterative cycles:

1. The external cycle is named *geometry optimisation* or *ionic relaxation* or minimisation cycles, which arranges the atoms or ions based on minimisation of the energy. When a molecule is in a minimum energy configuration, the force upon each ion should be zero,

[29] We describe density of states and band gap in sec. 3.5.2.
[30] A full comparison between different functionals (e.g. semi locals and hybrids) in prediction of band gap for a large variety of materials are presented by Tran and Blaha in 2017 [182].

implying that the there is no force on each ion to move it around. However, in practice, it is impossible to achieve complete zero. Therefore, we define a criterion that sets the maximum allowable value of the components, F_x, F_y, and F_z. In VASP, the related tag is EDIFFG in the INCAR file [31], and we set values from 0.01 to 0.05 eV Å^{-1}, depending on the required precision in our projects.

2. The internal cycle is referred to as the *energy convergence* or *self-consistency* cycles, which aim to determine the ground state energy starting from an initial guess of $\rho(\mathbf{r})$. This test verifies the consistency of $\rho(\mathbf{r})$ with the new $\rho(\mathbf{r})$ derived from the wave KS equation (Eq. 3.20). We can impose a criterion for this cycle by setting the EDIFF tag in the INCAR file. Once self-consistency is achieved, the cycle stops and the $\rho(\mathbf{r})$ will be sent to the ionic minimisation cycle. Having done some tests for graphdiyne (GDY) in the earlier phase of our projects and made a trade-off between precision and CPU time, we selected EDIFF=1×10^{-6} eV for this tag [7]. We have used this value throughout our projects.

Fig. 3.1 depicts a schematic flow chart of the cycles [62, 165, 183], assuming a selected exchange-correlation functional. We should mention the three necessary criteria in determining $\rho(\mathbf{r})$ [165]. The first one implies that the variations of E against $\rho(\mathbf{r})$ should be less than EDIFF, corresponding to the minimum energy against $\rho(\mathbf{r})$:

$$\left.\frac{\delta E\big(\rho(\mathbf{r})\big)}{\delta \rho(\mathbf{r})}\right]_{E_{min}} < EDIFF \tag{3.28}$$

The second and third criteria are the constraint of the fixed number of electrons and orthonormality of the orbitals that we discussed in sec. 3.3.4. Based on Eq. 3.14, the integral of $\rho(\mathbf{r})$ should equal N_e (number of electrons). Moreover, all the single-electron wavefunctions must satisfy the conditions of orthonormality and orthogonality, summarised in the following equation:

$$\int \psi_i^* \psi_j \, d\mathbf{r} = \delta_{ij} \tag{3.29}$$

[31] For description of tags and input parameters, refer to Appendix 2A and 2C.

where δ_{ij} is Kronecker delta [184], which is *0* for $i \neq j$ and *1* for $i=j$. The asterisk (*) indicates the complex conjugate [165]. We note that the above equation is a simplified form of Eqs. 3.17 and 3.18.

3.3.5 van der Waals (vdW) correction

3.3.5.1 Theory of vdW forces

We reviewed van der Waals' forces in sec. 3.1.1, which are forces due to temporary dipole-dipole (or quadrupole-quadrupole) interactions between atoms or molecules. The energy due to van der Waals' interactions (E_{vdw}) comes from particles that are not directly bonded [167]. We should distinguish between the energy of vdW (E_{vdw}) and energy of electrostatic forces (E_{el}) (that are mainly due to a particle's charge) and Coulombic forces. The summation of these two types of energy equals the non-bonded energy between two particles. E_{vdw} exists in all types of substances with different intensity, such as methane, water or iron. It is notable that it is the only force that exists between the atoms of non-polar gases, such as argon. The vdW forces between noble gas atoms are often well represented by the Lennard-Jones force field. If two atoms are far from each other, the dipole moment of the outer orbital causes an attraction between two atoms, which renders the effect of vdW forces important as a long-range force. However, at close distances, the repulsion forces are dominant. The vdW attractive forces (long distances) vary with an inverse of sixth power of distance ($\sim 1/r^6$). Nonetheless, the power of distance may increase in close distance depending on the type of moments (dipole, quadrupole, etc.).

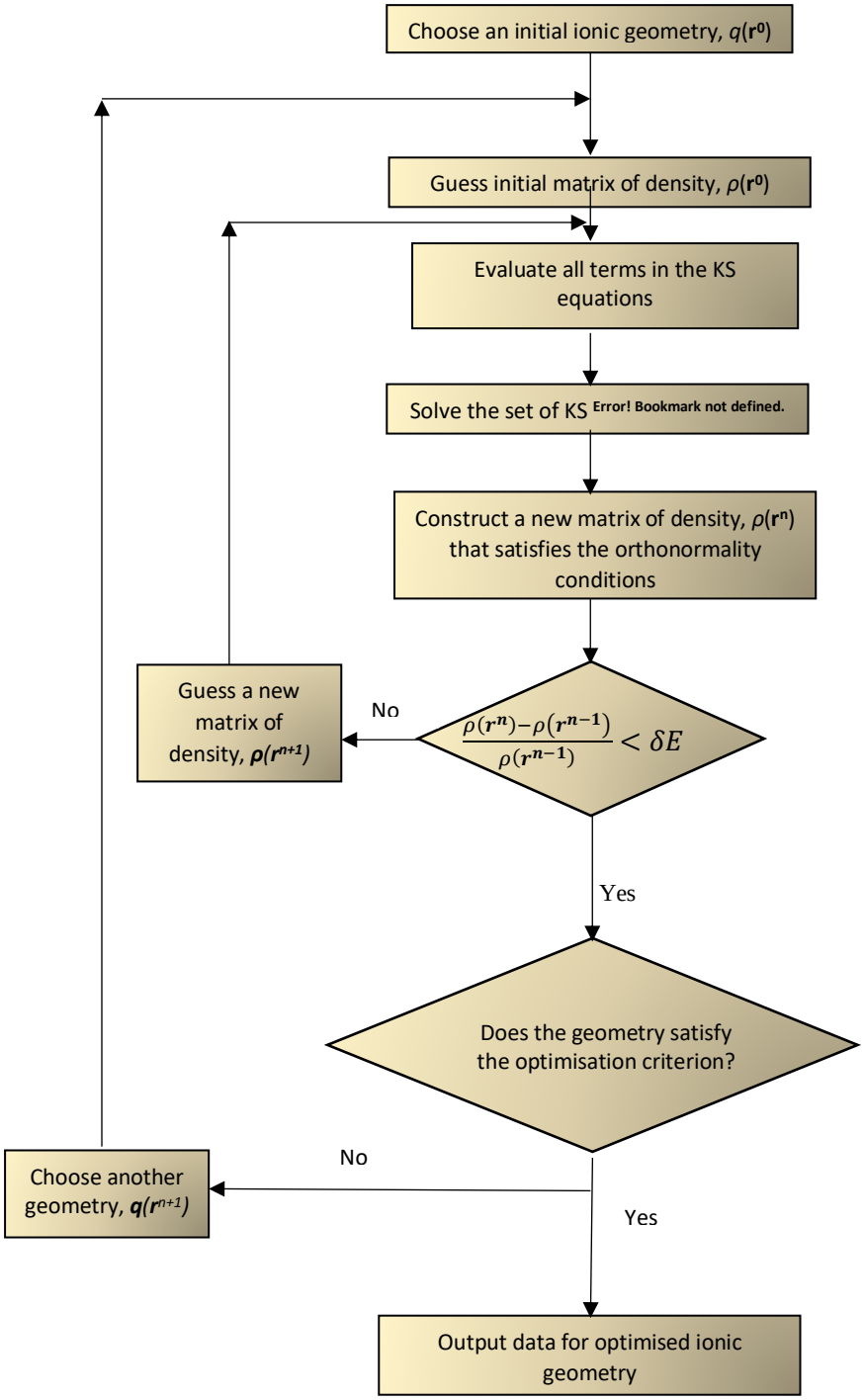

Fig. 3.1. The overall flow chart of DFT computations. The internal cycle indicates the *self-consistency* cycle, and the external cycle indicates the *ionic optimisation* or *ionic minimisation cycle* [62, 183]

In 2D graphene-based materials, vdW forces are responsible for the forces between the atoms of neighbouring layers. The vdW forces are much smaller between two neighbouring carbon atoms in the same layer than the strong interaction between them that leads to a covalent bond. vdW forces are also important between adsorbent and adsorbed adatom (like Na atoms over graphdiyne, GDY). Regarding the DFT method, the exchange correlation terms that appear in the Kohn-Sham equation do not usually represent the long-range vdW interactions particularly well. Rather, it is more concentrated on short range forces that are important for chemical bonding. Specifically, LDA and GGA types of xc functional need to be corrected to include those forces [185, 186]. In 1995, Lundqvist et al. [186] mathematically reformed the xc functionals to include nonlocal vdW forces. Following these works, much effort was made to include those nonlocal forces in the xc functionals and propose different models, such as vdW-DF xc functionals [187]. We review some of the most important models in the next section. These are partly selected due to their availability in the computer package that we use, VASP.

3.3.5.2 Comparison and selection of vdW models

VASP does not automatically set any vdW correction by default (when no tag is set). However, the designers include vdW corrections in this package. The governing equation for this incorporation can be formulated, as follows[42]:

$$E_{DFT\text{-}vdW}=E_{KS}+E_{vdW} \tag{3.30}$$

Therefore, the correction term of vdW is added directly to the KS equation. The main vdW corrections in VASP are: DFT-D2 [188, 189], DFT-D3 [64, 190], DFT-D3 [32], with Becke-Johnson damping (D3-BJ) [64, 190], Tkatchencko-Scheffler, many body dispersion, and dDsC dispersion correction methods [42]. We have only used DFT-D2 and DFT-D3-BJ throughout our project. The main reason for this is that these two methods have been widely used and tested in other theoretical papers in the field of DFT of similar systems to those we have used (as discussed below).

[32] Grimme proposed the DFT-D models (D2, D3) during 2004 and 2011 in several papers, and we cite some of the important ones.

Tsai et al. [33] compared the result of various vdW methods with experimental data. The models were DFT-D2, DFT-D3, DFT-D3-BJ, revPBE, optPBE, optB86, optB88, DF2 and revDF2. They selected a system of graphite with one adsorbed Li over that (LiC_6) for testing the performance of the vdW methods. They compared the result of lattice parameters (*a*, *b* and *c*) and binding energy of Li on graphite (E_b) with experimental data. *c* indicated the interlayer distance of the graphite layers. According to the Tsai result, optPBE showed the closest values to the experimental values. Among the D-Grimme models [12], D2 overestimated the E_b to the highest degree (-0.7 eV against -0.14 eV of experimental value) and D3-BJ yielded a value of -0.07 eV. Other models (D3, optB86, optB88, etc.) showed similar deviations of 50% or more. Therefore, we observed that D3-BJ was a good choice for DFT computations due to its reasonable accuracy.

In numerous papers between 2004 and 2011, Grimme proposed DFT-D models [64, 188-190]. These models are based on an atomic, pair-wise additive treatment of the dispersion energy. In Grimme's [189] DFT-D2 method, the van der Waals interactions were described via a simple pair-wise force field, which was optimised for several popular DFT functionals [42]. Generally, the DFT-D Grimme method used the following equation for the dispersion energy [190]:

$$E_{disp}^{DFT\text{-}D} = -\frac{1}{2}\sum_{n=6,8,10,\ldots}\sum S_n \frac{C_n^{AB}}{R_{AB}^n} f_{damp}(R_{AB}) \tag{3.31}$$

where the summation is over all atomic pairs in the system, C_n^{AB} is the averaged (isotropic) n^{th} order dispersion coefficient, $n = 6, 8, 10, \ldots$ for an atom pair *AB*, and R_{AB} is their inter-nuclear distance. The term S_n is the global scaling factor for correcting the repulsive behaviour of the chosen exchange correlation functional, and f_{damp} is the damping function that determines the short-range behaviour of the dispersion correction. This method attempts to avoid near singularities for small R_{AB} and double counting effects of electron correlation at intermediate distances [190]. One form of the f_{damp} is:

$$f_{damp}(R_{AB}) = \frac{1}{1 + exp\left[-\gamma\left(\frac{R_{AB}}{S_{r,n}\, R_0^{AB}} - 1\right)\right]} \tag{3.32}$$

where R_0^{AB} is a cut-off radius for atom pair of AB, $S_{r,n}$ is radii scaling factor, and γ is a parameter that determines the steepness of the function for small R_{AB} [189]. Generally, the introduction of a damping function corrects the vdW result for two particles that are close.

In our project, we selected D2 for the GDY topic (Chapter 4). Following the result of Tsai et al., we changed our vdW model to D3-BJ for the rest of the topics (4H1-MVG) in Chapter 5, F-GNR in Chapter 6, and r-GO in Chapter 7). We also tested optPBE [33] for geometry optimisation of 4(H1-MVG) material (Chapter 5). It did not complete after 150 hours of running (exceeding the wall time of the supercomputing clusters we used), whereas the D3-BJ model finished the optimisation after 48 hours and 34 minutes. This result shows a considerable time difference between D3-BJ and optPBE. We should note here that D2 is controlled by the tag LVDW=.TRUE in the INCAR file. Similarly, DFT-D3-BJ is controlled by IVDW=12 [42] [33].

3.4 Solid structure modelling in DFT

To perform DFT computations for a specified solid material, we must define a cell structure for the entire periodic system. In solid state physics, we normally do this by defining the unit cell and lattice vectors for the system. In addition, many of the calculations of the periodic system need to be carried out in reciprocal space. Therefore, we briefly review the required theoretical basis of these concepts in this section.

3.4.1 Unit cell and supercell

In DFT computations, we must define our system comprised of different atoms by defining a *unit cell* [159]. The unit cell, defined in real space, is the smallest unit of atoms that produces the whole system when it is periodically repeated in all directions of coordinates. We need to define the periodic boundary conditions (PBC) and supercell [165] to determine the full periodic structure. Many solid structures are regular or periodic in terms of atomic structure, and others can be approximated by sufficiently large periodic systems. The full structure is produced by repeating the unit cell. These types of solids are called *periodic systems*. Figures 3.2 a and b show the top views of the unit cell of graphene (as a 2D material) and the supercell of that structure, with 6×6 repeated unit cells (containing 6×6 hexagonal rings), respectively.

[33] Refer to Appendix 2A and 2C for the list of tags and parameters.

By supercell, we mean a limited repetition of a unit cell. This generally provides a better computational result. Fig. 3.3 displays a schematic view of a supercell for two parallel graphene layers, with lattice vectors of n_1, n_2, and n_3. According this figure, the angle between the n_1 and n_2 vectors is 120° and the n_3 vector is perpendicular to the xy plane.

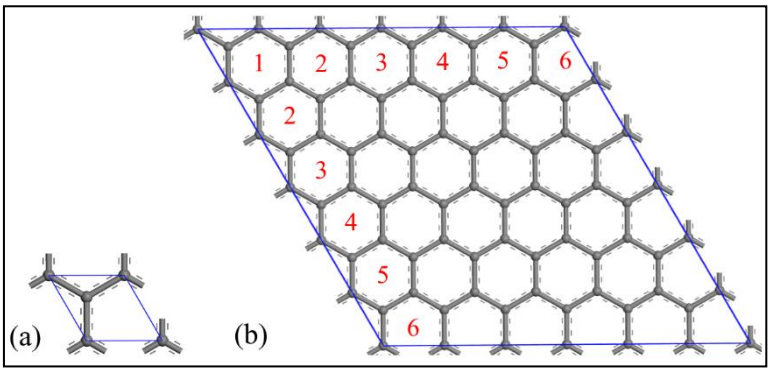

Fig. 3.2. a) The blue rhombus represents a unit cell of graphene, b) The blue rhombus represents a 6×6 supercell for graphene, and the numbers indicate the number of rings in horizontal and vertical directions.

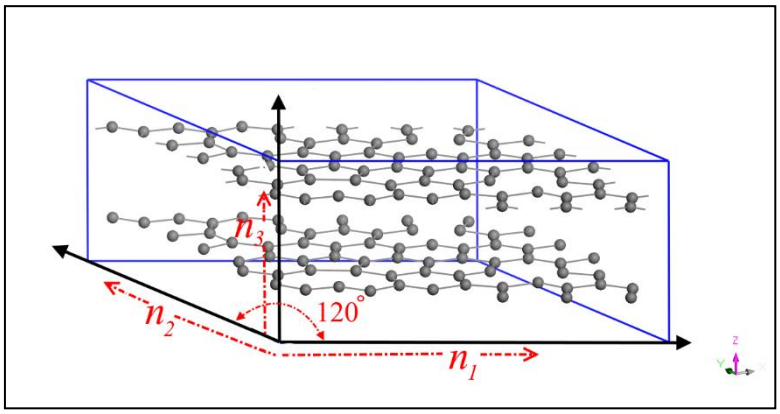

Fig. 3.3. A perspective view of a supercell for two parallel layers of graphene; the lattice vectors are n_1, n_2, and n_3 (coloured in red).

3.4.2 Bloch Theorem and plane wave basis set

Many solid structures are periodic. This implies that the local properties (i.e. properties at position **r**) are periodic:

$$u_k(\mathbf{r}+\mathbf{L})=u_k(\mathbf{r}) \tag{3.33}$$

where $u_k(\mathbf{r})$ is a periodic function representing any property of the system, such as potential energy $U(\mathbf{r})$, or electron density $\rho(\mathbf{r})$. **L** is an integer combination of the lattice vectors of the

periodic system. The Bloch [34] theorem states that, for a periodic wavefunction or Bloch function, $\psi_k(\mathbf{r})$ can be stated as [167, 169]:

$$\psi_{\mathbf{k}}(\mathbf{r}) = u_{\boldsymbol{k}}(\mathbf{r})\chi_{\mathbf{k}}(\mathbf{r}) = u_{\mathbf{k}}(\mathbf{r})e^{i\mathbf{k}\cdot\mathbf{r}} \tag{3.34}$$

Therefore, the wavefunction $\psi_k(\mathbf{r})$ becomes a product of the two waves: $u_k(\mathbf{r})$ and $\chi_k(\mathbf{r})$. The function $\chi_k(\mathbf{r})$ appearing in Eq. 3.34 is called a *plane wave* and **k** is the wave vector in *k*-space or reciprocal lattice space. The concept of *k*-points is derived from this parameter and we will discuss it in sec. 3.4.4.

The periodic function $u_k(\mathbf{r})$, can be expressed as a Fourier series of plane waves and reciprocal space lattice vector, **G**, based on its periodicity [169]:

$$u_{\boldsymbol{k}}(\mathbf{r}) = \sum_{\mathbf{G}}^{\infty} \mathbf{G} c_{\mathbf{G}} exp(i\mathbf{G}\cdot\mathbf{r}) \tag{3.35}$$

where $c_{\mathbf{G}}$ is the Fourier expansion coefficient. By combining Eqs. 3.34 and 3.35, we can express the Bloch wave equation (Eq. 3.34) in the form of Fourier series, as follows [169]:

$$\psi_{\boldsymbol{k}}(\mathbf{r}) = \sum_{\mathbf{G}}^{\infty} c_{\mathbf{k}+\mathbf{G}}\ exp[i(\mathbf{k}+\mathbf{G})\cdot\mathbf{r}] \tag{3.36}$$

The above expression is the Fourier expression of the Bloch wavefunction. There are an infinite number of electron states described by $\psi_k(\mathbf{r})$ in any selected solid material and an infinite number of **G** vectors as well. This means that mathematical approximations are required to evaluate Eq. 3.36.

The periodic nature of the plane wave (Eq. 3.36) renders all of the mentioned properties periodic over the repeating supercell. The approach described above uses *plane-wave basis sets*, and most DFT packages for calculation of periodic systems, such as VASP, use this approach. In this method, the chosen plane wave basis sets are independent of the ionic (atomic)

[34] Felix Blöch, Swiss physical scientist, 1905-1983

positions due to their *non-local* nature; therefore, they cover the space equally. Nonetheless, the atoms might be unequally positioned.

3.4.3 Cut-off Energy (E_{cut})

The plane waves in Eq. 3.36, with coefficients $c_{\mathbf{k}+\mathbf{G}}$, have a kinetic energy of [169, 191, 192]:

$$E_k = \frac{\hbar^2}{2m} |\mathbf{k}+\mathbf{G}|^2 \tag{3.37}$$

Since Eq. 3.36 is the sum over infinite numbers of **G**, it is necessary to truncate that expression. The plane-waves with higher kinetic energy are less important, so it is reasonable to truncate this expression based on the E_k by defining G_{cut}. This gives the corresponding E_{cut}, based on the following equation [169]:

$$E_{cut} = \frac{\hbar^2}{2m} G_{cut}^{\ 2} \tag{3.38}$$

where E_{cut} is called *cut-off energy*. This parameter should be defined before doing DFT calculations to limit the kinetic energy, and G_{cut} and then the Fourier expression of the wavefunction, Eq. 3.36.

E_{cut} is normally chosen to balance accuracy and computation time. We optimised E_{cut} for a GDY single layer; the results are depicted in Fig. 2B.1 in two separate curves. The converged value of E_{min} could be achieved with E_{cut} of 1000 eV, with acceptable CPU time. Therefore, we used this E_{cut} throughout our computations for GDY. In the same way, we did similar calculations for a graphene sheet with 6×6 rings, and the result is depicted in Fig. 2B.2. According to the result, E_{cut} of 700 eV showed fair accuracy for E_{min} and reasonable CPU time in comparison with higher values. We used this E_{cut} for the all the 4(H1-MVG), F-GNRs, *N*-HCS and r-GO topics (Chapter 5 to 7), respectively.

3.4.4 *k*-point sampling and selection

In computational chemistry, the primary supercell of a material is mapped to the Brillouin zone (BZ) in reciprocal space (or *k*-space) [65]. Moreover, as we mentioned in sec. 3.4.2, Eq. 3.34, **k** is the wave vector in *k*-space. The point of the **k** vector is referred to as the *k*-point. When a system in real space is converted to a system in the Brillouin zone in the reciprocal space, there

will be unique *k*-points in the BZ for the KS wavefunctions. In theory, there are an infinite number of *k*-points. However, if functions do not vary quickly with **k**, a finite grid of points can be used. The selection of *k*-points depends on the size of the system. As the reciprocal space lattice vectors (and therefore the size of the BZ) become smaller with increases in real system size, fewer *k*-points are needed. The number of *k*-points are also sensitive to the type of material. For example, metals require a better sampling than insulators because the occupancy of the KS states varies rapidly with wave vector [191, 192]. Furthermore, careful selection of the *k*-points (selection of *special set*) will allow for faster convergence, although the choice depends on the Bravais lattice[35]. In 1976, Monkhorst and Pack [193] developed a comprehensive mathematical method (M-P method) to create *k*-points with equal distance, removing those related by symmetry. In addition, the centre of the Brillouin zone is selected and referred to as the Γ-point, which is a numerical solution to an orbital function in *k*-space, $f(\mathbf{k})$ or Bloch-type wave vector, as described in sec. 3.4.2. The VASP package [42] uses the M-P method, and we used this method extensively in our project. As an example, this method creates only 10 *k*-points for a primary supercell, with 4×4×4 grids (64 points in total) [165].

3.4.5 Selection of *k*-points

There is an inverse relationship between system size and the number of *k*-points needed. This is due to the inverse relationship between the real space and *k*-space. Therefore, it is possible to select the centre of the BZ or Γ point for sufficiently large systems only; this has a huge impact in CPU time reduction, although it is necessary to check the accuracy for any system. We often used Γ-point for the F-GNRs topic in Chapter 6, since the supercell of F-GNR contains at least 114 carbon atoms in a supercell consisting of 8×6 hexagonal rings.

For a 2D system, such as a graphene sheet, there is large vacuum in the direction perpendicular to the material (e.g. the *z* direction), with only a thin layer of the material. In this case, selection of a grid of $k_x \times k_y \times 1$ is sufficient [165].

A suitable, practical way to select an appropriate number of *k*-points is testing the systems with different *k*-point grids and checking their minimum energy, E_{min}, and the CPU time. Yang et al. used this method for testing the *k*-point grid of Na adsorbed within bilayer graphene with

[35] It is a common phrase for a distinct lattice, and there are five Bravais lattices in two dimensions [65].

AB stacking [73]. Similarly, once the E_{min} turns out to be stable within a reasonable time of computation, they selected that *k*-point grid for further computations. We used this test for GDY single layer. Fig. 2B.3 (Appendix 2B) depicts the variation of E_{min} and CPU time of GDY against different grids. According to Fig. 2B.3, for grids finer than 2×2×1, the E_{min} curve tries to converge around a final value across a horizontal line. Due to the symmetry of the system, even grids (e.g. 2×2×1 or 4×4×1) demanded more computational time compared with odd grids, e.g., 13.7 versus 3.7 hour for 2×2×1 and 3×3×1 *k*-point grids, respectively. Therefore, we have selected a 3×3×1 grid for the GDY single layer. While it provided enough accuracy (in comparison with the others), it took a reasonable CPU time than was deemed to be economical for our computations.

We also did such a calculation for the graphene sheet, including 36 carbon rings with *k*-point grids, varying from 1×1×1 to 7×7×1. First, we should note here that the selection of 36 rings was mainly because we were interested in calculating the binding energy (E_b) of Na on a hexagonal ring and comparing the CPU computation time. The result of this test is depicted graphically in Fig. 2B.4 (Appendix 2B). Based on this graph that depicts a value of E_b for Na over the sheet and the computation time, we selected 6×6 rings for the graphene sheet. The selection of graphene sheet and its result for the number of rings and *k*-points were used for calculations involving 4(H1-MVG), F-GNR and r-GO (used in Chapters 5, 6 and 7, respectively), because these materials are considered to be derivatives of graphene. Fig. 2B.5 depicts the result of the *k*-point grid tests for the graphene sheet with 6×6 hexagonal rings. According to the graph, again, 3×3×1 *k*-point grid gave an acceptable relative accuracy for E_{min} compared with the higher *k*-point grid, although E_b is higher than that obtained with 2×2×1 *k*-point grid. However, the CPU time for a 3×3×1 grid is lower than 2×2×1 and also the higher *k*-point grids. Similar to GDY, odd grids are more suitable for the geometry of the graphene sheet in the *k*-space rather than even grids. Moreover, by increasing the grid number, the accuracy of the calculation may not increase in all cases [42]. Therefore, the CPU times for odd *k*-point grids are lower than even *k*-point grids for the graphene sheet according to the Fig. 2B.5.

To conclude, we selected a 3×3×1 *k*-point grid for GDY (Chapter 4), 4(H1-MVG) (Chapter 5), F-GNR (Chapter 6), *N*-HCS, and r-GO (Chapter 7) single layers. For bulk layers of these materials, we selected a 3×3×2 *k*-point grid, as there are two parallel layers within the supercell.

3.5 Other parameters and methods

3.5.1 Pseudopotentials

The electron-nuclei attraction is singular near the core of the atom, so this leads to KS wavefunctions that have sharp peals (rapidly varying) at high wavenumber and would require a fine grid of *k*-points to give accurate results. Pseudopotentials represent the energy of the core orbitals. The contribution of the core electrons to the bonding is significantly low, in contrast to the outer orbitals, which have the highest contributions. So, this approximation does not affect bonding [165]. This method reduces the number of required basis set for the electrons; hence, it significantly reduces computation time. This technique effectively replaces the electron density ($\rho(\mathbf{r})$) of the internal electrons with some fixed values, which are applicable in all electron calculations for a particular atom. This process is called *pseudisation* or designing a pseudopotential. In summary, in this process, we mathematically fit the wavefunctions of valence electrons and their potentials with the real ion's property [165].

In 1990, Vanderbilt [194] defined an approach for providing pseudopotentials, called *ultrasoft pseudopotentials* or USPP. They are constructed using a generalised orthonormality condition. It also uses augmentation charges to the core region to recover the correct electron density [184]. Moreover, the electron density is subdivided into a delocalised, smooth part and a localised, hard part in the core regions [184]. As the name suggests (USPP), the pseudo wavefunctions possess reduced amplitude, which enable a dramatic reduction in the size of the basis set. Therefore, the computational speed can be faster by as much as 10 times [165]. USSP is normally based on a number of empirical parameters for each atom, which is a disadvantage of this method [169].

A newer type of determining pseudopotentials is the projector augmented-wave (PAW) method, developed by Blöchl in 1994 [195]. This approach combines both the pseudopotential method and the linear augmented plane wave (LAPW) method in a natural way. For materials with strong magnetic moments or with atoms that have large differences in electronegativity, the PAW approach gives more reliable results than USPPs [169]. In 1999, Kresse and Joubert [196] modified the PAW for plane-wave calculations and also the USPPs for small molecules and extended solids, resulting in good agreement with all-electron calculations. In summary, this method, which is classified as a frozen core all-electron (AE) potential, incorporates both core and valence wavefunctions, indicated by ψ_{core} and ψ_{inter} respectively. The ψ_{inter} is

represented with PW expansions, whereas ψ_{core} is projected on a radial grid at the atom centre. After augmenting these two terms, the overlapping wave, ψ_{net}, is subtracted from the total to give the PAW wave, ψ_{PAW}. The result is close to the AE wavefunction that renders this method quite reliable, economical and fast [165]. The pseudopotentials for all elements are individually calculated and written in files, called POTCAR files in VASP [42]. The VASP package provides a library of pseudopotentials for each element. They are also named with hard and soft pseudopotentials based on their cut-off energy values: The higher values of cut-off energy (En_{max}) correspond to hard pseudopotentials, and the lower values (En_{min}) correspond to soft pseudopotentials. For example, the cut-off energy for soft carbon (ver. 2000) varies between 205.4 and 273.9 eV. These values for hard carbon (ver. 2004) are 500.0 and 700.0 eV, respectively. All of the POTCAR files that we have used in our projects are PAW, GGA-PBE type [36], which are available in the library of VASP versions 5.3.5 and 5.4.4. [37] We should note here that, for our graphdiyne calculations (Chapter 4), we used hard carbon pseudopotentials (ver. 2004, En_{max}=700 eV). We used soft carbon pseudopotentials for the rest of the topics (4(H1-MVG), F-GNR, N_G, r-GO) in our projects (ver. 2002, En_{max}=400 eV) [38].

3.5.2 Density of states and conductivity

Band structures and density of states can be used in determination of the conductivity of a solid material. Materials can be categorised as conductors, semiconductors and insulators. Generally, anode materials of rechargeable batteries should be conductors, or at least semiconductors, to allow the electrons to move around the anode freely.

The density of states (DOS) of a solid material describes the number of electronic states per unit energy and unit volume that can be occupied by the electrons in different orbitals [65, 165]. The electronic DOS, $\rho(E)$, can be used to determine the number of electronic states with energies in interval (E, $E+dE$) by evaluating $\rho(E)dE$. A DOS of zero means that there are no states at that energy level. The Fermi level is defined as the energy at a given temperature for which there is a 50 percent probability of occupation. For a system at T=0 K, the Fermi level is the point of zero chemical potential for an electron, and it is equal to Fermi energy. The most

[36] We described GGA-PBE in sec. 3.3.3.
[37] We reviewed POTCAR files in sec. 3.5.1.
[38] We discussed the E_{cut} in sec. 3.4.3.

applicable definition of a metal is that metals are materials with a nonzero DOS at the Fermi level [169]. A DOS plot can be done for the whole system (total DOS or TDOS) or for a specific atom of the system (partial DOS, or PDOS). The valence band is the band of energies occupied by the valence electrons at 0 K. The conduction band is the lowest range of vacant electron states.

The empty space between the valence band and conduction band is called *bandgap*. The width of the bandgap and its relative position with respect to the Fermi level determines the type of conductivity of the material. If there is no bandgap at the Fermi level (or nonzero DOS), it is a metal. If there is a small bandgap, it is a semiconductor, and if there is a large bandgap, it is an insulator [165]. The valence electrons of conductors partially occupy the conduction band, because they can move freely between the two bands, with no barrier. However, the electrons of semiconductors and insulators do not occupy the conduction band at low temperature, because there is an energy barrier against their movement. However, in small (or narrow) bandgap materials, conduction can occur at a sufficiently high temperature. In VASP, we use single point calculation with tag Lorbit=10 in the INCAR file to receive the DOSCAR file required for the DOS plots [39]. The DOSCAR file is then split into many subfiles for each atom. We used split_dos script [40] to do this operation. The resulting plots have Fermi level adjusted exactly at the vertical axis (x=0). We have sketched a number of DOS plots for GDY, 4(H1-MVG) and F-GNRs, which are available in Chapters 4, 5 and 6.

3.5.3 Bader Charge Analysis

Using the results of DFT calculations, we can obtain an indication of the amount of charge transfer from the adsorbate to the adsorbent. This provides atomic scale information from which an understanding of trends in a material's capacity, diffusion pathways, energy barriers and conductivity can be gleaned. For this purpose, the Bader charge analysis had been developed by RFW Bader in 1990 [197]. This method uses the electronic charge density to divide the real space of the material into atomic volumes surrounding each atom. Each volume contains specific charge density of that atom and separated from the other atoms' charge density. These volumes are called Bader volumes [198]. The boundary between Bader volumes

[39] The list of the required tags is given in Appendix 2A.
[40] Ref: http://theory.cm.utexas.edu/vasp/scripts.html

is a surface on which the charge density is a normal vector with its minimum value or 'zero flux surfaces', meaning the gradient of charge density equal zero at this boundary. Indeed, these dividing surfaces lie in between the atoms, with minimum charge density at that point. Therefore, the major calculation in Bader method is the calculation of Bader volumes, such that a grid of volumes is generated. The Bader method has an advantage over other partitioning methods such as Mulliken population method, since it is based on the charge density, which can be calculated by methods such as DFT. Furthermore, in a converged electronic structure calculation, the charge density is insensitive to the basis set used. In this regard, the Bader analysis is more robust than wavefunction-based population methods [198].

Serval algorithms have been proposed for the Bader volume or grid generations so far [198-201]. For example Tang et al [198] presented the grid-based approach using accurate off-lattice steepest ascent pathways with respect to the grid points. In summary, in this method, first we should choose the initial grid point. Then to create a Bader volume, a pathway between the grid points are created in such a way that they form the steepest ascent pathway. For each of the 26 grid points, (*i, j, k*), the gradient of the charge density is calculated through the following equation:

$$\nabla\rho(i,j,k)\ .\ \hat{\boldsymbol{r}}(di,dj,dk)=\frac{\Delta\rho}{|\Delta\hat{\boldsymbol{r}}|} \qquad (3.39)$$

where (*di*, *dj*, *dk*) is the unit vector of integers as the step between the two neighbouring grids. The integers *di, dj,* and *dk* take the values [−1, 0, 1], excluding *di* = *dj* = *dk* = 0. The $\hat{\boldsymbol{r}}(di, dj, dk)$ is the unit vector normalized to the neighbour reached by the grid step (*di, dj, dk*). By using this method, each of the 26 grid points are determined. The created steepest ascent pathway determines the maximum charge density. In this method, all the points along the created pathway are associated with the created Bader volume around the maximum charge density. Finally, the total charge in each Bader volume is evaluated by integrating the charge density over the grid points of that volume. Moreover, the surface surrounding the Bader volume can be visualized by plotting the charge density of that Bader volume [198]. More information of the lattice bias is given in Tang et al's paper.

Having selected the required tag for the Bader charge analysis [41] in VASP, three files are produced: AECCAR 0, 1 and 2. They include the electronic charge information of the core (nucleus and interior orbitals) and the valence orbitals. By using 'chgsum.pl' script we combine the two AECCAR 0 and 2 to produce CHGCAR_sum file. Then by using 'bader' script for CHGCAR and CHGCAR_sum as the reference files, three informative files of ACF.dat, BCF.dat and Atomic Volumes.dat are produced. The ACF file contains the coordinates of each atom based on the Bader partitioning. It also contains the charge associated with each Bader volumes. The BCF file contains the coordinates of each Bader maxima and the charge within the Bader volumes. The AtomVolumes file contains the number of each volume that has assigned to each atom. Having done all the required calculations for Bader partitioning, we normally read the charge of each atom in the ACF file as a reference for charge transfer calculations. We have used this method extensively in Chapters 4 to 6.

3.5.4 Charge density difference and electrostatic potential visualisations

The electron localisation function gives a measure of the probability of finding an electron in the neighbourhood of another with the same spin. It usually highlights locations of bonds, lone pairs and atomic shells, etc. We can visualise an isosurface of the charge density for a solid structure, such as graphene with di-vacancy (DV) (as shown in Fig. 2B.6). Fig. 2B.6a depicts a constant charge density isosurface of graphene drawn by VESTA package via using the CHGCAR file [42]. Fig. 2B.6b depicts the electron localisation function by using the ELFCAR file [43], which is similar to the charge density of that structure.

We have also carried out charge density difference (CDD) calculations by using the following generic equation [44]:

$$\Delta\rho = \rho_{Subs+M} - \rho_{Subs} - \rho_{M} \qquad (3.40)$$

[41] Tags required for electron localisation calculation in VASP is given in item 6 of Appendix 2A with ref: http://theory.cm.utexas.edu/henkelman/code/bader/

[42] Charge density was previously defined (sec. 3.3.1). These figures show isosurfaces of these properties that are calculated on a 3D grid in real space.

[43] Tags required for electron localisation calculation in VASP is given in item 6 of Appendix 2A.

[44] Tags required for CDD calculation in VASP is given in item 7 of Appendix 2A.

Where ρ is the charge density of the systems specified as $e\ a_0^{-3}$ (a_0: Bohr radius). Indices *Subs+M*, *Subs* and *M* indicate the substrate with adsorbate metal, pristine substrate, and isolated metal atom, respectively. We have depicted charge density difference (CDD) visualisations in Chapters 4 to 6 with blue and red clouds indicating electron rich area (or induced negative charge) and electron deficient area (or induced positive charge), respectively.

We have also depicted the electrostatic charge potential mapped onto a constant charge density isosurface for F-GNRs in Chapter 6 [45]. The electrostatic potential is the potential of a unit positive charge at any point around atoms due to electron density of the atoms [202]. The measurement of electrostatic potential in chemistry is important as it indicates the chemical reactivity of atoms, molecules and surfaces. The electrostatic potential for a molecule or group of atoms can be calculated by the following equation [202]:

$$\Phi(\mathbf{r}) = \int \frac{\rho_{\text{total}}(\mathbf{r})}{|\mathbf{r}-\mathbf{r}'|} \mathrm{d}\mathbf{r}' \tag{3.41}$$

where ρ_{total} represents the charge of the nuclei and electrons. The integration is done over the system volume, and $\mathbf{r}'$ represents the atomic position relative to the same origin.

The VASP package can be used to calculate the electrostatic potential at a grid of points. A visualization package can then be used to give a spectral colour (from blue to red) to the calculated potential energy and then visualize it based on the charge density isosurfaces. We give further details in Chapter 6, sec. 6.4.3.

3.5.5 Transition states and nudged elastic band (NEB) method

In an energy hypersurface of a chemical process, there might be many local minima and maxima. Between these energy minima, there are *transition states* (or TS) or *saddle points* [167]. For a particle or ion to travel from a local minimum to another, it has to pass through the saddle point. Consequently, there will be a true pathway between these local minima. The higher vertical distance between the local minima and saddle point, the higher the energy

[45] Tags required for electrostatic charge potential calculation in VASP is given in item 8 of Appendix 2A.

required for the ion to pass through the saddle point. This energy is called *barrier energy* or E_b. Fig. 3.4 shows a schematic view of the local minima, maxima and saddle points.

The lower the E_b, the higher the probability for the ion to move across the plane. Nudged elastic band (NEB) is a method of locating TS points. Jonsson and co-workers [203-205] developed this method for prediction of TS points. This method considers several images[46] along an imaginary pathway as an approximation to the minimum energy pathway (MEP). This pathway begins from the first local minimum to the final point, passing through the proposed TS points. Fig. 3.5 depicts a schematic preview of the NEB method, developed by Henkelman and Jonsson [205]. The NEB method sums up the energy of all the images and defines a function based on that [205]:

$$T_{NEB}(R, P, x_1, x_2, \ldots, x_M) = \sum_{i=1}^{M} E(x_i) + \sum_{i=1}^{M=1} \frac{1}{2} k(x_{i+1}-x_i)^2 \qquad (3.42)$$

where k is the *spring constant* and $(x_{i+1}-x_i)$ is the distance between the two subsequent images. The images do not need to be evenly distributed. R and P represent the initial and final points of the pathway, L.M.1 and L.M.2, respectively, which depend on the variation of energy along the pathway and its trend. The NEB method minimises T_{NEB} with respect to the coordinates of the images (x_i) so that it converges towards the true pathway.

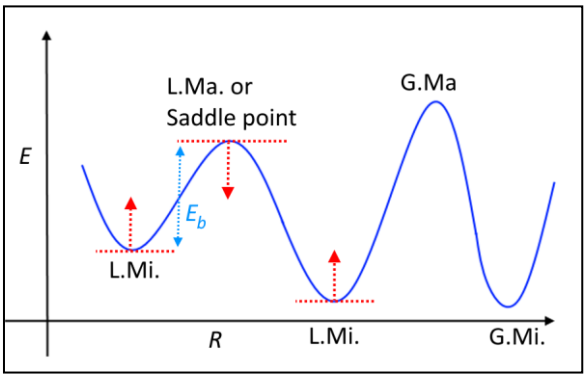

Fig. 3.4. a) A typical energy graph of a structure. L.Mi.: Local minimum, L.Ma.: Local maximum. G.Mi.: Global minimum, G.Ma.: Global maximum. The red arrows show the direction of second derivative vectors. E_b shows the barrier of energy from the local minimum toward the saddle point.

[46] Image or replica is a point that is proposed to be close to the minimum energy pathway. In VASP, the users can define images arbitrarily.

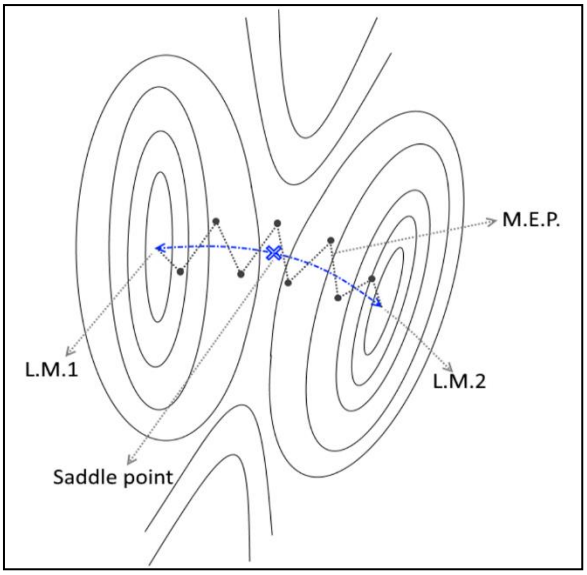

Fig. 3.5. A schematic view of an energy plane, indicating two local minima, saddle point (blue cross), and minimum energy pathway (MEP). The images are indicated by black dots.

The VASP package uses the NEB method to find TS points [203, 204]. By setting the tag Spring = -5 in the INCAR file, the NEB method is set. Then, we must define the number of images in the INCAR file by the tag IMAGE[47]. We should also estimate the approximate position of TS points in a series of numbered folders in the calculation directory (01, 02, 03, etc.). These estimates are quite important, and they should be close to the real position of TS points. Otherwise, the calculations might diverge. We carried out NEB calculations for the Na transition pathways on GDY, and we present the description and results in Chapter 4.

3.6 VASP files and parameters used in our projects

The VASP package is designed to carry out DFT calculations for periodic systems. In this thesis, we have used VASP versions 5.3.5 and 5.4.4 [42]. VASP uses plane wave basis sets as described in sec. 3.4.2, and the general calculation cycles are consistent with those outlined in sec. 3.3.4. In the next section, we describe the input and output files of VASP, which are required for the calculations we carried out.

[47] The full list of the required tags is given in Appendix 2A.

3.6.1 Input files

For our computations in VASP, the following files are required:

- INCAR file: For setting up the input tags and parameters. A list of these tags is given in Appendix 2A. The types of calculation that we have used throughout our projects are:

    1. Geometry optimisation.
    2. Single point calculation.
    3. Transition state calculation, by NEB method.
    4. Density of state analysis.
    5. Bader charge analysis.
    6. Charge density difference (CDD) analysis.
    7. Electron localisation function.
    8. Electrostatic charge potential calculation.

- POSCAR file: Designed for introducing the lattice parameters (or vectors) and coordinates of atoms to the package. We produced the initial arrangement of the systems in Material Studio (MS) software. Then, we converted them to a format readable by the VESTA package. A view of a typical POSCAR script is given in Appendix 2A.

- POTCAR file: Containing the pseudopotential parameters for the elements. They are uploaded in the VASP package. As we mentioned in section 3.5.1, all pseudopotentials that we used in our projects are PAW-PBE type.

- KPOINTS file: Designed for the *k*-point grids (sec. 3.4.4).

We give a summary of the selected tags and parameters in Appendix 2C. Moreover, Chapters 4, 5, and 6 state the selected parameters in their methodology sections.

3.6.2 Output files

The following items are the main files that are produced by VASP as a result:

- OUTCAR file, which includes the information from each of the cycles (SCF and ionic minimisation), and also:

- Energy (E), entropy (S), and force components (F_x, F_y, F_z).
- Free energy (eV) as the minimum energy (E_{min}) recorded at the end of last cycle.
- Magnetic moment (μ_B, Debye) of the system, recorded at the end of each cycle.

- OSZICAR file gives the summary of energy and ionic cycles. It records the energy (E), difference in the converged energy (dE), and magnetic moment (μ_B).
- CONTCAR file gives the optimised lattice parameters and coordination of the atoms.
- CHGCAR file includes the charge density information. It is used to provide a charge density visualisation or charge density difference visualisation by VESTA.
- DOSCAR file includes the density of states of the systems (sec. 3.5.2). It is applicable for sketching the DOS plots for the system.

The following chapter contains the published paper in the Journal of Power Sources, Vol. 343 (2017), p. 354-363 [28].

Amir Farokh Niaei[1], Tanveer Hussain[1], Marlies Hankel[1] and Debra J. Searles[1,2, 48]

[1] Centre for Theoretical and Computational Molecular Science, Australian Institute for Bioengineering and Nanotechnology, The University of Queensland, Brisbane, QLD 4072, Australia

[2] School of Chemistry and Molecular Biosciences, The University of Queensland, Brisbane, QLD 4072, Australia

Contributors	Statement of contribution
Amir H. Farokh Niaei (candidate)	Presented the topic and idea (60%) Conducted computations (100%) Analysed the result data (70%) Wrote and reviewed the paper (55%)
Hussain T.	Analysed the result data (5%) Reviewed and edited paper (10%)
Hankel M.	Presented the topic and idea (20%) Analysed the result data (10%) Reviewed and edited the paper (10%)
Searles D.J.	Presented the topic and idea (20%) Analysed the result data (15%) Wrote and edited the paper (25%)

[48] Corresponding Author: Debra J. Searles, Australian Institute for Bioengineering and Nanotechnology, The University of Queensland, Brisbane, QLD 4072, Australia, Telephone: +61 7 33463939, Fax: +61 7 3346 3992, Email: d.bernhardt@uq.edu.au

Chapter 4

Sodium-intercalated bulk graphdiyne as an anode material for rechargeable batteries

4.1 Abstract

We present the results of a density functional theory study of sodium storage and mobility on graphdiyne (GDY) and consider the applicability of GDY intercalated with sodium (Na) as an anode material for rechargeable batteries. The maximum capacity, energy barriers for Na diffusion throughout the layers, and expansion of the layers due to Na insertion are determined. The calculations indicate that Na intercalates within the GDY bulk layers with a capacity of $NaC_{5.14}$ without expansion (316 mA h g^{-1}) and $NaC_{2.57}$ with expansion of 28% (497 mA h g^{-1}). The energy barrier for movement of Na in the slit pore formed by two GDY bulk layers is found to be 0.82 eV for bulk GDY with an AB-2 stacking, and the barrier for movement through a GDY sheet is found to be 0.12 eV. The barrier for movement in the slit pore formed by sheets becomes even lower for AB-3 stacking, with values of 0.68 and 0.40 eV found for different pathways. Movement from one GDY sheet to another for the AB-3 stacking also has a moderate energy of 0.37 eV. Therefore, GDY intercalated with Na is proposed to have potential as an anode material for rechargeable batteries.

Keywords: anode material; rechargeable batteries; graphdiyne; density functional theory; transition state barrier; diffusion

4.2 Introduction

Rechargeable batteries are widely used in many different applications as important devices for storage of energy. The ability to manufacture small, light-weight rechargeable batteries has had significant impact, with mobile phones, implantable devices and portable tools being well developed technologies that rely on rechargeable batteries. By charging the batteries using renewal energy sources, rechargeable batteries provide a way of enabling a continual supply of clean energy. However, two main problems with currently available portable batteries are their discharge time and the battery lifetime. To improve their performance, various new materials have been proposed for the anode, cathode and electrolyte. Currently the most common commercial-scale rechargeable battery is the lithium ion battery (LIB) in which lithium intercalated graphite forms the anode [5, 50, 53]. However recently, interest in sodium ion batteries (NIB) has intensified. This has been largely due to the possibility that we might exhaust the supplies of lithium due to the increasing demand for LIBs [206], and companies have already been established to advance NIB technology and make it available [207, 208]. Therefore, materials for NIBs are being sought with an aim to produce a battery with high performance, with materials that are readily available at low cost.

A challenge for the replacement of Li with Na is that the Na is significantly larger than Li, with the atomic radii of Na being 1.70 Å, and 11.8% higher than Li at 1.52 Å [2]. Graphite has a very low capacity for Na because its interlayer distance of ~3.35 Å [29] prohibits intercalation and movement of Na within the pores created by the graphene layers [25]. The barrier for diffusion of Li through a graphene sheet is already significant, and it is higher for Na. Therefore, 2D materials with a larger interlayer space and/or larger pores in the 2D sheets themselves, are required for intercalation and diffusion of Na throughout the electrode material.

Consequently, many new NIB electrode materials have been proposed both experimentally and theoretically [6, 8, 15, 18]. Many of these are based on carbon materials due to the variety of structures that can be formed, their success in LIBs, their light weight and their conductivities. As a guide to the structure of a desirable material, Cao et al. [25] indicated that the minimum inter-layer distance for ready insertion of Na between graphitic layers should be 3.70 Å. They found that at this separation there is a moderate energy barrier for insertion of Na of 0.053 eV, which is significantly lower than the barrier of 0.12 eV when the separation is equal to that observed in graphite (note that k_BT is 0.0256 eV at 298 K). Therefore, work has been carried out to develop materials with sufficient spacing between layers. An alternative approach is to

use 2D sheets that have pores in them. Among these, the carbon allotrope graphdiyne (GDY) is of particular interest. GDY has 4-atom chains of carbon atoms with sp hybridisation, linking 6-carbon rings with sp^2 hybridisation and resulting in a 2D material with a large 18-atom triangular pore (area ~36 $Å^2$), as shown in Fig. 4.1. The area of this pore is ~5.5 times larger than that of the 6-member rings in both graphene and GDY (~6.5 $Å^2$), which suggests that Na atoms would be likely to be able to sit between the layers of GDY, even though the spacing between layers is not very much different to that in graphite.

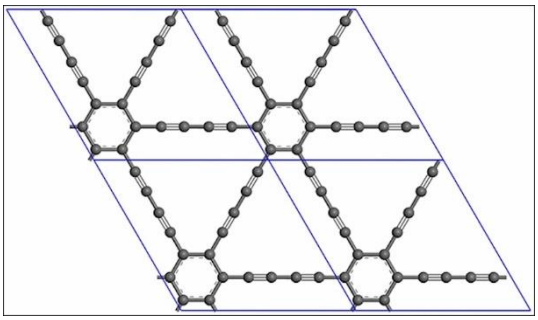

Fig. 4.1. A schematic diagram of the 4 unit cells of GDY. Grey balls represent carbon atoms. The unit cells are marked by blue lines.

The stacking of GDY has been considered computationally by Luo et al. [118] and Zheng et al. [119]. Luo et al. identified four stacking configurations for bulk GDY with binding energies only differing by ~0.01 eV $atom^{-1}$. They found that the two AB stackings shown in Fig. 4.2, which they refer to as AB-2 and AB-3, are most stable (AB-3 slightly more stable than AB-2), and are convertible with barriers of 1.1 meV $atom^{-1}$ (AB-2 to AB-3) and 1.5 meV $atom^{-1}$ (AB-3 to AB-2). They also measured the lattice constants to be 9.46 × 9.46 × 6.75 Å for AB-2 and 9.46 × 9.46 × 6.71 Å for AB-3, indicating an interlayer spacing of 3.38 and 3.36 Å, respectively [118]. Zheng et al. [119] considered double layer configurations using supercells of 9.45 × 9.45 × 40 Å; and also found the AB-2 and AB-3 stackings to be most stable, with the inter-layer distances of the two models being 3.42 and 3.40 Å, respectively.

The use of GDY as an anode material in LIBs has been demonstrated theoretically and computationally. Sun and Searles [27] used density functional theory (DFT) calculations to study the capacity for Li intercalation between GDY layers and the mobility of Li. They showed that the maximum adsorption capacity of GDY was LiC_3 (equivalent to 624 mA h g^{-1}), which is higher than the capacity of graphyne at LiC_4 (equivalent to 487 mA h g^{-1}) and graphene at LiC_6 (equivalent to 372 mA h g^{-1}) [27, 117].

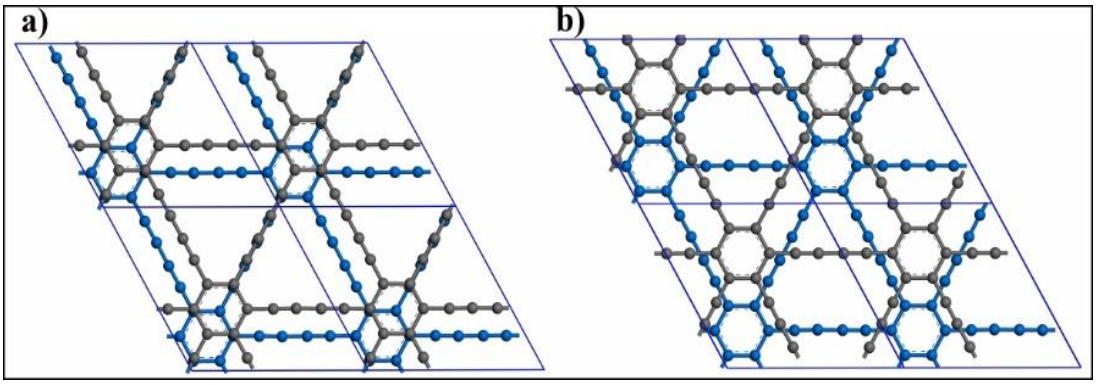

Fig. 4.2. Schematic views of two layers of bulk GDY with (a) AB-2 and (b) AB-3 stackings. In each case a 2×2×1 supercell is shown. Grey and blue balls represent carbon atoms. The two layers have been coloured differently to distinguish between them. The interlayer spaces are very similar (3.38 Å for AB-2 and 3.36 Å for AB-3).

In addition, they found that the most energetically favourable site for the Li atom was on the 18-carbon pore, but off-centre and near the corner of the pore. They also showed that the energy barriers for in-plane diffusion of Li (i.e. parallel to the GDY sheet) within the 18-carbon pore (corner to corner), from the 18-carbon pore to the 6-atom ring, from one pore to an adjacent pore and out-of-plane (i.e. through the GDY sheet) were 0.18, 0.84, 0.70, 0.27 eV, respectively. The energy barrier for the path through the GDY sheet was found to be lower than that for movement of a Li from one 6-membered ring to another in graphene (0.32 – 0.34 eV, [10, 66]), indicating that the mobility of Li in bulk GDY could be greater than that in graphite.

Zhang et al. [116] also used DFT calculations to study the intercalation of Li in GDY. Similarly, to Sun and Searles they found a capacity of LiC_3 for a GDY single layer. For the single layer, Zhang et al. considered a triangular placement of 3 Li atoms near the corners of each triangular pore and on the both sides of GDY single layer and calculated an average binding energy of 1.60 eV. We note that this is similar to the cohesive energy of Li, 1.630 eV [65], so these results indicate that clustering of Li atoms could occur. They also considered bulk GDY, with an AB stacking such that the centre of a hexagon on one layer is above the centre of the triangular pore for another. We note that this stacking is different from the four low energy stackings identified by Luo et al. [118]. For this bulk GDY, they predicted a loading corresponding to LiC_6, with an average binding energy of 2.19 eV Li^{-1}. Further addition of Li to this structure resulted in buckling of the sheets. As well as the binding energies, Zhang et al. evaluated the energy barriers for Li diffusion on the GDY sheet: within the 18-carbon pore triangular pore; from the triangular pore to the 6-carbon hexagon; from one triangular pore to the adjacent one;

and through the GDY sheet, finding energies of 0.13, 0.72, 0.51, 0.07 eV, respectively. The differences in the results obtained by Sun and Searles, and Zhang et al. can be accounted for by the different in methodology such as the size of the supercell and the treatment of van der Waals interactions, although we note that the trends are the same and the values within 0.2 eV of each other.

To test the utility of GDY in LIBs, Huang et al. [29] experimentally considered a Li intercalated GDY electrode and found a maximum reversible capacity of 520 mA h g^{-1} after 500 cycles at 500 mA g^{-1}, and 420 mA h g^{-1} after 1000 cycles at 2 A g^{-1}. They measured the interlayer distance of the GDY at 3.65 Å using scanning electron microscope (SEM) and transmission electron microscope (TEM) [29]. These experiments confirmed that GDY performs well as an electrode for LIBs.

Recently, Xu et al. [77] also carried out DFT calculations of Na binding to GDY and indicated that it should be a good candidate for an anode in NIBs. Using a similar methodology to Zhang et al. [116], they considered a number of symmetric loadings of Na on the GDY and concluded that the arrangement of 6 Na atoms close to the corners of a pore in a single layer is the most stable arrangement of those considered (NaC_3). They also found 3 Na atoms can be placed between layers of a unit cell in bulk GDY (with the same AB stacking considered by Zhang et al. [116]) to give a capacity corresponding to NaC_6. In addition, they calculated the energy barriers for various transition pathways across and through a GDY sheet and found that the barriers for Na diffusion from near the corner of triangular pore to the 6-carbon hexagon, from one pore to adjacent pore in a direct pathway (in-plane) and from one side of the layer to other side in a perpendicular direction (out-plane) were 1.09, 0.64 and 4.5 eV, respectively. Clearly, as expected, these values are large compared to the barriers for diffusion of Li. The last value is for out-plane movement of Na at the corner of pore. This is unlikely to be the lowest energy path and therefore we will further explore if movement directly through the pore along another path might be possible.

The work of Xu et al. has provided important information on the binding of Na on single and bulk GDY, and diffusion on a single GDY sheet. In this manuscript we present additional results on these systems and also use DFT calculations to determine the maximum loading of Na on a single GDY sheet and bulk GDY. Furthermore, we carry out comprehensive calculations on the energy barriers for diffusion of Na across a GDY layer, and in-plane and out-of-plane diffusion between GDY layers in bulk systems. We demonstrate that both in-

plane and out-of plane diffusion should be possible in GDY. We also explain the observations by considering the charge density distribution, Bader charges and density of states (DOS) analysis.

4.3 Computational Methods

To study the interaction of Na with GDY, DFT calculations were performed as implemented in Vienna *ab initio* Simulation Package (VASP), version 5.3.5. The system is considered to be periodic in the three dimensions, and a plane-wave basis set is used. Within this package, the generalised gradient approximation (GGA) with projector-augmented wave (PAW) method was used. A Gaussian smearing with the smearing parameter, σ set to 0.05 was selected. To account for the van der Waals interactions, the DFT-D2 method of Grimme [189] was used. For calculations considering a single layer of GDY, the Brillouin zone was sampled with a 3×3×1 *k*-point mesh and the bulk layers were sampled with 3×3×2 *k*-point mesh, using the Monkhorst-Pack scheme. The cut-off energy for the plane-wave basis set was selected to be 1,000 eV, which is quite high due to the existence of single and triple bonds in the carbon chains of GDY which required a hard carbon PAW potential (C_h) to account the shorter bond length accurately. We also used the Na_sv potential for Na, which treats the 2p and 2s semi-core states as valence states leading to 9 valence states. The energy convergence criterion was selected to be 1×10^{-6} eV and the force convergence criterion was selected to be between 0.05 eV $Å^{-1}$ and 0.01 eV$Å^{-1}$. The number of k-points and cut-off energy, force and energy convergence criteria were optimised in preliminary calculations.

In calculations of Na on the 2D GDY layer, a single GDY unit cell was used, and the optimised cell lattice parameters for the pristine GDY layer were determined to be 9.46×9.46 Å. A vacuum of 20 Å above the layers was selected, which was shown to be sufficient to ensure that interactions between layers were small compared to the binding energies we obtain. For the bulk system calculations, a single GDY unit cell was also used and both the AB-2 and AB-3 stackings were considered. In both cases, full lattice optimisations of the a, b and c lattice parameters gave values of 9.46×9.46×6.58 Å, corresponding to a GDY layer spacing of 3.29 Å. We also considered different van der Waals corrections to Grimme's DFT-D2 scheme, [189] including vdW-opt88 and vdWopt86b, however like Klimeš [209] found almost the same lattice parameters as obtained using DFT-D2. We therefore used DFT-D2 vdW corrections in all our calculations for consistency. The transition state structures and their energies were

determine using the Nudged Elastic Band (NEB) approach with the climbing image method [210] in conjunction with tangent definition given in [205].

After optimisation of the GDY 2D sheet and the bulk system, the maximum loadings were determined by adding Na to the materials while ensuring that the binding energy was higher than the cohesive energy of Na (which would result in clustering of the Na and inhibit its mobility), and that the material did not become severely distorted. The binding energy between each Na atom and the GDY substrate is determined by:

$$E_b = \frac{E(GDY.Na_n) - nE(Na) - E(GDY)}{n} \tag{4.1}$$

where $E(GDY.Na_n)$, $E(Na)$ and $E(GDY)$ are the total energy values of GDY with n Na atoms adsorbed, the energy of Na as an isolated atom in gas phase, and the energy of GDY as standalone 2D sheet, respectively. Therefore, a negative binding energy indicates that the binding is favourable. The theoretical electrical capacity of the anode material in mA h g^{-1} is:

$$E\ (mA\ h\ g^{-1}) = \frac{n_{Na}F}{3.6(n_{Na}m_{Na} + n_C m_C)} \tag{4.2}$$

where m_{Na} and m_C are the atomic masses of the Na and C atoms in g, n_C and n_{Na} are the number of C and Na atoms in a unit cell and F is Faraday's constant, 9.648×10^4 C mol^{-1}.

4.4 Results and Discussion

4.4.1 Na interaction with single layer GDY

In order to examine the strength and nature of the interaction of Na with GDY, the structures formed and the maximum likely loading of Na on GDY, we initially considered a single GDY sheet. Loadings of 1 – 9 atoms on the unit cell (18 carbon atoms) were considered. With each loading, all likely minimum energy structures were selected as initial configurations and the structures were optimised. The likely structures for systems with higher loadings were determined based on the low energy structures with lower loadings. Over 40 different initial configurations were considered overall. In all cases, the initial structures either had all Na atoms on one side of the GDY sheet, or in the plane of the sheet, although in some cases one

or more Na atoms moved to the other side during optimisation. One-sided or in-plane binding was considered since our ultimate aim is to look at bulk systems which, as a simplistic first approximation, can be considered as an assembly of single sheets with Na bound to one side. Loadings of more than 7 Na atoms on GDY either formed highly distorted structures or the Na atoms moved further from the GDY layer, so a loading of 7 was considered to be the maximum capacity of the first layer of Na adatoms formed above the GDY. Fig. 4.3 shows the average binding energies and corresponding structures for some of the systems considered. The upper curve connects the binding energies corresponding to the minimum energy structures at each loading that had a low level of distortion judged by examination of the structures, and their corresponding structures are shown above the curve. In addition, some energies and structures that resulted in distorted GDY are shown and connected by the lower curve. We note that the structures with visible distortion were often found to have stronger binding energies (more negative E_b); however, there is likely to be a large energy barrier for achievement of those configurations, and they might not be observed in experiment except under extreme conditions. Therefore, we focus on the undistorted structures. As expected, the average binding energies of these configurations gradually decrease with an increase in Na loading.

The values of the average binding energies and average distance of the Na from the sheet for a number of the structures considered are given in Table 4.1. Energetically, the favourable structure obtained by adsorption of a single Na atom on the GDY sheet is with the atom in the plane of the sheet and at the centre of the pore. This position was more than 1 eV lower in energy than the position over the 6-carbon ring, and initial placements of the Na at different positions on the pore all resulted in this same minimum energy position. This conclusion is similar to that obtained by Xu et al., and is in contrast to the Li atom, which preferred to settle closer to the pore's corner [27, 116].

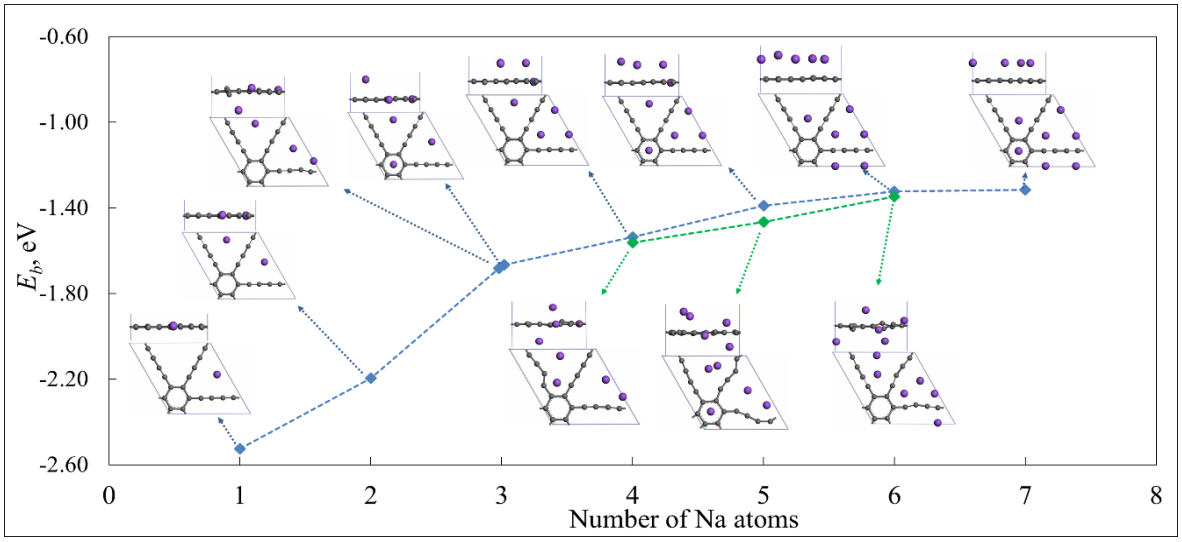

Fig. 4.3. Binding energy as a function of the number of Na atoms on a single GDY sheet. The grey balls represent carbon and the purple balls sodium. Top and side view of the structures are shown. The blue diamonds show binding energies for the undistorted structures and the green diamonds shown binding energies for distorted structures. The lines serve as guides to the eye. We note that all the binding energies are stronger than the cohesive binding energy of Na in this case (-1.113 eV), however addition of more Na will either lead to weaker binding and movement of the Na further from the GDY, or a highly distorted structure.

Our average E_b value for 6 atoms over the pores (-1.32 eV Na^{-1}) is similar to that reported value of Xu et al. at -1.30 eV Na^{-1} [77], and the structures and distances of the Na atoms from the sheet are also similar. However, we also found that 7 Na could be adsorbed on the sheet with a similar average binding energy and distance between the Na atoms and the sheet. In this case, as well as three Na near the corners of the triangular pore, one was situated above the 6-carbon ring, and the average binding energy was found to be -1.32 eV Na^{-1}. The ability of a Na atom to bind above the 6-carbon ring is consistent with the calculated binding energy of a single Na above the 6-carbon ring of -1.48 eV Na^{-1} (see Table 4.1). Therefore, our calculations indicate that the maximum Na capacity of GDY in single layer of metal atoms is Na_7C_{18} or $NaC_{2.57}$ with the Na atoms situated above the sheet (at a distance of $h_{ad} \approx 2.0$ Å), equivalent to theoretical electrical capacity of 497 mA h g^{-1}.

Table 4.1. Average binding energies and distances of Na on a single GDY sheet.

Na atoms per unit cell	Position	Average Na-GDY distance h_{ad} (Å)	Strongest E_b (eV per Na atom)	Strongest E_b (eV per Na atom) undistorted configuration
1	Over hexagonal ring	1.77	-1.479	-1.479 [a]
1	Centre of triangular pore	0.0	-2.527	-2.527 [a]
2	Centre of two triangular pores	0.0	-2.196	-2.196 [a]
3	Centre of two triangular pores and over ring	0.0, 2.24	-1.683	-1.666
4	One at centre of pore and three over another pore	variable	-1.563	-1.538
5	One over ring, one at centre of pore and three over another pore	variable	-1.466	-1.391
6	Three over each pore	~ 2.0	-1.347	-1.324
7	Three over each pore and one over ring	~ 2.0	-1.317	-1.317 [a]

[a] In these cases, the configuration with the most strongly bound Na was not distorted

4.4.2 Na intercalation in bulk GDY

Na intercalation between the GDY bulk layers was considered by studying a unit cell with two GDY layers, which was periodic in all dimensions, and with lattice vectors set to be those of the optimised bulk GDY. We considered AB-2 and AB-3 stackings of the GDY layers (see Fig. 4.2), but in this section we focus on the results of the AB-2 stacking due to its low energy and the large pore that is formed perpendicular to the GDY sheets, which we anticipated would be most easily able to accommodate a Na atom. We note that this differs for the work by Xu et al. [77] who also considered two layers in a periodic cell, but a different stacking. It also differs in that they allowed variation of the lattice vectors on loading, so allowed the system to expand if required. The real experimental system will be intermediate between these, with expansion being restricted by the surroundings, and we discuss this further in another section. The optimised length of the cell in the direction perpendicular to the sheets was 6.58 Å, giving an interlayer distance of 3.29 Å which can be compared with the experimental value of 3.65 Å [29]. The small differences between our result and other calculated results by Zheng et al.

[119] (3.42 Å for bi-layer AB-2 GDY), Luo et al. [118] (3.38 Å for bulk AB-2 GDY) and Xu et al. [77] (3.5 for bi-layer GDY) are likely to be due to the method used for van der Waals interactions (see a comparison of different methods in [118]). We note that this interlayer distance is very similar to that observed in graphite, and if the bulk material is able to accommodate Na it must therefore be due to the existence of large pores and the space created due to the stacking of the layers.

As in the case of the single GDY sheet, Na atoms were added to the unit cell at all likely initial positions and the structures were optimised. A loading of 1 to 12 Na atoms per unit cell (which contains 36 C atoms) was considered. Over 25 different initial structures were selected. Fig. 4.4 shows the average binding energies and corresponding structures for some of the bulk systems considered, as a function of the number of Na atoms in the unit cell. A blue dashed line connects the binding energies of systems where little distortion of the structure is evident, whereas a green dotted line connects the strongly binding distorted structure energies. Structures of the distorted configurations have been placed below the lines, and undistorted configurations above the lines. In addition, Table 4.2 gives E_b and the average distance between the Na atoms and the closest sheet, for various loadings.

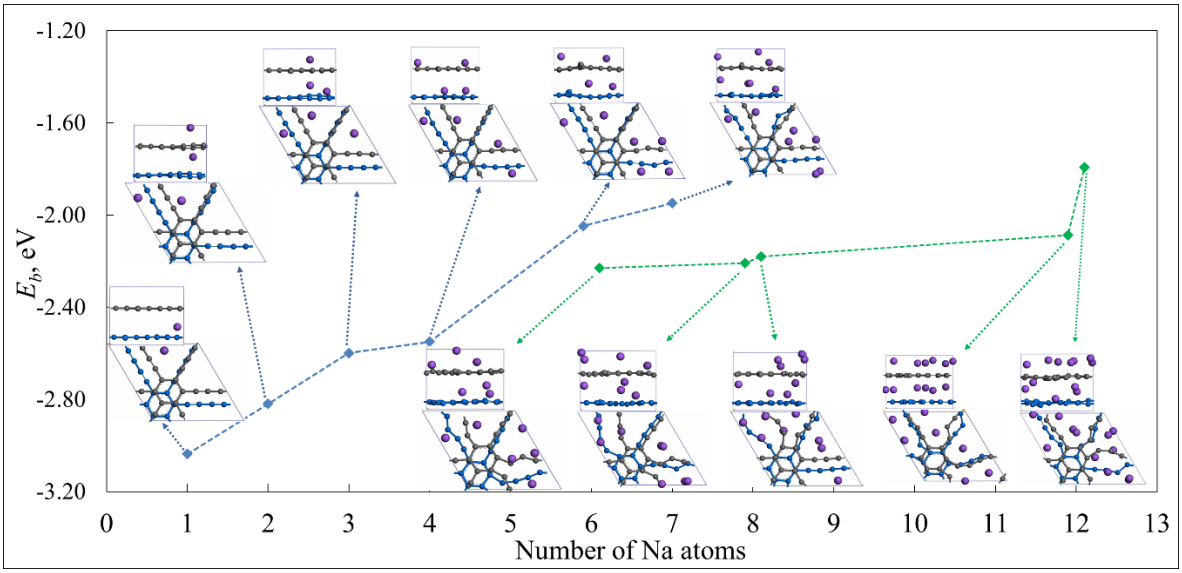

Fig. 4.4. Binding energy as a function of the number of Na atoms intercalated in bulk GDY. Grey and blue balls represent carbon atoms. The two layers have been coloured differently to distinguish between them. Purple balls represent sodium. The top and the side view of each structure are shown. The blue diamonds show binding energies for the undistorted structures and the green diamonds shown binding energies for distorted structures. The lines serve as guides to the eye.

Table 4.2. Binding energy values for Na intercalation on the GDY bulk layers with AB-2 stacking

Na atoms per unit cell	Strongest E_b (eV per Na atom)	Strongest E_b (eV per Na atom) – undistorted configuration
1	-3.04	-3.04
2	-2.82	-2.82
3	-2.60	-2.60
4	-2.55	-2.55
6	-2.23	-2.05
7	-1.95	-1.95
8	-2.21	NA
12	-2.09	NA

All the E_b values obtained have a magnitude larger than 1.113 eV (cohesive energy of Na), so no clustering of Na atoms is expected for the systems shown, and indeed this is not observed in the structures. Although a maximum loading of 12 Na atoms in the unit cell was considered, after 7 atoms all the initial structures considered became significantly distorted. As noted, we did not allow the bulk material to expand on addition of Na for the systems shown in Fig. 4.4, however this possibility is also considered later in this manuscript.

Overall, our results suggest that the maximum Na capacity of bulk GDY without significant distortion and without expansion of the supercell is Na_7C_{36} or $NaC_{5.14}$, equivalent to 316 mA h g^{-1}. We note that the single GDY layer had a capacity of Na_7C_{18} or $NaC_{2.57}$, which is twice that of the prediction for bulk GDY. This is due to the size of the pore, since in the single sheet case higher loadings involved Na atoms located about 2 Å above the sheet, which is more than half the interlayer spacing in bulk GDY.

However, the loading obtained for bulk GDY is more likely to be representative of the bulk loading that can be attained. Furthermore, a capacity of 316 mA h g^{-1} is comparable to existing materials, and if the mobility is high will make bulk GDY an interesting material for consideration as a Na battery anode. This will be explored in the next section.

We also observe that, in contrast to the single layer cases where the Na atoms have minimum energy structures with the Na atom in the plane of the GDY sheet, in the bulk cases Na atoms tend to be between the layers, even when there is only a single Na atom. We will later

demonstrate that there is little change in the potential energy as the Na moves between the sheets along an appropriate path. Finally, the very slightly distorted configuration of 6-Na atom in Fig. 4.4 (on the blue curve) is of significance since it corresponds to a case where 3 atoms are placed near the corners of each pore, forming a symmetric conformation. This structure is similar to that obtained with 6 Li and Na atoms placement on double layers of GDY, in the works of Zhang [8] and Xu [9], respectively.

For the AB-3 stacking, the single Na atom in GDY has minimum energy structure with the Na located at very similar site as in the case for a single Na atom in GDY with AB-2 stacking (see Appendix 3, Fig. 3A.1), and the Na atom has a binding energy of -3.01 eV which is also similar to the result for the AB-2 stacking. The energy for the system with the Na atom in the plane of the membrane is just 0.05 eV higher.

4.4.3 Energy barriers for transitions across, and through, GDY

In this section, we present calculated energy barriers for Na movement across GDY layers in GDY single sheet and bulk systems. The energy barriers determine the mobility of the Na, and therefore affects the charge and discharge rates in a battery. Either single point calculations along a desired trajectory, or NEB calculations were used to determine the energy barriers and configurations at the transitions state. To give an idea of the magnitude of the energy barriers, we can compare them with those for hopping of a Li between rings of graphene of 0.32 eV [10], in graphite of 0.34 eV [66], and the barrier for movement of Li from one pore to another in GDY of about 0.51 eV [116], 0.70 eV [27].

For the single GDY sheet, we consider three pathways between local and global minima which are presented in Fig. 4.5. The energy barriers and distance of the Na atoms from the GDY sheet are summarised in Table 4.3. Fig. 4.5a shows the transition from a Na atom at the centre of the triangular pore (and in the plane of the GDY sheet) to a Na above the centre of the 6-carbon ring. At the transition state, the Na atom is directly above a carbon-carbon bond of the 6-carbon ring. The energy barrier for movement of the Na atom from the pore to the ring is relatively large at 1.17 eV and therefore this transition will be unlikely under typical conditions. There is also a barrier for movement from the ring to pore of 0.13 eV, but it is relatively low and therefore it is anticipated that the Na will move off the ring to the pore quite readily. These values are similar to those obtained by Xu et al. (1.09 eV and 0.18 eV).

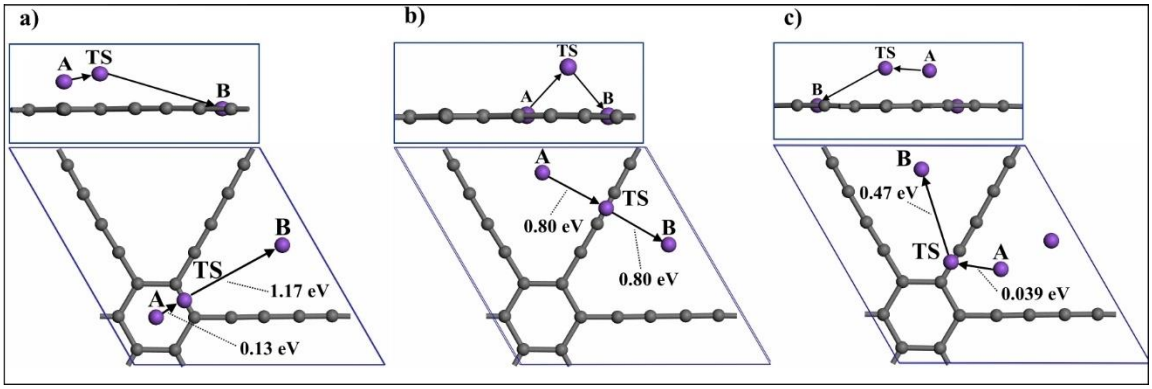

Fig. 4.5. Transition states for movement of a Na across the GDY single sheet (a) between the ring and pore, (energy barrier from A to TS: 0.13 eV, from TS to B: 1.17 eV); (b) from one pore to another, (energy barrier from A to TS: 0.80 eV, from TS to B: 0.80 eV); and (c) from one pore to another in the presence of another Na atom (energy barrier from A to TS: 0.039 eV, from TS to B: 0.47 eV). The top and side view of the pathway are shown. Grey balls represent carbon and purple balls represent sodium atoms.

Table 4.3. Values of energy barriers for Na movement for 3 different pathways and distance of the Na atom from the GDY surface.

Transition	**Na-GDY distance, h_{ad} (Å)**			**Energy barrier (eV)**	
	Initial State (A)	Transition State (TS)	Final State (B)	Initial to Final State	Final to Initial State
See Fig. 4.5a	1.77	2.26	0.00	0.13	1.17
See Fig. 4.5b	0.00	2.16	0.00	0.80	0.80
See Fig. 4.5c	2.10	2.25	0.00	0.039	0.47

The second pathway was between the centres of two adjacent pores is shown in Fig. 4.5b. The initial and final positions are global minima and it is found that the Na will move across the middle of the 4-carbon chain with a barrier of 0.80 eV. This value is larger than the hopping energy of Li on graphene, and similar to the barrier for transition between the triangular pores of GDY for Li. It is comparable with the result of Xu et al. who found a barrier of 0.64 eV using a different methodology. This barrier is smaller than that for movement from the centre of the triangular pore to the 6-carbon ring, and therefore this is a more likely pathway.

In both the cases described above, situations where there is a single Na atom in the supercell were considered. In the third case (see Fig. 4.5c), one Na atom was fixed at the global minimum at the centre of the triangular pore, and another was situated above the same pore such that the overall structure was a local minimum, and there are two Na atoms in the supercell. The barrier for movement of the second Na atom to the centre of the adjacent pore was found to be just

0.039 eV (see Fig. 4.5c and Table 4.3), with a transition state over the carbon chain, and therefore this Na would be very mobile. The barrier for the reverse pathway is moderate at 0.47 eV, and is much smaller than the barrier for movement of the Na at the centre of the pores when there is only one Na in the supercell. Therefore, as the loading increases, the mobility of the Na is likely to become greater. As can be seen from Fig. 4.3, at low loading the Na tends to be situated at the very stable position at the centre of the triangular pore, but as loading increases the Na atoms are more likely to be situated out of the plane and this will also enhance mobility.

Finally, for the GDY sheet, we can consider the energy profile as an Na atom moves directly through the centre of the GDY plane. Because the Na is at a minimum energy position in the plane, there is an energy barrier in this direction which is equal to binding energy, 2.53 eV and therefore is quite high.

To judge if GDY is suitable for use as an electrode, it is important to consider the mobility of Na in bulk GDY. This is particularly true for the Na/GDY system because the lowest energy state changes from being in the plane of the GDY for the sheet, to between the pores for the bulk and therefore the energy barriers, pathways and mobility will change. In addition, at high loading the Na atoms are about 2 Å above the single sheet whereas the gap between the GDY sheets is only about 3.3 Å.

Firstly, we consider the AB-2 stacking. This was selected due to the large pore perpendicular to the plane of the GDY sheet (see Fig. 4.2a), which we anticipated could provide a passage with relatively low energy barriers. However, this needed to be tested, especially in light of the large binding energy for Na at the centre of the GDY triangular pore, the known extremely high energy barrier for diffusion through the 6-carbon rings of graphene and the result of Xu et al. [77] who showed that there is a very large barrier (4.5 eV) to out-of-plane movement through a pore of the single layer sheet, at a position close to the corner of the triangular pore.

We tested two pathways for movement within the interlayer gap of GDY with AB-2 stacking, between the GDY layers, and one for movement between the planes shown in Fig. 4.6a-c. Unlike in the single layer case, the binding energy of a Na atom did not vary greatly over a large region between the overlapping triangular pores. In fact, many local minima were identified in this region, with energy differences of only approximately 0.05 eV using force convergence criterion of 0.01 eV $Å^{-1}$. Furthermore, using a force convergence criterion of 0.05 eV $Å^{-1}$ gave results differing consistently in binding energy from those with 0.01 eV $Å^{-1}$ by about 0.17 eV. We therefore estimate the global minima energies for the bulk system to have

errors of up to approximately 0.1 eV. However, the reported energy barriers in all the pathways of Fig. 4.6, except Fig. 4.6c which as calculated by the force convergence criteria of 0.01 eV $Å^{-1}$, are calculated by the force convergence criteria of 0.05 eV $Å^{-1}$.

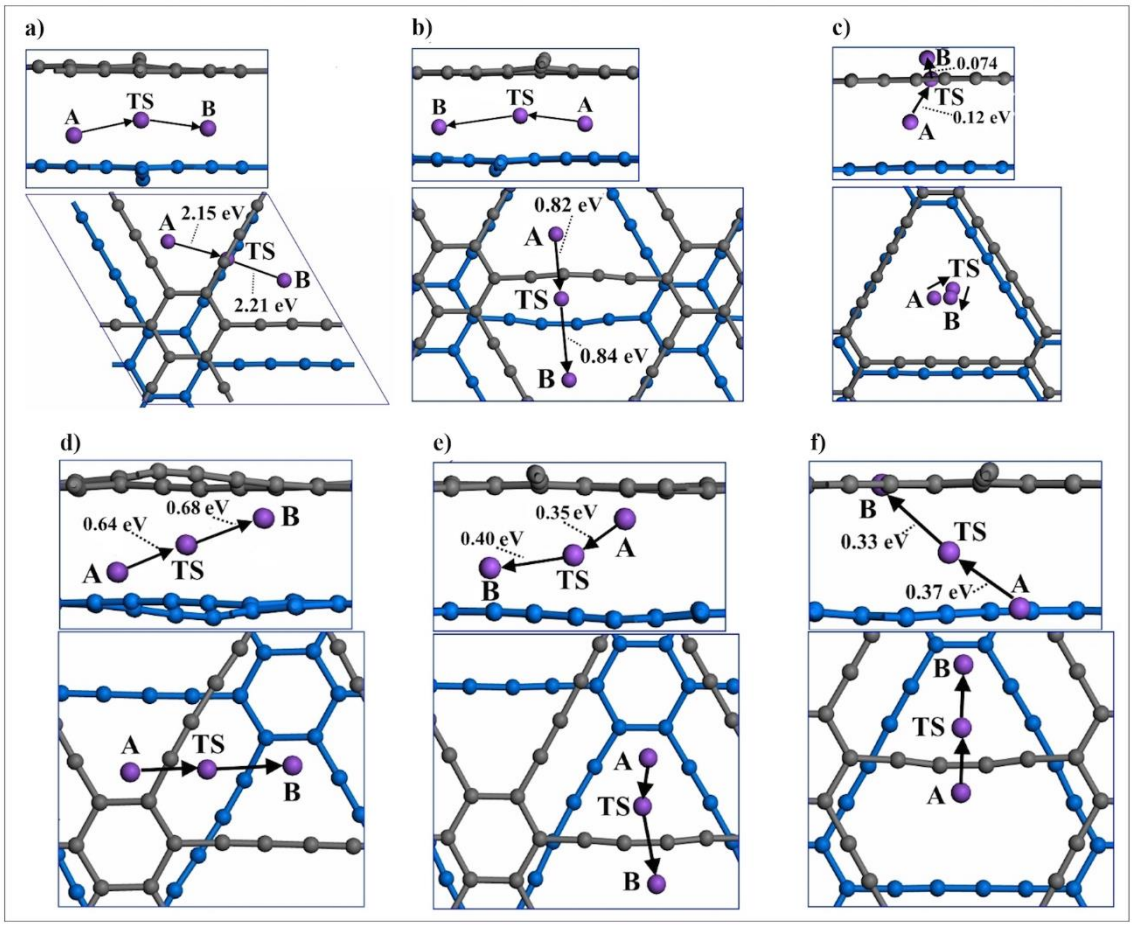

Fig. 4.6. Transitions state for movement of a Na atom in bulk GDY with (a)-(c) AB-2 stacking and (d)-(f) AB-3 stacking. (a), (b) are pathways between GDY layers and (c) is through a GDY layer. The top and side view of the movement are shown. (d) and (e) are both paths between layers and (f) is for a path from the centre of a pore on one layer to the centre of a pore on another layer. The top and side view of the pathway are shown. Grey and blue balls represent carbon atoms in different layers to distinguish between layers. Purple balls represent sodium atoms.

In Fig. 4.6a we show the pathway for a single Na between the layers from a minimum energy position on one pore to another on an adjacent pore, passing between the 4-carbon chains that lie directly above each other in the AB-2 stacking. There is a very high energy barrier of 2.2 eV due to the proximity of the Na to the carbon chains at the transition state. At that point, the carbon chains are distorted to accommodate the Na atom, and the average distance between the two sheets increases by about 8.5%, however the strong bonding in the chain prevents too much distortion, developing strain in the chain that contributes to the large energy barrier. The size

of the energy barrier indicates that in the bulk system, movement of a Na atom between the chains is highly unlikely under standard operating conditions. The small difference in the two energy barriers (Fig. 4.6a) is due to slightly different initial and final geometries of the transition pathways. This is most evident in the side view, and occurs because of the many local minima of similar energy, as discussed above.

The second pathway, which is shown in Fig. 4.6b, is between the layers from a minimum energy position on one pore to another on an adjacent pore, but in this case it passes between the two 4-carbon chains that do not lie directly above each other. The transition state is mid-way between the chains and some distortion of the chains is observed, however these carbon chains are 4.69 Å apart when the Na is not present, making space for the Na to move and the energy barriers are greatly reduced to 0.82 and 0.84 eV. This value is similar to the barriers observed for movement across the carbon chains in the single GDY sheet.

The third transition studied was through the GDY sheet, from a minimum energy position at the centre of a pore, through the sheet to a minimum energy position on the other side of the sheet. The barriers for the forward and reverse paths were both low: 0.12 eV and 0.074 eV, respectively. These values are both smaller than the hopping of Li between rings on graphene and only ~$5k_BT$ and $3k_BT$ at 298K, so would be expected to be easily overcome. This result is very encouraging for the use of AB-2 stacked GDY in NIBs.

Attempts to find transitions states in the pathway from one side of the slit pore formed by the two sheets to the other were problematic due to the very flat potential energy surface in this region. Therefore, in order to get an idea of the energy landscape across the pore, single point energies were calculated along a zig-zag path that connected to the local minima at the centre of the slit pore, and the local minima in the plane of the sheet. The results are shown in Fig. 4.7. Clearly the barriers are very low.

Due to the very low energy barriers perpendicular to the sheets in the AB-2 stacked GDY, and the moderate energy barriers parallel to the sheet, across the carbon chains the diffusion would be predominantly through the triangular pores (so one-dimensional). This is not ideal as blockages are more likely to prevent diffusion. For this reason, AB-3 stacked GDY was also considered.

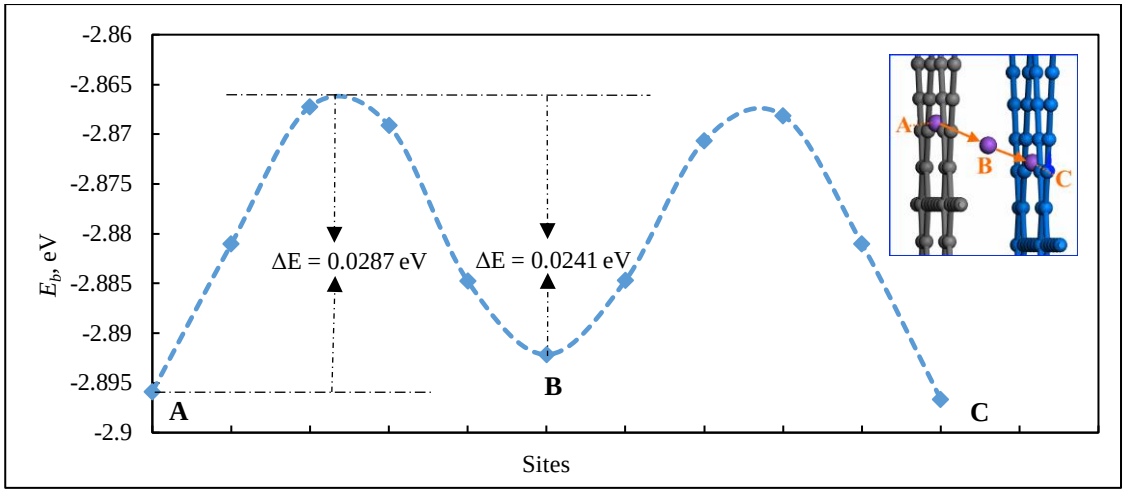

Fig. 4.7. Energy profile for movement of an Na atom through bulk GDY, from minimum energy positions at the centres of the pores. The position of the Na atom at sites A, B and C is shown in the inset.

As discussed above, AB-3 stacked GDY has very similar stability to AB-2, and has been predicted to be more stable [118]. Due to the greater distance between the 4-carbon chains and poorer alignment of the triangular pores in AB-3 GDY, we would expect the barriers parallel to the sheet to be reduced, and those perpendicular to the sheet to be increased.

Again, the potential energy surface between the triangular pores is very flat, so many local minima were identified, and the results are sensitive to the selection of the force convergence criterion. Two significant pathways for transition of a Na atoms within the interlayer spacing are shown in Fig. 4.6d-e. In Fig. 4.6c, the transition is from a minimum energy position located above a triangular pore on one sheet, between two 4-carbon chains, to a similar minimum energy position in an adjacent triangular pore of the sheet on the other side. The energy barrier of approximately 0.68 eV in this case is lower than any of the transitions within the interlayer spacing observed with an AB-2 stacking.

The second transition pathway is shown in Fig. 4.6e. In this case, the initial position is similar to the final position in 4.6d, but passes over a single carbon chain to reach a final position is close to the sheet on the other side of the slit formed by the two pores. The energy barrier for this is just 0.35 eV, and for the reverse pathway is 0.40 eV. These barriers are quite similar to those for Li hopping on graphene, and therefore we anticipate that such a diffusion path would be likely in a NIB.

In Fig. 4.6f, the pathway from a position at the centre of one pore, in the membrane plane to the centre of another pore in the plane of the adjacent membrane is shown. The barriers in this

case are 0.37 and 0.33 eV, showing that the barriers for movement from one plane to another are sufficiently low that this is likely to occur. Clearly using the pathways shown in Fig. 4.6f zig-zag pathways could be constructed with a barrier of approximately 0.37 eV.

According to the Luo et al. [118], the AB-3 and AB-2 stackings are convertible to each other with a maximum barrier of energy of 1.5 meV $atom^{-1}$, which is quite low. Hence the two configurations can coexist in real experiment. These results indicate that the barriers for diffusion are low, even with a cell that is not able to expand. In addition, the loadings that can be obtained are high, making this a very promising material for NIBs.

4.4.4 Expansion of bulk GDY due to loading with Na

So far, all calculations of loading and diffusion have been done with the lattice parameters fixed. On loading, if there is insufficient space for a Na atom in an interlayer spacing, the slit pore might expand to accommodate it. As in our simulated bulk systems we have two inequivalent slit pores in the simulation cell, there was some freedom for one pore to expand, and expansion of up to about 5.5 % was observed with a loading of 7 Na atoms. This would lead to contraction of the other spacing and therefore it is somewhat contained. Here we consider what expansion might occur if there is no restriction on the lattice parameters. The results presented here are for an idealised situation where the loading is uniform and bulk GDY is free to expand. As mentioned above, real systems will be an intermediate between the restricted case considered above and that considered here. Of course, the mobility within a slit pore will be even greater if the lattice parameter is allowed to increase.

In order to look at the degree of expansion that might be expected, we considered a number of loadings of the AB-2 stacking system. In all cases except one (described below) we took the minimum energy, undistorted structures shown in Fig. 4.4, and incrementally changed the lattice parameter by 1%, re-optimising the structure at each stage and calculating the energy of the system. We found that when 1 Na atom is placed above each of the triangular pores in the unit cell (4 atoms in total or NaC_9), the interlayer spacing contracts by 1% to 3.26 Å. This suggests that each Na is binding to both surfaces of the slit pore containing it, and that this is a very stable system. As the loading increases we see expansion of the interlayer spacing, and when 7 Na atoms are inserted (Na_7C_{36}), giving the maximum capacity indicated above (see configuration in Fig. 4.4), the lattice spacing is optimal with at 12% expansion of the layers (3.29 Å to 3.69 Å). In addition, the binding energy increased from -1.95 to -2.07 eV $atom^{-1}$.

To incorporate 14 Na atoms in the unit cell, we placed the Na atoms on each sheet in a configuration corresponding to the loading of a single GDY sheet with 7 Na shown in Fig. 4.3, and then allowed the sheets to gradually come together. In this case the GDY sheets did not distort greatly and an expansion of 28% was observed with a binding energy of -1.80 eV atom^{-1}.

These results indicate that a loading of much greater than Na_7C_{36} (i.e. $Na_{14}C_{36}$) could be obtained when if expansion is allowed, which is equal to the loading obtained with the single sheet. This is similar, but slightly higher, than the loading observed by Xu et al. which can be attributed to a different selection of initial configurations, the computational parameters used and the different stacking. It shows that the calculations that we have carried out on the bulk system are the worst case predictions, and give further indication that a GDY NIB is a promising alternative to existing rechargeable batteries.

4.4.5 Charge density, Bader and DOS analysis

In order to provide a deeper understanding of the binding between the Na and GDY and the nature of the material formed by adsorption of Na on GDY, we have carried out charge density calculations, Bader and DOS analyses.

Fig. 4.8 presents charge density difference isosurfaces, $\Delta\rho = \rho_{GDY.Na} - \rho_{GDY} - \rho_{Na}$ where ρ is the charge density of the combine or separated systems, when 1, 3 and 7 Na atoms are placed on the unit cell of the GDY sheet. In all cases there is a clear transfer of charge from the Na to the GDY sheet, with the red colour indicating an electron deficient isosurface ($\Delta\rho$ = - 0.0012 eÅ^{-3}), and the blue colour indicating an electron rich isosurface ($\Delta\rho$ = 0.0012 eÅ^{-3}). When 1 or 3 atoms are placed on the surface, the electron transfer from the Na atoms is quite localised although the electrons are distributed to all bonds of the GDY sheet. The isosurface is between the Na atom on the 6-carbon ring and the ring, indicating the charge on that Na atom is lower than those over the triangular pore. As the number of Na atoms increases to 7 Na, the region of electron depletion becomes more widely distributed; and the electron rich region remains around the carbon chains and ring.

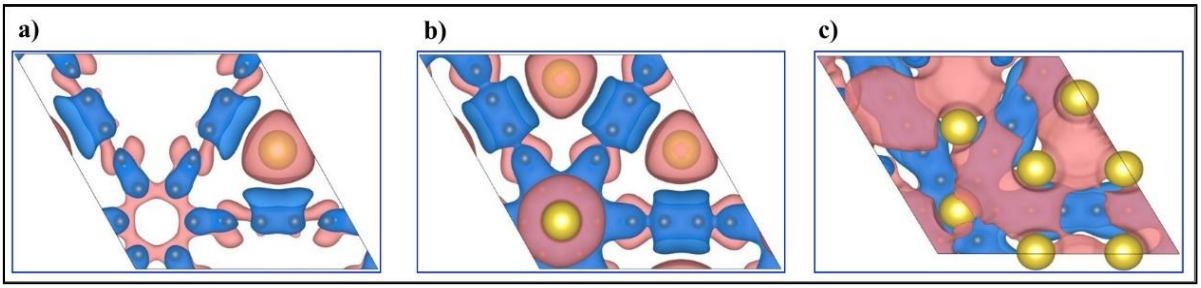

Fig. 4.8. Charge density difference for (a) GDY Na_1, (b) GDY Na_3, and (c) GDY Na_7. The red colour indicates an electron deficient isosurface ($\Delta\rho$= - 0.0012 eÅ^{-3}) and the blue colour indicates an electron rich isosurface ($\Delta\rho$= 0.0012 eÅ^{-3}).

In order to further characterise the degree of charge transfer, a Bader charge analysis [198, 199] was carried out for each of these systems. In all cases the charge on the carbon atoms was similar for each carbon. When 1 Na atom was present, its Bader charge was +0.81. When 3 Na atoms distributed as in Fig. 4.8b), the two Na atoms on the pore have Bader charges of +0.81 but that on the ring has a charge of +0.59, indicating that the charge transfer for the Na atom over the ring is lower. For the case when 7 Na atoms were adsorbed, the charge transfer from each of the Na atoms was reduced with 4 of the atoms on the pore having a charge of +0.45 to +0.46 and the other 2 on the pore having a charge of +0.25 to +0.26. The Na on the ring has a small charge transfer with a Bader charge of +0.01. Although the sum of the charges on the Na atoms increases with the loading, the average charge on each does not due to the limit on the capacity of the GDY to accept electrons.

Finally, insight into the change in the electronic properties of pristine GDY due to adsorption of Na is given by consideration of the DOS (Density of States) analysis of pure GDY, GDY Na_1 and GDY Na_7. The results indicate that pure GDY has a small band gap of 0.37 eV, in agreement with previous results obtained using PBE functionals, [118], and suggesting that it has a semiconducting behaviour. However, the insertion of Na atoms introduces states within the band gap transforming it into a metallic system (see Fig. 3A.2). The partial DOS was also carried out in each of these cases (see Fig. 3A.3 in Appendix 3).

4.5 Conclusion

In conclusion, we propose that Na on GDY is potentially a suitable anode for rechargeable batteries. Na is cheaper and more abundant than Li, and GDY provides large pores and space for a Na to intercalate in and then move throughout. According to the results, the maximum capacity of GDY for Na atoms is $NaC_{2.57}$ for a single GDY layer (equivalent to 497 mA h g^{-1}),

and $NaC_{5.14}$ for GDY bulk layers (equivalent to 316 mA h g^{-1}) if we do not allow expansion of the GDY bulk unit cell. If expansion is allowed, then this capacity is likely to increase to $NaC_{2.57}$. We have provided the first calculations of the energy barriers for transitions of Na between sites in the bulk GDY. The results indicate that Na atoms would readily move through the triangular pores normal to the GDY sheets in bulk GDY with an AB-2 stacking, and that they would readily move in directions both parallel and normal to the GDY sheets with an AB-3 stacking. Barriers are either lower or similar to those observed for Li on graphene.

4.6 Acknowledgements

The authors thank the Australian Research Council for support of this project through the LIEF program. This research was undertaken with the assistance of resources provided at the NCI National Facility systems at the Australian National University through the National Computational Merit Allocation Scheme supported by the Australian Government, from the Queensland Cyber Infrastructure Foundation (QCIF) and the University of Queensland Research Computing Centre.

The following chapter contains the published paper in the Carbon journal, 2018, Vol. 136, p. 73-84 [76]

Amir H. Farokh Niaei[a], Tanveer Hussain[a], Marlies Hankel[a] and Debra J. Searles[a,b, 49]

[a] Centre for Theoretical and Computational Molecular Science, Australian Institute for Bioengineering and Nanotechnology, The University of Queensland, Brisbane, QLD, 4072, Australia

[b] School of Chemistry and Molecular Biosciences, The University of Queensland, Brisbane, QLD, 4072, Australia

Contributors	Statement of contribution
Amir H. Farokh Niaei (candidate)	Presented the topic and idea (80%) Conducted the computations (100%) Analysed the result data (80%) Wrote and reviewed the paper (60%)
Hussain T.	Reviewed and edited the paper (5%)
Hankel M.	Reviewed and accepted the topic and idea (5%) Reviewed and Edited the paper (5%)
Searles D.J.	Reviewed and accepted the topic and idea (15%) Analysed the result data (20%) Wrote and edited the paper (30%)

[49] Corresponding author. Centre for Theoretical and Computational Molecular Science, Australian Institute for Bioengineering and Nanotechnology, The University of Queensland, Brisbane, QLD, 4072, Australia. E-mail address: d.bernhardt@uq.edu.au (D.J. Searles).

Chapter 5

Hydrogenated defective graphene as an anode material for sodium and calcium ion batteries: A density functional theory study

5.1 Abstract

Recent experimental studies indicated that hydrogenation improves the performance of graphitic materials used as anodes in lithium and sodium ion rechargeable batteries. Here, results of density functional theory calculations are presented to demonstrate that this is also effective for both sodium and calcium ion batteries. It is shown that this can be explained by the increase in binding strength of the metal adatom to the hydrogenated graphene, compared to its binding to graphene, and also an increase in the interlayer spacing of the layered materials. According to our calculations, whereas Na and Ca bind weakly to the graphene sheet with binding energies of -0.763 and -0.817 eV, they bind more strongly to the single layer of the proposed hydrogenated graphene sheet ($C_{68}H_4$) with binding energies of -1.670 and -2.756 eV, respectively. Furthermore, although Na does not intercalate strongly in the layers of the $C_{68}H_4$ material, up to 16 Ca can intercalate into the bulk layers of this material giving an electrical capacity of 591.2 mA h g^{-1} and a 29.3% expansion of the interlayer distance. Thus, hydrogenated defective graphene provides an anode material that might enhance the performance of rechargeable batteries compared to graphene, using metals that are cheaper than lithium. However, the degree of expansion could be problematic in some applications.

5.2 Introduction

Recently, investigations on the possibility of developing sodium (Na) and calcium (Ca) ion rechargeable batteries have become more widespread. Since 2000 when Stevens and Dahn [15] inserted sodium into hard carbon materials, much theoretical and experimental work has been carried out to see if efficient Na ion batteries (NIB) and Ca ion batteries (CIB) can be realised through the selection of appropriate electrode materials [6, 8, 11, 17, 18]. The electrode materials that have been considered include a variety of two-dimensional carbon materials and non-carbon materials [11, 17]. Since Na/Ca are more abundant than lithium (Li), NIBs and CIBs are cheaper, and therefore favourable alternatives to lithium ion batteries (LIBs). In addition, Ca has the advantage that its ion has a +2 charge compared with +1 for Li and Na [20-22], although its atomic mass is higher.

Graphite has been most widely used as the anode material for LIBs [5, 53]; however, graphite does not bind Na and Ca atoms sufficiently strongly for Li to be replaced by them [7, 10, 66]. Moreover, graphite has an interlayer distance of 3.35 Å and intercalation of Li is readily achieved, whereas intercalation of Na and Ca is not [25, 211]. This is because the atomic radii of Na (1.86 Å) and Ca atoms (1.97 Å) are significantly larger than Li (1.52 Å); 22% and 30% larger, respectively [2]. Cao et al. [25] suggested that the minimum interlayer distance required for Na intercalation would be 3.70 Å. In accordance with this, Komaba et al. [212] found that the interlayer distance of the disordered carbon (or hard carbon) that they studied, which was 3.80 Å, making it possible for Na to intercalate. Another issue that prevents the development of NIBs using Na is that Na has been found to bind more weakly to graphene than other alkali metal and alkaline earth metal atoms. Liu et al. [7] found that the weak binding of Na (and Mg) on a graphene layer can be attributed to the relative magnitudes of ionisation energy of the metal atoms and coupling between the graphene and the metal cations. Thus, two possible ways of designing electrodes for NIBs and CIBs based on layers of carbonaceous materials are to select materials where the binding of the metals to that material is stronger and the interlayer spacing is larger than for graphite.

A solution that has been considered to address the issue of weak binding is the use of defective graphene, including graphene with Stone-Wales (SW) defects, mono-vacancies (MV) (graphene with a single C atom removed) and di-vacancies (DV) (graphene with two adjacent C atoms removed). These structures have been synthesised and considered for metal atom

adsorption [30, 31, 121, 122, 124, 125]. Fig. 5.1 shows a schematic view of these defects in graphene.

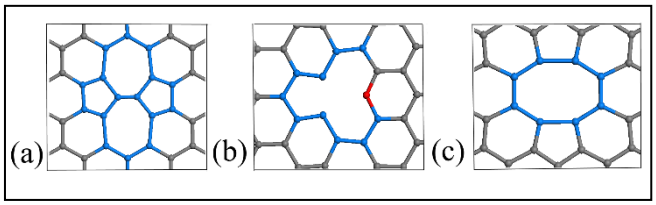

Fig. 5.1. Optimised structures of graphene with (a) a Stone-Wales defect, (b) a mono-vacancy and (c) a di-vacancy. All atoms are carbon atoms. Blue atoms are those surrounding the vacancies or defects and the red atom in (b) indicates an under-coordinated carbon atom.

Vacancies in graphene layers can be produced by ion bombardment using ions such as Ar^+ at various energies [31, 121] with MVs and DVs, being the most likely defects formed after radiation of low energy beams over the graphene layer. Vacancies can also be produced using synthetic methods. For example, they can be formed from reduction of graphene oxide [47, 48, 126] or following an annealing process (thermal heating from 1000 to 1500 K), which can lead to very large defects [127]. Vacancies with odd numbers of C atoms removed have an under-coordinated carbon atom (commonly denoted to have a 'dangling bond' on the carbon atom), and introduces asymmetry in the configurations [122]. Moreover, the removal of a C atom results in a strain in the system, which can be partly compensated for by rearrangement of the structure in the vicinity of the vacancy. Due to the strain, C-C bond lengths around the vacancy can be longer than the normal C-C bond; for example, Carlsson and Scheffler observed bond lengths between 1.42 and 1.8 Å in defective graphene materials they considered [122]. Strain and dangling bonds can cause the carbon atoms in the vicinity of the vacancy to be more reactive than other C atoms in graphene.

There have been a number of studies that considered the effect of defects and vacancies (mainly SW, MVs and DVs) on the adsorption of Na or Ca with an aim to enhance the properties of electrodes for rechargeable batteries [32, 33, 73]. The theoretical electrical capacity of the anode material in mA h g^{-1} is:

$$C_E\ (mA\ h\ g^{-1}) = \frac{n_e\ n_M\ F}{3.6(n_M m_M + n_H\, m_H + n_C m_C)} \qquad (5.1)$$

where m_M, m_H and m_C are the atomic masses of the metal (M), hydrogen (H) and carbon (C) atoms; n_M, n_H and n_C are the number of M, H and C atoms in a unit cell and F is Faraday's

constant, 9.648×10^4 C mol^{-1}. The value of n_e is given by the valency of the metal atoms (1 for Na and 2 for Ca). Considerable increase in the Na and Ca capacity has been observed on defective graphene sheets compared to pristine sheets. For example, Datta et al. could obtain capacities of 646 mA h g^{-1} and 927 mA h g^{-1} for graphene sheets with DVs with a 25% defect rate [32] (note that in the paper of Datta et al., capacities of 1450 mA h g^{-1} and 2900 mA h g^{-1} are reported because the mass of Na and Ca are not included in the definition of the capacity, unlike in the current work where it is defined by Eq. 5.1. Adsorption of Na or Ca was allowed on both sides of the sheet in that study. Tsai et al. found a loading of NaC_8 (225 mA h g^{-1}) could be obtained in a graphene bi-layer with an AA stacking and a DV on one of the layers, which resulted in the expansion of the interlayer distance from 3.35 Å to 4.50 Å [33]. In a similar study, Yang et al. found that a loading of Na_6C_{35} (228 mA h g^{-1}) could be obtained in bi-layer graphene with an MV and an AA stacking [73]. In each of the studies mentioned above, Na or Ca accumulation near the vacancy or defect was observed.

Despite increased metal atom capacities, graphene layers with MVs are not expected to be suitable materials for batteries due to the dangling bonds on the carbon atoms, which make them quite reactive [72]. This could lead to bonding between layers and reduce the interlayer distances. However, the under-coordinated C atoms can be hydrogenated to form more stable structures [45, 130, 132, 133]. Casartelli et al. [45] applied density functional theory (DFT) to investigate the effect of the presence of C-H bonds on the structure of graphene by considering a hydrogenated MV. They considered 1 to 6 H atoms (2 for each carbon) on the three carbon atoms around a vacancy. They found that at 0 K, the fully hydrogenated system was most stable. However, due to entropic effects, at higher temperatures various degrees of hydrogenation could be achieved. Fig 5.2 shows the lowest energy structures for the MV with 1 or 2 H atoms.

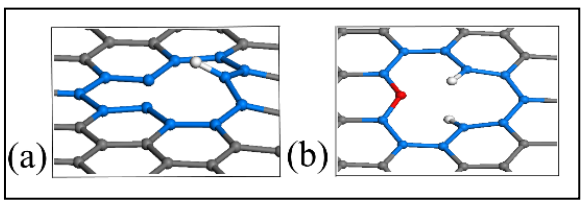

Fig. 5.2. Side views of the most stable structure of (a) graphene with an MV and a single H atom, (b) graphene with an MV and two H atoms. The grey, blue and red atoms are C atoms, with those surrounding the vacancy coloured blue and the under-coordinated carbon atom coloured red. The white atoms are hydrogen atoms.

According to Casartelli et al. [130], the creation of a C-H bond in the MV leads to a C-H bond directed out of the plane of the graphene sheet, as seen in Fig. 5.2a. The carbon atom lies 0.694 Å above the graphene plane [130]. This is of interest as it indicates that hydrogenated MVs (H-MVs) may increase the interlayer distance in layered bulk materials.

This possibility is consistent with experimental results of Yoon et al. [44]. They used a new synthetic route, using supercritical alcohol and which is referred to as a modified Hummers method, to fabricate hydrogen-enriched porous carbon nanosheets (H-PCNs) with an H/C ratio of 2.3. The new material was then tested and found to be suitable for the anode of NIBs. The electrical capacity of the anode was 300 mA h g^{-1} at 50 mA g^{-1}, with a cycling stability of 2000 at 1-5 A g^{-1}. They suggested that the enhanced capacity could be attributed to the high number of hydrogen-terminated groups, a large number of defects on the sheets and the large interlayer spacing of 3.8 Å between the material layers. Likewise, other researchers achieved a high electrical capacity using a hydrogenated carbonaceous material as anode materials for LIBs and NIBs [16, 43, 74, 75, 135], with the highest value for NIBs reported in these papers being 491 mA h g^{-1} [74].

In order to examine if hydrogenated defective graphene might be a useful material for Na and Ca ion battery electrodes due to strengthening binding energies compared to graphene and/or increasing interlayer spacing in graphitic materials, we carried out a comprehensive study on a series of defective graphene sheets. Initial DFT calculations of the binding energies of Na on graphene sheets with vacancies and hydrogenated vacancies were carried out to determine which structures would be most likely to enhance alkali metal atom binding. We then examined the binding of multiple Na and Ca atoms on single layers of this structure and a model of the bulk, layered material. We expected similar enhanced binding for Ca as was observed for Na on the single layer. However, the different valency and similar size of the Ca atom suggested there could be an enhanced capacity with Ca. The Na and Ca binding energies and the expansion of the material with loading were determined to ascertain hydrogenated defective graphene could provide a suitable material for NIBs and CIBs. The results obtained should guide the selection of electrode materials for further experimental investigation.

5.3 Methodology

To study the interaction of Na and Ca on the hydrogenated defective graphene, DFT calculations were performed as implemented in the Vienna *ab initio* Simulation Package (VASP, ver. 5.3.5 and 5.4.4) [42]. The system is considered to be periodic in two dimensions for the single layer studies and periodic in three dimensions for bulk layer studies. A plane-wave basis set was used. Within this package, the generalised gradient approximation (GGA) with projector-augmented wave (PAW) method was selected [177, 195]. The Gaussian smearing parameter was set to 0.05 eV. To account for the van der Waals interactions, the DFT-D3 method of Grimme [64, 190] was used. For calculations considering a single layer of graphene with a defect, the Brillouin zone was sampled with a 3 × 3 × 1 *k*-point mesh and the bulk layers were sampled with 3 × 3 × 2 *k*-point mesh, using the Monkhorst-Pack scheme. For the density of states (DOS) calculations, a 11 × 11 × 1 *k*-point grid of was used. The cut-off energy for the plane-wave basis set was selected to be 700 eV. The energy convergence criterion was selected to be 1×10^{-6} eV for most of the cases and 1×10^{-4} eV for the bulk cases. The force convergence criterion was selected to be between 0.05 eV $Å^{-1}$ and 0.01 eV $Å^{-1}$. The number of *k*-points and cut-off energy, force and energy convergence criteria were optimised in preliminary calculations [28]. Moreover, the cell sizes were optimised by cell size variation or using automatic cell size optimisation in VASP for more complex bulk cases with a high number of atoms. Charges on the atoms were calculated using a Bader charge analysis [198, 199].

The binding energy between metal atoms and the substrate was determined by:

$$E_b = \frac{E(S.M_n) - n_M E(M) - E(S_o)}{n_M} \tag{5.2}$$

where $E(S.M_n)$ is the total energy of the substrate loaded with n_M metal atoms (Na or Ca), $E(M)$ is the energy of the metal (M) as an isolated atom, and $E(S_o)$ is the energy of the 2D substrate material in its optimal geometry. Using this definition, a negative binding energy indicates that the binding is energetically favourable.

In order to calculate the contribution of the binding energy due to the interaction between a group of adsorbed Na or Ca atoms and the substrate [69], we also define an 'interaction energy' as follows:

$$E_{int} = \frac{E(S.M_n) - E(M_n) - E(S_d)}{n_M} \qquad (5.3)$$

where, $E(M_n)$ is the total energy of n_M metal atoms considered as an isolated group and $E(S_d)$ is the energy of the substrate only, in the configuration it adopted after adsorption of the metal adatoms (the deformed substrate). The value of $E(S_d)$ is higher than the value of $E(S_o)$, the substrate before metal adsorption. A negative value of E_{int} indicates a favourable interaction between groups of metal adatoms and the substrate [69].

5.4 Results and discussion

Graphene sheets with five different vacancies were considered in this work, and their optimised structures are shown in Fig. 5.1b and c and Fig. 5.3. They differ due to the number of C atoms removed and are referred to as a mono-vacancy graphene (MVG, Fig. 5.1b), di-vacancy graphene (DVG, Fig. 5.1c), tri-vacancy graphene (TVG, Fig. 5.3a), quad-vacancy graphene (QVG, Fig. 5.3b) and 24-vacancy graphene (24VG, Fig. 5.3c) [72]. 24VG was selected as a representative large pore so see the effect of size on the results.

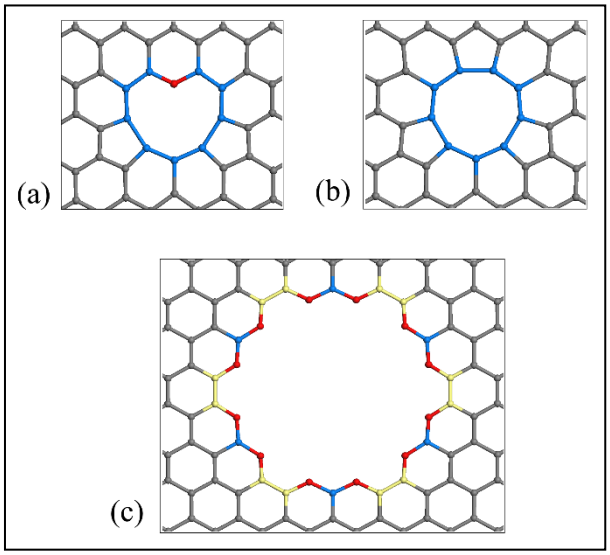

Fig. 5.3. Top view of graphene with a (a) tri-vacancy, (b) quad-vacancy, and (c) 24-vacancy. All atoms are carbon atoms. Those coloured in red denote under-coordinated carbon atoms and those coloured in blue surround the vacancy. In (c) carbons in armchair type and zig-zag type configurations around the vacancy are also distinguished by colouring in yellow and blue, respectively.

The presence of vacancies caused stress in the system, changes in the bonding of the C atoms, and changes in the cell size of the periodic structures in the defected sheets compared to that

of pristine graphene. The optimised cell parameters are shown in Table 5.1 where we assumed $a=b$.

Note the systems considered in Fig. 5.3a and b were formed smaller supercells of the graphene sheets (14.81 Å) than that in Fig. 5.3c which is formed from a larger graphene supercell with length 22.20 Å. According to the results shown in Table 5.1, there are small changes in the cell sizes induced by the vacancies.

Table 5.1. The lattice vector lengths for graphene sheets with various vacancies

Material	Lattice vector lengths (a = b) / Å	% difference from graphene
Graphene	14.81	-
MVG	14.77	- 0.3 (contraction)
DVG	14.67	- 0.9 (contraction)
TVG	14.65	- 1.1 (contraction)
FVG	14.54	- 1.8 (contraction)
24VG	22.27	+ 0.3 (expansion)

5.4.1 Hydrogenated vacancies in graphene

Casartelli et al. [45] showed that hydrogenation of an MV by up to 6 H atoms formed energetically stable structures. Similarly, we considered various degrees of hydrogenation of the five defect models used here. The hydrogenation energy (ΔE_H) for the reaction:

$$C_nH_i+H \longrightarrow C_nH_{i+1} \tag{5.4}$$

was calculated in the usual way:

$$\Delta E_H=E(C_nH_{i+1})-E(C_nH_i)-E(H) \tag{5.5}$$

where $E(C_nH_i)$ denotes the energy of the reactant, i = 0, 1… and $E(H)$ denotes the energy of the isolated H atom. The structures and formation energies for the hydrogenated MV are shown in Fig. 4A.1 and presented in Table 4A.1, and the structures of selected hydrogenated DVG, TVG, QVG and 24VG structures are shown in Fig. 4A.2. Note that the notation used to refer

to the different structures (e.g. H2-MVG) gives the number of hydrogen atoms after 'H' and the type of vacancy after the dash. It should be noted that H2-MVG has a carbon atom with a dangling bond on it, which is indicated in red in Fig. 4A.1b. The result of ΔE_H obtained for the hydrogenated MVs (Table 4A.1) are in good accord with those of Casartelli et al. [45, 130].

For the DVG, QVG and 24VG, various degrees of hydrogenation were considered. These structures are shown in Fig. 4A.2, and it is clear that for the smaller vacancy defects, the H atoms and some of the C atoms around the vacancy are out of the plane of graphene sheet. However, for H12-24VG the H and C atoms are in the plane, indicating the movement out of the plane was due to the proximity of other atoms. Once the pore size is increased to that of 24VG, there is sufficient space for the H atoms to become planar. This would limit the utility of hydrogenation in increasing the spacing between layered sheets, although the large pore itself might somewhat compensate for that, providing space to accommodate Na and Ca atoms. For TVG, there is a dangling bond on one carbon atom around the vacancy, so adding 1 H atom will saturate that. This structure is shown in Fig. 4A.2c, and it is clear that the H and C atoms are all in the plane of the graphene sheet; therefore, this structure might not increase the interlayer spacing greatly. The hydrogenation energy of H1-TVG is -4.92 eV, which has a higher absolute value than the ΔE_H of H1-MVG (-4.25 eV).

5.4.2 Na adsorption on defective and hydrogenated defective graphene

The capabilities of the defective and hydrogenated graphene materials to adsorb (or bind) Na atoms over different sites were considered. For this study, Na was considered because it binds more weakly to graphene than Ca (-0.763 eV and -0.817 eV, respectively for a single metal atom on C_{72}). However, we expected that if enhancement was observed for Na, it would also be observed for Ca. Four different types of binding site are distinguished, as shown in Fig. 5.4a. In Fig. 5.4b, the binding energy of Na at each of these sites on a range of different materials is given, with the blue solid line indicating the cohesive binding energy of Na (-1.113 eV), and the black dashed line indicating the binding energy on pristine graphene (-0.763 eV). In addition, the binding energies of multiple Na atoms at their optimised positions is given to provide an indication of the maximum loading. The values of the binding energies are presented in Table 4A.2.

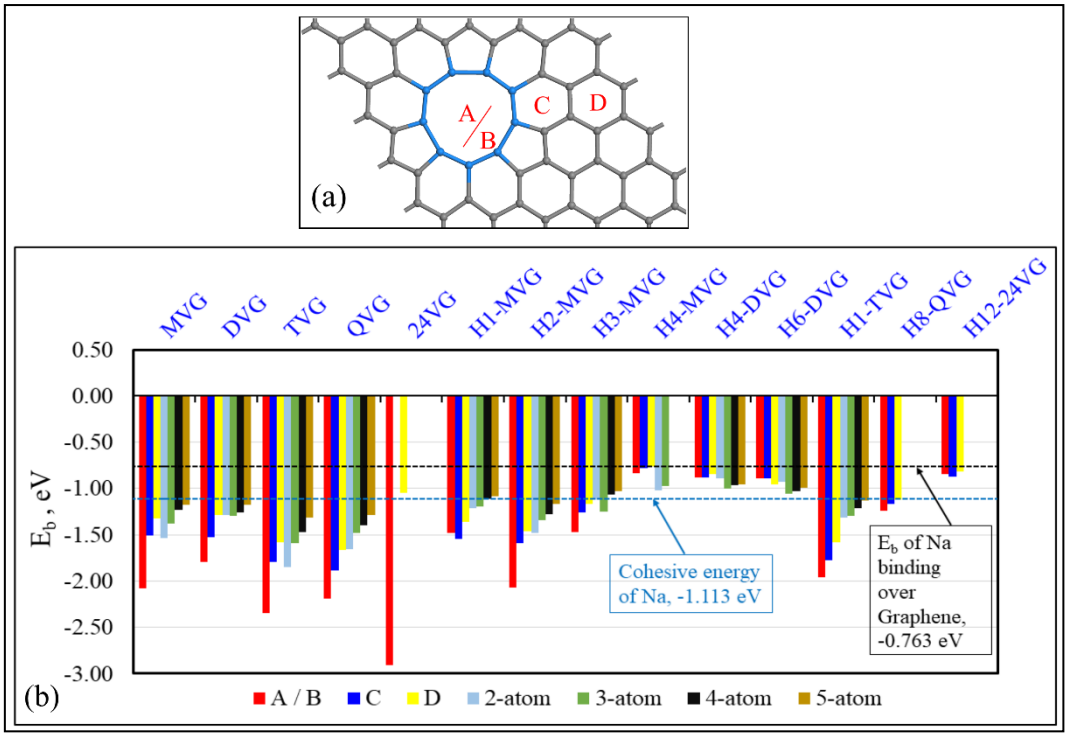

Fig. 5.4. (a) Schematic diagram identifying the different positions for adsorption of Na in a graphene material with typical vacancies. Sites A (over the centre of a vacancy defect) and B (near the edge of a vacancy defect) generally represent the most stable sites over the defect. Sites C and D are the first and second most stable ring away from the vacancy, respectively. (b) A bar chart showing the E_b of Na at the various sites shown in (a) and for 2, 3, 4 and 5 Na atoms in their minimum energy positions over and around the vacancy including the rings nearby. If there is no coloured bar seen for a material and its site, it means that Na was not able to be adsorbed at that site. For 24VG and H12-24VG we did not consider 2 or more Na adatoms.

According to Fig. 5.4b, all graphene sheets with vacancies (MVG, DVG, TVG, QVG and 24VG) bind Na strongly at sites A and B. The binding energies at sites C and D are also stronger than the cohesive energy and the binding energy of Na on pristine graphene. The binding at A and B was the strongest for systems with under-coordinated carbon atoms, and increased as the pore became larger. This behaviour is consistent with that demonstrated previously [32, 33, 72]. Our recent calculations for Na bound to graphdiyne showed similar behaviour, in that the Na preferred to bind in the large pores (-2.53 eV) than over the six-membered ring (-1.48 eV) [28]. For the material to be suitable as an electrode in rechargeable batteries, the binding should not be so strong that the desorption of Na becomes difficult during the discharge process. Moreover, it should not vary too much from site to site which would cause the mobility to be

too low. In most cases, the binding at sites A and B is expected to be problematic due to these reasons.

In contrast to the materials with vacancies, the hydrogenated defective materials in the bar chart show varied results for adsorption of a single Na atom. The materials H1-MVG, H2-MVG, H3-MVG and H1-TVG had E_b values that are stronger than the cohesive energy of Na [10]. Although most other materials bound Na more strongly than graphene, in some cases the E_b was weaker than the Na cohesive energy, which could lead to the clustering of the atoms if more than one Na atom was available. For example, cases with higher number of H atoms in the vacancy resulted in weaker binding as shown in Fig. 5.4b, which shows the effect of the number of hydrogen atoms on the binding energies. However, this is not the case for H2-MVG, which of all the hydrogenated materials binds Na most strongly. This is due to the third carbon atom around the vacancy having a dangling bond, which is not saturated with hydrogen as shown in Fig. 5.2b and Fig. 4A.1b. H2-MVG is expected to be difficult to produce experimentally due to its reactivity and because it is less stable than other materials [45]. However the other materials have Na binding energies at sites A/B that are approximately 0.1 – 1.0 eV higher than the cohesive energy of Na [84], and are expected to be suitable materials for an anode according to this constraint.

Another point to note is that four graphene materials with vacancies (MVG, DVG, TVG and QVG), H2-MVG and H1-TVG can all bind up to at least 5 Na atoms over the vacancy or around it (*i.e.*, the average binding energy is less than the cohesive binding energy). Moreover, H1-MVG and H3-MVG bind 3 adatoms (see Table 4A.2). This indicates that these materials could be of interest for NIB electrode materials. Fig. 5.5 depicts the positions of the 5 Na adatoms on the defective and hydrogenated defective graphene sheets for structures where the binding energy per Na atom was stronger than the cohesive binding energy of Na, or close to it. According to Fig. 5.4b, even when Na atoms are away from the vacancy and over the hexagonal rings, the average magnitude of the E_b values are larger than the cohesive energy of Na (in Fig. 5.4a, sites C and D, blue and yellow bars). This is consistent with the results of Tsai et al. [33] and Yang et al. [73].

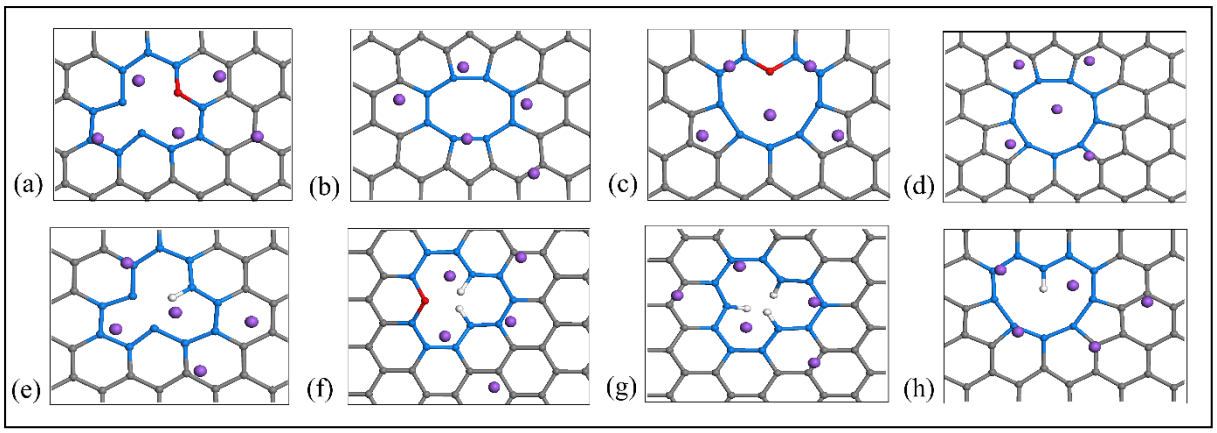

Fig. 5.5. The position of 5 Na adatoms on various materials: (a) MVG, (b) DVG, (c) TVG, (d) QVG, (e) H1-MVG, (f) H2-MVG, (g) H3-MVG and (h) H1-TVG. The white atoms are hydrogen atoms, the purple atoms are Na atoms and all others are C atoms. The red atoms in (a), (c) and (f) indicate a carbon atom with a dangling bond and the blue atoms are those surrounding a vacancy.

5.4.3 Na adsorption on large pores of 24VG sheets

As already discussed, Na binds strongly to the 24VG sheet, but not to the H12-24VG sheet, which is consistent with the result of Okamato [72] for the Li adsorption on the similar defective graphene. However, in both cases, there are different sites at which the Na can bind, and it is of interest to consider the relative binding energies at several different sites in/near the pores. Fig. 5.6 shows the sites considered on each of the two materials and Table 5.2 summarises the values of E_b for those sites.

From Fig. 5.6a and the binding energies in Table 5.2 we see that that the strongest binding is at site B (in front of the armchair type edge within the pore). Site Z (in front of zig-zag type edge within the pore) is the second most stable site, and this is consistent with Okamato's result for lithium adsorption [72]. The sites indicated by NS in Fig. 5.6a do not bind Na, and if initially we put Na at these sites, they move to sites B or Z on geometry optimisation. Further from the pore at R2, the value of E_b is -1.043 eV. This is still stronger than the binding of Na to graphene, but weaker than the cohesive energy of Na. The high magnitude of the binding energy at sites B and Z can be directly attributed to the existence of 12 dangling bond carbon atoms around the vacancy edge. By contrast, when we hydrogenate the 24VG to get H12-24VG, as seen in Fig. 5.6b and Table 5.2, the magnitude of the E_b values decrease greatly to values that are too weak to prevent clustering.

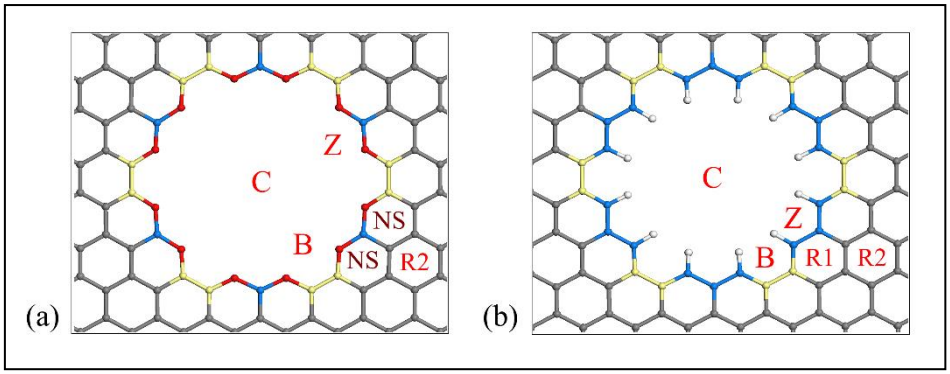

Fig. 5.6. (a) Structure of 24VG, with possible adsorption sites labelled. Site C is at the centre of the vacancy, site Z is adjacent to the zig-zag type edge, and site B is adjacent to the armchair type edge. NS denotes sites where adsorption does not occur, and atoms initially placed there will move to site B. (b) Structure of H12-24VG with the possible adsorption sites labelled (C, Z, and B). Sites R1 and R2 are the two rings away from the vacancy that were considered. Armchair type and zig-zag type carbons around the vacancy are also distinguished by colouring in yellow and blue, respectively. Red coloured carbon atoms are those with a dangling bond.

Table 5.2. The binding energy of Na and its distance from the 24VG and H12-24VG materials for various sites

Sites defined in Fig. 5.6	24VG		H12-24VG	
	E_b / eV	h_{ad} / Å	E_b / eV	h_{ad} / Å
C	-0.968	0.0	-0.249	0.0
B (Armchair)	-2.909	0.69	-0.842	2.18
Z (Zig-Zag)	-2.706	0.0	-0.724	2.25
R1	NS[a]	-	-0.871	2.20
R2	-1.043	2.23	-0.817	2.20

[a] NS denotes that Na does not stably bind at this site

These results indicate that neither the non-hydrogenated nor hydrogenated 24VG sheets are suitable for battery materials: 24VG has many dangling bond carbon atoms which is likely to lead to binding with other sheets (although it strongly binds Na); and H12-24VG does not bind Na sufficiently strongly. However, it is interesting to observe that the position at which Na binds most strongly is in the pore for 24VG but over the defective graphene surface for H12-24VG. In summary, the above results show that large pores within graphene will not enhance Na binding sufficiently. When it is passivated by hydrogen and will have problems associated with instability or reactivity if it is not passivated [72]. Therefore, we focus on the small vacancies in the following sections.

5.4.4 Na adsorption on single layer and bulk graphene with MV and DVs

Due to the fairly strong binding of Na to a H1-MVG evident from Fig. 5.4b, it is of interest to examine how the binding energies of Na vary on sheets containing several MVs and the maximum number of atoms that could be expected to be adsorbed. We firstly optimised a defective graphene sheet with 4 MVs in a 6x6 graphene supercell (C_{68} which we refer to as 4MVG), as shown in Fig. 5.7a. This structure has a 5.55% defect concentration with respect to graphene, and adding more defects in the supercell was found to disrupt the structure of the layer. The geometrically optimised 4MVG structure (Fig. 5.7a) is planar due to the triplet electronic state [130].

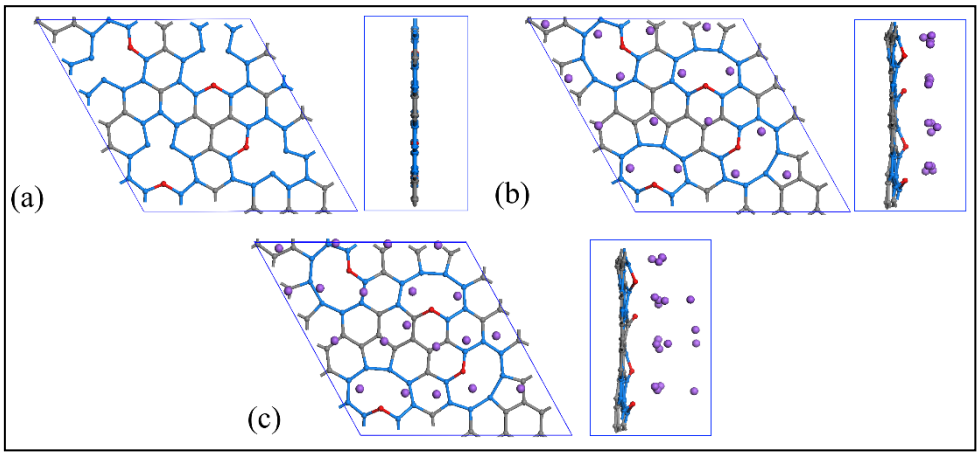

Fig. 5.7. Top and side view of the optimised structure of (a) graphene sheet with 4 mono-vacancies (4MVG) (b) 16 Na atoms adsorbing on the 4MVG material (c) 20 Na atoms adsorbing on the 4MVG material, 4 of which are forming a second layer on top of the first layer. Blue colours are those surrounding vacancies, red atoms are those with a dangling bond, and purple atoms are Na atoms.

In order to evaluate the ability of this structure to adsorb Na atoms, we optimised several initial configurations and found that a maximum of 16 Na atoms can bind to the 4MVG sheet in a single layer. The average E_b is -1.369 eV (stronger than the cohesive energy of Na), and the average height of adsorption (h_{av}) is 2.48 Å. The top and side views of the material with this loading are shown in Fig. 5.7b. Examination of the top view in Fig. 5.7b indicates that a fairly regular network of Na atoms is situated above the material, with the Na-Na distances varying between 3.5 and 4.2 Å. This is similar to the distances between the closest Na atoms in a single layer of Na arranged in the structure corresponding to that of the (110) surface of the bulk metal (Fig. 4A.3a) (3.54 – 3.64 Å). On addition of more Na atoms, the atoms start to form a second layer further from the sheet as shown in Fig. 5.7c.

To test the intercalation of Na atom within the bulk layers of 4MVG, we optimised the structure with an AA stacking. This AA stacking was the most stable of the possible stackings considered and results in overlaying the two mono-vacancies in adjacent layers. The average interlayer distance of this stacking is 3.37 Å, which is very similar to the interlayer distance of graphene (3.35 Å [25]). Therefore, as expected, the vacancy defect does not result in a significant increase in the interlayer distance. Moreover, this distance is smaller than the values of 3.70 Å reported by Cao et al. [25] and 3.94 Å reported by Tsai et al. [33] as the distance required for Na intercalation. Therefore, intercalation of Na within the 4MVG with AA stacking is likely to be difficult.

Fig. 5.8a depicts top and side views of the 4MVG bulk layers intercalated with 1 Na atom over the mono-vacancy in AA stacking. The under-coordinated carbon atoms of the two adjacent MVs moved out of their planes and formed a bond of length 1.37 Å, which is a very similar value to a carbon-carbon double bond length of 1.33 Å [2]. This is a shortcoming of the 4MVG material, because it causes a decrease in interlayer distance of the 4MVG bulk layers to 3.32 Å. It also keeps the layers in fixed positions relative to each other and prevents them from sliding as normally seen in graphene stacking types (AB, ABA, ABC) [213]. These problems indicate that graphene sheets with a mono-vacancy would not be suitable for use as materials for NIBs.

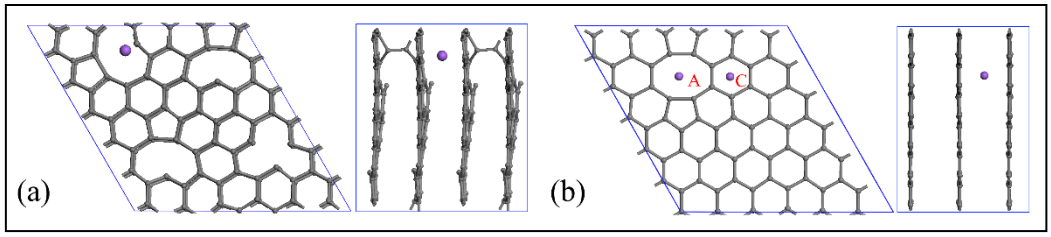

Fig. 5.8. (a) Top and side view of the structure formed from geometry optimisation of 4MVG bulk layers intercalated with a Na atom (purple). This results in bonding between the layers as shown in the right panel, with a carbon-carbon bond length of 1.37 Å. (b) Top and side view of the structure formed from geometry optimisation of DVG bulk layers with an AA stacking intercalated with a Na at sites A or C. In the side views the Na atoms at the A and C sites are eclipsed.

We also inserted a Na atom between the layers of DVG with an AA stacking, which was the optimal stacking for the bulk layers. Even though Na bound strongly at both sites A and C (defined in Fig. 5.4) of a single layer DVG material (E_b values of -1.79 and -1.52 eV, respectively), in the bulk material these values are changed to -1.74 and -0.71 eV, respectively.

A large difference of 0.81 eV in the binding energy at site C in the bulk system indicates that Na atoms would bind strongly in the centre of the defect but weakly at site C, which means that this material is unlikely to be a suitable option for anode material since diffusion of the Na would be slow. Suitable bulk layers must provide strong binding energy at all the sites including the sites near the defects for a number of adatoms to intercalate.

5.4.5 Na and Ca binding on H-MVG single and bulk layers

Of the hydrogenated MVGs considered above, only the H1-MVG and H2-MVG materials bound Na strongly at locations near the MV. Indeed, H2-MVG has a dangling bond on the vacant carbon atom around the vacancy, as shown in red in Fig. 5.2b. Therefore, C-C binding as shown in Fig. 5.8a may occur for this structure. The optimised structure for H1-MVG is shown in Fig. 5.2a, and it is found that the C-H bond length is 1.077 Å. In contrast to the planar MVG structure, the C atom in H1-MVG is 0.748 Å above the plane. By hydrogenating the 4MVG material (Fig. 5.7a) with one hydrogen atom at each MV, $C_{68}H_4$, denoted by 4(H1-MVG), is obtained as seen in Fig. 5.9a. Different structures can be formed with different combinations of direction of the C-H bond such as those shown in Fig. 5.9. The structure in Fig. 9.9a has all the H atoms on the same side of the sheet, which we refer to as cis-4(H1-MVG), and that in Fig. 9.9b has two on one side and two on the other side, and we refer to it as trans-4(H1-MVG).

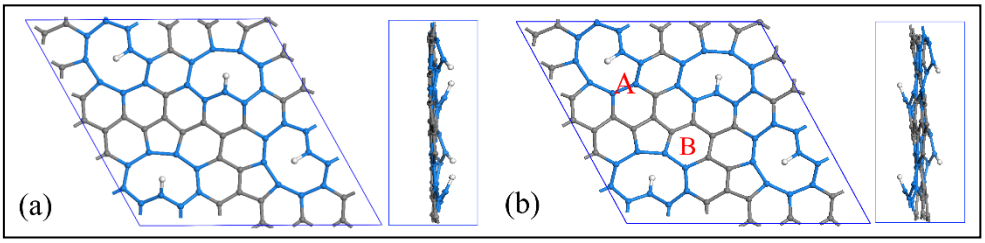

Fig. 5.9. Top and side view of the 4(H1-MVG) sheet with (a) H atoms all on one side of the sheet and (b) half the H atoms on one side and half on the other. In (b) binding sites, A and B, are labelled. Blue colours are those carbon atoms surrounding vacancies, and white atoms are hydrogen.

The trans-4(H1-MVG) has a lower total energy than cis-4(H1-MVG), -628.50 eV versus -628.08 eV with 0.42 eV difference. Therefore, we selected trans-4(H1-MVG) for the rest of our computations. Table 5.3 presents the binding energies of Na to trans-4(H1-MVG) at the two sites (A and B) indicated in Fig. 5.9b. Initially we added 1 and 2 Na atoms to compare the binding energies at different sites. It is also of interest to compare the binding energy of Ca

with that of Na, since Ca has two valence electrons (Na has one) and this is relevant to the electrical capacity (n_e = 2 in equation 2). In order to determine the maximum capacity of one side of the single layer, we have considered the binding energy of 12, 14 and 16 atoms on the same side. In addition, we considered the binding energy of 8, 10, 12, 14 and 16 atoms to each side of the sheet, (totals for both sides of 16, 20, 24, 28 and 32 atoms, respectively). The results are presented in Table 5.3.

Table 5.3. Average binding energies and Bader charges for Na and Ca on trans-4(H1-MVG)

Number of atoms and binding site		Na		Ca	
		Average E_b eV atom^{-1}	Average Bader charge / *e* atom^{-1}	Average E_b eV atom^{-1}	Average Bader charge / *e* atom^{-1}
1 (@ A)	Binding to one side	-1.506	0.819	-2.115	1.352
1 (@ B)		-1.670	0.824	-2.756	1.336
2 (@ A & B)		-1.597	0.814	-2.376	1.005
12		-1.248	0.273	-2.137	0.507
14		-1.241	0.218	-2.103	0.493
16		-1.250	0.179	[a]	-
Max. capacity [b] / mA h g^{-1}		360.8 (16 Na)	-	547.0 (14 Ca)	-
16	Binding to both sides	-1.214	0.258	-1.960	0.607
20		-1.184	0.210	-2.008	0.582
24		-1.162	0.171	-2.074	0.550
28		-1.160	0.142	-2.063	0.531
32		-1.182	0.105	[a]	-
Max. capacity [b] / mA h g^{-1}		551.0 (32 Na)		780.4 (28 Ca)	

[a] In this case we were unable to bind a single layer of Ca atoms

[b] We define the maximum capacity as the point after which there might be sheet disruption (e.g. in the case of 16 Ca) or formation of another surface over the sheet (e.g. in the case of 20 Na)

Fig. 5.10 depicts the top and side views of the single layer loaded with Na and Ca. According to the results of Table 5.3, all the E_b are stronger than the cohesive binding energies of Na (-1.113 eV) and Ca (-1.840 eV) [10], and Ca has a stronger binding to the sheet. For both metal atoms, the preferred binding site is site B (see Fig. 5.9). The average Bader charges [198, 199] on the metal atoms are higher for Ca (1.336 for a single atom at site B) than for Na (0.824 for a single atom at site B) as expected from their valencies.

The distance between the Na-Na atoms in the case with 16 Na atoms on one side varies between 3.5 and 3.8 Å (Fig. 5.10a). This is similar to the arrangement of the 16 Na atoms over the 4MVG sheet (see Fig. 5.9b), and is also similar to the distance between two neighbouring Na atoms in a single layer of atoms arranged in the structure corresponding to the (110) surface of the bcc metal, 3.54 and 3.64 Å (Fig. 4A.3a). Similarly, for Ca adsorption (Fig. 5.10b), the Ca-Ca distance varies between 3.5 and 5.1 Å, which is similar to the distance between Ca in a single layer of atoms arranged in the structure corresponding to the (100) surface of the fcc metal of 3.57 and 5.05 Å (Fig. 4A.3b). These similarities suggest that there is likely to be interactions between the Ca atoms.

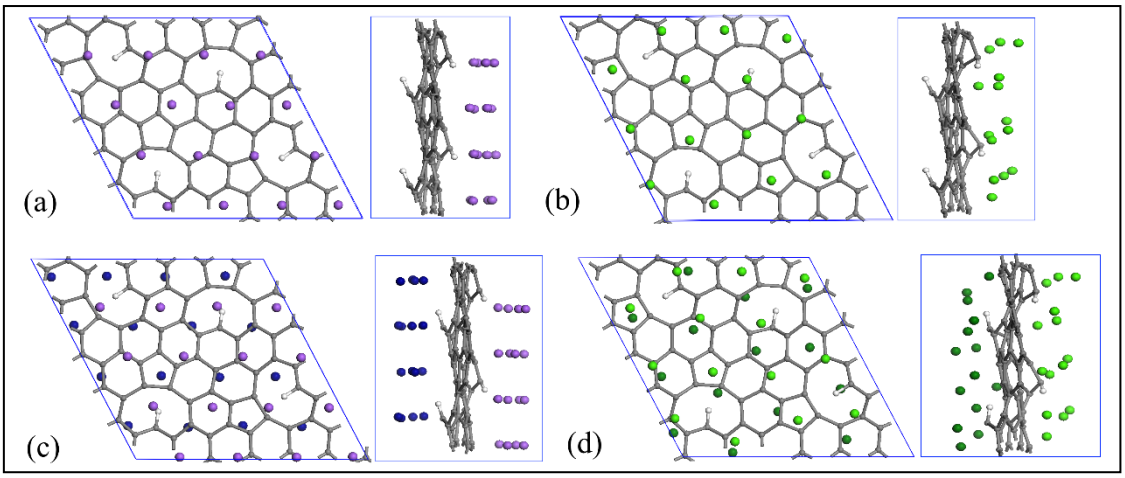

Fig. 5.10. Top and side views of the trans-4(H1-MVG) with (a) 16 Na, (b) 14 Ca, (c) 32 Na, and (d) 28 Ca atoms. In (a) and (c) light and dark purple atoms are those Na atoms located over and behind the layer, respectively. In the same way in (b) and (d), light and dark green atoms are those Ca atoms located over and behind the layer, respectively.

We note that as the loading becomes high, the average charges on the metal atoms drop (see Table 5.3) which is in accordance with the previous result of Li on graphene [63]. Consideration of the charge distribution indicates that there is a general drop in charge for all the metal adatoms (e.g. with 16 Na atoms the charges range from -0.02 *e* to 0.34 *e* and with the 14 Ca atoms from 0.20 *e* to 0.84 *e*). The same trends generally hold for the E_b of the adatom on the surface, except two cases: going from 14 to 16 Na adatoms on one side and from 28 to 32 Na adatom on the both sides. A small increase in the absolute value of E_b, the low values of the Bader charges on the atoms and the fact that the distances between the atoms are similar to that in the single atom metal sheets suggest that the interaction between the metal adatoms might be starting to dominate the behaviour, and that a metal surface is forming over the substrate. To get a better indication of the interaction between the metal adatoms and substrate,

we have reported E_b, E_{int} (defined in equations 2 and 3) and E_f (the formation energy of the metal cluster from single isolated atoms) for Na and Ca, and the results are presented in Table 5.4.

As shown in Table 5.4, the values of E_f for the isolated clusters of Na or Ca atoms in the structures they formed on the substrate are mostly higher than the formation energy of Na and Ca atoms in ideal (110) and (100) configurations (Figs. 4A.3a and 4A.3b). In the cases of 14 and 16 Na atoms and also 12 and 14 Ca atoms, the formation energies are close to, or lower than the formation energies of surface 110 and 100, respectively. Therefore, it reveals the fact that Na and Ca metal surfaces are about to form above the substrate. In addition, in all the cases, the E_{int} between the cluster and the substrate was lower in magnitude than E_b, especially for 14 and 16 Na atoms. This indicates that part of E_b was due to interactions between the metal atoms. The fact that the formation energy of the metal clusters is more positive than either E_b or E_{int}, except with 14 and 16 Na atoms, indicates that the metal atoms are interacting significantly with the substrate. This difference is larger for the smaller Na and Ca clusters; reflecting the fact that the isolated Na and Ca clusters may form a metal surface as their size increases and the fact that their structure is highly affected by the strength of their interaction with the substrate.

Table 5.4. Values of E_{int} and E_f for Na and Ca adsorbed on the 4(H1-MVG) single layer material and comparison with E_f for the 2D metal surface.

Substrate + adatom	Number of metal adatoms	E_b / eV atom^{-1}	E_{int} / eV atom^{-1}	E_f / eV atom^{-1}	Energy of surface formation of pure metal atoms / eV
4(H1-MVG) single layer + Na	12 Na	-1.248	-0.781	-0.495	-0.894[a]
	14 Na	-1.241	-0.467	-0.799	
	16 Na	-1.250	-0.456	-0.814	
4(H1-MVG) single layer + Ca	8 Ca	-2.188	-1.420	-0.778	-1.024 [a]
	10 Ca	-2.137	-1.305	-0.911	
	12 Ca	-2.137	-1.200	-1.055	
	14 Ca	-2.103	-1.193	-1.061	

[a] Energy of metal surface formation in the Na (110) and Ca (100) configurations (Figs. 4A.3a and b)

5.4.6 The intercalation of Na and Ca in the 4(H1-MVG) bulk layers

In order to investigate the intercalation of Na and Ca within the bulk trans-4(H1-MVG) ($C_{68}H_4$) layered materials, we have carried out computations for 4 different types of stacking. The optimised structures of 4 different stackings are presented in Fig. 4A.4. It is found that the AA stacking has the lowest energy with an average interlayer distance of 3.49 Å (separation of centre of mass of the carbon atoms in each layer), which is approximately 4% higher than the interlayer distance in graphene and the AB2 stacking is least favourable with an energy that is 1.8 eV higher and an interlayer distance 13.4% higher than that in graphene. We might not expect the distance to be much greater than that for graphene, due to the van der Waals forces between the layers [33, 118]. Comparing the energies of the 4 stackings (Fig. 4A.4), we observe that the lower energy, the smaller the interlayer distance.

Selecting the AA stacking for the 4(H1-MVG) bulk layers, we calculated the Na and Ca intercalation energies, (see Table 5.5) while keeping the interlayer distance fixed to be that of the minimum energy 4(H1-MVG) structure with no metal atoms. Fig. 5.11 depicts the two sites in between the layers at which we placed Na or Ca adatoms. These were selected based on the results obtained for the monolayers. Site A is over the mono-vacancy and between the layers and site B is over a hexagonal ring close to the MV and between the layers.

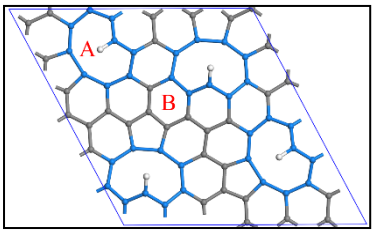

Fig. 5.11. Location of sites A and B on 4(H1-MVG) bulk material with AA stacking type. In both cases, the Na or Ca atoms are located in between the layers. Blue atoms are those carbon atoms surrounding vacancies, white atoms are hydrogen all other atoms are carbon atoms.

Table 5.5. The E_b and Bader charge values for Na and Ca atoms at the sites A and B of the 4(H1-MVG) bulk layers

Atom	Site A, E_b / eV	Site B, E_b / eV	Bader Analysis	
			Charge on atom at Site A / *e*	**Charge on atom at Site B / *e***
Na	-0.649	-0.303	0.748	0.739
Ca	-2.793	-2.048	1.339	1.301

According to the results shown in Table 5.5, Na does not bind strongly between the bulk layers, with the E_b values being much weaker than the cohesive energy. As a result, clustering may occur when a number of Na atoms are intercalated between the layers. It was also found that the Bader charge values of Na is +0.75 *e* which is even lower than the Bader charge of 1 Na on a single layer of 4(H1-MVG) at 0.819 and 0.824 *e* (Table 5.3).

By contrast, Ca is found to bind strongly within the layers, with all the binding energies stronger than the cohesive energy of Ca (-1.840 eV). It is interesting to recall that both Na and Ca bound to the 4(H1-MVG) single layer, although Ca was still stronger. The binding energy of the Na is much weaker in the bulk system than on the single layer, whereas Ca is similar on single layers and in the bulk. Moreover, the amount of charge on the Ca when intercalated in the bulk 4(H1-MVG) (1.34 *e*) is very similar to that when it is on a single layer (1.35 *e*, see Table 5.3).

In order to investigate the effect of interlayer distance of 4(H1-MVG) bulk layers on Na binding we considered the variation of E_b with expansion of the 4(H1-MVG) bulk layers intercalated with 1 Na atom on each layer at site A (Fig. 5.11) (2 Na atoms in the supercell). This is similar to way that Tsai et al. [33] considered Na in bi-layers of graphene and defective graphene. The results are presented in Fig. 5.12.

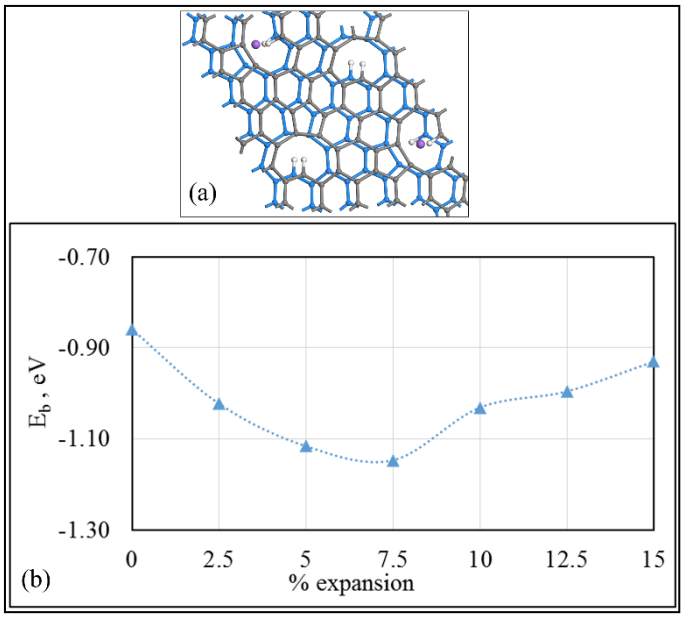

Fig. 5.12. (a) Bulk 4(H1-MVG) intercalated with Na atoms (purple) at sites A. The white atoms are hydrogen and all others are carbons in the two different layers; (b) Variation of E_b for Na intercalated in 4(H1-MVG) bulk, with the % expansion of the interlayer spacing compared to the material without Na.

From Fig. 5.12b, we see that the minimum E_b occurred at approximately 7.5 % expansion of the layers compared to that of the material with no Na and the binding energy (-1.148 eV) is just a little stronger than the cohesive energy of Na. Therefore, expansion of layers does not improve the Na binding sufficiently to suggest that bulk 4(H1-MVG) would be a useful material for NIBs. The expansion of the of 4(H1-MVG) bulk layers on intercalation of Ca is considered in the next section.

5.4.7 Loading 4(H1-MVG) bulk layered materials with multiple Ca atoms

In this section, we investigate the loading of 4(H1-MVG) bulk layers in a AA stacking with a number of Ca atoms in order to determine the maximum capacity and the expansion of the layers. We considered 2 to 32 Ca atoms in the supercell, with equal number of Ca atoms in each slit-pore. Fig. 5.13a and b show the top and side views of the systems loaded with 2 and 32 Ca atoms. Fig. 5.13c shows the variation of E_b values and expansion of the layers as a function of the number of Ca atoms that are intercalated.

From Fig. 5.13, it can be seen that with 2 Ca atoms E_b is -3.65 eV and the bulk material has undergone a 6.6% expansion. With 32 Ca atoms E_b is -2.84 eV and expansion is 29.3%. Overall, the binding energy per atom becomes weaker with an increase in loading which is expected. The deviation of the behaviour from this trend is due to the symmetry of the system and/or the fact that there are many local minimum energy arrangements, and in some cases the global minimum might not have been found. The maximum value of expansion was found to be 31% with 6 Ca atoms, and it corresponds to the interlayer distance of 4.56 Å. Similar expansion was observed in graphdiyne bulk layered materials loaded with 7 Na atoms on each layer ($C_{2.57}Na$) at 28% [28]. With more than 32 Ca atoms, we were unable to obtain a stable structure with a single layer of Ca atoms between the 4(H1-MVG) layers, so 32 was taken as the maximum loading. Furthermore, the Bader analysis shows that the average charge on a Ca atom with 32 Ca atoms is 1.17 *e*, which is higher than that obtained with 14 Ca atoms on one side of a single layer of 4(H1-MVG) (0.493 *e*) or 28 Ca atoms on both sides of the single layer (0.531 *e*) (see Table 5.4).

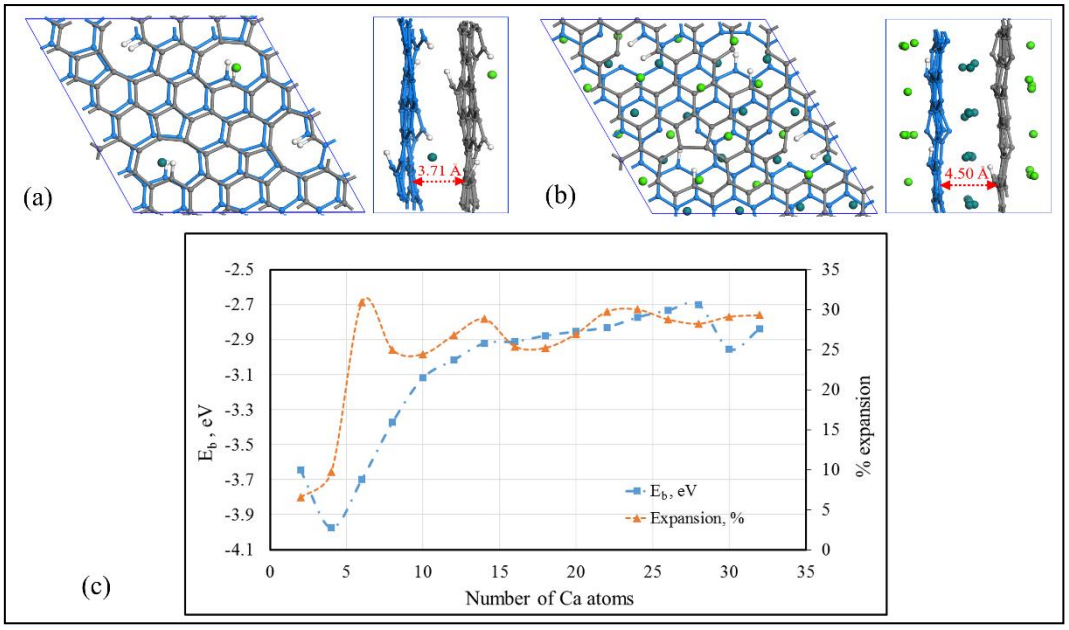

Fig. 5.13. Binding energies per Ca atom for 4(H1-MVG) loaded with (a) 2 Ca atoms and (b) 32 Ca atoms. The H atoms are coloured white, the Ca atoms are light or dark green depending on which slit pore they are located in, and the carbon atoms are gray or blue depending on the sheet they are in (c) Variation of the binding energy per atom, E_b, and expansion % of the bulk systems as a function of Ca loading. Note that the binding energies are significantly stronger than the cohesive energy of Ca (-1.84 eV).

We note that intercalation of a relatively small number of Ca atoms results in expansion of the layers of 4(H1-MVG) and this expanded material allows other Ca atoms to intercalate. In addition, the existence of apical (non-planar) C-H bond in the basal defect (mono-vacancy) makes the interlayer spacing sufficiently large to allow intercalation of the first Ca atom. Moreover, there is no disruption in the structure of the 2D material. According to this result and the definition above, the maximum capacity of 4(H1-MVG) bulk layers is 32 Ca atoms or $C_{68}H_4Ca_{16}$, equivalent to an electrical capacity of 591.2 mA h g^{-1}; this capacity is compatible with the electrical capacity of 300 mA h g^{-1} at 50 mA g^{-1} achieved by Yoon et al. for hydrogen enriched porous carbonaceous material [44] and 491 mA h g^{-1} achieved by Pramudita, et al. [74] for hydrogenated graphene (H-TEGO) selected for NIBs. Consequently, the combination of Ca with 4(H1-MVG) is predicted to be a promising anode material for CIBs.

5.4.8 Electronic properties – density of states (DOS)

In this section, we briefly report the electronic properties of the studied systems through total (TDOS), partial density of states (PDOS) and charge density. Fig. 4A.5 depict the TDOS and

PDOS for 4(H1-MVG) substrate, and 4(H1-MVG) + 1 Na and 1 Ca atoms. A single layer of 4(H1-MVG) is considered.

According to the TDOS in Fig. 4A.5a, there is no band gap, so the 4(H1-MVG) sheet is conductive as is desired for an anode material. The same holds for the two indicated carbon atoms as indicated in Fig. 4A.5b. Likewise, Figs. 4A.5c and d indicate that there is no band gap for 4(H1-MVG) intercalated with 1 Na or 1 Ca atom. In addition, Fig. 4A.5e depicts the PDOS of the Ca and also the indicated carbon atom (red colour). According to this figure there is an overlap of the Ca states (blue curve) over the C states (yellow curve), which suggests bonding between the Ca atom and the indicated carbon atoms.

Charge densities for the 4(H1-MVG) with Na and Ca atoms adsorbed were also determined. The charge density difference is given by:

$$\Delta\rho = \rho_{4(H1\text{-}MVG)+Na/Ca} - \rho_{4(H1\text{-}MVG)} - \rho_{Na/Ca} \qquad (5.6)$$

where ρ is the charge density of the systems specified ($e\ Bohr^{-3}$). The charge density differences for the systems with single Na or Ca are shown in Fig. 5.14a and b, with the blue colour indicating greater electron density on the carbon atoms and the red colour indicates positive charge around the Na or Ca cations. Regarding Fig. 5.14c and d, there is also a considerable charge transfer from the 16 Na and 14 Ca atoms to the substrate. In this case, the positive charge is delocalised among the Na and Ca, suggesting that the layer is becoming metallic. The system with 14 Ca atoms (Fig. 5.14d) has more charge transfer (seen as a greater region of blue in Fig. 5.14d). This is consistent with the higher valency for Ca than Na.

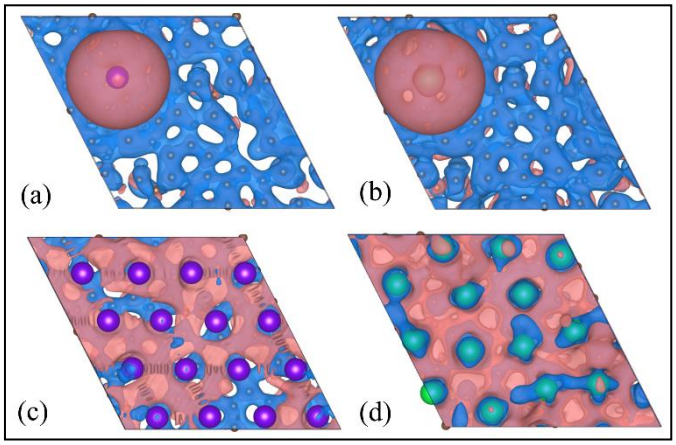

Fig. 5.14. Charge density difference, the red and blue colours indicate regions where the charge becomes more positive or more negative, respectively, compared to the isolated metal atoms or substrate. a) 4(H1-MVG) + 1 Na, $\Delta\rho$ =0.0001 $e\ Bohr^{-3}$, b) 4(H1-MVG) + 1 Ca, $\Delta\rho$ =0.0001 $e\ Bohr^{-3}$, c) 4(H1-MVG) + 16

Na, $\Delta\rho$ =0.0007 *e Bohr*$^{-3}$, and d) 4(H1-MVG) + 14 Ca, $\Delta\rho$ =0.0007 *e Bohr*$^{-3}$. In c) and d), purple spheres are Na atoms and green spheres are Ca atoms, respectively.

5.5 Conclusion

The effect of vacancies with and without hydrogen on the binding of Na and Ca atoms to a variety of defective carbon-based 2D sheets have been considered. If the defects result in under-coordinated carbons, the binding of the metal atoms could be so large that the desorption process is difficult. Moreover, these materials are likely to result in linking of the adjacent layers, which would diminish the battery's performance. The material with hydrogenated mono-vacancies considered (4(H1-MVG) or $C_{68}H_4$), has apical C-H bonds on the basal plane. This results in an increase in the spacing between layers compared with graphite and was found to have enhanced binding of both Na and Ca compared to pristine graphene. However, only Ca provides sufficiently strong binding to the bulk layers of 4(H1-MVG) to prevent cohesion of the metal atoms. The bulk material provides a maximum capacity of 16 Ca within each AA stacked layer. This is equivalent to $C_{68}H_4Ca_{16}$ and 591.2 mA h g^{-1} electrical capacity which is comparable with experimental results for hydrogenated graphene [44, 74], which found that such materials could be useful as anodes for rechargeable batteries. The expansion of the stacked layers after Ca intercalation varies from 6.6% to 31.0%. These calculations demonstrate that the enhanced performance of hydrogenated anode materials compared to pristine graphene [7, 10] could be both because of the stronger binding of the metal atoms to the substrate and the expansion of the material before addition of any metal atoms. This expansion is mainly due to the apical C-H bond that acts as a side arm to expand the layers and enable intercalation. It also proposed that synthesis of structures similar to 4(H1-MVG) could be beneficial for battery materials.

5.6 Acknowledgements

The authors thank the Australian Research Council (LE160100051) for support of this project through the LIEF program. This research was undertaken with the assistance of resources provided at the NCI National Facility systems at the Australian National University, the PAWSEY supercomputing centre located in Western Australia with their Magnus supercomputing clusters, the Queensland Cyber Infrastructure Foundation (QCIF) for the Euramoo supercomputing clusters, the University of Queensland Research Computing Centre (RCC) with their Tinaroo supercomputing clusters, and Goldenorb supercomputing clusters at

Australian Institute for Bioengineering and Nanotechnology (AIBN) at the University of Queensland. AFN also acknowledges support from the Australian Government through an Australian Government Research Training Program Scholarship (RTP).

The following chapter contains the published paper in the Journal of Physical Chemistry C, 2019, Vol. 123, p. 14895-908 [214]

Amir H. Farokh Niaei,[a] Tanglaw Roman,[a] Tanveer Hussain,[a, 50] and Debra J. Searles[a,b 51]

[a] Centre for Theoretical and Computational Molecular Science, Australian Institute for Bioengineering and Nanotechnology, The University of Queensland, Brisbane, QLD, 4072, Australia

[b] School of Chemistry and Molecular Biosciences, The University of Queensland, Brisbane, QLD, 4072, Australia

Contributors	Statement of contribution
Amir H. Farokh Niaei (candidate)	Presented the topic and idea (65%) Conducted computations (100%) Analysed the result data (80%) Wrote, reviewed and edited the paper (67%)
Roman T.	Analysed the result data (5%) Reviewed and edited the paper (10%)
Hussain T.	Presented the topic and idea (15%) Reviewed and edited the paper (3%)
Searles D.J.	Presented the topic and idea (20%) Analysed the result data (15%) Reviewed and edited the paper (20%)

[50] Current address: School of Molecular Sciences, The University of Western Australia, Perth, WA, 6009, Australia
[51] Corresponding author.
E-mail: d.bernhardt@uq.edu.au (Debra J. Searles)

Chapter 6

A computational study on the adsorption of sodium and calcium on edge-functionalized graphene nanoribbons

6.1 Abstract

Computational methods are used to show that graphene nanoribbons bind sodium (Na) and calcium (Ca) more strongly than graphene sheets. The binding strength is further enhanced by functionalizing the edge of the nanoribbon with oxygen-containing groups. Strengthening of the binding of these metal atoms to graphitic materials is important for applications including metal-ion batteries. Our results are obtained using density functional theory calculations of the binding of sodium and calcium to hydrogen, hydroxyl, carbonyl, and carboxyl groups at the edge of zigzag and armchair nanoribbons. Both hydrogen passivation and hydroxyl functionalization result in moderate binding of Na and Ca with binding energies varying from -1.0 to -1.9 eV for the nanoribbons considered. An increase in binding compared to graphene does not just occur at the edge, but extends across the nanoribbon. Furthermore, carbonyl and carboxyl groups bound both metal atoms more strongly, with binding energies between -1.6 and -3.1 eV. Increasing the number of these groups at the edge increases the binding strength of the metal adatoms. When there is a high number of oxygen-containing groups at the edge,

the effect of the oxygen-containing groups is also evident away from the edge of the nanoribbon for sodium and calcium. It is demonstrated that this is at least partly due to the change in the electronic structure spanning the entire width of the nanoribbons considered.

6.2 Introduction

Following the synthesis of graphene, a two-dimensional carbonaceous material with unique properties, interest in graphene nanoribbons (GNRs) has escalated [46]. Of particular interest are investigations of the physical and chemical properties of the GNRs functionalized with chemical groups. Such functionalization can be used to tune the properties of GNRs, leading to a wide range of applications. For example, GNRs have been utilized as catalysts for chemical reactions [143-145], as materials with variable electronic and optical properties through bandgap tuning [148-151], and as energy storage materials for rechargeable batteries [36, 140, 152-154] and supercapacitors [215]. In addition, in computational materials science, GNRs have been used as models for the edges of large pores in a graphene sheet or its derivatives.

Graphene, GNRs, graphene oxide (GO), graphene nanosheets (GNS) and reduced graphene oxide (r-GO) have been considered as electrode materials for rechargeable metal-ion batteries. Of particular interest in this work are oxygen-functionalized GNRs and r-GOs which often have edges that are functionalized with carbonyl, hydroxyl, ether and carboxyl groups, in addition to basal-plane defects with non-graphitic carbons [47, 135, 137, 216]. This is important for rechargeable metal-ion battery technology because the binding of metal atoms such as sodium (Na) and calcium (Ca) on defect-free graphene or graphite is too weak to make them useful [76].

In 2009 Uthaisar et al. studied lithium (Li) adsorption over the edge and basal plane of hydrogenated zigzag and armchair GNRs using density functional theory (DFT) calculations [152]. They found that the zigzag edges adsorb Li adatoms more strongly than the armchair edges; and in both cases the binding was stronger than that to graphene's basal plane. In addition, they considered Li adsorption on various oxygen-containing groups on the basal plane and the edge of r-GO and GNRs [37, 140]. They found that carbonyl groups at the edge increased the amount of the Li atoms adsorbed [37, 140] more than the other groups (hydroxyl, ether and carboxyl). However, in materials with carboxyl groups at the edge, covalent bonds formed between Li and the groups. As a result, irreversibility and capacity reduction of the

electrode occurs [140]. In addition, Uthaisar et al. found that mild annealing of GO (at ~ 250 °C) decreased the number of oxygen-containing groups such as epoxides on the GO basal plane. These groups became more concentrated at the defects and edge sites. Overall, these groups were responsible for adsorbing Li with binding energies of magnitude approximately 2.2 eV [37]. Therefore, annealing of GO has an important role in the development of new carbonaceous materials for Li-ion batteries (LIBs).

The effect of oxygen-containing groups present in GNSs was also investigated by Vargas et al. [156]. Out of the materials they studied, they found that graphene oxide thermally treated at 300°C had the highest oxygen content (22.6%). These groups were proposed to be responsible for maximizing the Li ion uptake, which was determined to be approximately 500 mA h g^{-1} after 100 cycles at 149 mA g^{-1}. Moreover, this GNS had the highest interlayer distance of 3.64 Å out of the materials obtained from all the treating methods. Other researchers also observed that the best electrochemical performance was obtained with GNS treated at 300°C and that an increase in the interlayer spacing of GNS occurred [157, 158].

Xiao et al. [153] found that GNRs synthesized by controlled unzipping of carbon nanotubes (CNTs) were highly active in adsorbing Li cations. Defects, the surface area of the unzipped CNT and the presence of oxygen-containing groups were proposed to play important roles in the Li ion uptake. However, in assessing the application of GNRs in LIBs, they noted that in cases where the functional groups adsorbed a considerable amount of Li atoms, the adsorption was irreversible [153].

Recently, Lin et al. [36] carried out a DFT study on GNRs with oxygen-containing functional groups such as carbonyl groups and ethers. They found that strong adsorption of Li occurs around the oxygen groups at the edge of the GNR, especially around carbonyl groups. For the carbonyl group, the Li/C atomic ratio was found to be 1.0, and for a carbonyl-ether pair (pyrone group) it was found to be 0.5. However, they found that Li uptake can be greater around epoxy and hydroxyl groups on the basal plane (graphitic carbon) with Li/C equal to 4 and 3, respectively [36].

The works mentioned above indicate the importance of oxygen-containing groups in adsorbing alkali metal atoms strongly. This is vital for development of the next generation of metal-ion rechargeable battery materials.

In recent years alternative metals to Li have been considered for battery applications. Many studies have considered sodium [6, 8, 11, 28] and some studies have considered calcium [20, 98]. Sodium and calcium are abundant in nature and can be processed at a cheaper price than Li. Sodium and calcium have similar redox potentials, E^0 (Na^+/Na) = -2.71 V, E^0 (Ca^{2+}/Ca) = -2.87 V [67]. However, Ca atoms have 2 valence electrons which can increase battery electrical capacity compared with alkali metals like Li or Na which have only 1 valence electron, even though the mass of Ca is higher [76]. However, the ionic diffusion of calcium within some host materials is slow [26, 97]. In addition, the anode, cathode and electrolyte materials need to be carefully selected to avoid electrode instability, chemical decomposition and Ca electroplating [20, 21, 23].

In testing the performance of Na-ion batteries (NIBs), Wang et al. [47] demonstrated that the GNSs containing oxygen and treated at 450°C had an electrochemical capacity of 174.3 mA h g^{-1} at a current density of 40 mA g^{-1}. This study suggested that oxygen functional groups formed by chemical etching (resulting mainly in carbonyl and hydroxyl groups) play an important role in the adsorption of Na metal atoms.

Our recent work [76] considered the improvement of Na and Ca binding to graphene sheets by hydrogenating the defective graphene sheet. It showed that the binding became stronger over the hydrogenated sites than over pristine graphene; although it was not so high that they bound irreversibly, as it was in the case of graphene with vacancy defects. Therefore, hydrogenated defective graphene could be considered as a potential anode material for sodium and calcium-ion batteries as cheaper alternatives to LIBs.

In this manuscript we firstly compare Na and Ca adsorption on graphene with their adsorption on nanoribbons passivated by hydrogen. We also consider the effect of functionalizing the nanoribbons with oxygen-containing functional groups (forming functionalized GNRs, that we refer to as F-GNRs). The oxygen-containing groups that we have considered in the present work are hydroxyl (HO-), carbonyl (O=), and carboxyl (HOOC-). They are commonly observed in the edge sites of r-GO and have been considered in the studies for Li adsorption on GNRs [36, 37, 140]. We calculate the binding energies and the charge transfer of Na and Ca at different sites of F-GNRs including over the hexagonal rings, over and in front of the functional groups using DFT methods. Finally, we study the effect of functional groups on the electronic and magnetic properties of the GNRs. The results of our study open up the way for

further experimental and feasibility studies of GNR applications in Na and Ca rechargeable batteries.

6.3 Methodology

To study the interaction of Na and Ca on the functionalized edge of nanoribbons, DFT calculations were performed as implemented in the Vienna Ab initio Simulation Package (VASP), version 5.3.5 [42], with a plane-wave basis set. The nanoribbons extend along the *y* direction in the selected coordinate system. Within this package, the generalized gradient approximation (GGA) of Perdew-Burke-Ernzerhof (PBE) [177] was used for exchange-correlation functionals along with projector-augmented wave (PAW) method. The s and p semicore electrons are included in the pseudopotentials for Na and Ca. Gaussian smearing was selected, with the smearing parameter set to 0.05. To account for the van der Waals interactions, the DFT-D3 method of Grimme [64, 190] was used. For optimization of GNRs the Brillouin zone was sampled at the Γ-point (1 × 1 × 1 *k*-point mesh), using the Monkhorst-Pack scheme. Our tests showed that a Γ-point sampling was adequate by comparing the results obtained with 1 × 3 × 1 and 1 × 5 × 1 *k*-point meshes. For example, the ground state energy of the fully hydrogenated zigzag nanoribbon with 128 atoms in a supercell (a typical system considered in this work) differed by only approximately 3 meV atom^{-1} using the Γ-point, 1 × 3 × 1 and 1 × 5 × 1 *k*-point meshes. However, compared with the Γ-point calculation, the calculations with 1 × 3 × 1 and 1 × 5 × 1 *k*-point meshes took two and three times longer, respectively. Therefore, we selected a Γ-point calculation as a suitable choice, due to the time required for calculations of large systems with multi-adatom adsorption. For the density of states (DOS) analysis, a 1 × 11 × 1 *k*-point mesh was used. The cut-off energy for the plane-wave basis set was selected to be 700 eV for all the species considered in the study. The energy convergence criterion for the relaxation of the electronic degrees of freedom was selected to be 1×10^{-6} eV and the force convergence criterion for geometry optimization was selected to be 0.05 eV Å^{-1}. We note that the energies of test cases with a cut-off of 0.01 eV Å^{-1} differed by less than 0.2 %. The cut-off energy, force and energy convergence criteria were optimized in preliminary calculations for similar carbonaceous materials [28, 76]. All the calculations allowed for spin polarization. Different initial magnetic states were considered since it is known that the energies of the ferromagnetic (FM) and antiferromagnetic (AFM) states of the hydrogenated ZGNR are slightly different [152, 155, 217]. We found that in these cases, the ZGNRs converged to an FM state if the initial magnetic moments were not set, and therefore it was necessary to test

both possible initial states. In addition, some other initial arrangements of the spin states were considered for the ZGNR cases, but for the systems we considered the lowest energy state was always found when the initial arrangement of magnetic moments corresponded to an AFM or FM state.

Charges on the atoms were calculated using Bader charge analysis [198, 199]. Cross-sections of electrostatic potentials and charge density difference were visualized using the VESTA package [218]. Two types of ribbons were considered: one with zigzag edges and the other with armchair edges. The optimized structures are shown in Fig. 6.1. We refer to these structures as 7-carbon zigzag GNR (7-ZGNR) and 14-carbon armchair GNR (14-AGNR) following the usual nomenclature based on counting the carbon atoms of the rings in the *x* direction, as shown in Fig. 6.1 [46, 142, 155]. Accordingly, in our study both types of ribbons have 6 complete hexagonal rings in the *x* direction and 8 rings in the *y* direction, as depicted in Fig. 6.1. The number of rings in the *x* direction was selected so that the variation in binding with the position of metal atoms across the ribbon could be measured. We found that for this narrow ribbon with 6 rings, the binding energy of a Na adatom over the middle ring was about 5% higher than the binding energy over the ring adjacent to the middle ring, as discussed in the results section. However, in the *y* direction we selected 8 rings. For the graphene supercell, the difference in Na binding energy to between 8 and 9 rings is only 0.025 eV whereas the computation time is 1.6 times longer (See Fig. 2B.41). Because we are mainly interested in comparing systems of similar size where the differences will be even smaller, this was considered an appropriate choice.

Nakada et al. [142] and Son et al. [155] found that the bandgap of an AGNR which is passivated with hydrogen is sensitive to the ribbon's width [46]. For example, for a 14-AGNR (N=3×4+2) there is no bandgap, so it is a metal. However, for N=12 or 13 there are bandgaps at the Fermi level and these armchair ribbons are semimetals. On the other hand, the sensitivity of a zigzag ribbon's bandgap to the ribbon width is quite low; all ZGNRs show a bandgap due to a staggered sublattice potential resulting from the magnetic ordering, which introduces bandgaps for electrons on a honeycomb hexagonal lattice. For both types of GNRs the bandgap reduces with increasing ribbon width [155]. Generally, in ZGNRs the AFM state is more stable than the FM state, and both are more stable than the non-magnetic state [155, 217].

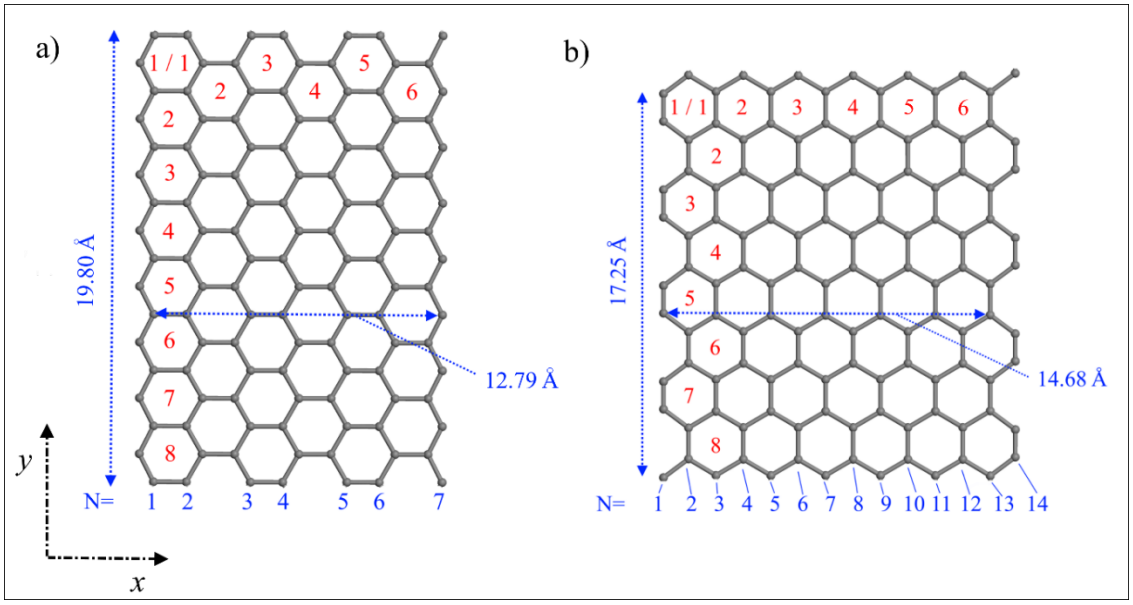

Fig. 6.1. Schematic view of supercells for a) 7-ZGNR, b) 14-AGNR. The numbers N (blue) label the carbon atoms according to the method of numbering for both ribbons used in Ref. [155], and the red numbers within the rings label the number of the rings horizontally and vertically. The blue arrows indicate the ribbon size in both *x* and *y* directions.

The supercell size for the zigzag ribbon we considered is 60 Å × 19.80 Å × 20 Å. The 60 Å and 20 Å are selected in *x* and *z* directions to allow enough space and avoid interactions between adjacent ribbons. Similarly, the cell size of the armchair type ribbon was 60 Å × 17.25 Å × 20 Å.

The binding energy between metal adatom and the F-GNR is determined by:

$$E_b = \frac{E(M_n@F\text{-}GNR) - nE(M) - E(F\text{-}GNR)}{n} \tag{6.1}$$

where $E(M_n@F\text{-}GNR)$, $E(M)$ and $E(F\text{-}GNR)$ are the energy of a F-GNR loaded with n metal atom (M = Na or Ca), the energy of M as an isolated atom in the gas phase, and the energy of the functionalized nanoribbon, respectively. Therefore, a negative binding energy indicates that the binding is energetically favorable.

To determine whether binding is predominantly occurring between the metal and the substrate or due to cohesion of the metal atoms, it is useful to define an interaction energy and a metal cluster formation energy. The strength of the interaction of a group of Na or Ca metal adatoms and a F-GNR can be quantified through the interaction energy defined as [69, 76]:

$$E_{int} = \frac{E(M_n@F\text{-}GNR) - E(M_n) - E(F\text{-}GNR_d)}{n} \quad (6.2)$$

where $E(M_n)$ and $E(F\text{-}GNR_d)$ are the energy of an isolated group of n metal adatoms in the structure they form on the substrate, and the energy of the substrate in the configuration it adopted after metal adsorption (or deformed substrate), respectively. The value of $E(F\text{-}GNR_d)$ will be higher than the value of $E(F\text{-}GNR)$, the substrate before metal adsorption. A negative value of E_{int} indicates a favorable interaction between groups of metal adatoms and the substrate. The formation energy of a group of metal adatoms from their isolated state in the gas phase (E_f) is given by:

$$E_f = \frac{E(M_n) - nE(M)}{n} \quad (6.3)$$

If the formation energy of the cluster is close to the cohesive energy of Na and Ca in the bcc and fcc structures [65], we can suggest that a metal cluster is probably formed. Otherwise, if the substrate is not greatly deformed, the interaction energy will be the main contribution to the binding energy. We have used this analysis to consider the interaction of metal atoms with hydrogenated defective graphene [76]. Bommier et al. carried out a similar analysis in their work on storage of sodium on hard carbons [219].

The theoretical electrical capacity of the anode material in mA h g^{-1} can be estimated by the following equation [28, 76]:

$$Q\ (mA\ h\ g^{-1}) = \frac{n_e\ n_M\ F}{3.6(n_M m_M + n_H\, m_H + n_C m_C)} \quad (6.4)$$

where m_M, m_H and m_C are the atomic masses of the metal adatom (M), hydrogen (H) and carbon atoms (C); n_M , n_H and n_C are the number of metal, hydrogen, and carbon (C) atoms in a unit cell and F is Faraday's constant, 9.648×10^4 C mol^{-1} . The value of n_e is given by the valency of the metal atoms (1 for Na and 2 for Ca).

6.4 Results and discussion

6.4.1 Structures of GNRs with functional groups at the edge

The optimized structures of the ZGNRs passivated with hydrogen (H), and functionalized with hydroxyl (HO-), carbonyl (O=) and carboxyl (HOOC-) groups are shown in Figs. 6.2a to d. For these F-GNRs, there is one functional group on each side of the GNR in the supercell, with all other edge carbon atoms passivated by hydrogen. The minimum energy structure for the H-, HO-, O- and HOOC-ZGNRs correspond to the antiferromagnetic (AFM) state for the edge atoms rather than ferromagnetic (FM) state which has a higher energy. This is consistent with previous studies [152, 155, 217, 220], which is interesting given that our ZGNRs do not have bilateral symmetry, unlike the GNRs considered those studies. The energy difference between these two states are found to be 1.4, 0.83, 1.4 and 1.4 meV / atom for these ribbons, respectively. We also considered ribbons that were fully functionalized by hydroxyl groups (with HOt- label, Fig. 6.2e) and carbonyl groups (with Ot- label, Fig. 6.2f). These were selected to help understand the effect of increasing the number of these groups on the binding of adsorbates (Na or Ca). It was not possible to fully functionalize the system with carboxyl groups due to steric hindrance. In addition to these systems, we considered alternating carbonyl-carboxyl groups at the ZGNR edge (labelled O_HOOC-, see Fig. 6.2g). The supercells of all the ZGNRs with functional groups are depicted in Fig. 5A.1. The optimized sheet and the H-, HO-, O-, and Ot-ZGNRs appear planar, in contrast to the HOOC- and O_HOOC-ZGNRs which have non-planar conformations due to steric effects [221, 222].

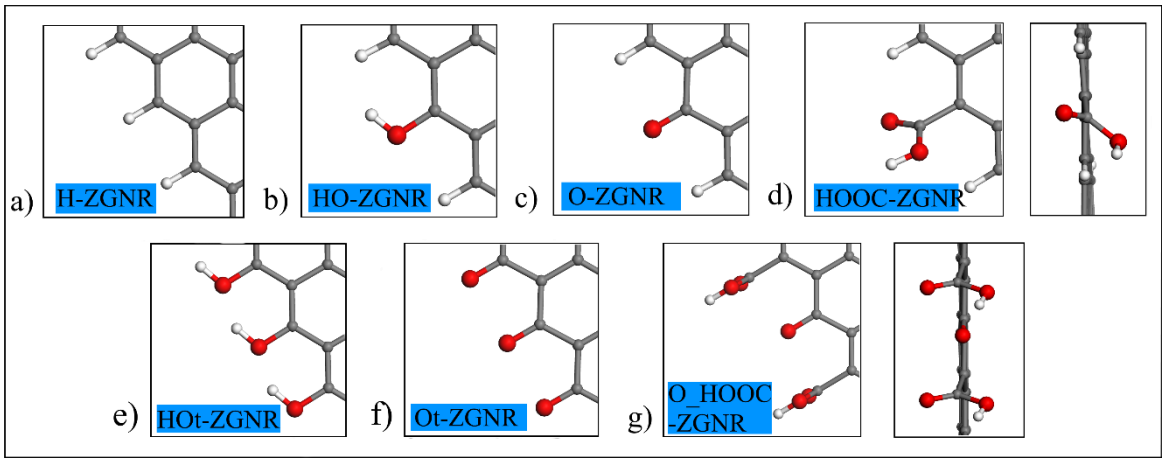

Fig. 6.2. Top views of functional groups bound to the edge of ZGNR: a) H-, b) HO-, c) O-, top and side views of non-planar configurations of d) HOOC-, e) HOt-, f) Ot-, and g) O_HOOC-. In the cases that there are no side views, the sheet is flat (or planar). Oxygen atoms are red, carbon atoms are grey and hydrogen atoms are white.

We also considered the corresponding AGNRs where possible. We note that there is a difference between the zigzag edge and armchair edge in terms of steric hindrance. The top and side views of the AGNRs functionalized with H-, HO-, O=, and HOOC- groups are depicted in Figs. 6.3a to d.

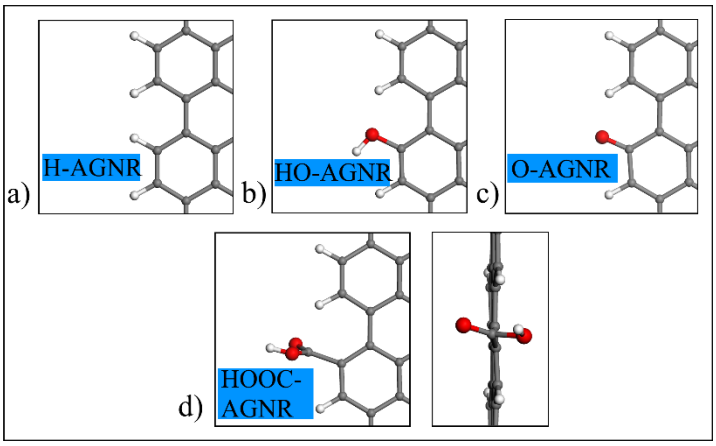

Fig. 6.3. Top views of functional groups bound to the edge of AGNR, a) H-, b) HO-, and c) O=. d) Top and side views of the non-planar configuration formed with functionalization of AGNR by HOOC-. Oxygen atoms are red, carbon atoms are grey and hydrogen atoms are white.

As with HOOC-ZGNR, the minimum-energy configuration of HOOC-AGNR is non-planar. Fig. 6.4a depicts the structure of HOt-AGNR, which is twisted and deformed out of the plane. Similarly, optimization of the Ot-AGNR structure forced adjacent pairs of O= groups to lie on opposites sides of the GNR plane, as shown in Fig. 6.4b. Again, these deformations are due to steric hindrance of the groups at the edge. As shown in Fig. 6.1a and b, the distance between neighboring carbon atoms is equal in the zigzag edge, whereas in the armchair edge, the edge carbon atoms are unequally spaced. Therefore, the zigzag edge can be fully functionalized with functional groups such as HOt-, Ot-, and O_HOOC- groups without distortion of the GNR. Comparing the energies of the structures, we found that HOt-ZGNR was about 0.442 eV more stable than HOt-AGNR (for the whole supercell, with the same number of atoms) and Ot-ZGNR was about 8.56 eV more stable than Ot-AGNR. This is consistent with the structural differences seen in Figs. 6.2e, f and Figs. 6.4a, b. The complete supercell of all the AGNRs with functional groups are depicted in Fig. 5A.2.

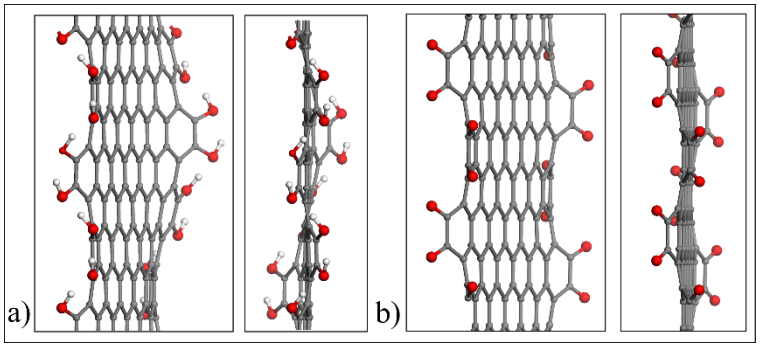

Fig. 6.4. Side views of distorted sheets formed with functionalization of AGNR: a) HOt-AGNR and b) Ot-AGNR. Oxygen atoms are red, carbon atoms are grey and hydrogen atoms are white.

6.4.2 Adsorption of Na and Ca on F-GNRs

In this section, we present the results of Na and Ca adsorption on different sites of the ZGNR and AGNRs, including over the basal-plane rings and the edges, to determine where the metal atoms are most likely to bind and to consider how far the effects of functionalization extend across the ribbon. The sites considered are categorized into 5 locations shown in Figs. 6.5a and b for both ZGNRs and AGNRs. As indicated in this figure, sites R3, R2, and R1 are on the hexagonal rings from the middle of the ribbon towards its edge. In addition, the sites 'over the edge' and 'in front of the edge' are indicated by V and F. Site V is a point over the functional group and site F is farther from the functional group and beyond the sheet, either coplanar with the sheet or above/below this plane.

Figs. 6.6 and 6.7 display bar charts for all E_b values for Na and Ca at the sites shown in Fig. 6.5. In addition, Tables 5A.1 and 5A.2 give the numerical values of E_b for each site. In the bar charts (Figs. 6 and 7), the absence of a bar indicates that the metal atom was not stable at that site. For example, in Ot-ZGNR, Na was not stable at sites R1 and V. We discuss this more in sec. 6.4.4.

By comparing the converged energies and spin states of structures starting with different initial spin states, we found that the H-, HO-, O-, HOOC-, and HOt-ZGNRs had ground state energies with AFM-like state rather than FM-like spin states.

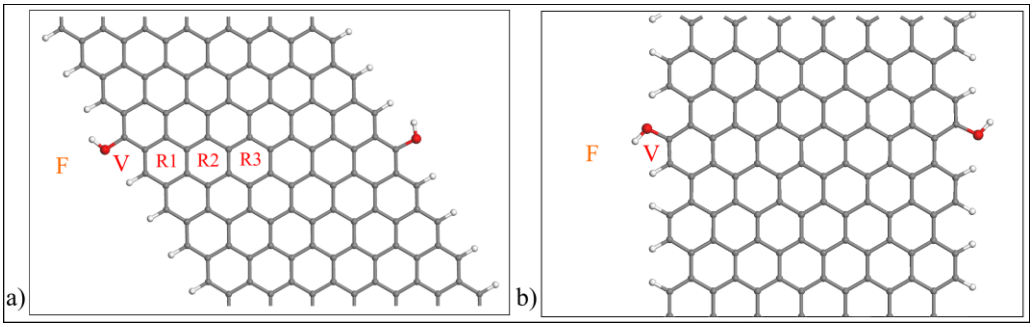

Fig. 6.5. Sites for metal atom binding over a representative a) F-ZGNR and b) F-AGNR. The red spheres are O atoms, white are H atoms and grey are C atoms. Note that the symbols V and F refer to any site over the functional group (V) or farther from the ribbon and the functional group (F).

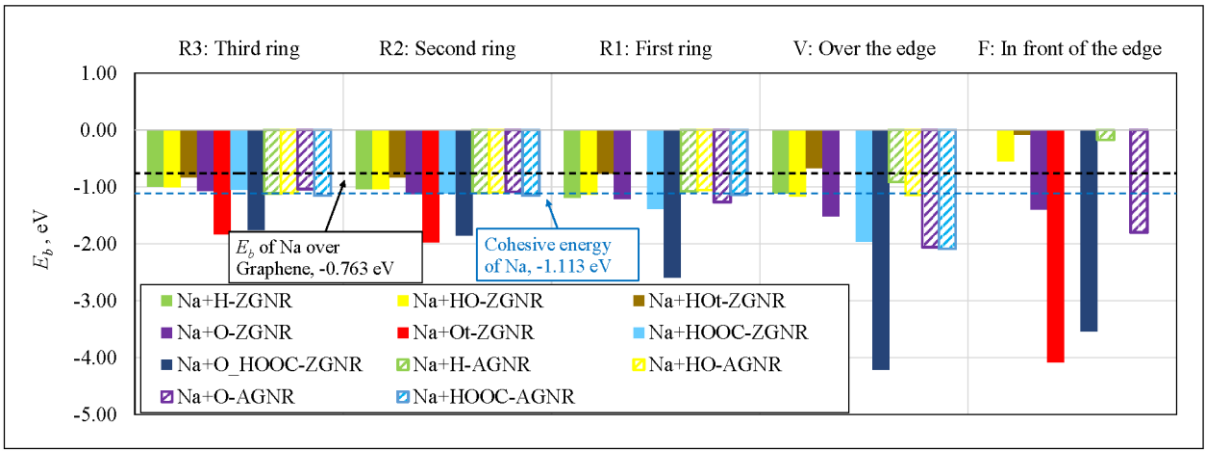

Fig. 6.6. Na binding energies over the five sites defined in Fig. 6.5. Solid bars are for adsorption on ZGNRs; striped bars for AGNRs. Bars are not shown for sites where local minima were not found. In those cases, when the Na atom was initially placed at the site, it would move to another site during the structural optimization. The numerical values of the binding energies are given in Table 5A.1.

Different possible spin states were also considered in the calculations for the ribbons with Na and Ca adsorbed, and the reported E_b values in Figs. 6.6 and 6.7 correspond to the ground state energy of the pure ribbon and adsorbed ribbon as appearing terms in Eq. 6.1. According to our calculations, whereas all the mentioned ribbons remained in AFM state after Na adsorption, they changed to FM state following Ca adsorption at sites R3 and R2 of all the ZGNRs. Fig. 5A.3 depicts the spin density of the O-ZGNR before and after adsorption of Na and Ca at sites R2 and V. According to Figs. 5A.3b and d, the Na and Ca tend to dampen the magnetization of the nearby carbon atoms in the first and second columns of the hexagonal rings.

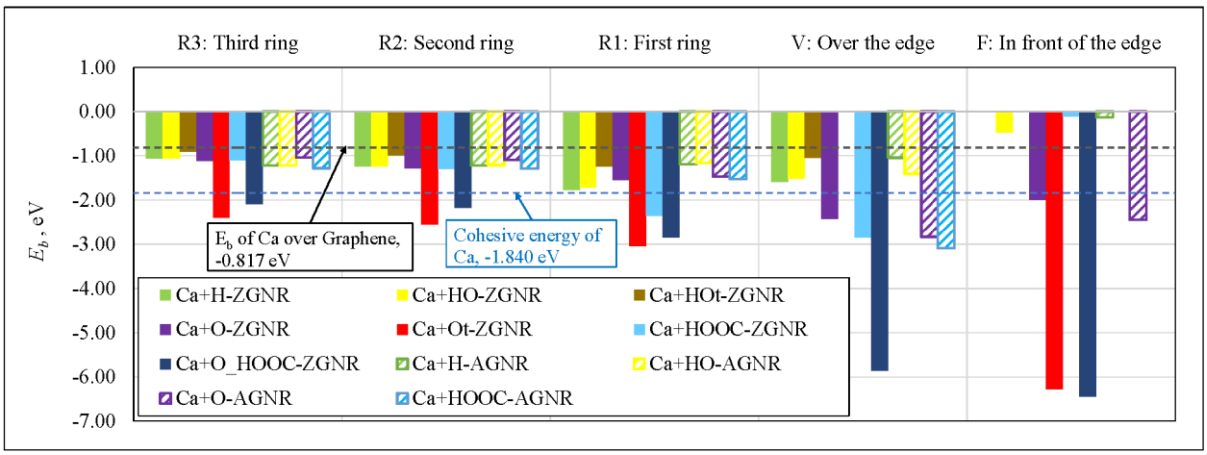

Fig. 6.7. Ca binding energies over the five sites defined in Fig. 6.5. Solid bars are for adsorption on ZGNRs; striped bars for AGNRs. Bars are not shown for sites where local minima were not found. In those cases, when the Na atom was initially placed at the site, it would move to another site during the structural optimization. The numerical values of the binding energies are given in Table 5A.2.

However, this phenomenon was not seen in the site V according to Figs. 5A.3c and e. As mentioned, except Ca at site R3, all the other adsorbed cases retained the AFM state of the ribbons. This is in contrast of the finding of Uthaisar et al. [152] who found a change to the FM state after Li adsorption over the H-ZGNRs. This is likely to be due to the difference in the methodology which includes a shorter ribbon in the supercell of Uthaisar et al. resulting in much higher number of Li per unit length.

Two lines are shown on both bar charts of Figs. 6.6 and 6.7. The black lines indicate the calculated E_b of Na and Ca on the basal plane of a graphene sheet represented by 6 × 6 rings in a supercell with periodic boundary conditions. We calculated these values to be -0.763 and -0.817 eV for Na and Ca, respectively (see Fig. 2B.4 for the E_b of Na). However, these values are higher (weaker in binding) than the cohesive energies of Na and Ca that are -1.113 and -1.840 eV, respectively [65], and are shown as blue dashed lines in Figs. 6.6 and 6.7. The cohesive energy is the binding energy of Na and Ca in their bulk bcc and fcc structures, respectively [65]. A value of E_b indicating weaker binding might result in metal cluster or dendrite formation for a number of metal atoms [28, 63, 69, 76]. Sodium and calcium are known to bind weakly over the graphene sheet compared with other alkali metals, as investigated by Liu et al. [7]. According to the two bar charts, all ZGNRs and AGNRs with hydrogen and oxygen-containing functional groups improved the E_b values compared to the E_b of Na and Ca on the graphene sheet. This enhancement of binding of Na and Ca to the F-GNRs is an important advantage of these materials, which is also consistent with the previous findings

for Li binding to the GNRs [36, 37, 140, 152]. Overall Na seems to be more suitable for use with F-GNR electrodes, as its binding energies in the middle of ribbon are closer to E_{coh} compared to Ca. Values of E_b slightly lower than E_{coh} are most desirable, as these suggest favourable and reversible adsorption/desorption of the metal adatoms to/from the functionalized carbon substrate.

The binding energies of Na and Ca over the rings and the edge of H-, HO- and HOt- Z / AGNRs are close to or weaker than the cohesive energies. However, they are generally stronger than that of Na and Ca to graphene, by about 0.26 eV for Na and 0.44 eV for Ca on average. We also observe that the enhancement in binding is observed both near the H-, HO- and HOt- functional groups and across the ribbon. This verifies the impact of the GNR structure (its finite width and the presence of edges) and the morphology of the edge in the binding strength. In previous work [76] we found that a single layer of hydrogenated defective graphene (with a hydrogen atom bound to the mono-vacancy of defective graphene) bound Na and Ca more strongly than graphene. This finding and also the present finding for H-Z/AGNR is consistent with the work of Yoon et al. [44] and Stevens and Dahn [16] who both found that hydrogen terminated groups in the carbonaceous materials improved Na and Li adsorption. Another observation from Figs. 6.6 and 6.7 (or Tables 5A.1 and 5A.2) is that H-ZGNR bound Na and Ca more strongly at sites R1 and V than H-AGNR, which is also consistent with the finding of Uthaisar et al. [152] for Li binding to similar sites.

Considering the adsorption strength relative to E_{coh}, we observe that O-, HOOC- for Na, and Ot-, O_HOOC-Z/AGNRs for both Na and Ca (purple, blue, red and dark blue bars) improved the binding over the hexagonal rings (R3, R2, R1) compared to that of graphene. Moreover, these oxygen groups resulted in stronger binding over the edge compared to that over the rings. This is an important consideration if r-GO is to be used as an anode material. These results are consistent with Uthaisar et al. [37, 140], Xiao et al. [153] and Lin and Kuo [36] who suggested that most Li adsorption occurs around oxygen-containing groups. Furthermore, regarding the binding energies of Ot- and O_HOOC-, we obviously see that they are stronger than single O= and HOOC- functional groups at the edge. It can therefore be concluded that the more oxygen groups at the edge, the stronger the binding over the rings and the edge. While full oxygenation at the edge of r-GO may be challenging to obtain experimentally, the calculations for Ot- and O_HOOC- represent a maximum limit for binding strength over the rings and the edge. These

results indicate that increasing the number of functional groups will strengthen binding both at the edge and in the centre of narrow GNRs.

Among the oxygen-containing functional groups, only adsorption on O-Z/AGNRs and HOOC-Z/AGNRs gave E_b values for Na and Ca at sites V and F that would be suitable for application as electrodes. These values vary from -1.40 to -2.09 eV for Na, and -1.99 eV to -3.09 eV for Ca. They are suitable for metal adatom binding on anode materials, because their excess bindings compared with their corresponding E_{coh} are between 0.15 to 1.25 eV, ensures clustering of metal atoms does not occur while not being so strong that the atoms are unable to be removed. On the other hand, we see that Ot-ZGNRs bound Na and Ca too strongly with E_b of -4.08 eV and -6.28 eV, respectively at site F. Similarly, O_HOOC-ZGNR had an E_b of -4.21 eV and -3.54 eV at sites V and F for Na, and -5.86 eV and -6.44 eV for Ca, respectively. These excessive binding energies mean that removal of the metal atoms from the GNR would be difficult.

As can be seen in the binding strength profiles of Na on HO- and HOt-GNRs, not all oxygen-containing groups strengthened the bindings of metals to the GNR compared to the H-passivated GNR. We also observe in the bar charts that the binding strength increases as the binding site is varied from the middle of the ribbon toward the edge for the oxygen-containing functional groups, O=, Ot-, HOOC- and O_HOOC-. The effects of such groups are greater at the edge over the groups where it caused a significant binding, although in the middle of ribbon (R3) the bindings are more similar to those of H- and HO-Z/AGNRs. By contrast, the hydrogen and hydroxyl groups (H-, HO-, and HOt-Z/AGNRs) showed almost uniform profiles for Na binding from the middle of the ribbon toward the edge. For Ca binding, the behaviour is similar, although the binding strength is greater in general.

From the binding strengths alone, it is unclear if these results obtained are due to differences in the electronic structure across the GNRs, due to different functionalization or due to interactions of the metal atoms with the functional groups. This will be explored in more detail in sections 6.4.3 and 6.4.6.

6.4.3 Charge transfer associated with Na/Ca adsorption

To provide an understanding of the very strong binding energies found for some of the systems considered in Figs. 6.6 and 6.7 (Tables 5A.1 and 5A.2), we have carried out a Bader charge

analysis to evaluate the amount of charge transfer from the metal atoms. These calculations considered Na and Ca bound at sites R3, V and F of the H-, O-, HOOC- and Ot-ZGNRs. The complete results are given in Table 6.1. According to the Bader charge analysis, the amount of charge transfer from Na in all cases varies between 0.81 and 0.84 *e*. For the Ca the amount of charge transfer varies between 1.0 and 1.5 *e* with one exception of 0.773 *e* for Ca at site F on the O-ZGNR. In this particular case, the position of the Ca atom in the optimized structure is 2.09 Å from a single O atom. We presume that the charge transfer of the Ca atom in this position is restricted by the availability of the acceptor atom. Although the amount of charge transfer from Na does not vary greatly according to the Bader charge analysis, for Ca variation is greater and is directly related to the binding strength, suggesting an ionic character for the bonding of Na and Ca to the F-GNRs.

Table 6.1. Binding energies and charge transferred from the metal atoms after adsorption to the H-, O-, HOOC- and Ot-ZGNRS

Type of ribbon	Atom	Site	Binding energy, E_b/ eV	Charge transferred from the metal atom / *e*
H-ZGNR	Na	R3	-0.990	0.825
		V	-1.117	0.809
	Ca	R3	-1.061	0.988
		V	-1.595	1.264
O-ZGNR	Na	R3	-1.078	0.827
		V	-1.523	0.805
		F	-1.401	0.828
	Ca	R3	-1.114	1.105
		V	-2.421	1.310
		F	-2.234	0.773
HOOC-ZGNR	Na	R3	-1.051	0.827
		V	-1.964	0.813
	Ca	R3	-1.099	1.049
		V	-2.845	1.409
Ot-ZGNR	Na	R3	-1.837	0.831
		F	-4.078	0.836
	Ca	R3	-2.407	1.395
		F	-6.281	1.491

Charge density difference calculations were carried out to determine the amount of charge transfer as a result of metal binding to the F-GNRs and is given by:

$$\Delta\rho = \rho_{Na/Ca\text{-}GNR} - \rho_{GNR} - \rho_{Na/Ca} \quad (6.5)$$

where ρ is the charge density of the systems specified as $e\ a_0^{-3}$ (a_0: Bohr radius). We present results for Na and Ca at the most stable sites over H-ZGNR, O-AGNR, Ot-ZGNR, HOOC-AGNR, and O_HOOC-ZGNR in Fig. 5A.4, and the results for the two most strongly binding systems of Na and Ca on O-AGNR are given in Fig. 6.8. The isosurface value is selected to be $\zeta = 0.0002\ e\ a_0^{-3}$ for all cases.

In Figs. 6.8 and 5A.4, the blue regions are where the electron density increases on addition of the metal atoms to the surfaces, which is mostly on the carbon atoms and the red regions are where the charge is reduced and is mainly on the metal atoms. In both cases, there is a significant charge transfer from Na and Ca to the AGNR. However, in the case of Ca (Fig. 6.8b) the red cloud is larger than Na and it extends over a larger area, reflecting the fact that there is more charge in the multivalent Ca atoms transferred to the substrate and that the valence electrons of Ca are in the third shell rather than the second shell for Na, as well as the size of the ions. The greater charge transfer from the Ca atoms than Na atoms is also evident in the greater extent of the changes across the ribbon for Ca.

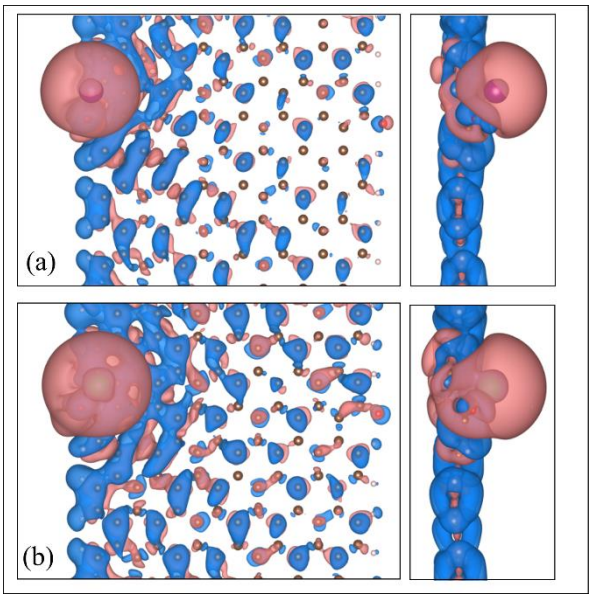

Fig. 6.8 Top and side views of charge density difference of H-AGNRs with a) 1 Na and b) 1 Ca atom adsorbed at site V. In both cases the value of isosurface is ζ=0.0002 e a_0^{-3} (a_0: Bohr radius). The red area indicates the electron deficient area, and the blue area indicates the electron rich area.

To examine the bonding more clearly, Fig. 6.9 depicts contour maps of the charge density differences for some cases when the metal atom is at site F and coplanar with the O- and Ot-GNRs. In addition, the charge received by the nearby oxygen atoms can be seen in each figure. As seen in Fig. 6.9a, the electron density midway between the Na atom and the oxygen atoms is low, indicating an ionic bond. This electron density rearrangement is greater on adsorption of Ca to the functionalized GNR, as seen in Fig. 6.9b. It is also consistent with an ionic interaction. Similar interactions are observed in Figs. 6.9c and d in the case of Ot-ZGNR, where the binding energies of -6.281 eV for Ca and -4.078 eV for Na are both strong. Likewise, Ca binds more strongly than Na to site F and there is a greater difference in charge.

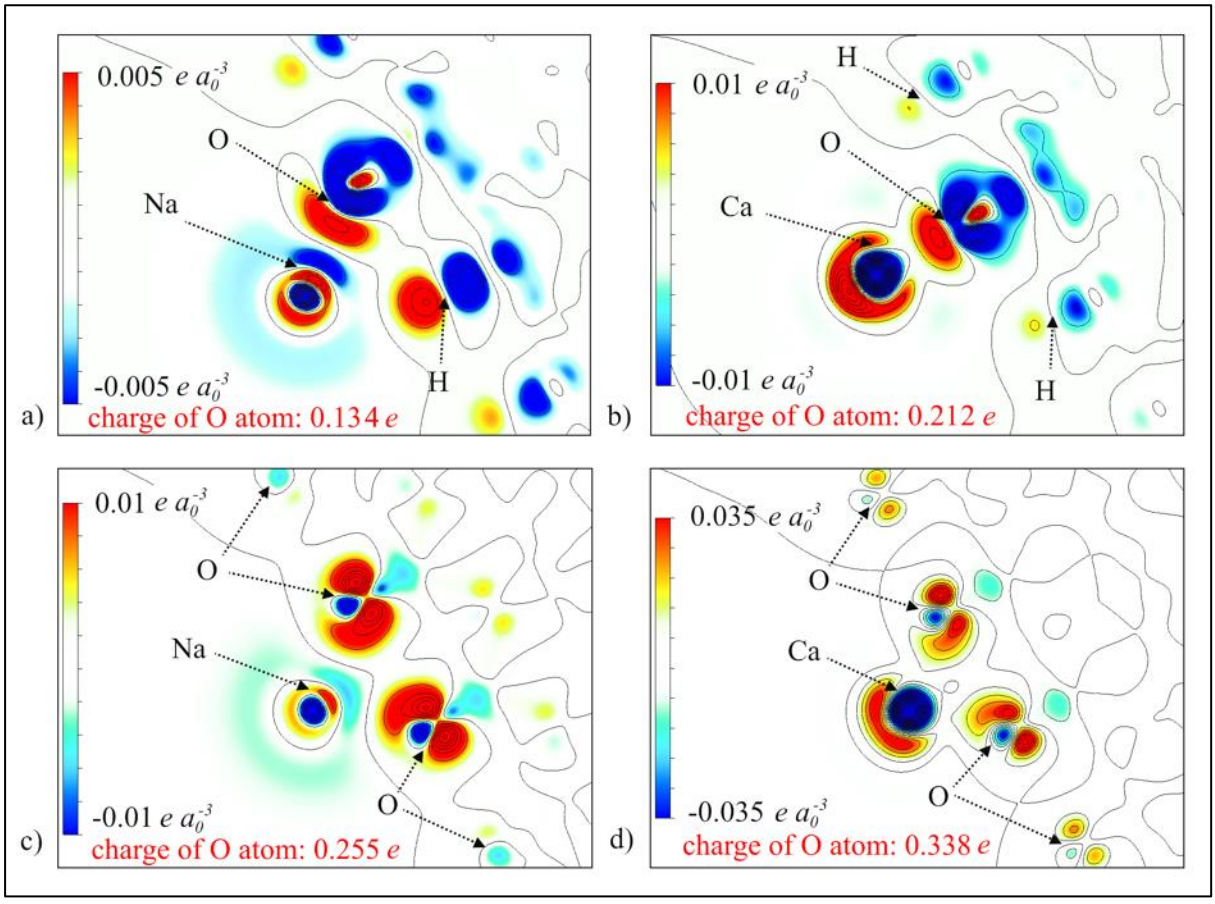

Fig. 6.9. Charge density difference contour maps of a) Na on O-ZGNR, b) Ca on O-ZGNR, c) Na on Ot-ZGNR, and d) Ca on Ot-ZGNR. The colour scale bar in each figure indicates the charge density difference, and the contour lines are a) between -0.1 and 0.05 e a_0^{-3} with interval of 0.004 e a_0^{-3} b) -0.2 and 0.04 e a_0^{-3} with interval of 0.005 e a_0^{-3} c) and d) -0.2 and 0.08 e a_0^{-3} with interval of 0.008 e a_0^{-3}. The red area indicates electron rich area and the blue area is located at the nuclei of the atoms (Ca and O). The charge transferred to the O atoms that are close to the metal atoms, according to a Bader charge analysis, is indicated on the figures.

6.4.4 Na and Ca binding sites

As we noted in the previous section, sites V and F are the most stable sites for Na or Ca binding over O- and HOOC-Z/AGNRs. Fig. 6.10 shows the top and side views of part of the GNRs depicting the most stable sites for the O- and HOOC-Z/AGNR.

From Fig. 6.10 we observe that the Na and Ca binding sites are similar. In HOOC- cases (Figs. 6.10e to h), we observe that the metal adatom is attracted by O atom that has a double bond to the carbon, rather than the HO- group. It can be seen that the distance between the metal adatom and O atom of the HOOC- group varies between 2.16 and 2.23 Å and that the strong interaction leads to partial distortion of the ribbon's plane (Figs. 6.10e to h). We note that HOOC-Z/AGNRs do not show stable binding at site F; an adatom initially located at site F is at site V after energy minimization.

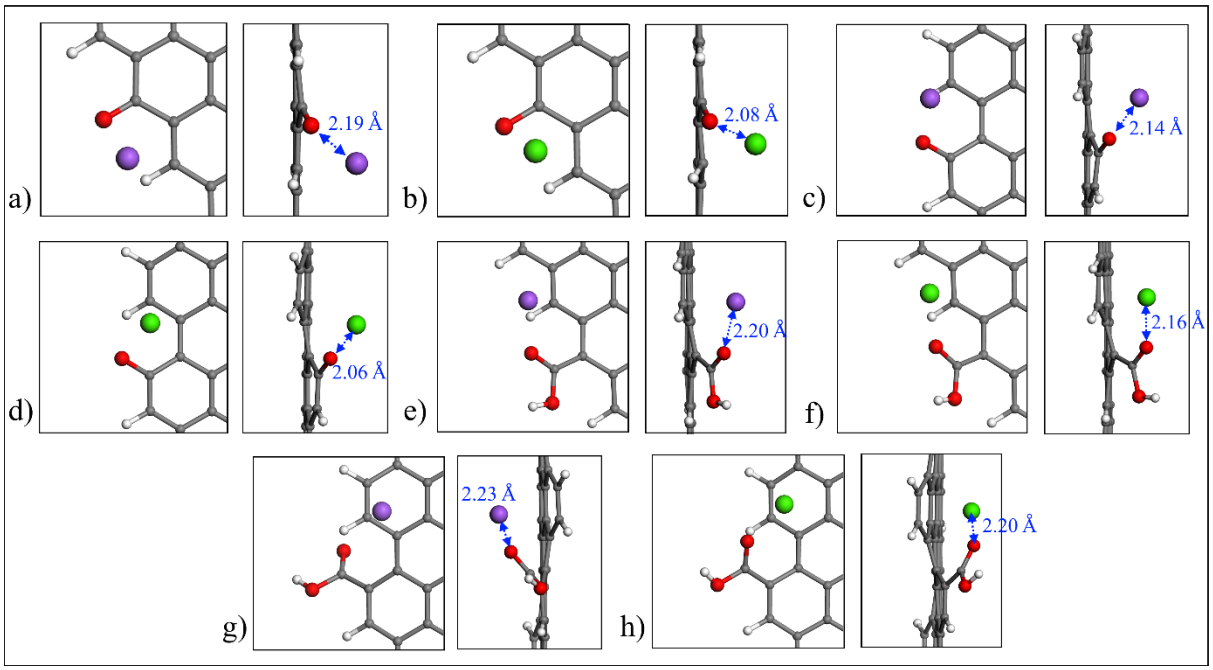

Fig. 6.10. Top and side views of the nanoribbons, depicting the most stable sites for Na and Ca binding, a) Na + O-ZGNR, b) Ca + O-ZGNR, c) Na + O-AGNR, d) Ca + O-AGNR, e) Na + HOOC-ZGNR, f) Ca + HOOC-ZGNR, g) Na + HOOC-AGNR, h) Ca + HOOC-AGNR. The blue values show the distance of metal adatom from the O atom. In all figures, the purple atoms indicate Na, green indicate Ca, red indicate O, white indicate H and grey indicate C atoms.

The other notable finding from Figs. 6.6, 6.7 and 6.10 is that whereas HOOC-Z/AGNR binds the metal atoms at V and R1 but not F, Ot-ZGNR bound the metal atoms at site F, and not V or R1. Fig. 6.11 depicts the configuration of the global minima for Na and Ca metals. This is likely to be due to the uniformity of the Ot-ZGNR edge compared to HOOC-Z/AGNR.

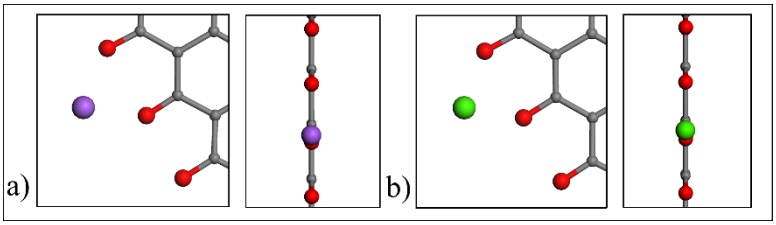

Fig. 6.11. Top and side views of GNRs with the metal atoms in front of the Ot-Z/AGNRs (site F), a) Na atom, and b) Ca atom. In all figures, the purple atoms indicate Na, green indicate Ca, red indicate O and grey indicate C atoms.

6.4.5 Effects of functional groups on the adsorption of multiple Na and Ca on GNRs

Having observed an enhanced binding of metal atoms to F-GNRs, in this section we consider adding a number of Na and Ca atoms to F-GNRs to see the extent of binding enhancement that can be attained. Firstly, we did tests to observe the binding of multiple Na adatoms over the H-ZGNR for 2 to 16 Na adatoms. The results are presented in Fig. 6.12, Fig. 5A.5 and Table 5A.3. According to those results, the binding energy stabilizes for a high number of Na adatoms (8, 12 and 16) at around -1.1 eV. This value is close to the E_{coh} of Na, so it may suggest that a metal sheet is being formed by those groups of Na adatoms. This value is indicated by an orange line in Fig. 6.12.

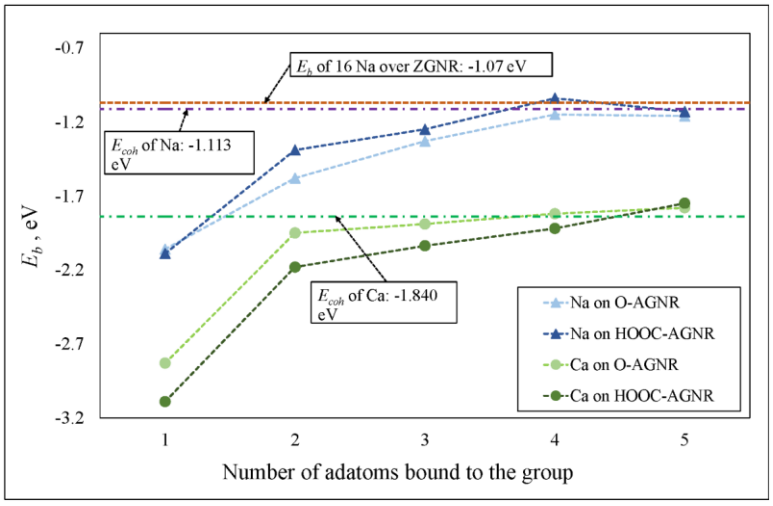

Fig. 6.12. Binding energies (E_b) of multiple metal atoms over O- and HOOC-AGNRs

In order to estimate the electrical capacity for H-ZGNR, we consider 16 Na as the maximum loading (Fig. 5A.5c). According to this structure and using Eq. 6.4, the electrical capacity is

248.0 mA h g^{-1}. For comparison, the binding of a single Na to a 6 × 6 or 8 × 8 graphene sheet is less than the cohesive energy (Fig. 2B.4), and therefore based on this measurement the loading would be zero. We therefore compare the loading of the H-ZGNR with the reported capacity of graphite loaded with Na which is proposed to be NaC_{64} [69], and equivalent to 33.9 mA h g^{-1} based on Eq. 6.4. Thus, H-ZGNR has almost 7.3 times higher capacity than graphite. This capacity is also comparable with the capacity of graphite loaded with Li at LiC_6 [11] equivalent to 339 $mAhg^{-1}$ based on Eq. 6.4. However, we should be very cautious on reporting an electrical capacity for the GNRs. In reality the capacity is highly dependent on the ribbon width, the loading capacity with the metal atoms, and the type of functional groups at the edge. For example, the greater the width of the ribbon, the less capacity.

We also examined the adsorption of 2 Na or Ca atoms over the hydroxyl group at the edge or HO-ZGNR. The values of E_b were -1.213 eV / Na, and -1.566 eV / Ca. For Ca the E_b was weaker than its cohesive energy [65] and therefore we did not continue to add more metal adatoms to HO-ZGNR.

Due to the strong binding between the metal atoms and O= and HOOC- groups, we carried out a detailed analysis of the effect of adding a number of Na and Ca atoms to O-AGNR and HOOC-AGNR to see the extent of binding enhancement by these groups. In order to see the effect of individual groups at the edge, we test the metal adatom binding when there is only one group at the edge (O= and HOOC-). In all cases, we selected reasonable initial configurations for the adatoms around the group, although other initial configurations could lead to other local minima. The results for Na and Ca binding over the O-AGNRs and HOOC-AGNR are also shown in Fig. 6.12, and Tables 5A.4 and 5A.5.

Fig. 6.12 shows that the O-AGNRs can bind as many as 5 Na or Ca atoms with moderate binding values of -1.16 and -1.78 eV, respectively, which are close to their corresponding E_{coh} values. If more atoms are added to the materials, the binding energies become weaker than the cohesive energies and clustering might occur. In a similar way, HOOC-AGNRs can bind up to 5 Na and Ca atoms around their functional groups. Fig. 6.12 also shows that the binding energies of 4 or more adatoms is approximately equal to E_{coh}. Figs. 6.13a to d depict the top and side views of 4 Na and Ca adatoms bound to O- and HOOC-AGNR.

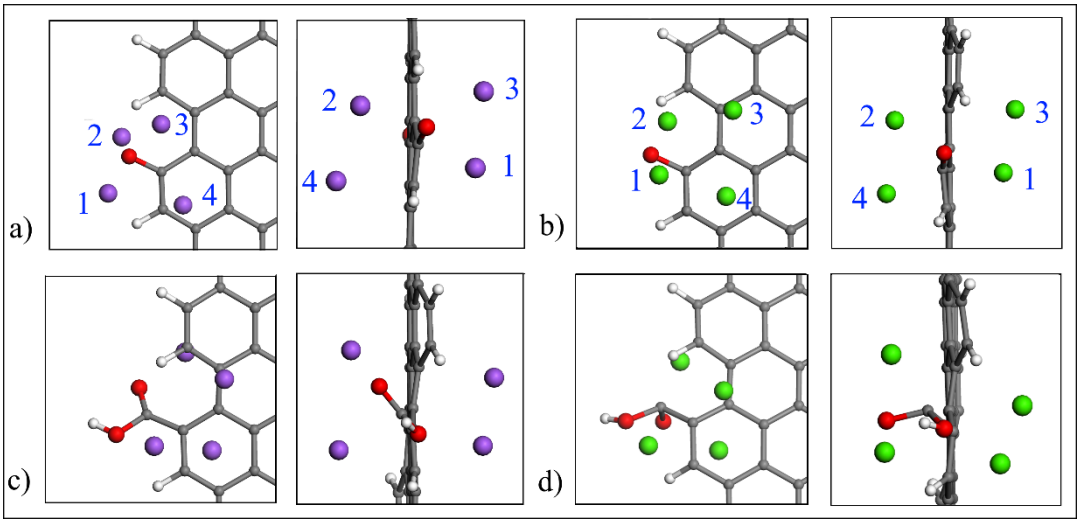

Fig. 6.13. Top and side views of 4 metal adatoms around O-AGNRs a) 4 Na, b) 4 Ca, and HOOC-AGNR c) 4 Na, d) 4 Ca. In all figures, the purple atoms indicate Na, green indicate Ca, red indicate O, white indicate H and grey indicate C atoms. In a) and b), the numbers in blue label the Na and Ca adatoms referred to in the text when considering the charge distribution and the interactions of individual metal atoms with the surface.

The overall configurations of the Na and Ca atoms over the two functional groups look similar. Two atoms are close to the functional group and the additional two are farther from the group and over the GNR plane rather than in front of the functional group (site F). This is due to the effect of the hexagonal rings across the ribbons in binding those adatoms. As we observed in the bar charts (Figs. 6.6 and 6.7), the binding over the hexagonal rings (R1, R2 and R3) of O-AGNR and HOOC-AGNR is greater than that on graphene by at least 0.28 eV for Na and 0.22 eV for Ca. Given the significant binding energy differences between the rings and the edge, we expect the edge sites V and F to be firstly occupied before the other metal atoms occupy inner locations.

Further analyses were carried out to determine the interaction of the different metal atoms with the AGNR and each other. Fig. 6.14 depicts the degree of charge transfer from the each of the metal atoms when 1 to 5 Na and Ca adatoms are adsorbed on O-AGNR. The values were obtained from a Bader charge analysis. The results show that as the number of atoms bound to the O-AGNRs increases, not only does the average charge transferred per atom decrease (see Table 6.2), but the charge on each atom decreases in most cases (Fig. 6.14). For example, the 1st adatom reduces its charge on the addition of other adatoms rather than the additional atoms just having lower charges. This suggests that the interaction of the metal atoms with the surface

decreases with loading and is consistent with the eventual formation of a metallic surface layer [76].

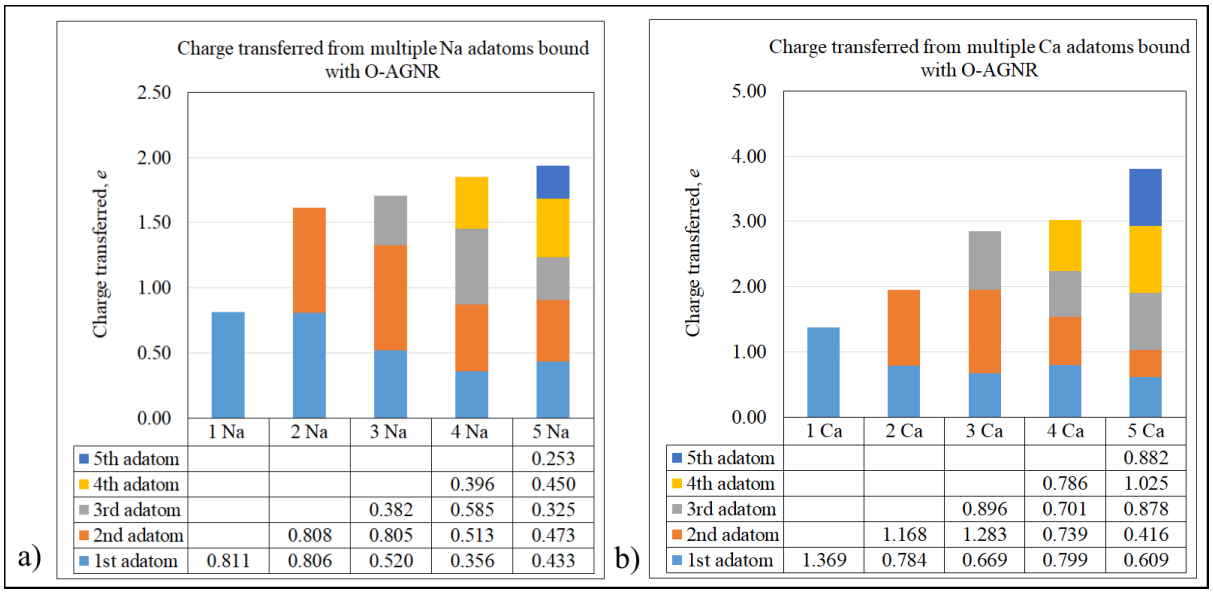

Fig. 6.14. Charge transferred from the metal adatoms bound to O-AGNR, a) 1 to 5 Na adatoms, b) 1 to 5 Ca adatoms. The configurations corresponding to the results of one metal atom are those shown in Figs. 6.10c and d. A second metal atom was added to that structure and the structure was optimized to give the results with 2 metal atoms, and this iterative process was repeated to obtain the results for the higher loadings. Each colour bar corresponds to the same adatom bound to the O-AGNR surface, near the O= group. The structures with 4 Na and Ca adatoms are shown in Figs. 6.13a and b, where the adatoms are numbered.

To further investigate the possibility of metal cluster formation between the adsorbed metal adatoms, we have calculated the interaction energy (E_{int}) between these groups and the F-GNR (Eq. 6.2), and the formation energy (E_f) of the adsorbed metal adatoms (Eq. 6.3). The results are presented in Table 6.2.

As shown in Table 6.2, with 1, 2 and 3 Na adatoms, and 1 and 2 Ca adatoms the E_{int} values are larger in magnitude than the E_b values, indicating a strong interaction energy between the group of Na and Ca adatoms and the O-AGNR. As the number of adatoms is increased to 5, we observe that the magnitude of the E_{int} is lower than that of E_b. This is consistent with an increasing interaction between the metal adatoms, which is also reflected in the increasing magnitude of E_f,. Weakening of the interaction between the metal atoms and the O-AGNR as the loading is increased is consistent with previous results.[63, 69, 76, 219] However, the results show that with 1-5 metal atoms there is still a strong interaction between the metal atoms and the surface, and the magnitude of the metal cluster formation energy is much less than that

of the cohesive energy. This reflects the advantage of oxygen functionalized GNRs for adsorbing Na and Ca adatoms.

Table 6.2. Binding (E_b), interaction (E_{int}) and metal cluster formation (E_f) energies for the multiple Na and Ca adsorbed on O-AGNR and the average charge transferred from the metal atoms.

Adatom	Number of Adatoms	E_b / eV atom^{-1}	E_{int} / eV atom^{-1}	E_f / eV atom^{-1}	E_{coh} of pure metal / eV atom^{-1} [65]	Average charge transferred from the metal atoms / e atom^{-1}
Na	1	-2.062	-2.173	-	-1.113	0.811
	2	-1.582	-1.687	-0.058		0.807
	3	-1.327	-1.384	-0.031		0.569
	4	-1.150	-0.955	-0.268		0.462
	5	-1.164	-0.907	-0.303		0.387
Ca	1	-2.833	-3.245	-	-1.840	1.369
	2	-1.949	-2.094	-0.188		0.976
	3	-1.894	-1.868	-0.343		0.949
	4	-1.819	-1.743	-0.305		0.756
	5	-1.783	-1.749	-0.558		0.762

We also evaluated the E_b of each individual adatom at the single site when they were adsorbed as multiple adatoms to determine if the weakening in binding with multiple atoms reflected the capacity of the surface to accept electrons from the metals or due to the interaction of the metal atoms. For this purpose, we have carried out single point calculations for each of the four adatoms bound to O-AGNR in the positions adopted in Figs. 6.13a and b, but with the other three metal atoms removed. We refer to these binding energies as E_{sp} and the results are given in Table 6.3.

As seen from the results in Table 6.3, each of the 4 adatoms has a different binding energy, E_{sp}, and all are much weaker than with 1 adatom in its optimal position (more than 0.3 eV for Na and 0.8 eV for Ca). Therefore, the weakening in binding with addition of metal atoms is not solely due to the capacity of the surface to accept electrons from the metal atoms, but is affected by the interaction of the metal atoms. Furthermore, the average E_{sp} is less than the corresponding E_b in magnitude which is consistent with the interaction between metal atoms discussed above. We also observe that E_{sp} for adatoms 1 and 2 have much greater magnitudes

than 3 and 4 which are positioned over the plane of the nanoribbon. This difference is not as evident in the charge transfer results shown in Fig.14.

Table 6.3. Single point energy (E_{sp}) calculation for each individual adatom bound to the O-AGNR

Adatoms adsorbed	E_b / eV atom^{-1}	**Adatom number***	E_{sp} / eV atom^{-1}	**Average of E_{sp} / eV atom^{-1}**
1 Na	-2.062	-	-	-
4 Na	-1.150	1	-1.483	-1.018
		2	-1.736	
		3	-0.263	
		4	-0.591	
1 Ca	-2.833	-	-	-
4 Ca	-1.819	1	-1.720	-1.256
		2	-1.974	
		3	-0.501	
		4	-0.828	

*: The adatom number are those indicated for Na and Ca in Figs. 6.13a and b.

Finally, we note that the metal atoms are more likely to move toward the GNR plane when there is a basal defect [76, 216], doping in the ribbon [154, 223], hydrogen [76], oxygen [37, 141] or nitrogen groups [39, 41] in that region. In these cases, the atoms and dopants also adsorb a number of metal adatoms, enhancing the GNR capacity as anode material.

6.4.6 Conductivity of the F-GNRs

We have carried out calculations of the density of states (DOS) in order to determine the conductivity of the F-GNRs, and with this we determine if F-GNRs can be used as substrates for battery anodes according to this criterion. We also investigated the magnetization of the proposed materials. The DOS results for H-Z/AGNRs are presented in Fig. 6.15, whereas results for HO-, O-, Ot- and HOOC-Z/AGNRs are presented in Fig. 5A.6.

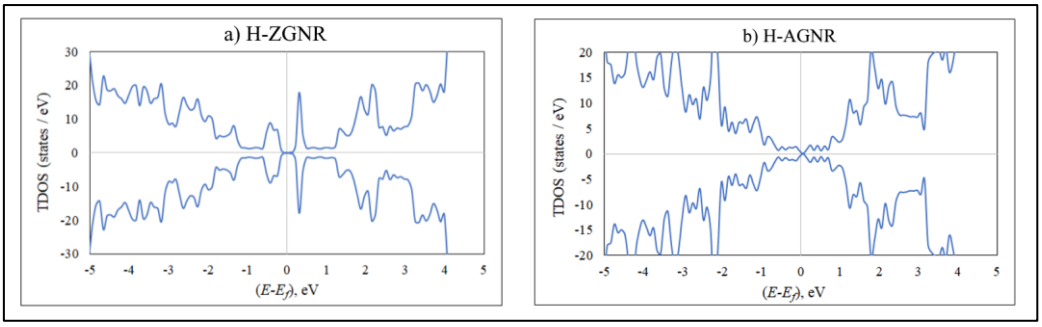

Fig. 6.15. Total density of states (TDOS) for a) H-ZGNR, and b) H-AGNR

Fig. 6.15a depicts the total DOS of H-ZGNR in the AFM state, which is the lowest energy state [217]. The bandgap is approximately 0.3 eV, therefore the ribbon is a semiconductor which is consistent with the result of Son et al. [155] and Uthaisar et al. [140]. Similarly, the DOS chart of H-AGNR (Fig. 6.15b) does not show any bandgap, which implies a metallic behaviour. This is consistent with results of Nakada, et al. [142] who found that an AGNR with N = 14 (N is defined in Fig. 6.1b) shows metallic behaviour, using a tight-binding band structure calculation within the Hückel approximation. Examination of the spin densities indicates that the AGNR is non-magnetic. The net magnetic moment of both H-Z/AGNRs are 0.0 μ_b and the spin curves are symmetric. Therefore, the magnetic moment of the last carbon atom, or the edge state effects, sum to zero [224].

The DOS charts of the HO-, O- and HOOC- Z/AGNRs (Fig. 5A.6a to g) depict the same behaviour with their corresponding H-Z/AGNRs in terms of edge type (zigzag or armchair). Indeed, the substitution of 1 H atom with HO-, O= and HOOC- groups within the same ribbon type (ZGNR or AGNR) does not qualitatively change the DOS greatly. However, in the case of O-AGNR, the curves at the Fermi energy are different from H-AGNR with a much higher DOS. In addition, in Ot-ZGNR the DOS are qualitatively and quantitatively different from the other F-ZGNRs, with a high DOS at the Fermi level of Ot-ZGNR. Both ZGNRs and AGNRs can be metallic [140]. These calculations demonstrate significant effects of multiple oxygen groups at the edge of the GNR on the DOS of the material.

6.4.7 Influence of the F-GNR Electrostatic Potentials on Binding

In order to understand the trends in the binding energy of Na and Ca due to functionalization of the GNRs, we consider the electron distribution across the material. We show in Fig. 6.16a to d the electrostatic potential mapped onto charge density isosurfaces of H-, O-, Ot- and

O_HOOC-ZGNRs without any adsorbates. In these visualizations, the regions coloured red indicate the electron-rich areas with the most negative electrostatic potential which are observed around the oxygen atoms and the blue coloured regions indicate areas that are relatively electron poor, such as around carbon atoms.

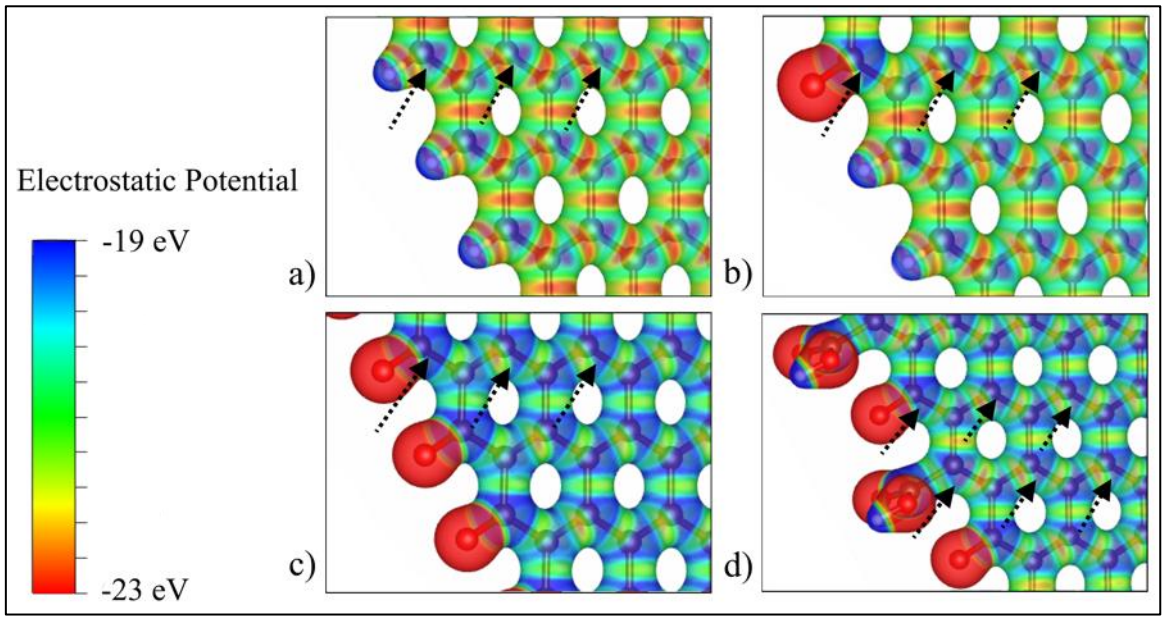

Fig. 6.16. Electrostatic potential mapped onto charge density isosurfaces for a) H-ZGNR, b) O-ZGNR, c) Ot-ZGNR, d) O_HOOC_ZGNR. The electrostatic potential is given by the colour bar and the isosurface has a charge density of 0.081 e a_0^{-3}.

According to the electrostatic potential maps shown in Fig. 6.16a, the spatial extent of the high-potential (blue) regions near the carbon atoms (indicated by black arrows) does not change greatly across the ribbon, showing a weak effect of hydrogen atom bound to the edge on the charge distribution across the width of the GNR. The carbon atom at the edge shows a slightly larger and more intense blue region. However, in Fig. 6.16b, it is clear that the O atom at the edge alters the electrostatic potential near the edge carbon more significantly than at other carbons. Furthermore, there is little difference in the electrostatic potential for the H-passivated and the O= functionalized GNR apart from those carbon atoms to which the H and O atoms are bound.

As we saw in the previous sections, the metal atoms had stronger binding over the carbon atoms near the edge of the O-ZGNRs (sites R1, or V) compared with the other sites. The visualizations in Fig. 6.16 verify that the charge distribution around the oxygen-containing functional group of the GNR results in stronger interaction with the metal atoms. Also, the data in Figs. 6.6 and 6.7 indicate that there is stronger interaction of the Na and Ca atom at the more inner positions

R2 and R3 in Ot-ZGNR than in O-ZGNR or H-ZGNR. Comparing Fig. 6.16a and c suggests that this is occurring due to the higher electrostatic potential over the middle carbon atoms of Ot-ZGNRs than those of O-ZGNR or H-ZGNR. The similarity of the electrostatic potential across the nanoribbon is also consistent with the small drop in E_b going from R2 to R3. Fig. 6.16d shows that the electrostatic potential changes more near the O= binding site compared to the HOOC- group in the O_HOOC-ZGNR. This is consistent with the double bond of the O= group to the GNR carbon. It results in the metal atom binding at site V and F of HOOC-ZGNR in comparison with the F position only for Ot-ZGNR (as seen in Figs. 6.6 and 6.7).

6.5 Conclusion

Using density functional theory calculations, we studied optimized structures of zigzag and armchair graphene nanoribbons with oxygen-containing functional groups at the edge, and the binding energies of Na and Ca to these structures. In all cases, the binding is stronger than on graphene. We showed that this is due to both the introduction of edges and the type of functionalization. The terminating functional groups considered were HO-, O= and HOOC- because these are commonly observed in reduced graphene oxide (r-GO) structures. We found that O= and HOOC- groups bound Na and Ca strongly (0.29 to 1.25 eV greater than the E_{coh}). Other groups such as H- and HO- also strengthened binding of Na and Ca to the edge sites compared to graphene by almost 0.26 eV for Na and 0.44 eV for Ca on average. On increasing the number of O= groups at the edge of the ribbons, the binding becomes very strong (E_b < -4.0 eV), making the ribbon less suitable for batteries due to the irreversible adsorption of the metal atoms.

The presence of edges not only changed the binding strength at the edges, compared to graphene. There was also a significant increase in the binding strength across the GNR for the width considered. For carbonyl and carboxyl groups, this effect increased with the number of functional groups, as seen for carbonyl groups in the 2-D contour plot of the charge density difference (Fig. 6.9) and also the calculated Bader charges. Furthermore, single carbonyl and carboxyl groups enabled adsorption of as many as 5 adatoms to the GNR with some of them binding over the hexagonal rings near the edge due to the high binding tendency in those areas. Analysis of the formation and interaction energies of multiple metal atoms with the GNRs revealed that for O-AGNR, although there is interaction between the metal atoms, it is much less than their respective cohesive energies when there are 5 Na and Ca. It also reveals strong

interaction between the adatoms and substrate. By considering the changes in the charge transferred from the metal atoms as the loading is increased, it is clear that the binding is being limited by both the ability of the carbon nanoribbon to accept electrons from the metal atoms and the interaction of between the metal atoms.

Electrostatic potential visualization showed that the oxygen-containing functional groups caused a change in the electrostatic potential near the functional groups, making them suitable sites for metal cation binding. It also showed that functionalization of the edges with one oxygen-containing group only did not change the electrostatic potential in the middle of the GNR greatly, suggesting that the strengthening of the binding of metal atoms in the center is due to through-space interactions with the functional groups.

The study confirms that functionalized GNRs are able to adsorb Na and Ca more strongly than graphene and therefore have greater potential capacity. Furthermore, the properties of the material can be tuned by changing the functional groups. Although our studies were on GNRs, for the binding strengths the GNRs would be representative of portions of r-GO where the material has a large defect. This therefore would help determine what type of functional groups would be desirable at the edges of r-GO for applications including electrode materials for NIBs and CIBs.

6.6 Acknowledgements

The authors thank the Australian Research Council for support of this project through the LIEF and DP programs (LE0882357, LE160100051 and DP140100193). This research was undertaken with the assistance of resources provided at the NCI National Facility systems at the Australian National University through the National Computational Merit Allocation Scheme supported by the Australian Government, support from the Queensland Cyber Infrastructure Foundation (QCIF), and the University of Queensland Research Computing Centre. It was also supported by resources provided by The Pawsey Supercomputing Centre with funding from the Australian Government and the Government of Western Australia. AFN also acknowledges support from the Australian Government through an Australian Government Research Training Program Scholarship (RTP). We also acknowledge helpful discussions with Dr Marlies Hankel.

Chapter 7

Adsorption of sodium, potassium, and calcium over nitrogen and oxygen functional groups in functionalised graphitic materials

7.1 Introduction

This chapter focuses on the effects of nitrogen and oxygen on the binding of metals. The selection of materials and metals studied was determined by experimental studies in terms of their performance as battery anodes.

We first present results for Na adsorption over nitrogen functional groups bound to graphitic and non-graphitic carbon atoms in graphene sheets. We carried out this study to understand why the binding of Na over a material that is comprised of nitrogen-rich hard carbon spheres (*N*-HCS) is enhanced, which led them to be considered an anode material for NIBs. Our collaborators, Gaddam, Kumar, and Zhao (GKZ), synthesised this material from mango pulp powder in 2017 (as described in [39]), and found it had a significant number of nitrogen-containing functional groups and performed well as an anode material. Therefore, it was interesting for us to study the binding of Na over graphene sheets with various nitrogen-containing functional groups that are likely to occur in the prepared material, *N*-HCS. We note that there might be some other nitrogen-containing functional groups that are not considered

here, which could further improve performance; nevertheless, we focus on those predicted to be present in the material experimentally. We have used DFT with a similar methodology to that described in Chapter 3 to understand which functional groups contributed to this improvement in performance. Overall, our results will be a guide for future experimental researchers to try increasing the proportion of groups that were helpful and decrease those that were not.

In the second part of this chapter, we undertake a DFT study on the adsorption of Na, K, and Ca over oxygen functional groups available in reduced graphene oxide (r-GO). We consider Na, K, and Ca for epoxide and hydroxyl groups bound to the basal plane of graphene and oxygen-doped graphene. For hydroxyl, carbonyl, and carboxyl groups at the edge of a graphene nanoribbon, we consider K in this chapter and compare results with those presented in Chapter 6 for Na and Ca adatoms. The current work was motivated by the work of our collaborators, GKZ, who synthesised this material by using specific chemical treatment methods, as described in sec. 7.2.1.

In the sections below, we describe the experimental work of GKZ to provide context to the calculations that we have carried out. However, it should be noted that no experiments were carried out as part of this thesis and the author did not contribute to the experimental work published in [39]. Nevertheless, the author did contribute to writing the paper, the interpretation of results, and he carried out all DFT calculations in [39].

7.2 Na binding over nitrogen-containing functional groups

7.2.1 Preparation of *N*-HCS

As reported in [39], GKZ synthesised *N*-HCS material from mango powder as a biomass through low-temperature pyrolysis and hydrothermal methods. They bought mango powder from an Australian shop, and they dissolved it in a solution of H_2SO_4 (>98%) and water. They hydrothermally treated the solution at 170 ˚C in an autoclave for 25 hours. Following separation and washing of the product, they treated it again in nitrogen gas at 900 ˚C for almost 2 hours. The sample was then oxidised by dissolving it in dilute solutions of H_2SO_4, $NaNO_3$, $KMnO_4$ (>99.0%) and H_2O_2 in consecutive steps. Then, these materials were used to introduce oxygen-containing groups and basal defects to the precursor. The prepared sample was comprised of hard carbon spheres (HCS) and chemically treated with ethylenediamine ($C_2H_8N_2$, >99%) to

introduce nitrogen-containing groups, such as amides to the precursor. They finally obtained the product, *N*-HCS, after washing it with methanol.

7.2.2 Material characterisation and nitrogen-containing functional groups

GKZ used X-ray diffraction (XRD), scanning transmission electron microscopy (STEM), field emission scanning electron microscopy (FESEM), X-ray photoelectron spectroscopy (XPS), and Raman spectroscopy methods to characterise different behaviour and morphology of the *N*-HCS. The characterisation led to identification of the structure and available functional groups in the product. For example, a high-resolution transmission electron microscopy (TEM) image of *N*-HCS displayed a graphitic microstructure with turbostratic[52] domains, typically observed in hard carbon materials. They showed *d*-spacing (interlayer distance) of 3.90 Å, which is larger than that of graphite (3.35 Å). The *d*-spacing of HCS (precursor) was recorded at 3.70 Å. Consequently, the observed difference verified the role of N groups in increasing the *d*-spacing, which is an important factor for Na intercalation.

The XPS spectra of HCS and *N*-HCS verified the existence of nitrogen and oxygen atoms. As depicted in Fig. 7.1, we observed strong peaks of oxygen, carbon and nitrogen groups in the blue curve for *N*-HCS in comparison with the green curves for HCS. The atomic weight percentage (at%) of N in *N*-HCS was recorded at 9.06%, whereas the oxygen and carbon percentage in HCS were 30.19% and 69.81%, respectively.

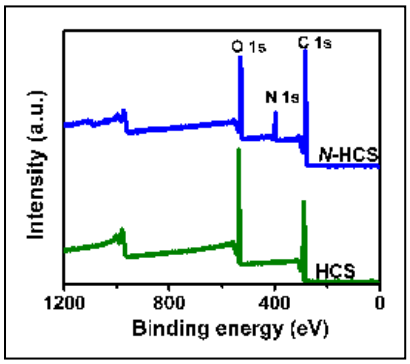

Fig. 7.1. XPS spectra of HCS (green) and *N*-HCS (blue) [53]

[52] Turbostratic structure implies that the carbon layers are arranged in a random way.
[53] Figs. 7.1 and 7.2 are taken from Gaddam et al. [39].

Fig. 7.2a depicts the XPS spectra (C 1s) of *N*-HCS. This figure indicates the presence of the nitrogen containing groups such as C-N, N-C=O, in addition to C-C (sp^2), C-C (sp^3), C-O-C, and C-OH. After deconvoluting the N peaks of this figure, GKZ obtained Fig. 7.2b, which depicts the high resolution XPS spectra of *N*-HCS for N groups (1s). This figure indicates the existence of N groups, such as graphitic N (Fig 7.3a), pyridinic N (Fig 7.3b), imine or amine (displayed by N-H in Fig 7.2b and shown in Fig 7.3c, d), amide (N-C=O) (Fig 7.3e), and pyrrolic N (Fig 7.3f). Therefore, we chose to consider these groups in our DFT study and to evaluate the Na binding strength over them.

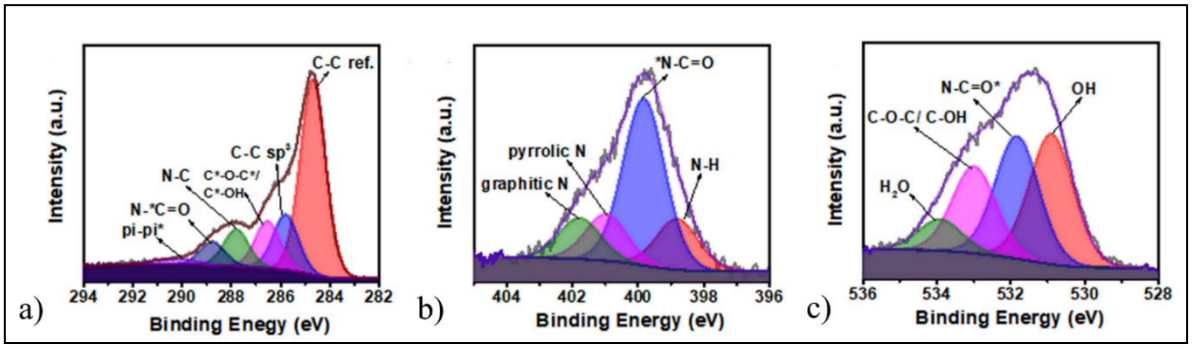

Fig. 7.2. XPS spectra of *N*-HCS, a) C (1s) focused, b) N (1s) focused and c) O (1s) focused [2]

We should note here that the XPS result of the HCS precursor indicated the existence of oxygen groups, such as OOC-C- or OOC- (ester or carboxyl), C-O-C (ether), C=O (carbonyl), N-C=O, and C-OH (hydroxyl). Similar groups were seen in the XPS result of *N*-HCS (Fig. 7.2c), although these oxygen groups were not the focus of the current study.

To simulate the effect of nitrogen functional groups interacting with Na atoms, we have considered the groups that could be present according to the XPS of Fig. 7.2b, and then optimised structures containing these via using DFT calculations with the VASP package. The first group is nitrogen doped within a graphene sheet or graphitic N (or quaternary N), as shown in Fig. 7.3a. Then, we considered a mono-vacancy (MV) within a graphene sheet and attached the N functional groups into that. These groups are pyridinic N, imine (-N-H), amine (-N-H_2), amide (-N-OH_2), and pyrrolic N (-N-H) (see Fig 7.3).

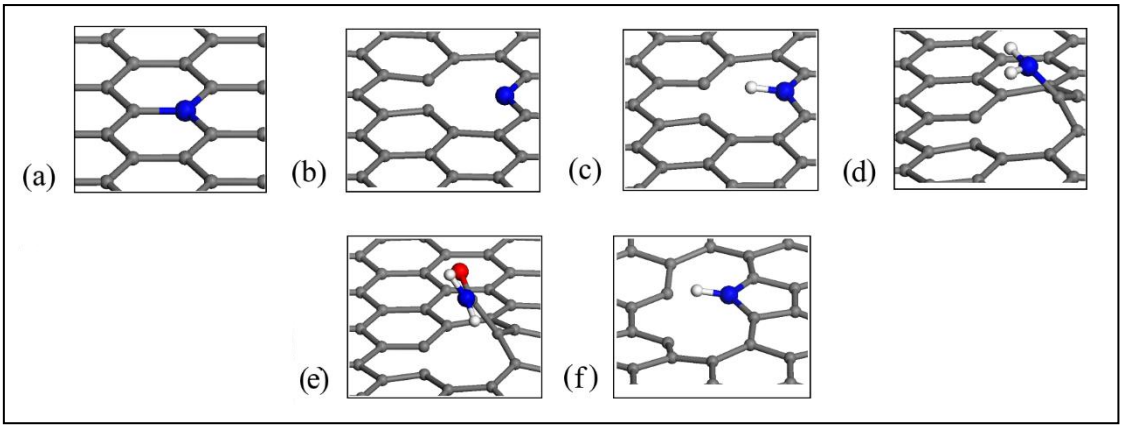

Fig. 7.3. Optimised structures of graphene sheets with a) graphitic N, b) pyridinic N, c) imine, d) amine, e) amide, and f) pyrrolic N group

7.2.3 Performance of the anode material, *N*-HCS

GKZ conducted some experimental tests to evaluate the performance of the HCS and *N*-HCS as materials for NIB anodes. The diffusion rate of the Na was determined from a cyclic voltammetry (CV) study. In this test, the voltage (*V*) varied from 0.005 to 3.0 V at a scan rate of 0.1 mV s^{-1}. The current (*I*, mA) of the material with adsorbed Na was measured, and using the current-voltage equation, $I=aV^b$, was fitted to the *I* and *V* data to obtain *a* and *b*. They found *b* for the *N*-HCS line was higher than that of HCS (0.79 vs 0.23), indicating a higher diffusion rate of Na within the *N*-HCS than HCS.

GKZ also carried out galvanostatic charge-discharge tests of the HCS and *N*-HCS materials in the voltage range of 0.005 to 3 V, with a current density at 20 mA g^{-1}. The very first cycles of *N*-HCS depicted a charge and discharge capacity of 445 and 1164 mA h g^{-1}, respectively. The difference gives the irreversible capacity, which is attributed to the formation of the solid electrolyte interface (SEI) and some irreversible chemical adsorption between Na and oxygen functional groups [39]. In the 1^{st} / 2^{nd} cycles, *N*-HCS and HCS delivered a specific discharge capacity of 1164/520 and 1036/380 mA h g^{-1}, respectively. Therefore, *N*-HCS showed a higher capacity retention from the 1^{st} to the 2^{nd} cycle compared with HCS, which could be attributed to the effect of N groups. However, the capacity stabilised after several cycles. For example, at a high current of 1 Ag^{-1}, *N*-HCS became stable over 1000 cycles with a capacity of 204 mA h g^{-1} [39], whereas the HCS anode electrode showed 113 mA h g^{-1} at the 1000^{th} cycle at the same current rate of 1 A g^{-1}. The capacity comparison verifies the superiority of *N*-HCS over HCS.

7.2.4 Adsorption of Na over the nitrogen-containing functional groups

To study the adsorption of Na over the N functional groups, we did a DFT study for the structures mentioned in sec. 7.2.2 (Fig. 7.3). The results of the study include the binding energy E_b of Na over the functional groups and the optimised structure of the adsorbed system. For these calculations, we considered the graphene base sheet as a 2D periodic system with a plane-wave basis set. The supercell lattice vector was 30 Å in the *z* direction to avoid interaction between the adjacent layers. We used generalised gradient approximation (GGA) with the projector-augmented wave (PAW) method and van der Waals' interaction as the DFT-D3 method of Grimme [64]. The Brillouin zone was sampled with 3×3×1 *k*-points using the Monkhorst–Pack scheme [193], and E_{cut} was set to 700 eV, the energy convergence criterion at 1×10^{-6} eV, and the force convergence criterion at 0.01 eV $Å^{-1}$.

The binding energies, E_b, and adsorption heights, h_{ad} (the distance of adatoms from the surface of carbon sheet) are depicted in Table 7.1 and Fig. 7.4. We have also indicated the distance of Na from the N atom.

Table 7.1. The binding energy (E_b) of Na adatoms over the eight N functional groups

Functional Group	**E_b, eV**	**Adsorption height, h_{ad} , Å**	**Distance of Na from N atom**
Pristine graphene	-0.763	2.22	NA
Graphitic N	-0.483	2.25	3.77
Pyridinic N	-2.281	2.25	2.36
Imine	-0.984	2.26	3.98
Amine	-1.608	3.04	2.35
Amide	-2.520	2.43	4.15 (from N) 2.13 (from O)
Pyrrolic N	H dissociated from N	NA	2.28

As shown in the first row of Table 7.1, the E_b of Na over a graphene sheet is weaker than the E_{coh} of the Na atoms at -1.113 eV [65], which renders the Na binding over graphene unfavourable [54]. Any E_b value lower than E_{coh} will be favourable and ensures that Na clustering

[54] This issue was discussed in sec. 2.1.2

is unlikely to occur. According to Table 7.1, the graphitic N weakened the binding of Na over the graphene sheet to a value of -0.483 eV. However, pyridinic N, amine, and amide strengthened the Na binding considerably to -2.28, -1.61 and -2.52 eV, respectively. These values are lower than the E_{coh} of Na, which renders the binding strong compared with the binding to graphene. Among these groups, the amide group has the strongest binding, which could be attributed to the existence of an oxygen atom in addition to nitrogen. We show in sec. 7.3 that oxygen-containing groups cause a strong binding of Na and Ca atoms.

Conversely, the imine group did not significantly improve the E_b, and it is weaker than the E_{coh}. The difference between this group and the pyridinic N group is the additional H atom attached to the N atom. The under-coordinated N atom in the pyridinic group binds more readily with Na than the imine group, which is saturated with an H atom. This is theoretically consistent with the strong Na binding to the mono-vacancy (MV), with an under-coordinated carbon atom [76]. As we discussed in Chapter 5, sec. 5.4.2, the E_b of Na over the MV was -2.08 eV, which is strong compared with binding over graphene.

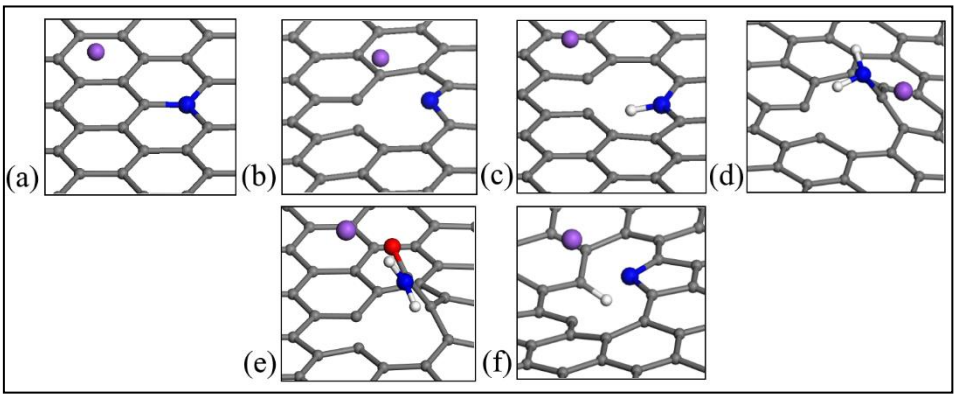

Fig. 7.4. Top views of the nitrogen and oxygen groups adsorbed with Na, a) graphitic (quaternary) N, b) pyridinic N, c) imine, d) amine, e) amide, and f) pyrrolic N

In the case of pyrrolic N, the H atom dissociated from the N atom and bound to a carbon atom around the vacancy as a result of Na adsorption, as shown in Fig. 7.4f. Therefore, we excluded this case from E_b measurement (in Table 7.1).

Overall, we found that nitrogen functional groups strengthened the binding of Na adatoms, which suggests that the presence of nitrogen functional groups is advantageous in rechargeable battery materials, such as the *N*-HCS materials considered in the experimental work described above.

7.3 Metals binding to the oxygen-containing functional groups in r-GO

In this section, we investigate the effect of oxygen-containing functional groups on graphene sheets on the binding strength of Na, K and Ca. In the first section, we investigate the adsorption of all the three atoms over O-containing groups in the graphene sheet. These groups are hydroxyl (HO-), epoxide (-C-O-C-), and we also consider the O-doped graphene sheet. In the next section, we specifically investigate the binding of K over the edge functional groups of HO-, O-, and HOOC-GNRs. The result of K adsorption is applicable in simulating the potassium ion battery (KIB), working with cellulose derivative material as the anode. GKZ conducted an experiment to investigate the innovative proposition of looking at KIBs with cellulose derivative material, and we briefly introduce the test they did and their results in sec. 7.4.

7.3.1 Adsorption of Na, K and Ca over oxygen-containing functional groups in a graphene sheet

As we mentioned in Chapter 2, sec. 2.5.1, there are various oxygen groups on the base and edge of r-GO. The number of these groups is considerably lower than the similar groups available in GO because of the chemical treatments following GO synthesis. These treatments include chemical reduction processes comprising annealing (varying from 700 to 1500 °C), chemical deoxygenation by $NaBH_4$, and dehydration by H_2SO_4. The most abundant groups in the r-GO sheet are hydroxyl and epoxide [46, 135-137]. For this purpose, we have optimised the structures of epoxide and several arrangements of hydroxyl groups in the graphene sheet. Fig. 7.5 depicts the optimised structures of epoxide (Fig. 7.5a), one hydroxyl (Fig. 7.5b), hydroxyl with one H atom bound to the neighbouring carbon atom (which we refer to as HO+1H, see Fig. 7.5c), and two hydroxyl groups on the either side of the sheet (which we refer to as 2HO, see Fig. 7.5d).

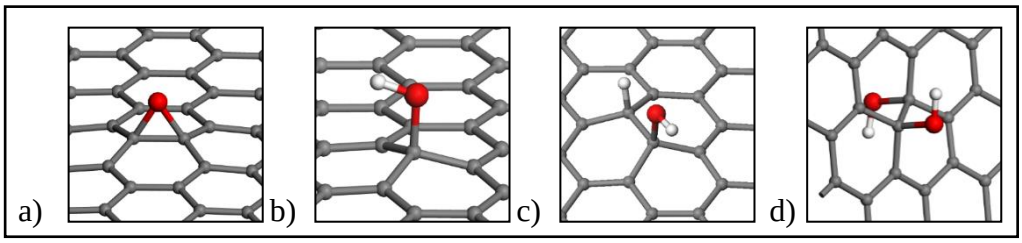

Fig. 7.5. Schematic views of a) epoxide group, b) hydroxyl group, c) hydroxyl group with one H atom bound to the neighbouring carbon atom (HO+1H), and d) 2 HO- groups on the either side of the sheet (2HO).

Fig. 7.5 depicts that epoxide and hydroxyl groups caused a basal carbon atom to move out of the sheet. Therefore, these groups became vulnerable to dissociation and formed MO or MOH, where M represents the metal atom. Table 7.2 presents the E_b for the most stable sites. When any dissociation occurred, we mentioned it directly. Moreover, Figs. 7.6 to 7.8 show the metal atoms adsorbed on materials with epoxide and hydroxyl groups, respectively.

Table 7.2. The result of binding of Na, K and Ca to epoxide and hydroxyl functional groups

Oxygen groups on the graphene sheet		E_b **, eV**		
		1 Na	1 K	1 Ca
Epoxide		-2.04	-2.33	-3.80
Hydroxyl	**No side H**	NaOH formation	KOH formation	Ca bound to OH
	Side H (HO+1H)	-1.44	-1.78	Ca bound to OH
	2 HO on two sides	-1.63	-2.01	Ca bound to OH

According to the results presented in Table 7.2, the epoxide group bound strongly with Na, K, and Ca, with binding energies of -2.04, -2.33 and -3.80 eV, respectively. However, as we see in Figs. 7.6a, b and c, the O atom detached from one of the carbon atoms and formed a single bond only with one carbon at distances of 1.41 and 1.47 Å. These distances are consistent with a C-O bond distance reported at 1.43 Å [67]. Therefore, these results (Figs. 7.6a to c) demonstrate the strong interaction between Na, K, and Ca with the O atom. Moon et al. reported an E_b of Na on top of the epoxide group of -1.02 eV. Moreover, they found that the O atom's binding with the two carbons remained intact after Na adsorption. They also reported Na distance from the O atom at 2.07 Å [141]. They used similar DFT methods to us[55], except they used a 5×5×1 *k*-points mesh and a graphene supercell of 4×4 hexagonal rings. We therefore considered a similar structure to that of Moon et al. in our the DFT calculations and obtained a similar E_b of -1.22 eV, equal distances of O from both carbon atoms, and Na atom on top of O atom, with 2.10 Å distance. This is therefore a local minimum and it could be expected that if Moon et al. considered a similar structure that we found, they would also find a lower energy structure. For Ca (Fig. 7.6c), the interaction between Ca and O was strong, with high E_b of

[55] Similar methods in terms of PAW, PBE, GGA and VASP package (Chapter 3, sec. 3.3.3, 3.4 and Appendix 2C).

-3.80 eV. However, we observed that Ca dissociated O from the sheet and made a bond with Ca to form CaO, as seen in Fig. 7.6d.

Interaction of the sodium atoms with one hydroxyl groups on graphene (Fig. 7.5 b) resulted in a NaOH formation, as seen in Fig. 7.7a. Moon et al. [141] and Dobrota et al. [82] achieved similar results in terms of HO- dissociation in contact with Na atom. Formation of such structures (NaOH) is likely to be detrimental to the performance of an anode material in rechargeable batteries and should be avoided. However, Na bound weakly to the other two hydroxyl groups types of HO+1H and 2HO on the two sides (Figs. 7.5c and d), with E_b of -1.44 and -1.63 eV, respectively (see Fig. 7.8a for Na over HO+1H). Likewise, Dobrota et al. [82] achieved similar results for Na adsorption on 2HO (Fig. 7.5d) with E_b of -1.62 eV, in which the structure of two HO- on the two sides of the sheet remained intact. Nonetheless, they used Quantum Espresso package with USPP [56] and DFT-D2 for vdW model [57], which would lead to some differences. We should note here that we considered some other cases for Na binding over HO+1H and 2HO structure (Figs. 7.5 c and d) with different initial configurations.

For some initial configurations, HO+1H was totally dissociated from the sheet and formed a H_2O molecule, as depicted in Fig. 7.8d, or NaOH formation in case of Na contact with 2HO structure (see Table 7.2). Therefore, the formation of NaOH is possible depending on the situation of Na toward the HO- group.

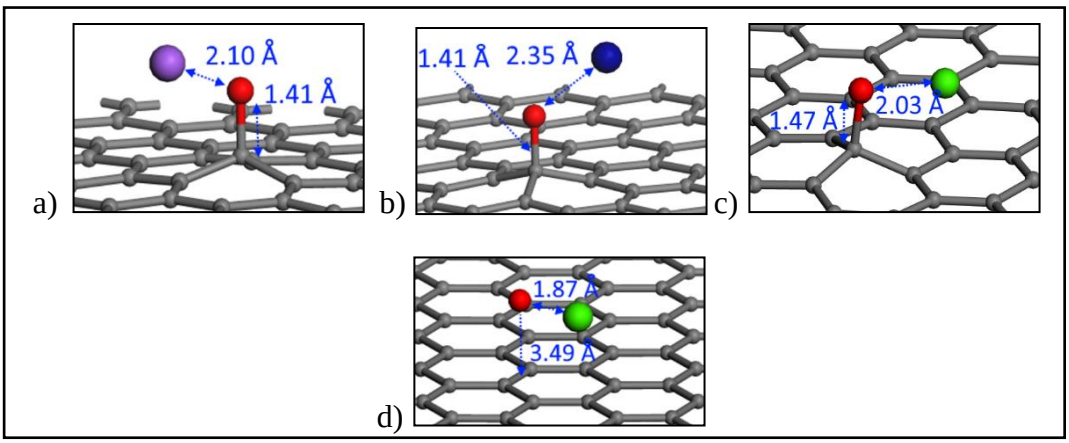

Fig. 7.6. Perspective views of a) Na, b) K, and Ca adsorbed by the epoxide group: c) without O dissociation and d) with O dissociation. The figures also show the distance between the O and the sheet, and the O and metal atom.

[56] Ultra soft pseudopotentials were described in sec. 3.5.1
[57] For vdW models, refer to sec. 3.3.5

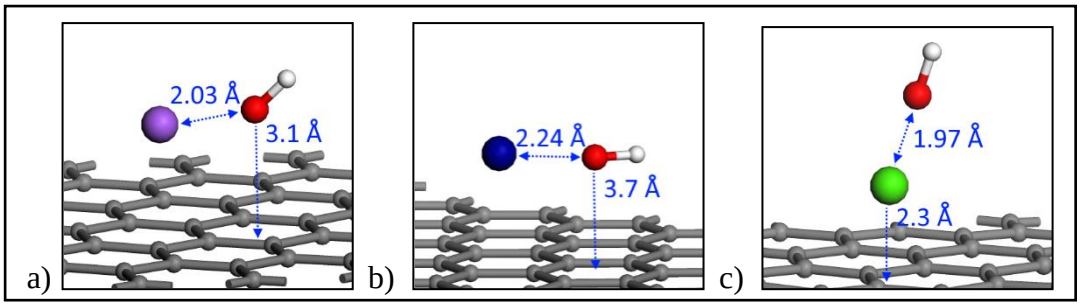

Fig. 7.7. Perspective views of a) Na, b) K and c) Ca in binding with hydroxyl group (HO-). The figures also indicate the distance between the O and the sheet, and between the O and the metal atom. The purple, dark blue and green atoms are Na, K and Ca atoms, respectively. Moreover, red adatoms are oxygen, and white are hydrogen atoms.

Regarding the interaction of Ca, it was found that Ca bound to OH in all the three structures of hydroxyl, HO+1H and 2HO (Figs. 7.5b, c and d). As seen in Fig. 7.8c, Ca dissociated only HO- from the sheet and bound to it with a high distance of 4.4 Å between the O atom and the sheet. However, KOH formed in only one case of one hydroxyl group on graphene, as seen in Fig. 7.7b. In the other cases of K over HO+1H and 2HO structures (Table 7.2), K showed a strong binding of -1.78 and -2.01 eV without showing any dissociation from the sheet. These bindings are obviously far stronger than the E_{coh} of K at -0.93 eV, and these differences are likely to be due to the much stronger binding of K to the graphene than Na and Ca.

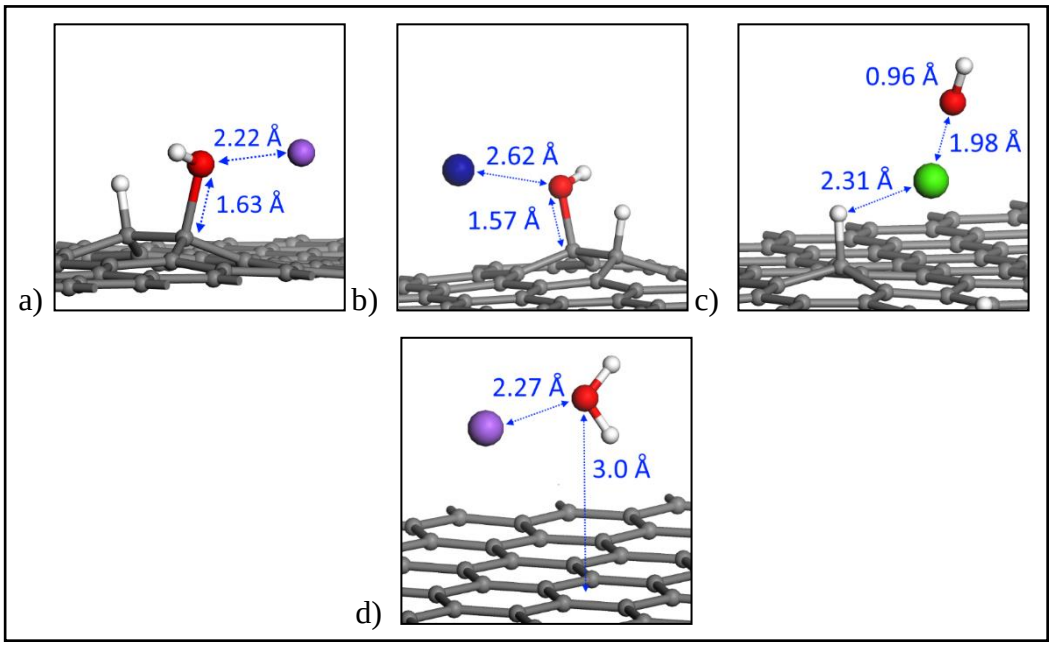

Fig. 7.8. Perspective views of a and b) Na, c) K, and d) Ca in binding with the hydroxyl group and 1 H atom bound to the neighbouring carbon atom (HO+1H). In (b) Na dissociated the total HO+1H from the sheet and formed H_2O molecule. The figures also indicate the distance between the O and the sheet, and between the O and the metal atom. The purple, dark purple and green atoms are Na, K and Ca atoms, respectively. The red atoms are oxygen and the white are hydrogen atoms.

Overall, we observe that Ca does not adsorb on the basal plane of r-GO having a single oxygen group such as epoxide and hydroxyl, as it binds to the O or OH group in most cases. Nonetheless, in real situations there are many oxygen-containing functional groups on the basal plane of GO. Therefore, Ca as a multivalent metal has the chance to make bonds with these groups at the same time. For example, Park et al. [207] verified that Mg and Ca bound with several oxygen groups on the two parallel layers of GO. These bindings increased the mechanical resistance of GO sheets against tensile strain. On the other hand, K as a single-valent alkali metal can be a good candidate for binding over r-GO because it did not show the formation of KOH in most of the cases.

7.3.2 Oxygen and hydrogen atoms in a mono-vacancy

We have also considered another structure containing oxygen and that is O doped within a graphene sheet having a mono-vacancy (MV). This structure is likely to occur in the r-GO in addition to epoxide and hydroxyl groups [82]. Figs. 7.9a and b depict the optimised structure of this group.

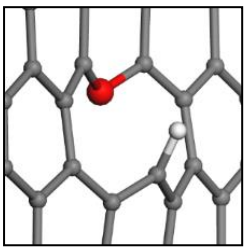

Fig. 7.9. Most stable structures of O doped graphene sheet having a MV. The red atom is oxygen and the white is a hydrogen atom.

This structure (Fig. 7.9) has an O atom made of two bonds with the two nearby carbon atoms in the MV, which can be considered an ether group in terms of O bonding with C atoms. Moreover, the H atom bound with the under-coordinated carbon atom in the MV to saturate it. This structure is also consistent with a similar structure, depicted by Dobrota et al. [82]. To see the adsorption of Na, K, and Ca atom over the mentioned structure, we first tested Na adsorption above the O atom. We depicted the structure of Na binding at the most stable site in Fig. 7.10.

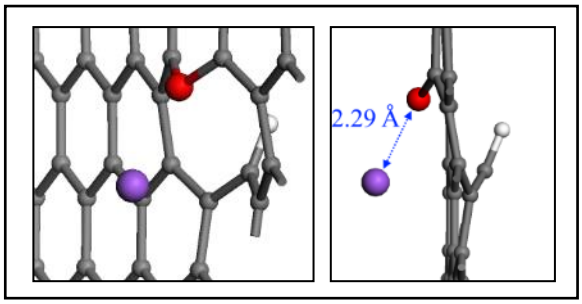

Fig. 7.10. Top and side views of Na binding to the O-doped graphene sheet. The red atom is oxygen, white is hydrogen, and purple is a sodium atom.

We found the E_b of Na at -1.67 eV, which indicates stronger binding than the E_{coh} of Na (-1.113 eV). The structure of this binding is shown in Fig. 7.10. The distance between Na and O is consistent with similar values shown in Figs. 7.7a and 7.8a, and also Dobrota et al.'s value for a similar system, reported at 2.37 Å [82]. We completed similar calculations, including -2.14 and -2.04 eV, for Ca and K binding over the O-doped graphene sheet. These indicate stronger binding than E_{coh} of K and Ca. Overall, the O-doped graphene (within a MV) would bind suitably with any of the three metal atoms.

7.4 Adsorption of K over F-GNRs

In this section, we investigate the adsorption of K over the edge and base of the functionalised edge of graphene nanoribbons (F-GNRs) with oxygen-containing functional groups. GKZ completed an experiment for adsorption of K over cellulose derivative material that was intended as an anode material for KIBs. Although they have not yet published their work, we complete a summary of their work in terms of material preparation and characterisation results in section 7.4.1. In sections 7.4.2 and 7.4.3, we present the results of DFT calculations for evaluating the performance of oxygen-containing functional groups in adsorbing K atoms and determine which groups have the greatest potential for improving the anode material performance according to these results. We expect that, as for Na and Ca, K will show a strong binding over the selected oxygen-containing functional groups. We carried out the binding evaluation of K over the oxygen groups in the base of graphene sheet in the previous sections and proposed suitable groups. Thus, combined with the results in the following section, we complete our evaluation of K binding over a wide range of possible oxygen-containing functional groups.

7.4.1 Cellulose derivative material as anode of KIB

A sample of cellulose in a quartz boat was placed in a tube furnace. The material was heated at 250ºC for about two hours in an argon atmosphere. GKZ then carried out carbonisation treatment at temperatures of 1000, 1300 and 1400 ºC for 2 hours in an argon atmosphere. The carbon obtained was used as an anode for a KIB.

XPS spectroscopy characterisation was carried out at each temperature. The results show that HO-, C=O (carbonyl), and C-O groups are the most abundant oxygen-containing functional groups in the precursor. The atomic concentration of oxygen was determined to be 1.36% compared with the carbon concentration at 98.64% from the full XPS for the sample heated at 1300 °C. To find the role of oxygen groups in adatoms in adsorbing K adatoms, we have undertaken a variety of calculations. We presented the results of K binding over oxygen containing groups in the graphene sheet in the previous sections (sec. 7.3.1 and 7.3.2). We saw that while K was found to have an E_b of -1.26 eV over the graphene sheet, it bound more strongly over oxygen containing groups, such as epoxide (E_b = -2.33 eV), hydroxyl (E_b = -1.78, and -2.01 eV), and ether in the graphene sheet (E_b = -2.04 eV). In the next section, we present the results of K binding to the edge (periphery) oxygen functional groups.

7.4.2 Adsorption of K over oxygen-containing functional groups at the edges of GNRs

We introduced oxygen-containing functional groups at the edge sites in Chapter 6 (sec. 6.4.2 to 6.4.4) when considering the adsorption of Na and Ca over those oxygen groups at the edge of GNRs. Moreover, we saw that both hydrogen and oxygen groups adsorbed Na and Ca at the base and the edge of GNRs more strongly than graphene. Table 7.3 shows the results of K binding at the most stable sites over the oxygen-containing functional groups of hydroxyl, carbonyl, and carboxyl.

Moreover, Fig. 7.11a to f show the top and side views of one K adatom binding to the most stable sites of the F-GNRs mentioned in Table 7.3.

Table 7.3. Binding of K over oxygen functional groups at the edge of GNRs

Functional group at the edge	**E_b , eV**				
	1 K	2 K	3 K	4 K	5 K
HO – ZGNR	-1.75	-1.62	-1.65	-1.13	-1.33
HO – AGNR	-1.55		ND*		
O – ZGNR	-1.95		ND*		
O – AGNR	-2.32	-1.95	-1.67	-1.47	-1.46
HOOC – ZGNR	-2.66		ND*		
HOOC – AGNR	-3.13		ND*		

*: Not Done because, for HO-Z/AGNRs and O-Z/AGNRs the binding of one K is not sensitive to the GNR type (zigzag or armchair), and for HOOC-Z/AGNRs the binding of one K is very high.

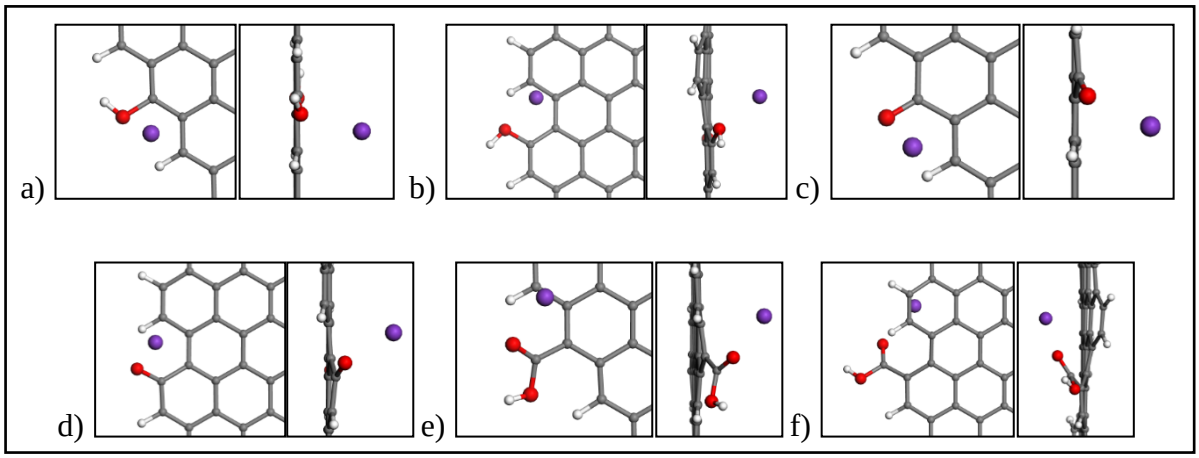

Fig. 7.11. Top and side views of one K adatom over a) HO-ZGNR, b) HO-AGNR, c) O-ZGNR, d) O-AGNR, e) HOOC-ZGNR, and f) HOOC-AGNR

As shown in Table 7.3, the binding energies vary between -1.55 to -3.13 eV, although they are all more negative than the E_b of K over G (-1.26 eV). If we consider -1.0 eV on top of the E_{coh} of K to be -1.93 eV, it can be considered a suitable value for K binding over anode material [84]. Using this criterion, we observe that whereas HO- and O- groups provided acceptable binding for K, and carboxyl groups caused bindings that were too strong, which could potentially lead to ionic bonds. In a similar way, we saw this strong attraction of carboxyl group against Na and Ca atoms in sec. 6.4.2 and graphs in Figs. 6.6 and 6.7. According to those graphs, carboxyl groups (HOOC-AGNR) caused stronger binding than the carbonyl group (O-AGNR), especially in adsorbing Ca adatoms for about 0.3 eV. However, carboxyl groups did not cause very strong binding for Na and Ca in comparison to their E_{coh} energies. According to Tables 5A.1 and 5A.2, the differences were -0.98 for Na and -1.25 for Ca, which are not high.

Therefore, these results suggest HOOC- GNRs could be a suitable option for reversible Na and Ca binding, but not K.

In all cases of Na, K and Ca, we see that HO-Z/AGNR caused a weaker binding than O- and HOOC- groups. However, the E_b of K over HO- groups (Table 7.3) is still stronger than E_{coh} of K (-0.934 eV), with differences of 0.62 to 0.82 eV. In a similar way for K over O-Z/AGNRs, this difference varies between 1.0 and 1.4 eV. According to Fig. 7.11, the distance of K from the closest O atom varies between 2.4 to 2.8 Å, which is also consistent with the similar distance in the epoxide and hydroxyl groups, as shown in Figs. 7.6 and 7.8. By contrast, the K adatom is closer to the O=C group in the carboxyl group (the O atom that is not bound to the H). This is similar to that observed for Na and Ca binding over a carboxyl group, as shown in Fig. 6.8. However, in those cases, the distance of Na and Ca adatoms from the O atom was about 2.2 Å.

Overall, our calculations suggest HO- and O- groups at the edge of the GNRs would provide sites for binding of K adatoms, with binding energies that would make them applicable for anodes of KIBs.

7.4.3 Adsorption of several K adatoms over HO-ZGNR and O-AGNR

Having observed single K adatom adsorption over HO- and O- groups in the previous section, we analyse the result of multi adatom adsorption over these groups in this section. We should note that we did not do the multi adatom adsorption over HOOC-Z/AGNR (denoted by ND in Table 7.3), because the single atom binding was high, as we mentioned in the previous section. According to Table 7.3, the average E_b of K adatoms extends to -1.33 for 5 K atoms, which indicates weaker interactions than E_{coh} of K. Therefore, we can say that these groups are able to adsorb several K adatoms around them. Moreover, Fig. 7.12 depicts the results of these multi adatom binding (for 4 and 5 adatoms only).

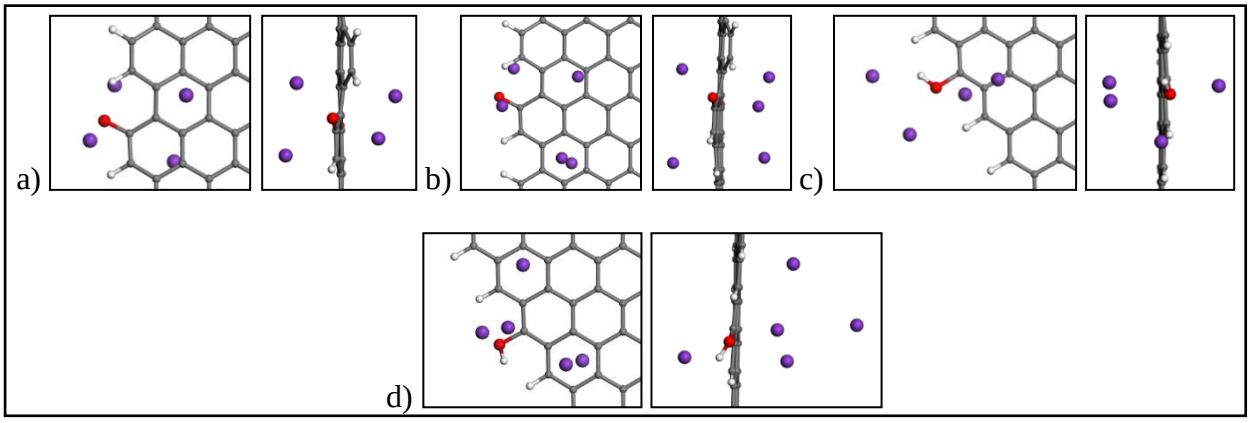

Fig. 7.12. Adsorption of 4 and 5 K adatoms around a and b) O-AGNR, c and d) HO-ZGNR

According to the Fig. 7.12, we observe that by increasing the number of K adatoms from 4 to 5, they become more spread throughout the GNR plane. This is particularly evident in Fig. 7.13d, where the adatoms became more spread, and some are elevated from the sheet. We note that these are typical configurations and are very dependent on the initial arrangement of the K adatoms, but it was not computationally feasible to fully optimise these structures. One reason that the K atoms bind far from the O-group is because K also binds strongly over a hexagonal ring of graphene (E_b = -1.26 eV). Compared with the E_b of 4 and 5 K adatoms (Table 7.3), we can say that that this fairly strong E_b (-1.26) had an important role in attracting the K adatoms toward the GNR plane. There is little difference between the E_b of K over hexagonal ring and binding of multiple K atoms over the edge of F-GNRs (Table 7.3). Therefore, this result indicates that the oxygen groups are not enhancing the binding of additional K adatoms.

Compared with the binding of multiple Na and Ca atoms over the F-GNRs (chapter 6, sec. 6.4.5, Fig. 6.13, and Tables 5A.1 and 5A.2), we saw that Na and Ca adatoms were closer to the functional groups (O- and HOOC-) than to the GNR sheet. This was mainly because Na and Ca bind more strongly over the O functional groups compared with hexagonal rings (-0.76 for Na and -0.82 eV for Ca). Therefore, the effect of oxygen functional groups was more significant in binding multiple Na and Ca atoms than K atoms.

7.5 Conclusion

DFT calculations on the binding of Na atoms to the nitrogen-doped graphene and graphene with nitrogen-containing functional groups showed that pyridinic N and groups, such as amines and amides, bound to Na with binding energies stronger than the Na cohesive energy. These selected nitrogen groups were groups that were likely to be found in the *N*-HCS material obtained from mango pulp that was experimentally demonstrated to be a good anode for the NIB. The calculations therefore suggest that the reason for the improved performance of *N*-HCS as an anode material could be due to the presence of these groups. Therefore, it can be a guide for experimental researchers to increase the portion of these groups in their proposed material and decrease the others that did not improve the binding of Na.

We also considered the ability of oxygen-containing functional groups in r-GO to adsorb Na, K, and Ca atoms. According to our results, the epoxide group bound Na, K, and Ca strongly, with E_b of -2.0, -2.3 and -3.8 respectively. In Ca adsorption over hydroxyl groups on the graphene sheets, Ca bound to OH formed in all cases due to the high charge of Ca as a

multivalent metal. K did not show KOH formation except when there was just one hydroxyl group over the basal plane. Therefore, K showed a better performance than Na and Ca in adsorbing over the oxygen-containing functional groups on the basal plane of the graphene. On the other hand, O-doped graphene (with a MV) bound all the metal adatoms with binding energies ranging from -1.67 to -2.14 eV. According to these calculations, K binds more strongly with r-GO than Na for the considered functional groups.

Furthermore, we considered the binding of K adatom to HO-, O-, and HOOC-GNRs and found that HO- and O-GNRs bound with K with energies that would seem suitable for use in rechargeable batteries. We did this study to investigate the effect of oxygen-containing functional groups available in the cellulose derivative material in adsorbing K atoms. HOOC functional groups on GNRs bound the K very strongly, which might render it problematic for rechargeable battery applications. It was possible to increase the number of K adatoms to 4 and 5 around the O groups at the edge while keeping the binding stronger than the cohesive energy, although we observed that some of the K were located away from the edge. This is because the binding of K on the graphene sheet is stronger than the cohesive energy. This result indicated that K strongly bound to the oxygen functional groups at the edge of GNRs more strongly than the graphene material, making KIBs an interesting area for further research.

Chapter 8

Conclusion

8.1 Overview of the results

In this thesis, graphdiyne (GDY), hydrogenated defective graphene (H-DG), functionalised graphene nanoribbons (F-GNRs), nitrogen rich hard carbon spheres (*N*-HCS) and reduced graphene oxide (r-GO) were considered as materials for alkali and alkaline earth metal ion rechargeable batteries. The charge transfer agents considered in our projects were Na, K, and Ca, although not all of them were tested for each of the proposed anode materials. In this chapter, we summarise the prominent results from the thesis. We also consider potential extensions of this work based on the results that we obtained, and we propose several topics for future studies.

8.2 Prominent results related to GDY as an anode material for NIB

In Chapter 4, we thoroughly investigated the adsorption and intercalation of Na adatoms over GDY by using DFT. Research had confirmed that Li could bind with GDY and it had been demonstrated to be suitable for use in rechargeable battery applications, both theoretically [27,

116] or experimentally [29]. Na has a larger atomic radius than Li (about 22% larger) and because of this, graphite cannot be used in NIBs. Therefore, we were interested in Na adsorption over GDY, because it has larger in-plane pores than graphene (area of 36 $Å^2$). So, if GDY can accommodate Na, it is considered to be an advantage for Na binding.

According to our results, GDY could suitably adsorb Na over the hexagonal rings and each corner of the triangular pores (Fig. 4.3), with binding energies of 1.32 eV on average (Table 4.1). However, we should note that the centre of the pores was the most stable place for Na settlement, with E_b of -2.53 eV. The maximum capacity of GDY for Na adsorption was found at Na_7C_{18} or $NaC_{2.57}$ on a single layer of GDY. This is equivalent to 497 mA h g^{-1}.

According to our bulk calculations for the layered materials of GDY, up to 7 Na could bind in-between the two stacked layers of GDY without any expansion of the layers, equivalent to $NaC_{5.14}$ and a capacity of 316 mA h g^{-1}. After allowing for expansion of the bulk layers, we achieved arrangement of $NaC_{2.57}$ with capacity of 497 mA h g^{-1} and 28% expansion of interlayer spacing. Finally, we calculated the energy barriers for transitions of Na between different sites in the GDY bulk layers. The results indicated that Na atoms would readily diffuse through the centre of slit pores of layered GDY (with AB-2 stacking), with only 0.0287 eV barrier of energy. Moreover, in AB-2 stacking, Na came up with the maximum barriers of 0.12 eV for out-plane movement (through the slit pore) and 0.84 eV for in-plane movement (through overlaid chians). For AB-3 stacking, these values were, at most, 0.68 eV and 0.40 eV, respectively. Indeed, these mentioned barriers of energy were not high, rendering the movement of the Na throughout the GDY bulk layers fairly easy; likewise, Li movement [27, 28]. The results are comparable with the experimental tests of Li on GDY, conducted by Huang et al. with capacity of 520 mA h g^{-1} [29]. At a similar time to our theoretical work, experimental results for Na on GDY by Zhang et al. [78] showed a capacity of 261 mA h g^{-1}.

In conclusion, we found that GDY with large pores is not only capable of accommodating a number of Na adatoms over its slit pores, but it also provides a pathway for Na atoms to pass through the slit pores with a minimum barrier of energy. It is therefore a useful material for experimental researchers to consider in further research and for development of new and affordable syntheses, so that it can be used more widely as an anode material for NIBs.

8.3 Prominent results related to 4(H1-MVG) as an anode material for NIB and CIB

In Chapter 5, we thoroughly investigated the structure of vacancies in graphene sheets, with and without hydrogen, on the binding of Na atoms. These vacancies in the graphene sheet were mono (MV), di (DV), tri (TV), quad (QV), and 24 (24VG). It was found that the binding energies of Na metal atoms over vacancies were very large, especially for those vacancies that had an under-coordinated carbon atom. This could make the desorption process difficult. The binding energies E_b varied from -2.08 eV for 1 Na over MV to -2.91 eV for 1 Na over 24VG. Moreover, materials with under-coordinated carbon atoms are likely to result in the linking of the adjacent layers, which would diminish the battery's performance. By contrast, Na bound less strongly to the hydrogenated vacancies, with E_b varying from -1.48 eV for H1-MVG to -0.84 eV for H12-24VG. Owing to the weaker binding of Na over H1-MVG (-1.48 eV), this was slightly lower than E_{coh} of Na (-1.11 eV), which made the desorption process easier. Therefore, we proposed that H1-MVG could potentially be a suitable option for the anode material.

Eventually, we selected a material with 4 repetitions of a H1-MVG in a supercell of graphene sheet, which we refer to as 4(H1-MVG) or $C_{68}H_4$, which has apical C-H bonds in the four sites. This resulted in an increase in the spacing between layers compared with graphite, in addition to the enhanced binding of both Na and Ca compared with pristine graphene. In terms of single layer binding, Na bound with a binding energy of -1.67 eV and Ca with -2.76 eV at the most stable sites. However, Na showed very weak binding at the two selected sites in the bulk layered materials: -0.65 and -0.30 eV, respectively. By contrast, Ca showed suitable binding values of -2.05 and -2.79 eV at the two similar sites. Using a Bader charge analysis, we attributed this phenomenon to the lack of charge for Na and more charge of Ca to transfer across the layers. The bulk materials of 4(H1-MVG) provided a maximum capacity of 16 Ca within each AA stacked layer. The E_b values varied from -3.64 eV for 2 Ca to -2.84 eV for 32 atoms on the two stacked layers. The corresponding expansion of the stacked layers after Ca intercalation varied from 6.6% to 31.0%. The maximum capacity was equivalent to $C_{68}H_4Ca_{16}$ or 591.2 mA h g^{-1} electrical capacity, which was comparable with experimental results for NIBs, with hydrogenated graphene reported at 300 mA h g^{-1} by Yoon et l. and 491 mA h g^{-1} by Pramudita [44, 74]. This expansion was mainly due to the apical C-H bond that acts as a side arm to expand the layers and enables intercalation.

In conclusion, 4(H1-MVG) material is not only capable of adsorbing up to 16 Na adatoms over its layers, but it also intercalates up to 16 Ca adatoms in between the bulk layers, with a capacity of 591.2 mA h g^{-1} and 31.0% expansion of the layers. Therefore, it would be of interest for experimental researchers to investigate a synthesis of hydrogenated defective graphene with a structure similar to 4(H1-MVG), which could be beneficial for anode of NIB and CIB.

8.4 Prominent results related to oxygen-containing functional groups at the edge of graphene nanoribbons (F-GNRs) for NIBs and CIBs

In Chapter 6, we simulated the edge structure of the r-GO, which had a number of oxygen-containing functional groups to adsorb Na and Ca metal adatoms. This could be applicable in anode materials of rechargeable batteries[47, 48]. We obtained the optimised structure of zigzag and armchair nanoribbons (Z/AGNRs) with different oxygen-containing functional groups at the edge. These groups were HO-, O-, and HOOC-, and these were selected because they are commonly observed in the r-GO structure. We found that O- and HOOC- groups bound the metal atoms with E_b of -2.08 and -2.09 eV for Na, and -2.83 and -3.09 eV for Ca, respectively. These values correspond to excess energy of -1.0 eV for Na and -1.25 eV for Ca, compared with their corresponding E_{coh} values. These strong bindings were mainly caused by the carbonyl group at the edge. The other group of HO- and also H- (only hydrogen passivated the edge) improved binding of Na and Ca compared with graphene by almost 0.41 eV for Na and 0.77 eV for Ca, although they could not increase the binding strength more than the E_{coh} of Na and Ca. This improvement could be attributed to the general morphology of the nanoribbons as well as the effect of the functional groups. Furthermore, O- and HOOC- groups adsorbed as many as 5 adatoms around; although the average E_b values were close to the E_{coh} of Na and Ca metal atoms. Moreover, we found that for a suitable anode material, the concentration of O- or HOOC- groups at the edge should not be so high that it renders the binding of Na and Ca too strong, because this makes the desorption process difficult.

In summary, the functionalised edge of GNRs, similar to the edge sites of r-GO that possess a number of oxygen-containing functional groups, constitute suitable sites for adsorbing Na and Ca adatoms with strong binding. This is applicable in anode materials for NIB and CIB.

8.5 Prominent results related to the adsorption of sodium, potassium, and calcium over nitrogen and oxygen functional groups in functionalised graphitic materials

In the first part of Chapter 7, we examined the adsorption of Na over the nitrogen containing functional groups in a graphene sheet. We did this as a theoretical DFT study for the *N*-HCS material used as an anode material for NIB [39]. Our experimental collaborators, GKZ, obtained this material from mango pulp by doing some chemical treatments, described in sec. 7.1. According to our results, Na bound strongly to amide and pyridinic N groups, with an E_b of -2.52 and -2.28 eV, respectively. Na bound to the amine group with an E_b of -1.61 eV, which is fairly strong in comparison with E_{coh} of Na (-1.113 eV). This result indicated that the nitrogen functional groups considered are capable of improving the binding of Na adatoms applicable in rechargeable battery materials, such as *N*-HCS in this study. Therefore, this can be a guide for the experimental researchers in this field to increase the portion of the groups that caused strong binding and decrease those groups that have binding that is too weak.

In the second part of this chapter, we carried out a DFT study to evaluate the binding of Na, Ca, and K over the oxygen groups in the basal plane of a graphene sheet. The oxygen groups studied were epoxide and hydroxyl in the basal plane because they are abundant in the r-GO basal plane. According to the results, Ca detached hydroxyl groups from the base and bound to them. However, K showed a strong binding with both epoxide and hydroxyl, with E_b that varied from -1.78 to -2.33 eV, which is far stronger than E_{coh} of K (-0.93 eV). Na showed fair binding with hydroxyl groups (-1.44 and -1.63 eV), although it showed hydroxyl dissociation of formation of NaOH in some cases. Even though in real r-GO there are a number of hydroxyl and epoxide groups in the neighbourhood, and dissociation may not occur easily, our findings can serve as a guide for experimental researchers using r-GO as a battery material.

Finally, in the third part of this chapter we investigated the adsorption of K over the oxygen containing functional groups at the edge of GNRs. This was a similar study to that which we did in Chapter 6 for Na and Ca, but in section 7.3, the metal was K. The results indicated that whereas HO- and O-GNRs bounded K with E_b values ranging from -1.55 to -2.32 eV, HOOC-GNRs caused very strong binding for K with E_b of -3.13 eV. Overall, K showed an increasing strength of binding beginning with HO- to O- and ending with HOOC-. In terms of multi K adsorption, up to 5 K adatoms bound around the oxygen groups at the edge, with bindings stronger than the E_{coh} of K. Some of the K atoms were located away from the edge on the

hexagonal rings of the GNR sheet, which was attributed to the fairly strong binding of K over the hexagonal rings of graphene. Overall, this result indicated that K showed a strong binding over those mentioned oxygen functional groups at the edge of GNRs. Therefore, they are suitable sites for K adsorption, which are applicable for rechargeable batteries.

8.6 Proposals for the anode design and scope of research in the future

Having presented the four types of anode materials for the rechargeable ion batteries, we present a brief proposition for the selection of anode materials for the commercial ion batteries. Based on our result, GDY can be a good candidate for NIBs with a high capacity of 497 mA h g^{-1} based on our result in Chapter 4, or 261 mA h g^{-1} based on Zhang et al's result [78]; however, the main challenge of GDY is the high cost of chemical synthesis due to its atomic unique structure, which affects the price of the battery. So we consider the other three proposed materials: 4(H1-MVG), F-GNRs, and nitrogen/oxygen functionalized graphitic carbon materials. The 4(H1-MVG) material can be also expensive to synthesis, since it can be potentially prepared by Hummers method [44], electron beams radiation or Ar^+ bombardment, all followed by hydrogenation [30, 31]. However, it can be easily done in research laboratories by means of suitable instrumentations and the trends seen for this material are expected for other hydrogenated carbon materials containing small pores. The other proposed materials in this thesis, F-GNRs simulating the r-GO and nitrogen/oxygen functionalized graphitic carbon can be even cheaper to produce through their corresponding synthesis methods as described in the sections 2.5.1, 7.2.1 and 7.4.1, respectively. In reality they are synthesized from their raw materials such as graphite, mango pulp and cellulose materials, respectively, as they are abundant in nature.

After carrying out a review of recent publications in the field of new materials for rechargeable batteries, we propose the use of the following items for future studies, based on the properties of the materials we have observed in this thesis. Many carbonaceous or non-carbonaceous materials have been proposed for batteries and other applications. We selected these because they are continuations of our topics in this thesis:

- Graphyne (GY) is a similar material to GDY, but with smaller pores (having two carbon atoms in each chain). It has been synthesised recently [225], studied for lithium ion batteries [27, 117], and partially for sodium ion batteries [77]. However, it would be of interest to continue study of this material for NIB, KIB and CIB.

- Doping has been shown to be effective in enhancing binding. We suggest that a systematic study of different kinds of doping within the graphene sheet could identify how to improve the binding of Na, K, and Ca. This would build on works on NIB or LIBs with nitrogen doping within carbonaceous material [38, 83, 154], graphitic carbon nitride [40, 41], and could consider even phosphorus, sulphur or fluorine doping to the graphene sheet [211, 226, 227].
- Magnesium (Mg) can also be considered as another multivalent alkaline earth metal for rechargeable batteries, because there is much room for studies on this metal [7, 99].
- There is much room for computational studies on non-carbonaceous materials for rechargeable batteries. Such materials as phosphorene for NIB [228-230], or a complex composite of $Na_{0.66}$ $[Li_{0.22}Ti_{0.78}]$ O_2 as anode materials for NIB [85] seem to have excellent potential.
- From the results we obtained on graphene oxide, it would be interesting to extend the calculations to consider their suitability for different applications, such water purification or desalination, in adsorbing available metal ions in the water (Ca^{2+}, Fe^{2+}, Mg^{2+}, Cd^{2+}, etc.) [231-234] and also as a strain-resistant material for mechanical applications [207, 222].

Bibliography

[1] Crompton TR. *Battery reference book*. 3rd ed. Oxford, England ; Boston: Oxford; **2000**.
[2] Blackman A, Bottle S, Schmid S, Mocerino M, Wille U. *Chemistry*. 2nd ed. Milton, Queensland, Australia John Wiley & Sons; **2012**.
[3] Zu C-X, Li H. *Thermodynamic analysis on energy densities of batteries*. Energy & Environ Sci **2011**; 4: 2614-24.
[4] Lombardi P, Schwabe F. *Sharing economy as a new business model for energy storage systems*. Appl Energ **2017**; 188: 485-96.
[5] Goriparti S, Miele E, De Angelis F, Di Fabrizio E, Proietti Zaccaria R, Capiglia C. *Review on recent progress of nanostructured anode materials for Li-ion batteries*. J Power Sources **2014**; 257: 421-43.
[6] Kundu D, Talaie E, Duffort V, Nazar LF. *The emerging chemistry of sodium ion batteries for electrochemical energy storage*. Angew Chem Int Ed **2015**; 54: 3431-48.
[7] Liu YY, Merinov BV, Goddard WA. *Origin of low sodium capacity in graphite and generally weak substrate binding of Na and mg among alkali and alkaline earth metals*. Proc Natl Acad Sci USA **2016**; 113: 3735-9.
[8] Balogun MS, Luo Y, Qiu WT, Liu P, Tong YX. *A review of carbon materials and their composites with alloy metals for sodium ion battery anodes*. Carbon **2016**; 98: 162-78.
[9] Hayner CM, Zhao X, Kung HH. *Materials for rechargeable lithium-ion batteries*. Ann Rev Chem & Biochem Eng **2012**; 3: 445-71.
[10] Chan KT, Neaton JB, Cohen ML. *First-principles study of metal adatom adsorption on graphene*. Phys Rev B **2008**; 77: 235430.
[11] Luo W, Shen F, Bommier C, Zhu H, Ji X, Hu L. *Na-ion battery anodes: Materials and electrochemistry*. Acc Chem Res **2016**; 49: 231-40.
[12] Barai A, Uddin K, Chevalier J, Chouchelamane GH, McGordon A, Low J et al. *Transportation safety of lithium iron phosphate batteries - a feasibility study of storing at very low states of charge*. Sci Rep **2017**; 7: 5128.
[13] Tarascon JM, Armand M. *Issues and challenges facing rechargeable lithium batteries*. Nature **2001**; 414: 359.
[14] IATA. *2017 lithium battery guidance document*. **2017**;
[15] Stevens DA, Dahn JR. *High capacity anode materials for rechargeable sodium-ion batteries*. J Electrochem Soc **2000**; 147: 1271-73.
[16] Stevens DA, Dahn JR. *The mechanisms of lithium and sodium insertion in carbon materials*. J Electrochem Soc **2001**; 148: 803-11.
[17] Peng L, Zhu Y, Chen D, Ruoff RS, Yu G. *Two-dimensional materials for beyond-lithium-ion batteries*. Adv Energy Mater **2016**; 6: 1600025.
[18] Palomares V, Serras P, Villaluenga I, Hueso KB, Carretero-González J, Rojo T. *Na-ion batteries, recent advances and present challenges to become low cost energy storage systems*. Energy & Environ Sci **2012**; 5: 5884-901.
[19] Irisarri E, Ponrouch A, Palacin MR. *Review-hard carbon negative electrode materials for sodium-ion batteries*. J Electrochem Soc **2015**; 162: A2476-A82.
[20] Lipson AL, Pan BF, Lapidus SH, Liao C, Vaughey JT, Ingram BJ. *Rechargeable Ca-ion batteries: A new energy storage system*. Chem Mater **2015**; 27: 8442-7.
[21] Ponrouch A, Frontera C, Barde F, Palacin MR. *Towards a calcium-based rechargeable battery*. Nat Mater **2016**; 15: 169-72.
[22] Tojo T, Sugiura Y, Inada R, Sakurai Y. *Reversible calcium ion batteries using a dehydrated prussian blue analogue cathode*. Electrochim Acta **2016**; 207: 22-7.

[23] Cabello M, Nacimiento F, González JR, Ortiz G, Alcántara R, Lavela P et al. *Advancing towards a veritable calcium-ion battery: $Caco_2o_4$ positive electrode material*. Electrochem Commun **2016**; 67: 59-64.
[24] Kim JG, Son B, Mukherjee S, Schuppert N, Bates A, Kwon O et al. *A review of lithium and non-lithium based solid state batteries*. J Power Sources **2015**; 282: 299-322.
[25] Cao Y, Xiao L, Sushko ML, Wang W, Schwenzer B, Xiao J et al. *Sodium ion insertion in hollow carbon nanowires for battery applications*. Nano Lett **2012**; 12: 3783-7.
[26] Hayashi M, Arai H, Ohtsuka H, Sakurai Y. *Electrochemical characteristics of calcium in organic electrolyte solutions and vanadium oxides as calcium hosts*. J Power Sources **2003**; 119-121: 617-20.
[27] Sun C, Searles DJ. *Lithium storage on graphdiyne predicted by DFT calculations*. J Phys Chem C **2012**; 116: 26222-6.
[28] Farokh Niaei AH, Hussain T, Hankel M, Searles DJ. *Sodium-intercalated bulk graphdiyne as an anode material for rechargeable batteries*. J Power Sources **2017**; 343: 354-63.
[29] Huang C, Zhang S, Liu H, Li Y, Cui G, Li Y. *Graphdiyne for high capacity and long-life lithium storage*. Nano Energy **2015**; 11: 481-9.
[30] Banhart F, Kotakoski J, Krasheninnikov AV. *Structural defects in graphene*. ACS Nano **2011**; 5: 26-41.
[31] Hashimoto A, Suenaga K, Gloter A, Urita K, Iijima S. *Direct evidence for atomic defects in graphene layers*. Nature **2004**; 430: 870-3.
[32] Datta D, Li J, Shenoy VB. *Defective graphene as a high-capacity anode material for Na- and Ca-ion batteries*. ACS Appl Mater Inter **2014**; 6: 1788-95.
[33] Tsai PC, Chung SC, Lin SK, Yamada A. *Ab initio study of sodium intercalation into disordered carbon*. J Mater Chem A **2015**; 3: 9763-8.
[34] Er D, Detsi E, Kumar H, Shenoy VB. *Defective graphene and graphene allotropes as high-capacity anode materials for mg ion batteries*. ACS Energy Lett **2016**; 1: 638-45.
[35] Boukhvalov DW, Katsnelson MI. *Chemical functionalization of graphene with defects*. Nano Lett **2008**; 8: 4373-9.
[36] Lin KH, Kuo CL. *Lithiation mechanisms and lithium storage capacity of reduced graphene oxide nanoribbons: A first-principles study*. J Mater Chem A **2017**; 5: 4912-22.
[37] Uthaisar C, Barone V, Fahlman BD. *On the chemical nature of thermally reduced graphene oxide and its electrochemical Li intake capacity*. Carbon **2013**; 61: 558-67.
[38] Zhang SL, Du HP, He JJ, Huang CS, Liu HB, Cui GL et al. *Nitrogen-doped graphdiyne applied for lithium-ion storage*. ACS Appl Mater Interfaces **2016**; 8: 8467-73.
[39] Gaddam RR, Farokh Niaei AH, Hankel M, Searles DJ, Nanjundan AK, Zhao XS. *Capacitance-enhanced sodium-ion storage in nitrogen-rich hard carbon*. J Mater Chem A **2017**; 5: 22186-97.
[40] Hankel M, Searles DJ. *Lithium storage on carbon nitride, graphenylene and inorganic graphenylene*. Phys Chem Chem Phys **2016**;
[41] Hankel M, Ye D, Wang L, Searles DJ. *Lithium and sodium storage on graphitic carbon nitride*. J Phys Chem C **2015**; 119: 21921-7.
[42] Georg K, Martijn M, Jürgen F. *Vasp user guide (ver. 5.2.2)*. Computational Materials Physics, Faculty of Physics, Universität Wien, Sensengasse, Wien, Austria: **Apr 2016**.
[43] Dahn JR, Zheng T, Liu Y, Xue JS. *Mechanisms for lithium insertion in carbonaceous materials*. Science **1995**; 270: 590-3.
[44] Yoon D, Kim DH, Chung KY, Chang W, Kim SM, Kim J. *Hydrogen-enriched porous carbon nanosheets with high sodium storage capacity*. Carbon **2016**; 98: 213-20.
[45] Casartelli M, Casolo S, Tantardini GF, Martinazzo R. *Structure and stability of hydrogenated carbon atom vacancies in graphene*. Carbon **2014**; 77: 165-74.

[46] Muellen K, Feng X. *Chemistry of carbon nanostructures*. Dresden, Germany: Walter de Gruyter GmbH; **2017**.
[47] Wang YX, Chou SL, Liu HK, Dou SX. *Reduced graphene oxide with superior cycling stability and rate capability for sodium storage*. Carbon **2013**; 57: 202-8.
[48] Kumar NA, Gaddam RR, Varanasi SR, Yang D, Bhatia SK, Zhao XS. *Sodium ion storage in reduced graphene oxide*. Electrochim Acta **2016**; 214: 319-25.
[49] An Q, Li Y, Deog Yoo H, Chen S, Ru Q, Mai L et al. *Graphene decorated vanadium oxide nanowire aerogel for long-cycle-life magnesium battery cathodes*. Nano Energy **2015**; 18: 265-72.
[50] Fergus JW. *Recent developments in cathode materials for lithium ion batteries*. J Power Sources **2010**; 195: 939-54.
[51] Liu C, Neale ZG, Cao G. *Understanding electrochemical potentials of cathode materials in rechargeable batteries*. Mater Today **2016**; 19: 109-23.
[52] Ma Z, Yuan XX, Li L, Ma ZF, Wilkinson DP, Zhang L et al. *A review of cathode materials and structures for rechargeable lithium-air batteries*. Energy & Environ Sci **2015**; 8: 2144-98.
[53] Scrosati B, Garche J. *Lithium batteries: Status, prospects and future*. J Power Sources **2010**; 195: 2419-30.
[54] Sun C, Liu J, Gong Y, Wilkinson DP, Zhang J. *Recent advances in all-solid-state rechargeable lithium batteries*. Nano Energy **2017**; 33: 363-86.
[55] Ivanovskii AL. *Graphynes and graphdyines*. Prog Solid State Chem **2013**; 41: 1-19.
[56] David L, Singh G. *Reduced graphene oxide paper electrode: Opposing effect of thermal annealing on Li and Na cyclability*. J Phys Chem C **2014**; 118: 28401-8.
[57] Kuo S-L, Liu W-R, Kuo C-P, Wu N-L, Wu H-C. *Lithium storage in reduced graphene oxides*. J Power Sources **2013**; 244: 552-6.
[58] Pumera M. *Graphene-based nanomaterials for energy storage*. Energy & Environ Sci **2011**; 4: 668-74.
[59] Cao Y, Li Xl, Zheng M, Yang M, Yang X, Dong Q. *Ultra-high rates and reversible capacity of Li-s battery with a nitrogen-doping conductive lewis base matrix*. Electrochim Acta **2016**; 192: 467-74.
[60] Feng K, Ahn W, Lui G, Park HW, Kashkooli AG, Jiang G et al. *Implementing an in-situ carbon network in si/reduced graphene oxide for high performance lithium-ion battery anodes*. Nano Energy **2016**; 19: 187-97.
[61] Zheng X, Li X, Wang Z, Guo H, Huang Z, Yan G et al. *Investigation and improvement on the electrochemical performance and storage characteristics of linio$_2$-based materials for lithium ion battery*. Electrochim Acta **2016**; 191: 832-40.
[62] Atkins PW. *Physical chemistry*. 10th ed. Oxford ; New York: Oxford University Press; **2014**.
[63] Garay-Tapia AM, Romero AH, Barone V. *Lithium adsorption on graphene: From isolated adatoms to metallic sheets*. J Chem Theo Comp **2012**; 8: 1064-71.
[64] Grimme S, Antony J, Ehrlich S, Krieg H. *A consistent and accurate ab initio parametrization of density functional dispersion correction (DFT-d) for the 94 elements H-Pu*. J Chem Phys **2010**; 132: 154104.
[65] Kittel C. *Introduction to solid state physics*. 8th ed. Hoboken, NJ: John Wiley & Sons; **2005**.
[66] Valencia F, Romero AH, Ancilotto F, Silvestrelli PL. *Lithium adsorption on graphite from density functional theory calculations*. J Phys Chem B **2006**; 110: 14832-41.
[67] Aylward GH, Findlay TJV. *Si chemical data*. 5th ed. Australia: John Wiley & Sons; **2002**.
[68] Luo W, Wan J, Ozdemir B, Bao W, Chen Y, Dai J et al. *Potassium ion batteries with graphitic materials*. Nano Lett **2015**; 15: 7671-7.

[69] Liang Z, Fan X, Zheng W, Singh DJ. *Adsorption and formation of small Na clusters on pristine and double-vacancy graphene for anodes of Na-ion batteries*. ACS Appl Mater Inter **2017**; 9: 17076-84.
[70] Xu Z, Lv X, Chen J, Jiang L, Lai Y, Li J. *Dispersion-corrected DFT investigation on defect chemistry and potassium migration in potassium-graphite intercalation compounds for potassium ion batteries anode materials*. Carbon **2016**; 107: 885-94.
[71] Li Z, Bommier C, Chong ZS, Jian Z, Surta TW, Wang X et al. *Mechanism of Na-ion storage in hard carbon anodes revealed by heteroatom doping*. Adv Energy Mater 1602894.
[72] Okamoto Y. *Density functional theory calculations of lithium adsorption and insertion to defect-free and defective graphene*. J Phys Chem C **2016**; 120: 14009-14.
[73] Yang S, Li S, Tang S, Dong W, Sun W, Shen D et al. *Sodium adsorption and intercalation in bilayer graphene from density functional theory calculations*. Theor Chem Acc **2016**; 135: 1-11.
[74] Pramudita JC, Pontiroli D, Magnani G, Gaboardi M, Ricco M, Milanese C et al. *Graphene and selected derivatives as negative electrodes in sodium- and lithium-ion batteries*. ChemElectroChem **2015**; 2: 600-10.
[75] Chen WF, Zhu ZY, Li SR, Chen CH, Yan LF. *Efficient preparation of highly hydrogenated graphene and its application as a high-performance anode material for lithium ion batteries*. Nanoscale **2012**; 4: 2124-9.
[76] Farokh Niaei AH, Hussain T, Hankel M, Searles DJ. *Hydrogenated defective graphene as an anode material for sodium and calcium ion batteries: A density functional theory study*. Carbon **2018**; 136: 73-84.
[77] Xu Z, Lv X, Li J, Chen J, Liu Q. *A promising anode material for sodium-ion battery with high capacity and high diffusion ability: Graphyne and graphdiyne*. RSC Advances **2016**;
[78] Zhang S, He J, Zheng J, Huang C, Lv Q, Wang K et al. *Porous graphdiyne applied for sodium ion storage*. J Mater Chem A **2017**; 5: 2045-51.
[79] Xu XJ, Ji SM, Gu MZ, Liu J. *In situ synthesis of mns hollow microspheres on reduced graphene oxide sheets as high-capacity and long-life anodes for Li- and Na-ion batteries*. ACS Appl Mater Interfaces **2015**; 7: 20957-64.
[80] Georgakilas V, Tiwari JN, Kemp KC, Perman JA, Bourlinos AB, Kim KS et al. *Noncovalent functionalization of graphene and graphene oxide for energy materials, biosensing, catalytic, and biomedical applications*. Chem Rev **2016**; 116: 5464-519.
[81] Peng S, Han X, Li L, Zhu Z, Cheng F, Srinivansan M et al. *Unique cobalt sulfide/reduced graphene oxide composite as an anode for sodium-ion batteries with superior rate capability and long cycling stability*. Small **2016**; 12: 1359-68.
[82] Dobrota AS, Pašti IA, Mentus SV, Johansson B, Skorodumova NV. *Functionalized graphene for sodium battery applications: The DFT insights*. Electrochim Acta **2017**; 250: 185-95.
[83] Yan D, Yu C, Zhang X, Qin W, Lu T, Hu B et al. *Nitrogen-doped carbon microspheres derived from oatmeal as high capacity and superior long life anode material for sodium ion battery*. Electrochim Acta **2016**; 191: 385-91.
[84] Bhauriyal P, Mahata A, Pathak B. *Graphene-like carbon–nitride monolayer: A potential anode material for Na- and K-ion batteries*. J Phys Chem C **2018**; 122: 2481-9.
[85] Wang YS, Yu XQ, Xu SY, Bai JM, Xiao RJ, Hu YS et al. *A zero-strain layered metal oxide as the negative electrode for long-life sodium-ion batteries*. Nat Commun **2013**; 4:
[86] Yabuuchi N, Kajiyama M, Iwatate J, Nishikawa H, Hitomi S, Okuyama R et al. *P2-type* $na_x\ [fe_{1/2}\ mn_{1/2}]o_2$ *made from earth-abundant elements for rechargeable Na batteries*. Nat Mater **2012**; 11: 512.

[87] Sun Y, Zhao L, Pan H, Lu X, Gu L, Hu Y-S et al. *Direct atomic-scale confirmation of three-phase storage mechanism in $li_4ti_5o_{12}$ anodes for room-temperature sodium-ion batteries*. Nat Commun **2013**; 4: 1870.
[88] Shi Z-T, Kang W, Xu J, Sun Y-W, Jiang M, Ng T-W et al. *Hierarchical nanotubes assembled from mos_2 - carbon monolayer sandwiched superstructure nanosheets for high-performance sodium ion batteries*. Nano Energy **2016**; 22: 27-37.
[89] Hu Z, Wang L, Zhang K, Wang J, Cheng F, Tao Z et al. *Mos_2 nanoflowers with expanded interlayers as high-performance anodes for sodium-ion batteries*. Angew Chem **2014**; 126: 13008-12.
[90] Mortazavi M, Wang C, Deng J, Shenoy VB, Medhekar NV. *Ab initio characterization of layered mos_2 as anode for sodium-ion batteries*. J Power Sources **2014**; 268: 279-86.
[91] Wang J, Liu J, Yang H, Chao D, Yan J, Savilov SV et al. *Mos_2 nanosheets decorated ni_3s_2@mos_2 coaxial nanofibers: Constructing an ideal heterostructure for enhanced Na-ion storage*. Nano Energy **2016**; 20: 1-10.
[92] Anasori B, Lukatskaya MR, Gogotsi Y. *2d metal carbides and nitrides (mxenes) for energy storage*. Nat Rev Mater **2017**; 2: 16098.
[93] Kim J-S, Ahn H-J, Ryu H-S, Kim D-J, Cho G-B, Kim K-W et al. *The discharge properties of Na/ni_3s_2 cell at ambient temperature*. J Power Sources **2008**; 178: 852-6.
[94] Yu DYW, Prikhodchenko PV, Mason CW, Batabyal SK, Gun J, Sladkevich S et al. *High-capacity antimony sulphide nanoparticle-decorated graphene composite as anode for sodium-ion batteries*. Nat Commun **2013**; 4: 2922.
[95] Hummers WS, Offeman RE. *Preparation of graphitic oxide*. J Am Chem Soc **1958**; 80: 1339-.
[96] Kovtyukhova NI, Ollivier PJ, Martin BR, Mallouk TE, Chizhik SA, Buzaneva EV et al. *Layer-by-layer assembly of ultrathin composite films from micron-sized graphite oxide sheets and polycations*. Chem Mater **1999**; 11: 771-8.
[97] Padigi P, Goncher G, Evans D, Solanki R. *Potassium barium hexacyanoferrate – a potential cathode material for rechargeable calcium ion batteries*. J Power Sources **2015**; 273: 460-4.
[98] Gheytani S, Liang Y, Wu F, Jing Y, Dong H, Rao KK et al. *An aqueous Ca-ion battery*. Adv Sci **2017**; 4: 1700465.
[99] Mortazavi B, Dianat A, Rahaman O, Cuniberti G, Rabczuk T. *Borophene as an anode material for Ca, mg, Na or Li ion storage: A first-principle study*. J Power Sources **2016**; 329: 456-61.
[100] Feng F, Lu RG, Zhu CB. *A combined state of charge estimation method for lithium-ion batteries used in a wide ambient temperature range*. Energies **2014**; 7: 3004-32.
[101] Hunt G. Usabc electric vehicle battery test procedures manual. Washington DC, USA1996.
[102] Jian Z, Luo W, Ji X. *Carbon electrodes for K-ion batteries*. J Am Chem Soc **2015**; 137: 11566-9.
[103] Komaba S, Hasegawa T, Dahbi M, Kubota K. *Potassium intercalation into graphite to realize high-voltage/high-power potassium-ion batteries and potassium-ion capacitors*. Electrochem Commun **2015**; 60: 172-5.
[104] Novoselov KS, Geim AK, Morozov SV, Jiang D, Zhang Y, Dubonos SV et al. *Electric field effect in atomically thin carbon films*. Science **2004**; 306: 666-9.
[105] Kim BG, Choi HJ. *Graphyne: Hexagonal network of carbon with versatile dirac cones*. Phys Rev B **2012**; 86: 115435.
[106] Haley MM. *Synthesis and properties of annulenic subunits of graphyne and graphdiyne nanoarchitectures*. Pure Appl Chem **2008**; 80: 519-32.

[107] Li G, Li Y, Liu H, Guo Y, Li Y, Zhu D. *Architecture of graphdiyne nanoscale films*. Chem Commun **2010**; 46: 3256-8.
[108] Zhou J, Gao X, Liu R, Xie Z, Yang J, Zhang S et al. *Synthesis of graphdiyne nanowalls using acetylenic coupling reaction*. J Am Chem Soc **2015**; 137: 7596-9.
[109] Matsuoka R, Sakamoto R, Hoshiko K, Sasaki S, Masunaga H, Nagashio K et al. *Crystalline graphdiyne nanosheets produced at a gas/liquid or liquid/liquid interface*. J Am Chem Soc **2017**; 139: 3145-52.
[110] Shi W, Lei A. *1,3-diyne chemistry: Synthesis and derivations*. Tetrahedron Lett **2014**; 55: 2763-72.
[111] Georgakilas V, Perman JA, Tucek J, Zboril R. *Broad family of carbon nanoallotropes: Classification, chemistry, and applications of fullerenes, carbon dots, nanotubes, graphene, nanodiamonds, and combined superstructures*. Chem Rev **2015**; 115: 4744-822.
[112] Li Y, Xu L, Liu H, Li Y. *Graphdiyne and graphyne: From theoretical predictions to practical construction*. Chem Soc Rev **2014**; 43: 2572-86.
[113] Jiao Y, Du A, Hankel M, Zhu Z, Rudolph V, Smith SC. *Graphdiyne: A versatile nanomaterial for electronics and hydrogen purification*. Chem Commun **2011**; 47: 11843-5.
[114] Inagaki M, Kang F. *Graphene derivatives: Graphane, fluorographene, graphene oxide, graphyne and graphdiyne*. J Mater Chem A **2014**; 2: 13193.
[115] Peng Q, Dearden AK, Crean J, Han L, Liu S, Wen X et al. *New materials graphyne, graphdiyne, graphone, and graphane: Review of properties, synthesis, and application in nanotechnology*. Nanotechnol Sci Appl **2014**; 7: 1-29.
[116] Zhang H, Xia Y, Bu H, Wang X, Zhang M, Luo Y et al. *Graphdiyne: A promising anode material for lithium ion batteries with high capacity and rate capability*. J Appl Phys **2013**; 113: 044309.
[117] Hwang HJ, Koo J, Park M, Park N, Kwon Y, Lee H. *Multilayer graphynes for lithium ion battery anode*. J Phys Chem C **2013**; 117: 6919-23.
[118] Luo G, Zheng Q, Mei W-N, Lu J, Nagase S. *Structural, electronic, and optical properties of bulk graphdiyne*. J Phys Chem C **2013**; 117: 13072-9.
[119] Zheng Q, Luo G, Liu Q, Quhe R, Zheng J, Tang K et al. *Structural and electronic properties of bilayer and trilayer graphdiyne*. Nanoscale **2012**; 4: 3990-6.
[120] Shen W, Wang C, Xu QJ, Liu HM, Wang YG. *Nitrogen-doping-induced defects of a carbon coating layer facilitate Na-storage in electrode materials*. Adv Energy Mater **2015**; 5:
[121] Hahn JR, Kang H, Song S, Jeon IC. *Observation of charge enhancement induced by graphite atomic vacancy: A comparative stm and afm study*. Phys Rev B **1996**; 53: R1725-R8.
[122] Carlsson JM, Scheffler M. *Structural, electronic, and chemical properties of nanoporous carbon*. Phys Rev Lett **2006**; 96: 046806.
[123] Ma J, Alfe D, Michaelides A, Wang E. *Stone-wales defects in graphene and other planar sp^2 -bonded materials*. Phys Rev B **2009**; 80: 033407.
[124] Lahiri J, Lin Y, Bozkurt P, Oleynik II, Batzill M. *An extended defect in graphene as a metallic wire*. Nat Nanotechnol **2010**; 5: 326-9.
[125] Botello-Mendez AR, Declerck X, Terrones M, Terrones H, Charlier JC. *One-dimensional extended lines of divacancy defects in graphene*. Nanoscale **2011**; 3: 2868-72.
[126] Erickson K, Erni R, Lee Z, Alem N, Gannett W, Zettl A. *Determination of the local chemical structure of graphene oxide and reduced graphene oxide*. Adv Mater **2010**; 22: 4467-72.
[127] Bagri A, Mattevi C, Acik M, Chabal YJ, Chhowalla M, Shenoy VB. *Structural evolution during the reduction of chemically derived graphene oxide*. Nat Chem **2010**; 2: 581-7.
[128] Duan XG, Sun HQ, Ao ZM, Zhou L, Wang GX, Wang SB. *Unveiling the active sites of graphene-catalyzed peroxymonosulfate activation*. Carbon **2016**; 107: 371-8.
[129] Dai L. *Graphene: Tunable superdoping*. Nat Energy **2016**; 1: 16041.

[130] Casartelli M, Casolo S, Tantardini GF, Martinazzo R. *Spin coupling around a carbon atom vacancy in graphene*. Phys Rev B **2013**; 88: 195424.
[131] Matsutsu M, Petersen MA, van Steen E. *Pt_{38} cluster on oh- and cooh-functionalised graphene as a model for pt/c-catalysts*. Phys Chem Chem Phys **2016**; 18: 25693-704.
[132] Ricco M, Pontiroli D, Mazzani M, Choucair M, Stride JA, Yazyev OV. *Muons probe strong hydrogen interactions with defective graphene*. Nano Lett **2011**; 11: 4919-22.
[133] Pontiroli D, Aramini M, Gaboardi M, Mazzani M, Sanna S, Caracciolo F et al. *Tracking the hydrogen motion in defective graphene*. J Phys Chem C **2014**; 118: 7110-6.
[134] Lerf A, He HY, Forster M, Klinowski J. *Structure of graphite oxide revisited*. J Phys Chem B **1998**; 102: 4477-82.
[135] Gao W, Alemany LB, Ci LJ, Ajayan PM. *New insights into the structure and reduction of graphite oxide*. Nat Chem **2009**; 1: 403-8.
[136] He H, Klinowski J, Forster M, Lerf A. *A new structural model for graphite oxide*. Chem Phys Lett **1998**; 287: 53-6.
[137] Gomez-Navarro C, Meyer JC, Sundaram RS, Chuvilin A, Kurasch S, Burghard M et al. *Atomic structure of reduced graphene oxide*. Nano Lett **2010**; 10: 1144-8.
[138] Casabianca LB, Shaibat MA, Cai WWW, Park S, Piner R, Ruoff RS et al. *Nmr-based structural modeling of graphite oxide using multidimensional c-13 solid-state nmr and ab initio chemical shift calculations*. J Am Chem Soc **2010**; 132: 5672-6.
[139] Kuo SL, Liu WR, Kuo CP, Wu NL, Wu HC. *Lithium storage in reduced graphene oxides*. J Power Sources **2013**; 244: 552-6.
[140] Uthaisar C, Hicks DJ, Barone V. *Li adsorption on edge-oxidized graphene nanoribbons predicted by DFT calculations*. Surf Sci **2014**; 619: 105-13.
[141] Moon HS, Lee JH, Kwon S, Kim IT, Lee SG. *Mechanisms of Na adsorption on graphene and graphene oxide: Density functional theory approach*. Carbon Lett **2015**; 16: 116-20.
[142] Nakada K, Fujita M, Dresselhaus G, Dresselhaus MS. *Edge state in graphene ribbons: Nanometer size effect and edge shape dependence*. Phys Rev B **1996**; 54: 17954-61.
[143] Kim H, Lee K, Woo SI, Jung Y. *On the mechanism of enhanced oxygen reduction reaction in nitrogen-doped graphene nanoribbons*. Phys Chem Chem Phys **2011**; 13: 17505-10.
[144] Gong Y, Fei H, Zou X, Zhou W, Yang S, Ye G et al. *Boron- and nitrogen-substituted graphene nanoribbons as efficient catalysts for oxygen reduction reaction*. Chem Mater **2015**; 27: 1181-6.
[145] Zou X, Wang L, Yakobson BI. *Mechanisms of the oxygen reduction reaction on b- and/or n-doped carbon nanomaterials with curvature and edge effects*. Nanoscale **2018**; 10: 1129-34.
[146] Dino WA, Miura Y, Nakanishi H, Kasai H, Sugimoto T, Kondo T. *H-2 dissociative adsorption at the armchair edges of graphite*. Solid State Commun **2004**; 132: 713-8.
[147] Sha XW, Jackson B. *The location of adsorbed hydrogen in graphite nanostructures*. J Am Chem Soc **2004**; 126: 13095-9.
[148] Chang SL, Lin SY, Lin SK, Lee CH, Lin MF. *Geometric and electronic properties of edge-decorated graphene nanoribbons*. Sci Rep **2014**; 4: 6038.
[149] Palacios JJ, Fernandez-Rossier J, Brey L, Fertig HA. *Electronic and magnetic structure of graphene nanoribbons*. Semicond Sci Tech **2010**; 25: 033003.
[150] Yazyev OV. *A guide to the design of electronic properties of graphene nanoribbons*. Acc Chem Res **2013**; 46: 2319-28.
[151] Chen YC, de Oteyza DG, Pedramrazi Z, Chen C, Fischer FR, Crommie MF. *Tuning the band gap of graphene nanoribbons synthesized from molecular precursors*. ACS Nano **2013**; 7: 6123-8.

[152] Uthaisar C, Barone V, Peralta JE. *Lithium adsorption on zigzag graphene nanoribbons*. J Appl Phys **2009**; 106: 113715.
[153] Xiao B, Li X, Li X, Wang B, Langford C, Li R et al. *Graphene nanoribbons derived from the unzipping of carbon nanotubes: Controlled synthesis and superior lithium storage performance*. J Phys Chem C **2014**; 118: 881-90.
[154] Lee HW, Moon HS, Hur J, Kim IT, Park MS, Yun JM et al. *Mechanism of sodium adsorption on n-doped graphene nanoribbons for sodium ion battery applications: A density functional theory approach*. Carbon **2017**; 119: 492-501.
[155] Son YW, Cohen ML, Louie SG. *Energy gaps in graphene nanoribbons*. Phys Rev Lett **2006**; 97: 216803.
[156] Vargas OAC, Caballero A, Morales J. *Can the performance of graphene nanosheets for lithium storage in Li-ion batteries be predicted?* Nanoscale **2012**; 4: 2083-92.
[157] Pan D, Wang S, Zhao B, Wu M, Zhang H, Wang Y et al. *Li storage properties of disordered graphene nanosheets*. Chem Mater **2009**; 21: 3136-42.
[158] Wan L, Ren Z, Wang H, Wang G, Tong X, Gao S et al. *Graphene nanosheets based on controlled exfoliation process for enhanced lithium storage in lithium-ion battery*. Diamond Relat Mater **2011**; 20: 756-61.
[159] Tsuneda T. *Density functional theory in quantum chemistry*. Tokyo, Japan: Springer; **2014**.
[160] Davarcioglu B. *The general characteristic of weak intermolecular interactions in liquids and crystals*. Int J Modern Eng Res **2011**; 1: 443-54.
[161] Prausnitz JM, Lichtenthaler RN, Azevedo EGd. *Molecular thermodynamics of fluid-phase equilibria*. USA: Prentice Hall; **1999**.
[162] Messiah A. *Quantum mechanics*. Amsterdam, The Netherelands: Elsevier Science B.V.; **1961**.
[163] Eisberg R, Resnick R. *Quntum physics of atoms, molecules, solids, nuclei, and particles* 2nd ed. United States of America: John Wiley & Sons; **1985**.
[164] Hanle PA. *Erwin schrödinger's reaction to louis de broglie's thesis on the quantum theory*. Isis **1977**; 68: 606-9.
[165] Gunn Lee J. *Computational materials science, an introduction* 2nd ed. New York: CRC Press, Taylor & Francis Group; **2017**.
[166] Shankar R. *Principles of quantum mechanics*. 2nd ed. Boston, USA: Springer; **1994**.
[167] Jensen F. *Introduction to computational chemistry*. 3rd ed. Chichester, England: John Wiley & Sons; **2017**.
[168] M. B, R. O. *Zur quantentheorie der molekeln*. Annalen der Physik **1927**; 389: 457-84.
[169] Sholl D, Steckel JA. *Density functional theory : A practical introduction*. Hoboken, NJ, USA: John Wiley & Sons; **2009**.
[170] Strout DL, Scuseria GE. *A quantitative study of the scaling properties of the hartree–fock method*. J Chem Phys **1995**; 102: 8448-52.
[171] Sidney Y. Handbook of materials modeling. Methods. 2965; Springer Netherlands: Dordrecht; 2005. p. 195-214.
[172] Hohenberg P, Kohn W. *Inhomogeneous electron gas*. Phys Rev **1964**; 136: B864.
[173] Kohn W, Sham LJ. *Self-consistent equations including exchange and correlation effects*. Phys Rev **1965**; 140: A1133-A8.
[174] Entwistle MT, Hodgson MJP, Wetherell J, Longstaff B, Ramsden JD, Godby RW. *Local density approximations from finite systems*. Phys Rev B **2016**; 94: 205134.
[175] Perdew JP, Chevary JA, Vosko SH, Jackson KA, Pederson MR, Singh DJ et al. *Atoms, molecules, solids, and surfaces - applications of the generalized gradient approximation for exchange and correlation*. Phys Rev B **1992**; 46: 6671-87.

[176] Perdew JP, Wang Y. *Accurate and simple analytic representation of the electron-gas correlation energy*. Phys Rev B **1992**; 45: 13244-9.
[177] Perdew JP, Burke K, Ernzerhof M. *Generalized gradient approximation made simple*. Phys Rev Lett **1996**; 77: 3865-8.
[178] Mattsson AE, Armiento R, Paier J, Kresse G, Wills JM, Mattsson TR. *The am05 density functional applied to solids*. J Chem Phys **2008**; 128: 084714.
[179] Perdew JP, Ruzsinszky A, Csonka GI, Vydrov OA, Scuseria GE, Constantin LA et al. *Restoring the density-gradient expansion for exchange in solids and surfaces*. Phys Rev Lett **2008**; 100: 136406.
[180] Stephens PJ, Devlin FJ, Chabalowski CF, Frisch MJ. *Ab initio calculation of vibrational absorption and circular dichroism spectra using density functional force fields*. J Phys Chem **1994**; 98: 11623-7.
[181] Perdew JP, Schmidt K. *Jacob's ladder of density functional approximations for the exchange-correlation energy*. AIP Conference Proceedings **2001**; 577: 1-20.
[182] Tran F, Blaha P. *Importance of the kinetic energy density for band gap calculations in solids with density functional theory*. J Phys Chem A **2017**; 121: 3318-25.
[183] Cramer CJ. *Essentials of computational chemistry : Theories and models*. 2nd ed. Chichester, West Sussex, England ; Hoboken, NJ: John Wiley & Sons; **2004**.
[184] Groß A. *Theoretical surface science, a microscopic perspective*. 2nd ed. Verlag Berlin Heidelberg: Springer; **2009**.
[185] Kristian B, Valentino RC, Kyuho L, Elsebeth S, Thonhauser T, Per H et al. *Van der waals forces in density functional theory: A review of the vdw-df method*. Rep Prog Phys **2015**; 78: 066501.
[186] Lundqvist BI, Andersson Y, Shao H, Chan S, Langreth DC. *Density functional theory including van der waals forces*. Int J Quantum Chem **1995**; 56: 247-55.
[187] Fernandez EM, Balbas LC. *Gga versus van der waals density functional results for mixed gold/mercury molecules and pure au and hg cluster properties*. Phys Chem Chem Phys **2011**; 13: 20863-70.
[188] Grimme S. *Accurate description of van der waals complexes by density functional theory including empirical corrections*. J Comput Chem **2004**; 25: 1463-73.
[189] Grimme S. *Semiempirical gga-type density functional constructed with a long-range dispersion correction*. J Comput Chem **2006**; 27: 1787-99.
[190] Grimme S, Ehrlich S, Goerigk L. *Effect of the damping function in dispersion corrected density functional theory*. J Comput Chem **2011**; 32: 1456-65.
[191] Tulip PR. Dielectric and lattice dynamical properties of molecular crystals via density functional perturbation theory: Implementation within a first principles code. UK: The University of Durham; 2004.
[192] Hasnip PJ, Refson K, Probert MIJ, Yates JR, Clark SJ, Pickard CJ. *Density functional theory in the solid state*. Phil Trans R Soc A **2014**; 372: 1 - 26.
[193] Monkhorst HJ, Pack JD. *Special points for brillouin-zone integrations*. Phys Rev B **1976**; 13: 5188-92.
[194] Vanderbilt D. *Soft self-consistent pseudopotentials in a generalized eigenvalue formalism*. Phys Rev B **1990**; 41: 7892-5.
[195] Blöchl PE. *Projector augmented-wave method*. Phys Rev B **1994**; 50: 17953-79.
[196] Kresse G, Joubert D. *From ultrasoft pseudopotentials to the projector augmented-wave method*. Phys Rev B **1999**; 59: 1758-75.
[197] Bader RFW. *Atoms in molecules : A quantum theory*. 1st ed. Oxford: Clarendon Press; **1990**.
[198] Tang W, Sanville E, Henkelman G. *A grid-based bader analysis algorithm without lattice bias*. J Phys Condens Matter **2009**; 21: 084204.

[199] Yu M, Trinkle DR. *Accurate and efficient algorithm for bader charge integration*. J Chem Phys **2011**; 134: 064111.
[200] Sanville E, Kenny SD, Smith R, Henkelman G. *Improved grid-based algorithm for bader charge allocation*. J Comput Chem **2007**; 28: 899-908.
[201] Henkelman G, Arnaldsson A, Jónsson H. *A fast and robust algorithm for bader decomposition of charge density*. Comput Mater Sci **2006**; 36: 354-60.
[202] Drissi M, Benhalima N, Megrouss Y, Rachida R, Chouaih A, Hamzaoui F. *Theoretical and experimental electrostatic potential around the m-nitrophenol molecule*. Molecules **2015**; 20: 4042-54.
[203] Jónsson H, Mills G, Jacobsen KW. Nudged elastic band method for finding minimum energy paths of transitions. Classical and quantum dynamics in condensed phase simulations. Chapter 16; World Scientific; 1998. p. 385-404.
[204] Mills G, Jónsson H, Schenter GK. *Reversible work transition state theory: Application to dissociative adsorption of hydrogen*. Surf Sci **1995**; 324: 305-37.
[205] Henkelman G, Jónsson H. *Improved tangent estimate in the nudged elastic band method for finding minimum energy paths and saddle points*. J Chem Phys **2000**; 113: 9978-85.
[206] Sawicki M, Shaw LL. *Advances and challenges of sodium ion batteries as post lithium ion batteries*. RSC Advances **2015**; 5: 53129-54.
[207] Park S, Lee K-S, Bozoklu G, Cai W, Nguyen ST, Ruoff RS. *Graphene oxide papers modified by divalent ions—enhancing mechanical properties via chemical cross-linking*. ACS Nano **2008**; 2: 572-8.
[208] McCarthy MC, Apponi AJ, Gottlieb CA, Thaddeus P. *Laboratory detection of five new linear silicon carbides: Sic3, sic5, sic6, sic7, and sic8*. Astrophys J **2000**; 538: 766.
[209] Klimes J, Bowler DR, Michaelides A. *Chemical accuracy for the van der waals density functional*. J Phys Condens Matter **2010**; 22: 022201.
[210] Henkelman G, Uberuaga BP, Jónsson H. *A climbing image nudged elastic band method for finding saddle points and minimum energy paths*. J Chem Phys **2000**; 113: 9901-4.
[211] Qie L, Chen W, Xiong X, Hu C, Zou F, Hu P et al. *Sulfur-doped carbon with enlarged interlayer distance as a high-performance anode material for sodium-ion batteries*. Adv Sci **2015**; 2: 1500195.
[212] Komaba S, Murata W, Ishikawa T, Yabuuchi N, Ozeki T, Nakayama T et al. *Electrochemical Na insertion and solid electrolyte interphase for hard-carbon electrodes and application to Na-ion batteries*. Adv Funct Mater **2011**; 21: 3859-67.
[213] Mikito K. *Stacking-dependent optical absorption in multilayer graphene*. New J Phys **2013**; 15: 015010.
[214] Farokh Niaei AH, Roman T, Hussain T, Searles DJ. *Computational study on the adsorption of sodium and calcium on edge-functionalized graphene nanoribbons*. J Phys Chem C **2019**; 123: 14895-908.
[215] Sahu V, Shekhar S, Sharma RK, Singh G. *Ultrahigh performance supercapacitor from lacey reduced graphene oxide nanoribbons*. ACS Appl Mater Interfaces **2015**; 7: 3110-6.
[216] Eigler S, Hirsch A. *Chemistry with graphene and graphene oxide-challenges for synthetic chemists*. Angew Chem Int Ed **2014**; 53: 7720-38.
[217] Pisani L, Chan JA, Montanari B, Harrison NM. *Electronic structure and magnetic properties of graphitic ribbons*. Phys Rev B **2007**; 75: 064418.
[218] Momma K, Izumi F. *Vesta 3 for three-dimensional visualization of crystal, volumetric and morphology data*. J Appl Crystallogr **2011**; 44: 1272-6.
[219] Bommier C, Ji X, Greaney PA. *Electrochemical properties and theoretical capacity for sodium storage in hard carbon: Insights from first principles calculations*. Chem Mater **2018**; 31: 658-77.

[220] Son YW, Cohen ML, Louie SG. *Half-metallic graphene nanoribbons*. Nature **2006**; 444: 347-9.
[221] Vajtai R. *Springer handbook of nanomaterials*. Verlag Berlin Heidelberg: Springer; **2013**.
[222] Soler-Crespo RA, Gao W, Xiao P, Wei X, Paci JT, Henkelman G et al. *Engineering the mechanical properties of monolayer graphene oxide at the atomic level*. J Phys Chem Lett **2016**; 7: 2702-7.
[223] Humberto T, Ruitao L, Mauricio T, Mildred SD. *The role of defects and doping in 2d graphene sheets and 1d nanoribbons*. Rep Prog Phys **2012**; 75: 062501.
[224] Wakabayashi K, Sasaki Ki, Nakanishi T, Enoki T. *Electronic states of graphene nanoribbons and analytical solutions*. Sci Technol Adv Mater **2010**; 11: 054504.
[225] Li Q, Li Y, Chen Y, Wu L, Yang C, Cui X. *Synthesis of γ-graphyne by mechanochemistry and its electronic structure*. Carbon **2018**; 136: 248-54.
[226] Wasalathilake KC, Ayoko GA, Yan C. *Effects of heteroatom doping on the performance of graphene in sodium-ion batteries: A density functional theory investigation*. Carbon **2018**; 140: 276-85.
[227] Wu M, Cao C, Jiang JZ. *Light non-metallic atom (b, n, o and f)-doped graphene: A first-principles study*. Nanotechnology **2010**; 21: 505202.
[228] Kim Y, Park Y, Choi A, Choi NS, Kim J, Lee J et al. *An amorphous red phosphorus/carbon composite as a promising anode material for sodium ion batteries*. Adv Mater **2013**; 25: 3045-9.
[229] Kulish VV, Malyi OI, Persson C, Wu P. *Phosphorene as an anode material for Na-ion batteries: A first-principles study*. Phys Chem Chem Phys **2015**; 17: 13921-8.
[230] Liu X, Wen Y, Chen Z, Shan B, Chen R. *A first-principles study of sodium adsorption and diffusion on phosphorene*. Phys Chem Chem Phys **2015**; 17: 16398-404.
[231] Gao Y, Ren X, Wu J, Hayat T, Alsaedi A, Cheng C et al. *Graphene oxide interactions with co-existing heavy metal cations: Adsorption, colloidal properties and joint toxicity*. Environ Sci Nano **2018**; 5: 362-71.
[232] Moubark M, Abdel Moghny T, Ahmed Mousa M, A.-A. El-Bellihi A-H, Awadallah A. *Absorption of calcium ions on oxidized graphene sheets and study its dynamic behavior by kinetic and isothermal models*. Applied Nanoscience **2016**; 6: 1105-17.
[233] Peng W, Li H, Liu Y, Song S. *A review on heavy metal ions adsorption from water by graphene oxide and its composites*. J Mol Liq **2017**; 230: 496-504.
[234] Sitko R, Turek E, Zawisza B, Malicka E, Talik E, Heimann J et al. *Adsorption of divalent metal ions from aqueous solutions using graphene oxide*. Dalton Transactions **2013**; 42: 5682-9.
[235] Alcántara R, Lavela P, Ortiz GF, Tirado JL. *Carbon microspheres obtained from resorcinol-formaldehyde as high-capacity electrodes for sodium-ion batteries*. Electrochem Solid-State Lett **2005**; 8: 222-5.
[236] Jache B, Adelhelm P. *Use of graphite as a highly reversible electrode with superior cycle life for sodium-ion batteries by making use of co-intercalation phenomena*. Angew Chem Int Ed **2014**; 53: 10169-73.
[237] Wen Y, He K, Zhu Y, Han F, Xu Y, Matsuda I et al. *Expanded graphite as superior anode for sodium-ion batteries*. Nat Commun **2014**; 5:
[238] Chen G-Y, Sun Q, Yue J-L, Shadike Z, Yang Y, Ding F et al. *Conversion and displacement reaction types of transition metal compounds for sodium ion battery*. J Power Sources **2015**; 284: 115-21.
[239] Zhu Z, Cheng F, Hu Z, Niu Z, Chen J. *Highly stable and ultrafast electrode reaction of graphite for sodium ion batteries*. J Power Sources **2015**; 293: 626-34.

[240] Bommier C, Surta TW, Dolgos M, Ji X. *New mechanistic insights on Na-ion storage in nongraphitizable carbon*. Nano Lett **2015**; 15: 5888-92.
[241] Liu Y, Fang X, Ge M, Rong J, Shen C, Zhang A et al. *Sno-2 coated carbon cloth with surface modification as Na-ion battery anode*. Nano Energy **2015**; 16: 399-407.
[242] Kang Y-J, Jung SC, Choi JW, Han Y-K. *Important role of functional groups for sodium ion intercalation in expanded graphite*. Chem Mater **2015**; 27: 5402-6.

Appendices

Appendix 1

Table 1A.1: Sample of proposed materials for sodium ion batteries (NIBs)

Table 1A.1: Sample of proposed materials for sodium ion batteries (NIBs) in chronological order										
Row	**Authors**	**Year**	**Charge Transfer Agent**	**Anode Material**	**Reported capacity, mA h g^{-1}**	**Capacity (Eq. 2.1), mA h g^{-1} ***	**Voltage, voltage**	**Current, A/g**	**Cycles**	**Ref.**
1	D.A. Stevens & R.J. Dahn	2000	Na	Glucose Precursor (hard carbon precursor pyrolyzed)	300	239				[15]
2	R. Alcantra, et al.	2005	Na	Carbon Microspheres	Max: 285 Normal: 247	229 204				[235]
3	Y. Cao, et al.	2012	Na	Hollow Carbon Nanowires (HCNWs)	149, 200, 251	132, 171, 207	0.01-1.20	0.05, 0.125, 0.5	200 (retain 90%) 400 (retain 82.2%)	[25]
4	Y. Kim, et al.	2013	Na	Amorphous red phosphorus / carbon composite	Max.: 1890 Normal: 1540	721 663	0.4	0.143-2.86		[228]
5	Y. Wang, et al.	2013	Na	$P_2 – Na_{0.66}$ [$Li_{0.22}$ $Ti_{0.78}$]O_2	60	57		1200		[85]
6	Wang, Y.X. et al.	2013	Na	Reduced graphene oxide (r-GO)	174.3, 141	151.6 126		0.04	250, 1000	
7	B. Jache, et al.	2014	Na	Graphite in Diglyme (DGM) based Electrolyte	100	92		1000		[236]
8	Yang Wen, et al	2014	Na	Expanded Graphite	Max.: 284 Normal: 184	228 159	0.3	0.02-0.1	200 (retain 73.9% of capacity)	[237]
9	Zhe Hu, et al.	2014	Na	Graphene-like MoS_2 nanoflowers (FG-MoS_2)	Max: 243 Min: 160	201 141	0.4	0.2 / 1 / 10		[89]

Table 1A.1: Sample of proposed materials for sodium ion batteries (NIBs) in chronological order										
Row	**Authors**	**Year**	**Charge Transfer Agent**	**Anode Material**	**Reported capacity, mA h g^{-1}**	**Capacity (Eq. 2.1), mA h g^{-1} ***	**Voltage, voltage**	**Current, A/g**	**Cycles**	**Ref.**
10	David L and Singh G.	2014	Na	Reduced graphene oxide (r-GO)	140	125		0.100	1000	[56]
11	Gu-Ying Chen, et al.	2015	Na	FeSe	253.7	208.4	1.2-3.0			[238]
12	Zhiqiang Zhu, et al.	2015	Na	Graphite in Tetraglyme (TGM) based Electrolyte	110	101	0.75	10	6000	[239]
13	Clement Bommier, et al.	2015	Na	Non-graphitisable Carbon (Hard Carbon)	300	239				[240]
14	Long Qie, et al.	2015	Na	Sulfur-Doped Carbon Nitrogen-Doped Carbon	Max.: 384.5 Normal: 116.9	289.1 106.2		0.5	500-700	[211]
15	Yihang Liu, et al.	2015	Na	Nanocomposite of SnO_2 on conductive carbon cloth (CC) with ALD Al_2O_3 coating + C/SnO_2/CC	Max: 501 375 (after 100 cycles)	350 284			100 (with 80% retention)	[241]
16	Kang, Y.J. et al.	2015	Na	Expanded graphite oxide (GO); epoxide only GO ($Na_{2.5}C_6O_3$)	930	517				[242]

Table 1A.1: Sample of proposed materials for sodium ion batteries (NIBs) in chronological order										
Row	**Authors**	**Year**	**Charge Transfer Agent**	**Anode Material**	**Reported capacity, mA h g^{-1}**	**Capacity (Eq. 2.1), mA h g^{-1} ***	**Voltage, voltage**	**Current, A/g**	**Cycles**	**Ref.**
17	Kumar, N.A. et al.	2016	Na	Reduced graphene oxide (r-GO)	272	221	0.005 – 3	0.05	More than 300	[48]
18	Gaddam R.R. et al.	2017	Na	Nitrogen-rich hard carbon (*N-HCS*)	~520	~360	0.005 – 3	0.02	More than 1000	[39]
19	Bhauriyal, P. et al.	2018	Na	C_3N	1072	558	0.13-0.26			[84]

Appendix 2A

List of the INCAR file's tags used for different types of calculations in our projects

1. Tags for geometry optimisation:

ISTART = 0	Indicates the beginning of a calculation from the base, or continue from the previous run (=1)
ICHARG = 2	Indicates constructing the charge density by superposition, or reading from the CHGCAR of the previous run (=1)
ISMEAR = 0	Indicates the *Gaussian smearing method* for smearing
SIGMA = 0.05	Determines the value of σ for the Gaussian smearing method
IBRION = 2	Indicates the *conjugate gradient algorithm* for ionic minimisation cycles
NSW = 1000	Indicates the maximum number of ionic minimisation cycles
ISIF = 2	Indicates the method used for the stress tensor calculation and lattice optimisation
ISPIN = 2	Indicates the inclusion of spin polarisation, or not (=1)
LPLANE = .TRUE	Parallelisation tag used for supercomputing clusters
NPAR = 1	Parallelisation tag for bundling the number of cores working on N bands.
LREAL = F	Indicates the projection done in reciprocal space rather than real space
PREC = NORMAL	Indicates the selection of ENCUT given in the INCAR file
ALGO = FAST	Indicates the speed/type of algorithm for electronic ionic minimisation

IVDW = 12	Indicates the method used for the vdW correction (discussed in sec. 3.3.5)
ENCUT = 700	Indicates the E_{cut} (discussed in sec. 3.4.2.2)
EDIFF = 1e-6	Indicates the energy convergence criteria (discussed in sec. 3.3.4)
EDIFFG = -0.05	Indicates the force convergence criteria (discussed in sec. 3.3.4)

2. Tags for single point calculations [58]:

IBRION = -1	Indicates the single point calculation without any ionic minimisation
NSW = 0	Indicates 1 cycle only for self-consistency test

3. Transition state calculation by NEB method [19]:

SPRING = -5	Indicates use of the NEB method (sec. 3.4.5)
LCLIMB = .TRUE	Indicates the use of climbing image methods [205]
IMAGES = 1	Indicates the number of images in-between the local minima

4. Tags for Density of States (DOS) [19]:

IBRION = -1	See above
NSW = 0	See above
PREC = ACCURATE	See above
LORBIT = 10	Indicates the calculation of DOSCAR file for the purpose of DOS analysis

5. Tags for Bader charge analysis[19]:

IBRION = -1	See above
NSW = 0	See above
PREC = ACCURATE	See above
LAECHG = .TRUE	Indicates getting the AECCAR0 1 and 2 files, including the charge values of all ions intended for Bader analysis

6. Tags for calculating the electron localisation function (ELF) [19]:

IBRION = -1	See above
NSW = 0	See above

[58] The other input tags required for this type of calculation are those we mentioned in item 1.

LELF = .TRUE	Indicates the writing of ELFCAR file intended for visualization
PREC = HIGH	See above

7. Tags for charge density difference (CDD) [19]:

IBRION = -1	See above
NSW = 0	See above
PREC = ACCURATE	See above
LCHARG = .TRUE	Indicates that the CHGCAR file will be written. This is intended for charge density visualisation
ENCUT = 1000	See above

8. Tags for electrostatic charge potential calculation [19]:

IBRION = -1	See above
NSW = 0	See above
LVTOT = .TRUE	See above

A typical POSCAR file for hydrogenated defective graphene (4H1-MVG) material (Chapter 5)

```
H4_MVG_4V68_Corr_dd08_CCS_out
1.0
     14.2063999176      0.0000000000      0.0000000000
     -6.4437380354     12.6609651587      0.0000000000
     -0.0353451698     -0.0535741904     19.9906978230
   C   H
  68   4
Direct
    0.998690009    0.998459995    0.469760001
    0.056320000    0.109569997    0.460559994
    0.161119998    0.980250001    0.484360009
    0.214530006    0.092179999    0.470140010
    0.327820003    0.992389977    0.519760013
    0.375959992    0.104780003    0.509869993
    0.511929989    0.011690000    0.529079974
    0.556720018    0.120630004    0.521849990
    0.017990001    0.182569996    0.479059994
    0.088859998    0.292620003    0.493889987
    0.161100000    0.145669997    0.445270002
    0.319880009    0.160319999    0.488680005
    0.365960002    0.275310010    0.487450004
    0.485520005    0.162650004    0.516099989
    0.541509986    0.270080000    0.503000021
    0.030139999    0.349260002    0.514429986
    0.075790003    0.460929990    0.521139979
    0.205559999    0.354820013    0.492190003
    0.240309998    0.468879998    0.495799989
    0.313300014    0.345840007    0.484699994
    0.389759988    0.453669995    0.476969987
    0.483480006    0.326579988    0.489439994
    0.549449980    0.434599996    0.477629989
    0.011930000    0.511690021    0.529030025
    0.056720000    0.620630026    0.521799982
    0.183809996    0.526910007    0.509339988
    0.235070005    0.644429982    0.511330009
    0.347739995    0.524869978    0.482710004
    0.405609995    0.634429991    0.488940001
    0.498690009    0.498459995    0.469749987
    0.556330025    0.609570026    0.460550010
    0.683809996    0.026910000    0.509379983
    0.735069990    0.144429997    0.511370003
    0.847729981    0.024870001    0.482730001
    0.905600011    0.134419993    0.488959998
    0.664550006    0.197090000    0.514119983
    0.850059986    0.190500006    0.510140002
    0.918219984    0.295850009    0.528659999
    0.655560017    0.304830015    0.506619990
    0.717769980    0.421530008    0.504920006
    0.864740014    0.349280000    0.553529978
    0.900829971    0.454059988    0.538240016
```

The file name

The lattice parameters in real space:

$$\begin{bmatrix} a_{1x} & a_{1y} & a_{1z} \\ a_{2x} & a_{2y} & a_{2z} \\ a_{3x} & a_{3y} & a_{3z} \end{bmatrix}$$

C: carbon (68 atoms),
H: hydrogen (4 atoms)

Coordinates of C and H atoms, r_x, r_y, r_z

0.661119998	0.480250001	0.484369993
0.714529991	0.592180014	0.470160007
0.827820003	0.492399991	0.519760013
0.875959992	0.604780018	0.509869993
0.985520005	0.662649989	0.516080022
0.041510001	0.770079970	0.502990007
0.164550006	0.697090030	0.514079988
0.350059986	0.690500021	0.510119975
0.418199986	0.795840025	0.528670013
0.517989993	0.682569981	0.479050010
0.588850021	0.792620003	0.493900001
0.983470023	0.826579988	0.489450008
0.049449999	0.934610009	0.477640003
0.155560002	0.804830015	0.506600022
0.217769995	0.921530008	0.504909992
0.364719987	0.849269986	0.553539991
0.400819987	0.954050004	0.538269997
0.530139983	0.849259973	0.514450014
0.575779974	0.960929990	0.521189988
0.661109984	0.645669997	0.445279986
0.819880009	0.660329998	0.488689989
0.865960002	0.775319993	0.487470001
0.705550015	0.854830027	0.492210001
0.740300000	0.968879998	0.495819986
0.813290000	0.845839977	0.484719992
0.889760017	0.953670025	0.476990014
0.286399990	0.804459989	0.573740005
0.205899999	0.223979995	0.425069988
0.705929995	0.723990023	0.425089985
0.786430001	0.304479986	0.573750019

Appendix 2B

Calculations to determine optimum E_{cut} and k-point grids for graphdiyne and graphene

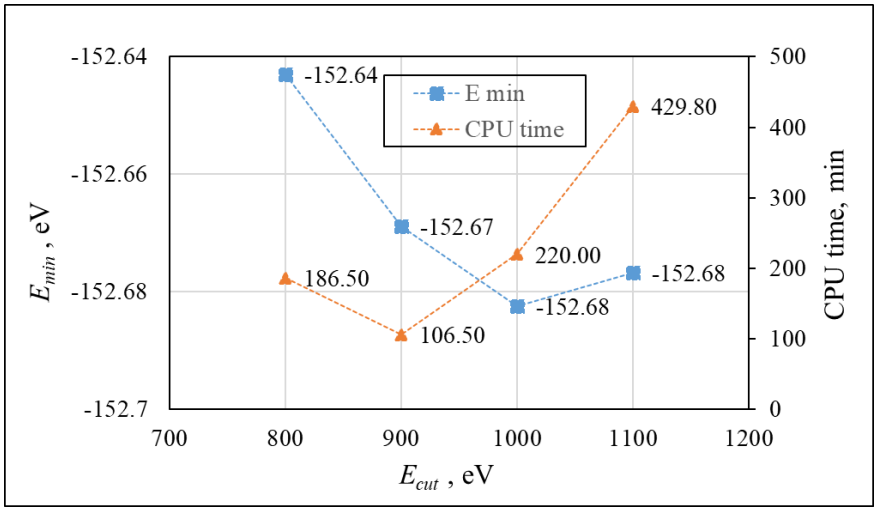

Fig. 2B.1: Variation of E_{min} and CPU time (minutes) against E_{cut} for GDY single layer

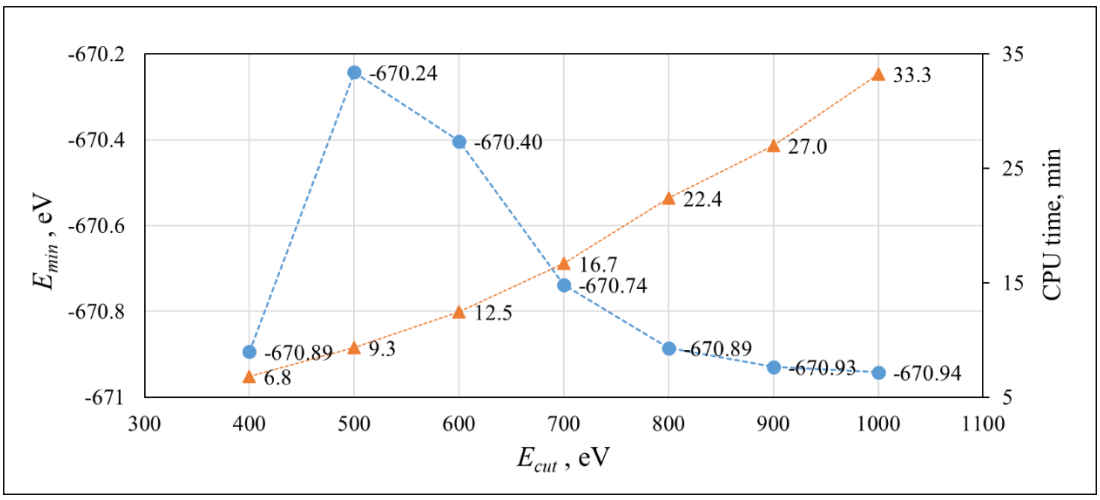

Fig. 2B.2: Variation of E_{min} and CPU time (min) against E_{cut} for graphene sheet (6×6 rings)

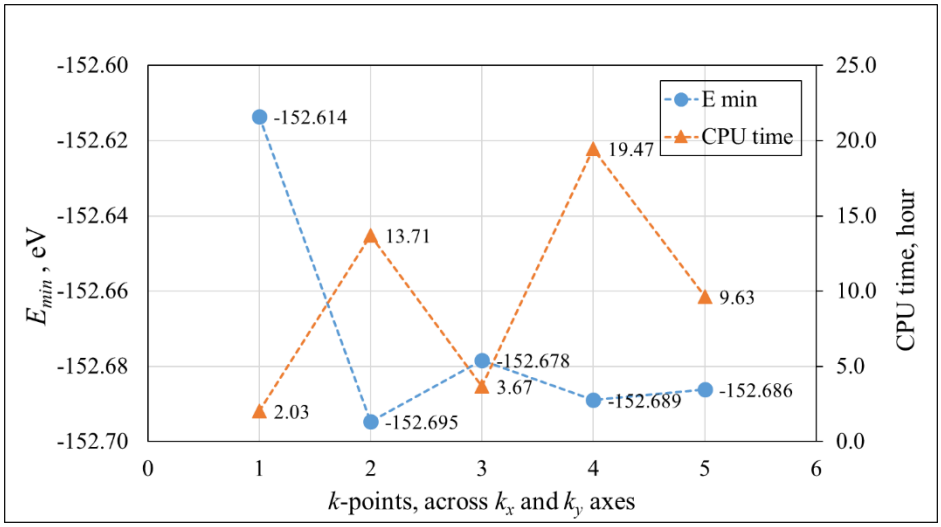

Fig. 2B.3 Variation of ground state energy (E_{min}) of GDY, depicted by the blue line, and CPU time (hours), depicted by the orange line. The values on the horizontal axis indicate the number of grid points for the lattice vectors in the GDY plane. For example, 3 represents 3×3×1 grid. The dashed lines serve as visual guides.

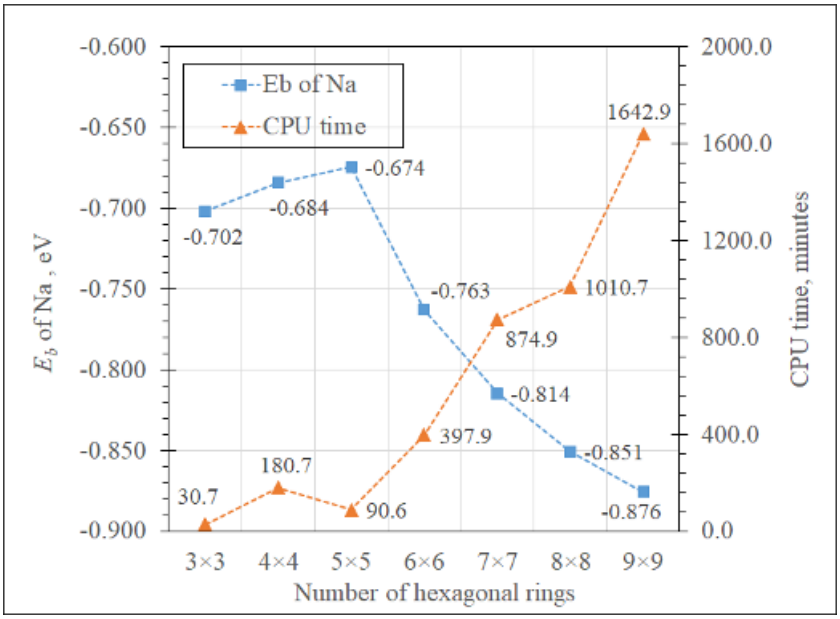

Fig. 2B.4 Variation of the binding energy (eV, blue line) of Na to a graphene sheet modelled as a supercell of various sizes with periodic boundary conditions and a 20 Å vacuum above the surface. All calculations were geometry optimization carried out using the parameters described in the Methods section of this study. The non-monotonic change in the binding energy is caused by the strong interactions between Na atoms in the periodic cells in the small systems which is consistent with previous results (Bommier et al. Chem. Mater. **2018**, 31, 658-677). The CPU computation time (minutes, orange line) is also plotted against the number of hexagonal rings in the supercell. The irregular change in the CPU time was due to different number of cores used in the calculations. The number of rings is set to be the same in both x and y directions. The dashed lines serve as visual guides.

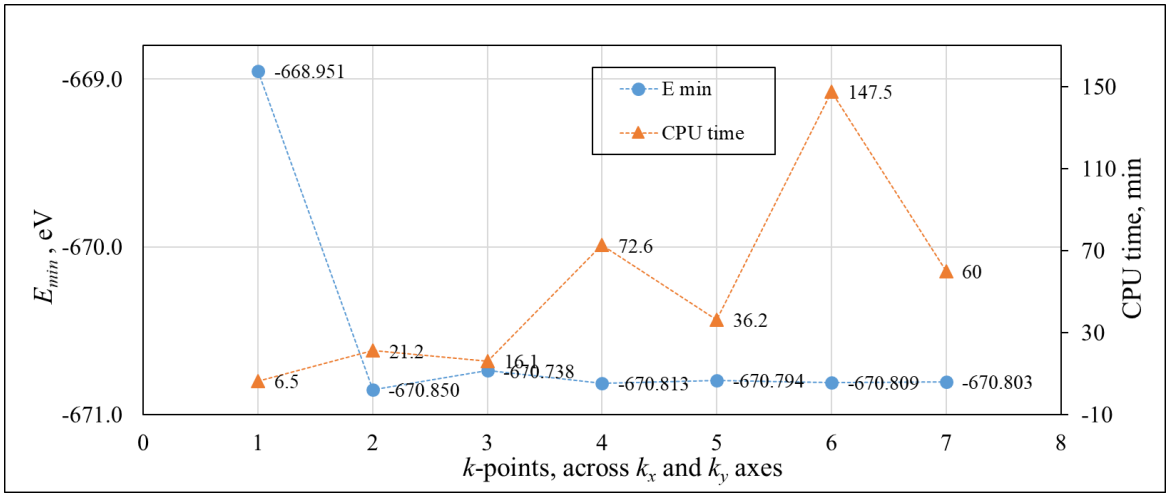

Fig. 2B.5 Variation of E_{min}, depicted by the blue line, and CPU computational time (minutes), depicted by the orange line for graphene sheet (6×6 rings). The values on the horizontal axis indicate the number of grid points for the lattice vectors in the graphene plane. For example, 3 represents 3×3×1 grid. The dashed lines serve as visual guides.

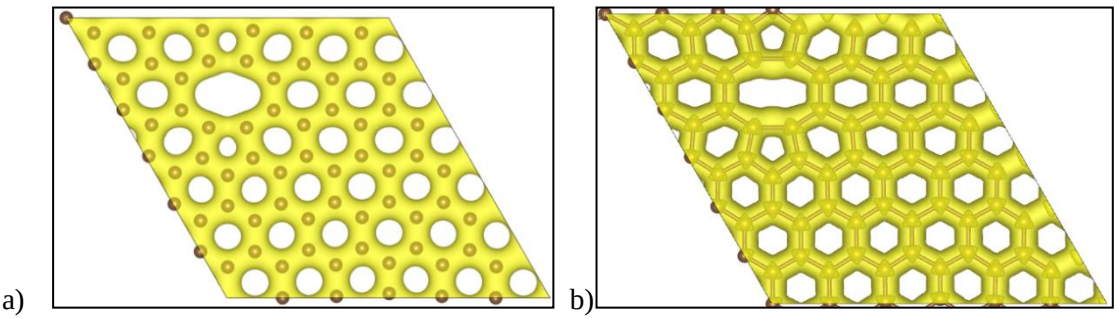

Fig. 2B.6: a) constant charge density isosurface using CHGCAR file, b) electron localisation isosurface using ELFCAR file for a di-vacancy (DV) in a graphene sheet

Appendix 2C

Summary of tags and parameters used for the DFT calculations in Chapters 4, 5, 6, and 7

The following items summarise the parameters of VASP used for the materials in our projects: GDY, 4(H1-MVG); F-GNR; *N*-HCS; and r-GO. We reviewed these parameters completely in sections 3.3 to 3.6.

- The sizes of supercells (obtained by optimisation) [59]:
    - GDY: 9.462 × 9.462 × 15 Å for single layer, 9.455 × 9.455 × 6.58, Å for bulk layers.
    - 4(H1-MVG): 14.21 × 14.21 × 20 Å for single layer, 14.21 × 14.21 × 6.97 Å for bulk layers.
    - H-ZGNR: 40 × 19.76 × 20 Å, H-AGNR: 60 × 17.16 × 20 Å [60].
    - *N*-HCS: 14.77 × 14.77 × 60 Å (all single layer).
    - r-GO: 14.80 × 14.80 × 20 Å (all single layer).

[59] The full descriptions of the optimised cell sizes are given in Chapters 4, 5, 6 and 7
[60] Other types of F-GNRs (HO1-, O1-, Ot-, and HOOC-Z/AGNRs) have close sizes to the size of H-Z/AGNR in *y* direction

- Gaussian method for smearing with σ=0.05
- Maximum cut-off energy (E_{cut}) of 1000 eV for GDY, and 700 eV for 4(H1-MVG), F-GNR, *N*-HCS and r-GO
- Energy convergence criteria, EDIFF = 1×10^{-6} eV
- Force convergence criteria, EDIFFG = -0.05 eV/Å as a medium precision for GDY, and F-GNRs; and -0.01 eV/Å as a high precision for GDY, H-rG, *N*-HCS and r-GO
- van der Waals' dispersion method of D2 Grimme [188, 189] for GDY, and D3-BJ Grimme [64, 190] for 4(H1-MVG), F-GNR, *N*-HCS and r-GO
- *k*-point grids: Monkhorst-Pack type [193]:
    - 3 × 3 × 1 for single layer of GDY, 4(H1-MVG), *N*-HCS and r-GO
    - 3 × 3 × 2 for bulk layers of GDY and 4(H1-MVG)
    - 11 × 11 × 1 for DOS analysis of 4(H1-MVG) single layers
    - *Γ*-point (1×1×1) for F-GNRs

Appendix 3

The minimum energy structure of AB-3 stacked GDY with a single Na atom per unit cell is shown in Fig. 3A.1. In Fig. 3A.2, the total density of states for a single layer of GDY with two different Na loadings is compared with pristine GDY, and in Fig. 3A.3 the partial density of states for the system of 1 Na atom on a single GDY layer is shown.

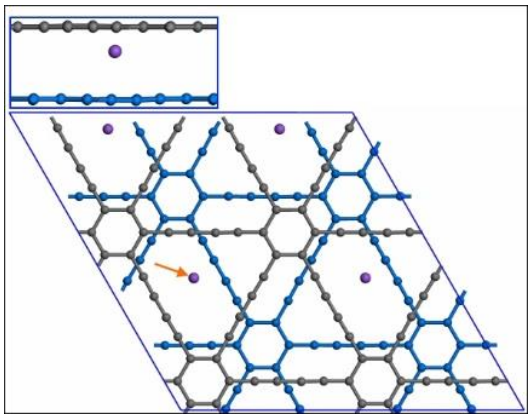

Fig. 3A.1. Minimum energy structure of a supercell (2 × 2 × 1 unit cells) of bulk GDY with AB-3 stacking, intercalated with 1 Na atom per unit cell (indicated by the orange arrow). The binding energy of the Na atom to the GDY, E_b, is -3.01 eV. Grey and blue balls represent carbon atoms with the different colours used to distinguish between the layers. Purple balls represent sodium atoms. The inset shows a side view of part of the supercell.

a)

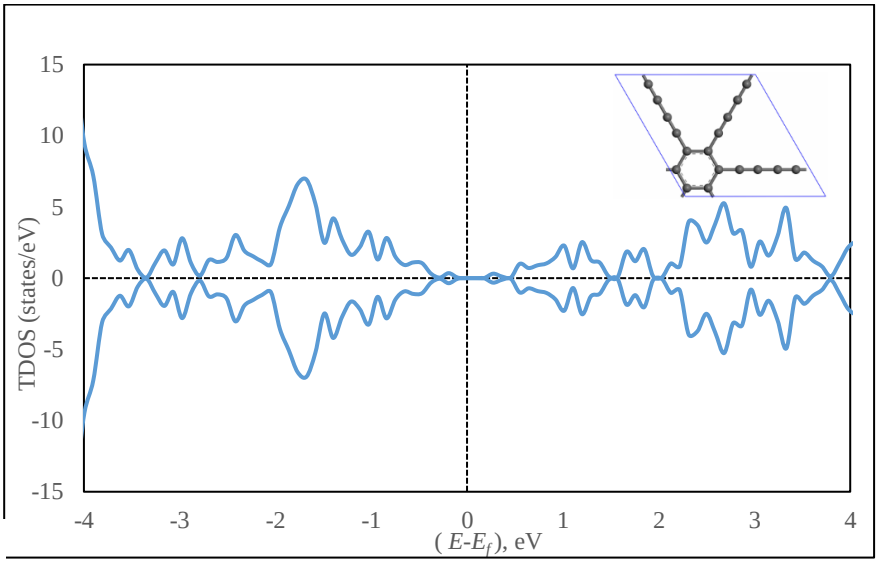

b)

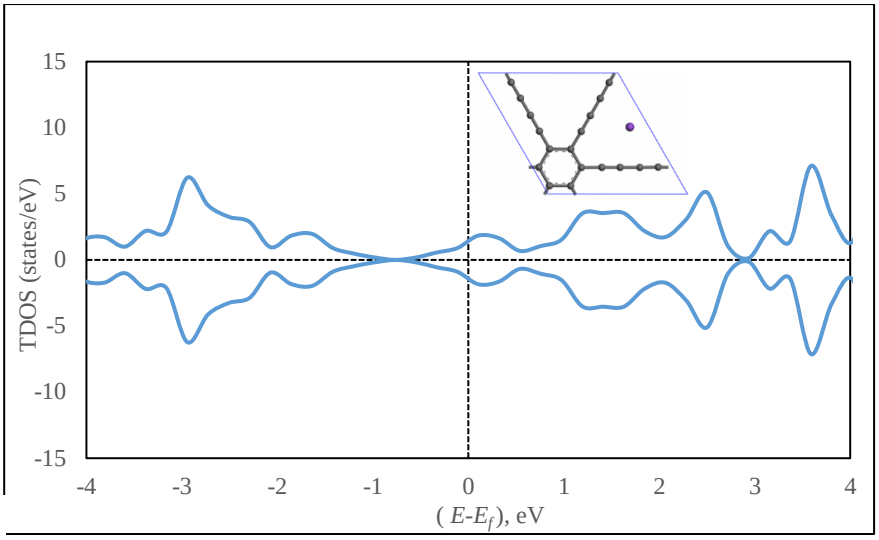

c)

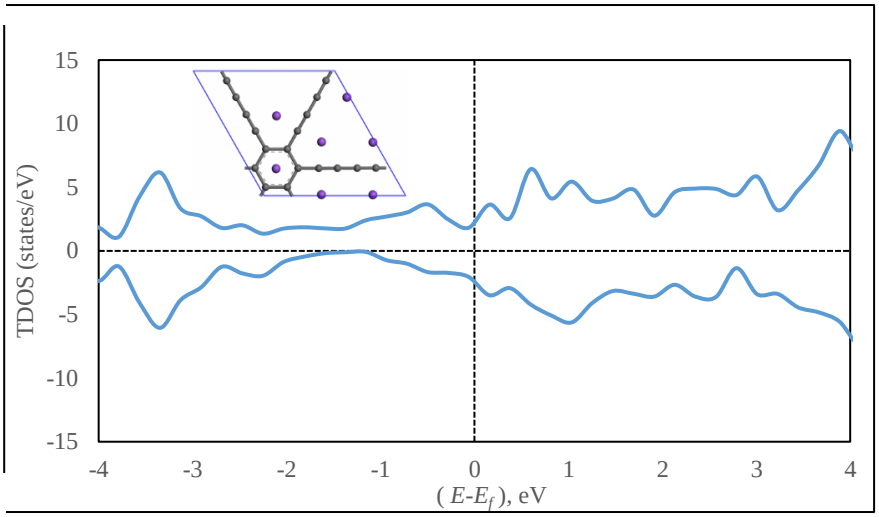

Fig. 3A.2. Total density of states (TDOS) for (a) pure GDY, (b) GDY Na and (c) GDY Na_7. The insets show the structures considered with C atoms represented by grey balls and Na atoms by purple balls. The energy shown is relative the Fermi energy, E_f.

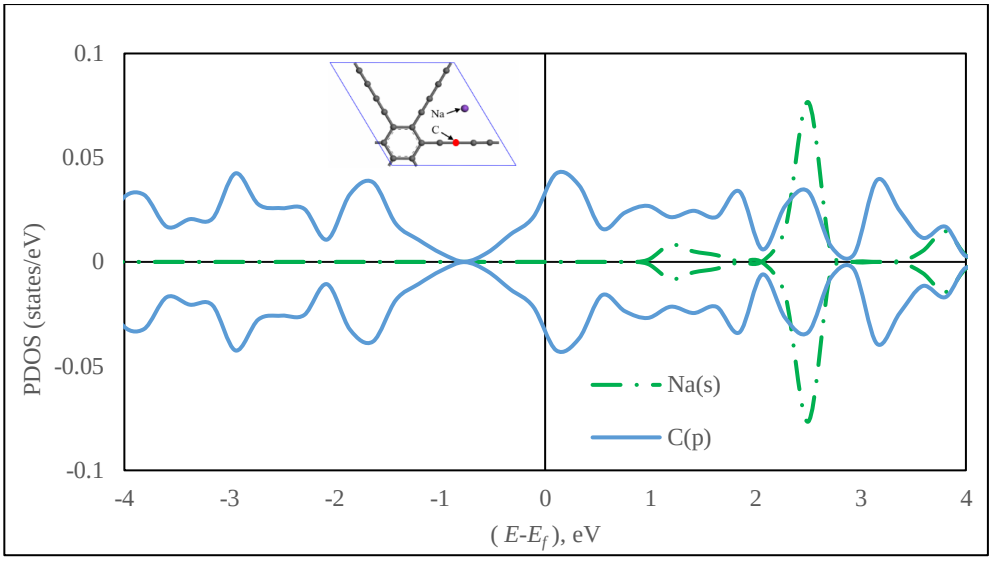

Fig. 3A.3. Na(s) (green dot-dashed line) and C(p) (blue solid line) partial densities of states for a system consisting of an Na atom on a single unit cell of GDY. The inset shows the structure of the system with the Na atom shown as a purple ball and the C atoms as grey balls. The C atom considered is highlighted in red (i.e. the second carbon atom of the 4-carbon chain of GDY). The energy shown is relative the Fermi energy, E_f.

Appendix 4

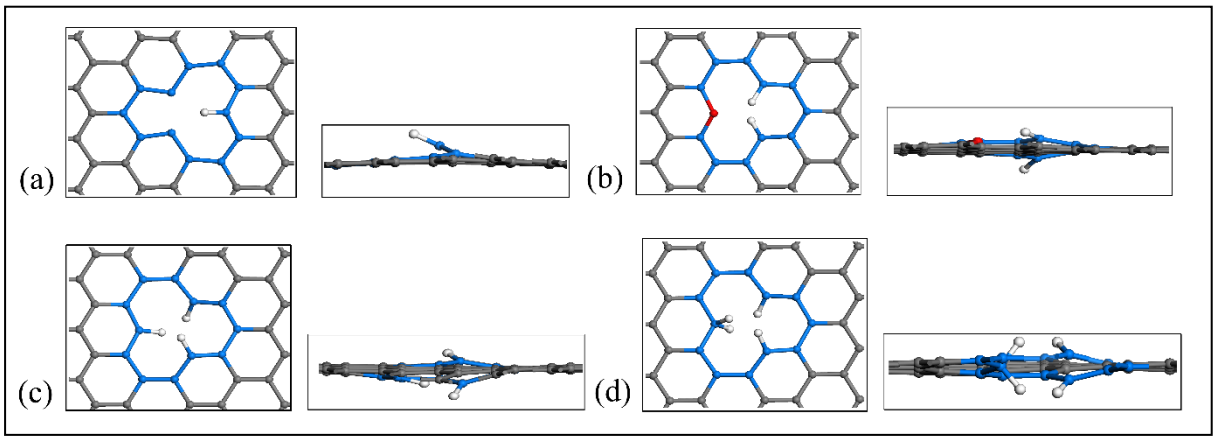

Fig. 4A.1. Top and side views of the optimised graphene sheets with hydrogenated MVs. (a) H1-MVG, (b) H2-MVG, (c) H3-MVG, and (d) H4-MVG. Note that the terminology used gives the number of hydrogen atoms after 'H' and the type of vacancy after the underscore. The white atoms are hydrogen atoms and all the others are C atoms. Those coloured in blue surround a vacancy.

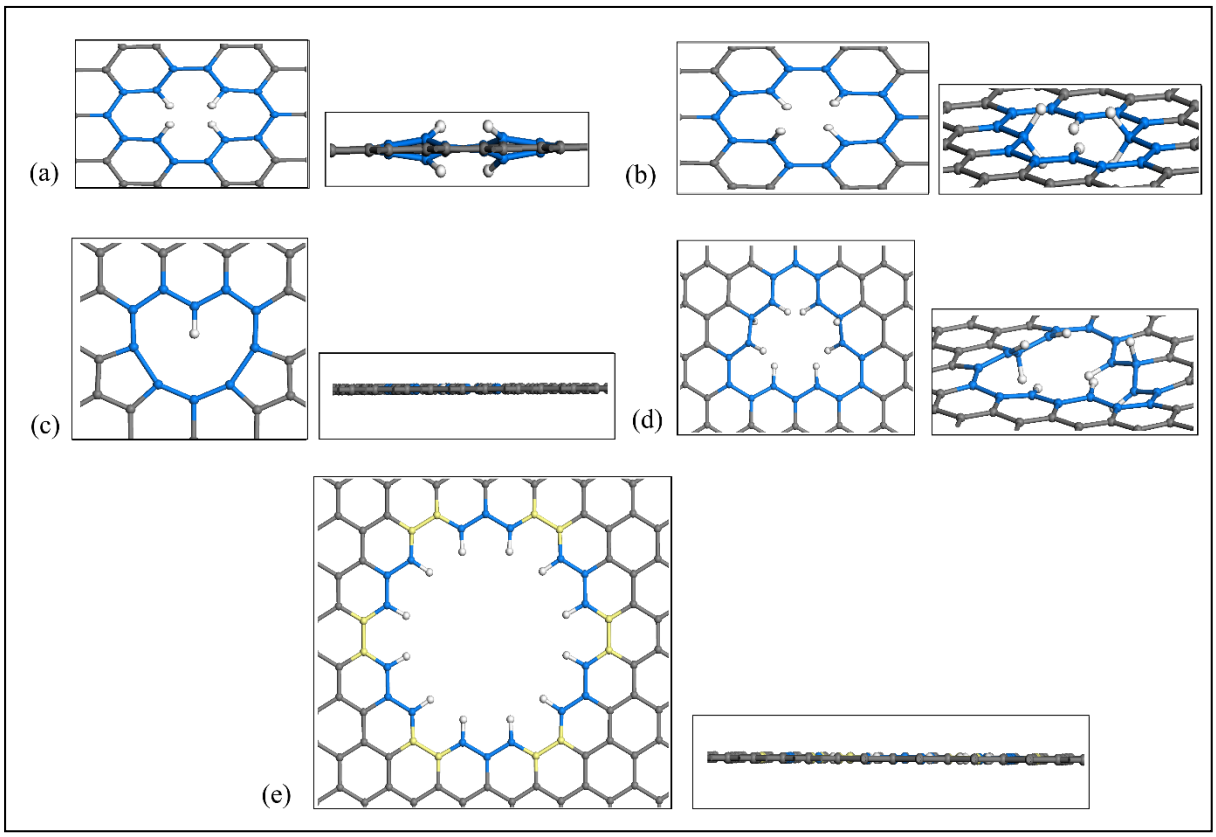

Fig. 4A.2. Top and side views of selected graphene materials with hydrogenated vacancies: (a) H4-DVG ($C_{70}H_4$), (b) H6-DVG ($C_{70}H_6$), (c) H1-TVG ($C_{69}H_1$), (d) H8-QVG ($C_{68}H_8$), and (e) H12-24VG ($C_{138}H_{12}$). The white atoms are hydrogen atoms and all others are C atoms. Those coloured in blue surround the vacancy. In e) boat type and zig-zag type carbons around the vacancy are also distinguished by colouring in yellow and blue, respectively.

Table 4A.1. Hydrogenation energy and average C-H bond lengths for graphene sheets with a hydrogenated mono-vacancy. ΔE_f is the formation energy of hydrogenation.

Material	Empirical formula	Optimal C-H bond configuration	Average C-H bond length / Å	ΔE_f / eV
H1-MVG	$C_{71}H_1$	-	1.08	-4.25
H2-MVG	$C_{71}H_2$	anti	1.09	-3.39
H3-MVG	$C_{71}H_3$	anti	1.07	-3.91
H4-MVG	$C_{71}H_4$	anti	1.08	-2.49

Table 4A.2. Binding energies (eV) of Na at different sites of defective graphene and hydrogenated defective graphene. For location of sites, refer to Fig. 5.4b.

Material	E_b at various sites eV Na^{-1}							
	Centre of vacancy	A / B (over vacancy)	C	D	2 Na over	3 Na	4 Na	5 Na
MVG	NS[a]	-2.083	-1.506	-1.320	-1.535	-1.376	-1.228	-1.173
DVG	NS[a]	-1.792	-1.524	-1.282	-1.285	-1.294	-1.256	-1.180
TVG	NS[a]	-2.350	-1.789	-1.581	-1.847	-1.588	-1.470	-1.313
QVG	-0.939	-2.185	-1.886	-1.666	-1.657	-1.480	-1.393	-1.290
24VG	-0.968	-2.909	NS[a]	-1.043	NC[b]	NC[b]	NC[b]	NC[b]
H1-MVG	NS[a]	-1.481	-1.546	-1.363	-1.214	-1.197	-1.111	-1.080
H2-MVG	NS[a]	-2.070	-1.588	-1.458	-1.484	-1.341	-1.279	-1.171
H3-MVG	NS[a]	-1.472	-1.261	-1.162	-1.120	-1.252	-1.069	-1.032
H4-MVG	NS[a]	-0.837	-0.783	-0.764	-1.022	-0.969	NC[b]	NC[b]
H4-DVG	NS[a]	-0.879	-0.878	-0.841	-0.890	-0.998	-0.965	-0.959
H6-DVG	NS[a]	-0.894	-0.888	-0.956	-0.929	-1.056	-1.026	-0.994
H1-TVG	NS[a]	-1.963	-1.773	-1.578	-1.315	-1.295	-1.214	-1.132
H8-QVG	-0.490	-1.241	-1.165	-1.118	NS[a]	NS[a]	DH[c]	DH[c]
H12-24VG	-0.249	-0.842	-0.871	-0.817	NC[b]	NC[b]	NC[b]	NC[b]

[a] NS: not a stable site (movement to another location like the nearest site)

[b] NC: not calculated

[c] DH: detachment of H atoms from substrate after Na adsorption

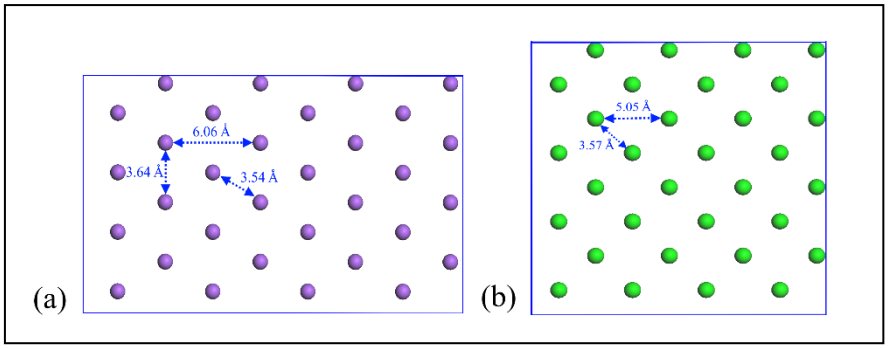

Fig. 4A.3. Supercell for a single layer of metal atoms arranged in a (a) 110 configuration for Na (purple coloured), and (b) 100 Ca atoms (green coloured). These structures were obtained by optimisation using DFT computations, including optimisation of the lattice parameters. The distances between neighbouring atoms are indicated.

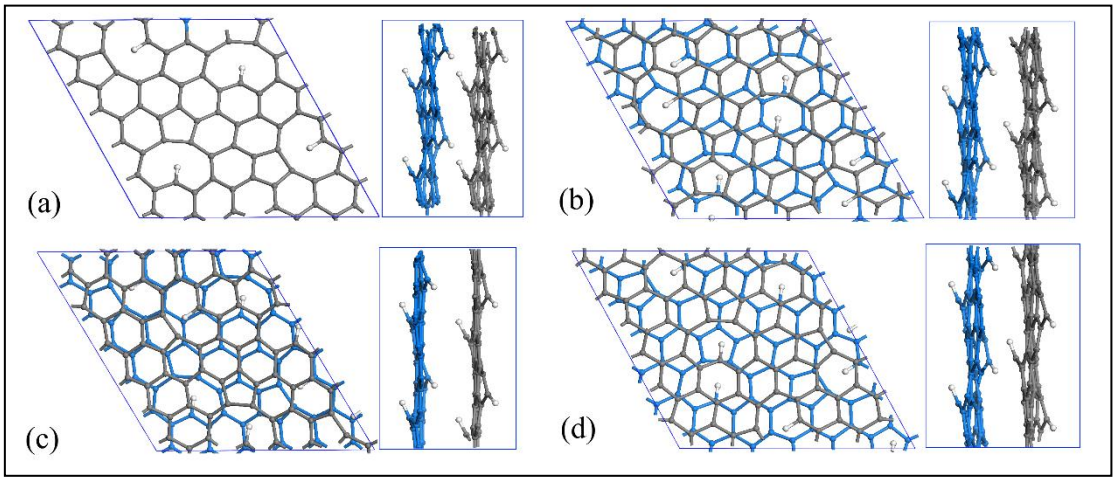

Fig. 4A.4. Structures of 4 different stackings of 4(H1-MVG) bulk layered materials with their ΔE (= $E_{ABi\ stacking} - E_{AA\ stacking}$), and inter-layer distances (D). (a) AA stacking with D = 3.49 Å, (b) AB1 stacking with ΔE = +0.9 eV, and D = 3.54 Å, (c) AB2 stacking with ΔE = +1.8 eV and D = 3.80 Å, (d) AB3 stacking with ΔE = +0.9 eV and D = 3.56 Å. The inter-layer distance (D) is measured through vertical distance between the two centres of mass of the two layers. In all the figures, the grey carbon atoms indicate the top layer, and blue carbon atoms indicate the bottom layer. White atoms are hydrogen.

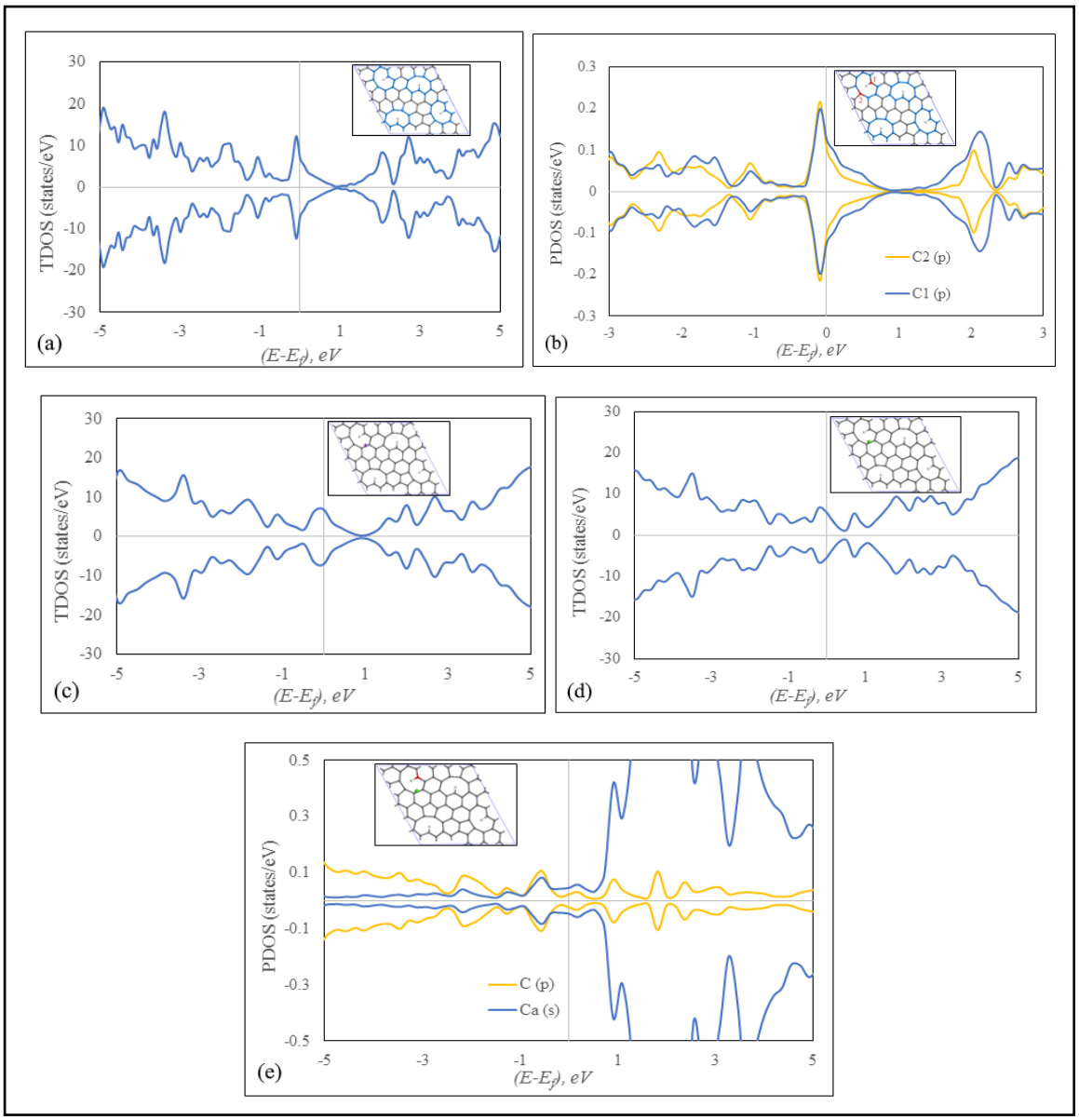

Fig. 4A.5. (a) TDOS for 4(H1-MVG) pristine, (b) PDOS for the two indicated carbon atoms in 4(H1-MVG) single layer, (c) TDOS for 1 Na + 4(H1-MVG), (d) TDOS for 1 Ca + 4(H1-MVG), (e) PDOS for 1 Ca and the indicated carbon atom (red).

Appendix 5

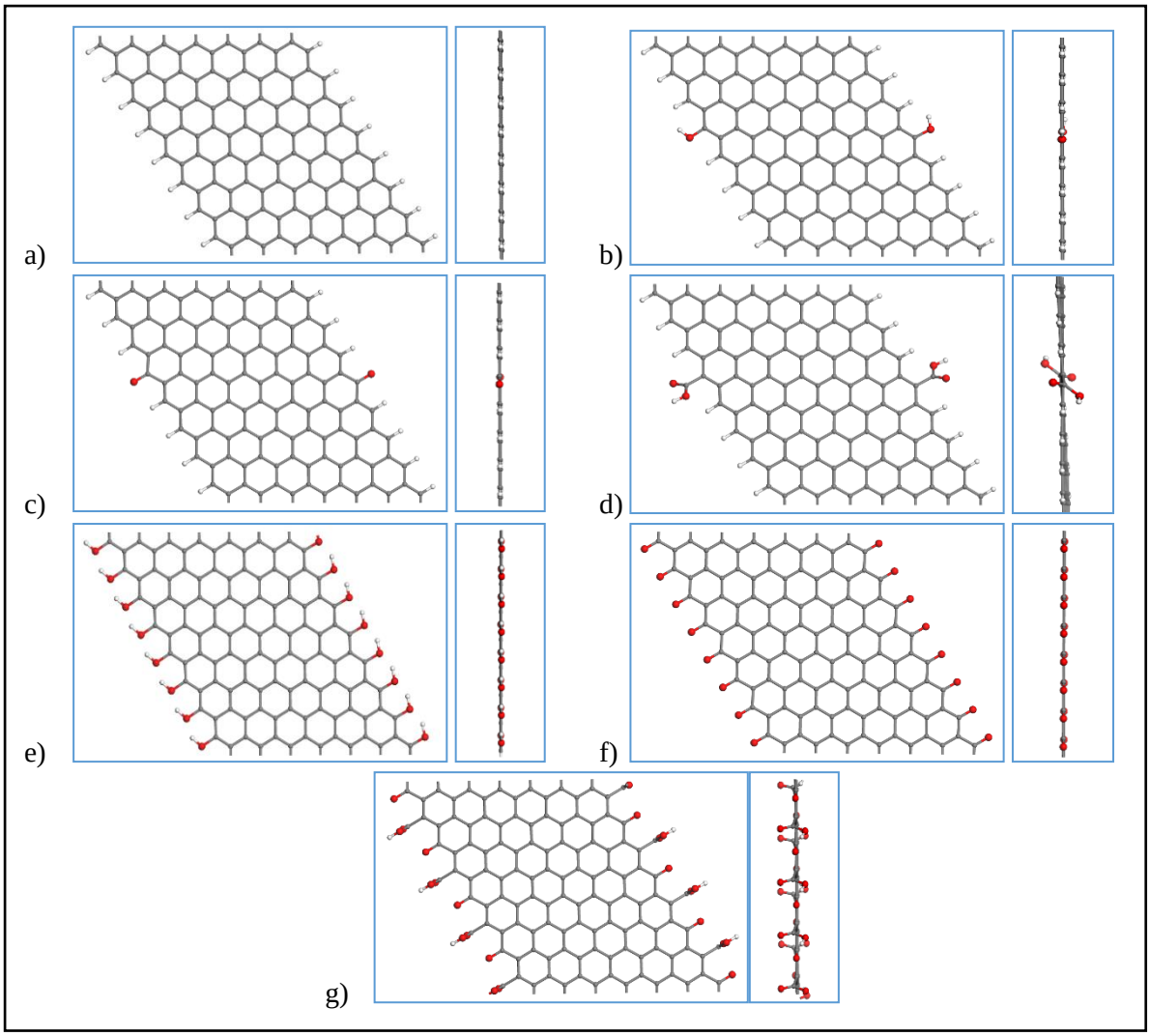

Fig. 5A.1: Top and side views of the supercells of the F-ZGNRs, a) H-ZGNR, b) HO-ZGNR, c) O-ZGNR, d) HOOC-ZGNR, e) HOt-ZGNR, f) Ot-ZGNR, g) O_HOOC_ZGNR

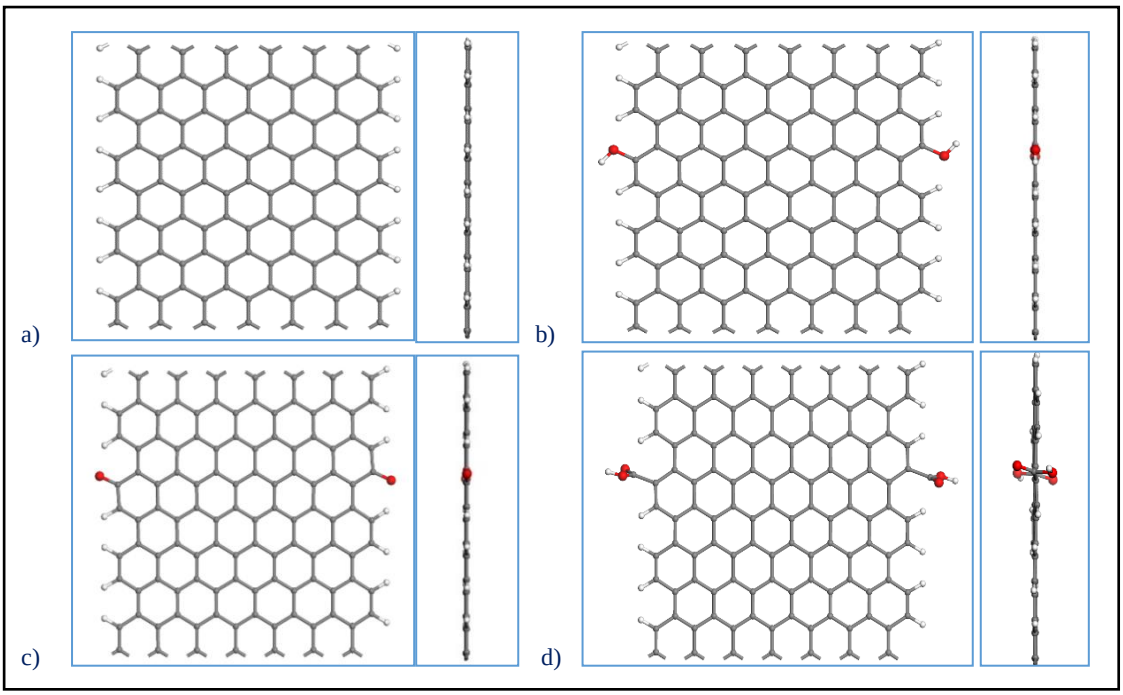

Fig. 5A.2: Top and side views of supercells of the F-AGNRs, a) H-AGNR, b) HO-AGNR, c) O-AGNR and d) HOOC-AGNR

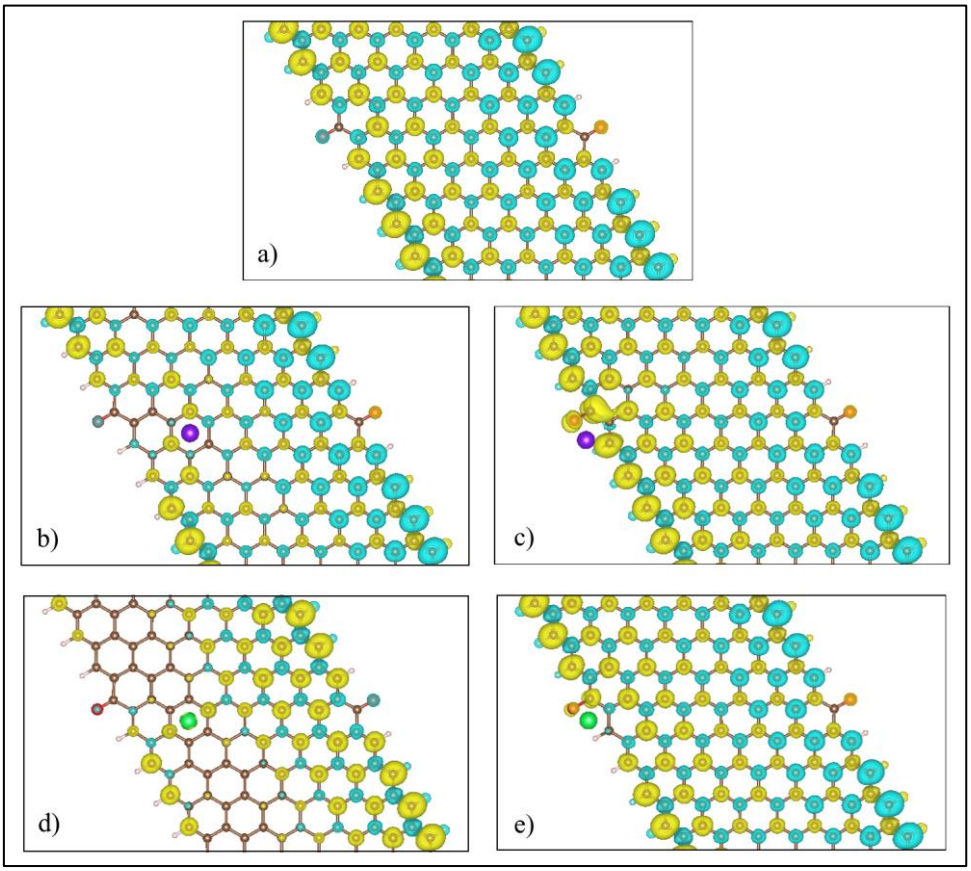

Fig. 5A.3: Spin density plots of a) O-ZGNR, b) O-ZGNR + Na at site R2 c) O-ZGNR + Na at site V, d) O-ZGNR + Ca at site R2, and e) O-ZGNR + Ca at site V. In all the figures the cyan and yellow colours indicate the opposite spin direction, e.g. up and down. For all the figures the isosurface is ζ=0.001 $e\ a_0^{-3}$

(a_0: Bohr radius). In all figures, the purple atoms indicate Na, green indicate Ca, red indicate O, white indicate H and grey indicate C atoms.

Table 5A.1: The binding energies (E_b) of Na adsorption over different sites of F-Z/AGNRs

		Binding Energy of Na / eV				
Edge Type	**Functional Groups**	**R3: Third ring**	**R2: Second ring**	**R1: First ring**	**V: Over the edge**	**F: In front of the edge**
Zigzag type	H-ZGNR	-0.990	-1.043	-1.188	-1.117	NS*
	HO-ZGNR	-1.003	-1.044	-1.138	-1.171	-0.546
	HOt-ZGNR	-0.834	-0.833	-0.763	-0.667	-0.080
	O-ZGNR	-1.078	-1.129	-1.217	-1.523	-1.401
	Ot-ZGNR	-1.837	-1.973	NS	NS	-4.078
	HOOC-ZGNR	-1.051	-1.117	-1.387	-1.964	NS
	O_HOOC-ZGNR	-1.753	-1.857	-2.585	-4.208	-3.539
Armchair type	H-AGNR	-1.118	-1.108	-1.076	-0.917	-0.174
	HO-AGNR	-1.110	-1.096	-1.056	-1.142	NS
	O-AGNR	-1.040	-1.088	-1.269	-2.062	-1.803
	HOOC-AGNR	-1.157	-1.153	-1.135	-2.090	NS

*: Not stable at the given site

Table 5A.2: The binding energies (E_b) of Ca adsorption over different sites of F-Z/AGNRs

		Binding Energy of Ca / eV				
Edge Type	**Functional Groups**	**R3: Third ring**	**R2: Second ring**	**R1: First ring**	**V: Over the edge**	**F: In front of the edge**
Zigzag type	H-ZGNR	-1.061	-1.247	-1.766	-1.595	NS*
	HO-ZGNR	-1.061	-1.235	-1.722	-1.520	-0.475
	HOt-ZGNR	-0.913	-0.987	-1.249	-1.046	NS
	O-ZGNR	-1.114	-1.289	-1.552	-2.421	-1.992
	Ot-ZGNR	-2.407	-2.551	-3.042	NS	-6.281
	HOOC-ZGNR	-1.099	-1.302	-2.365	-2.845	-0.105
	O_HOOC-ZGNR	-2.095	-2.177	-2.852	-5.858	-6.441
Armchair type	H-AGNR	-1.222	-1.217	-1.193	-1.045	-0.131
	HO-AGNR	-1.220	-1.213	-1.168	-1.405	NS
	O-AGNR	-1.038	-1.095	-1.472	-2.833	-2.452
	HOOC-AGNR	-1.284	-1.293	-1.529	-3.092	NS

* : Not stable at the given site

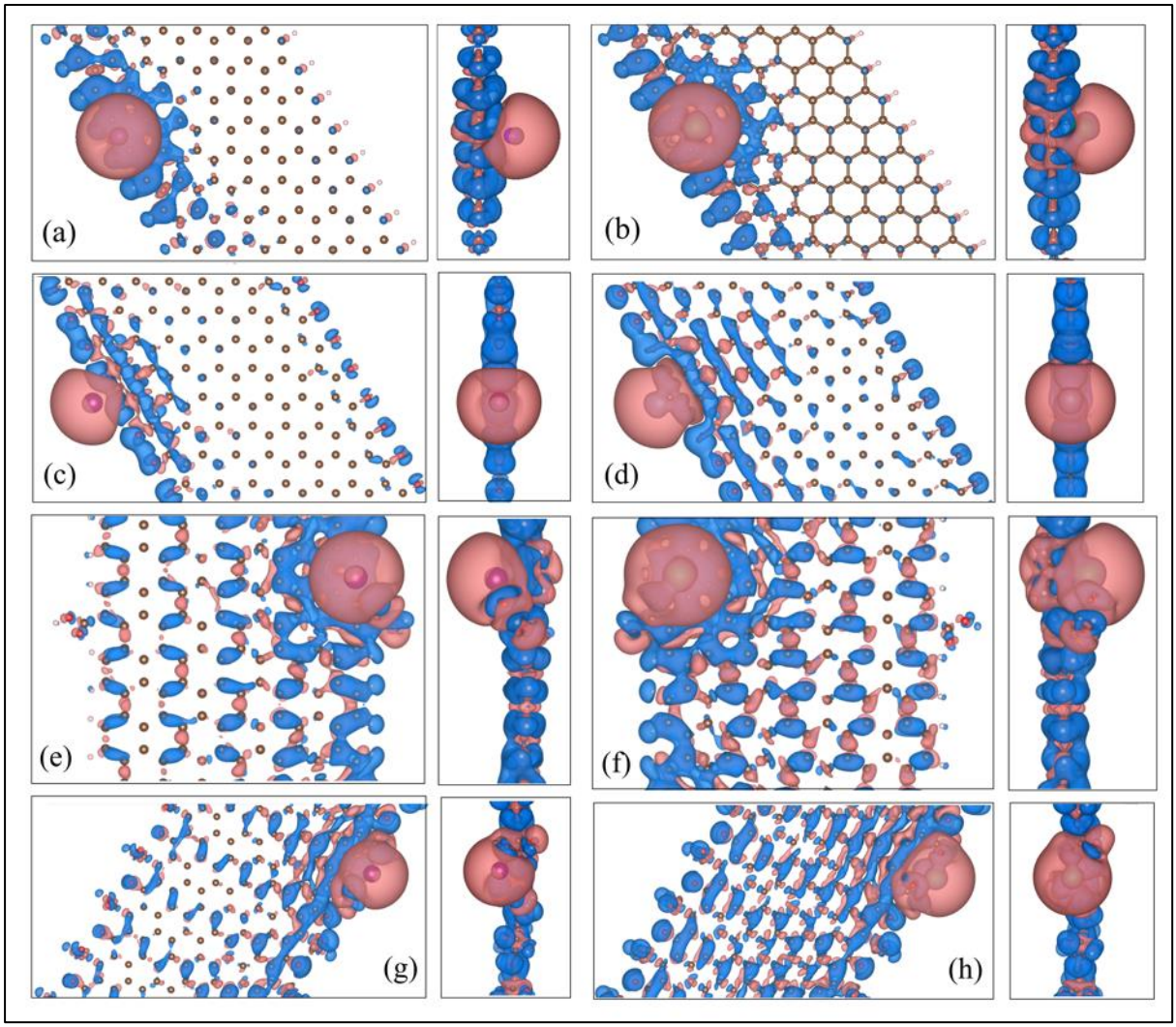

Fig. 5A.4: Top and side views of charge density difference of the F-Z/AGNRs with 1 Na or Ca adatoms, a) Na + H-ZGNR, b) Ca + H-ZGNR, c) Na + Ot-ZGNR, d) Ca + Ot-ZGNR, e) Na + HOOC-AGNR, f) Ca + HOOC-AGNR, g) 1Na + O_HOOC-ZGNR and h) 1Ca + O_HOOC-ZGNR. In all the cases the value of isosurface is ζ=0.0002 $e\ a_0^{-3}$ (a_0: Bohr radius).

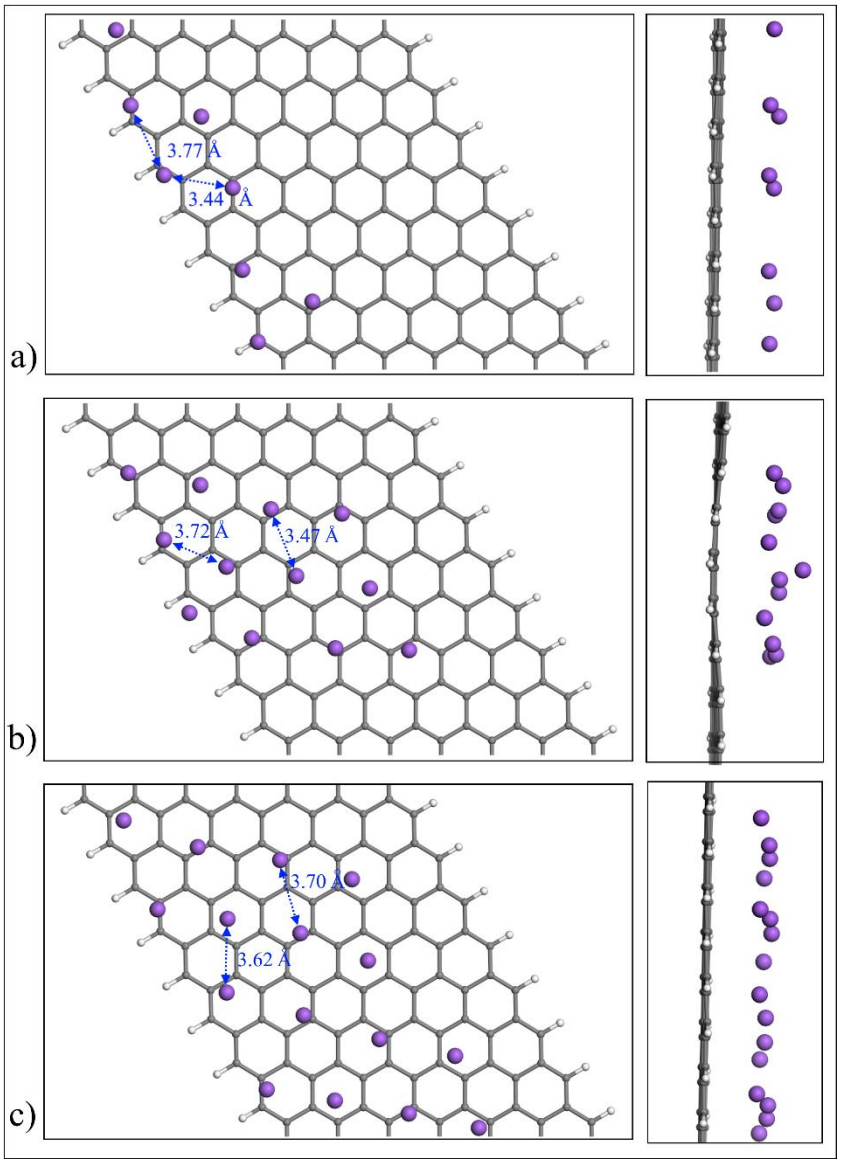

Fig. 5A.5: Top and side views of multiple Na adsorption over H-ZGNRs, a) 8 Na, b) 12 Na and c) 16 Na adatoms

Table 5A.3: Binding energies for multiple Na adatoms over H-ZGNR

Functional group	Binding energies / eV				
	2 Na	3 Na	8 Na	12 Na	16 Na
H-ZGNR	-1.04	-1.08	-1.09	-1.08	-1.07

Table 5A.4: Binding energies for multiple Na adatoms over O- and HOOC-AGNR

Functional group	Ribbon	Binding energies per atom / eV			
		2 Na atoms	3 Na atoms	4 Na atoms	5 Na atoms
O-	AGNR	-1.58	-1.33	-1.15	-1.16
HOOC-	AGNR	-1.39	-1.25	-1.04	-1.13

Table 5A.5: Binding energies for multiple Ca adatoms over O- and HOOC-AGNR

Functional group	Ribbon	Binding energies per atom / eV			
		2 Ca atoms	3 Ca atoms	4 Ca atoms	5 Ca atoms
O-	AGNR	-1.95	-1.89	-1.82	-1.78
HOOC-	AGNR	-2.18	-2.04	-1.92	-1.75

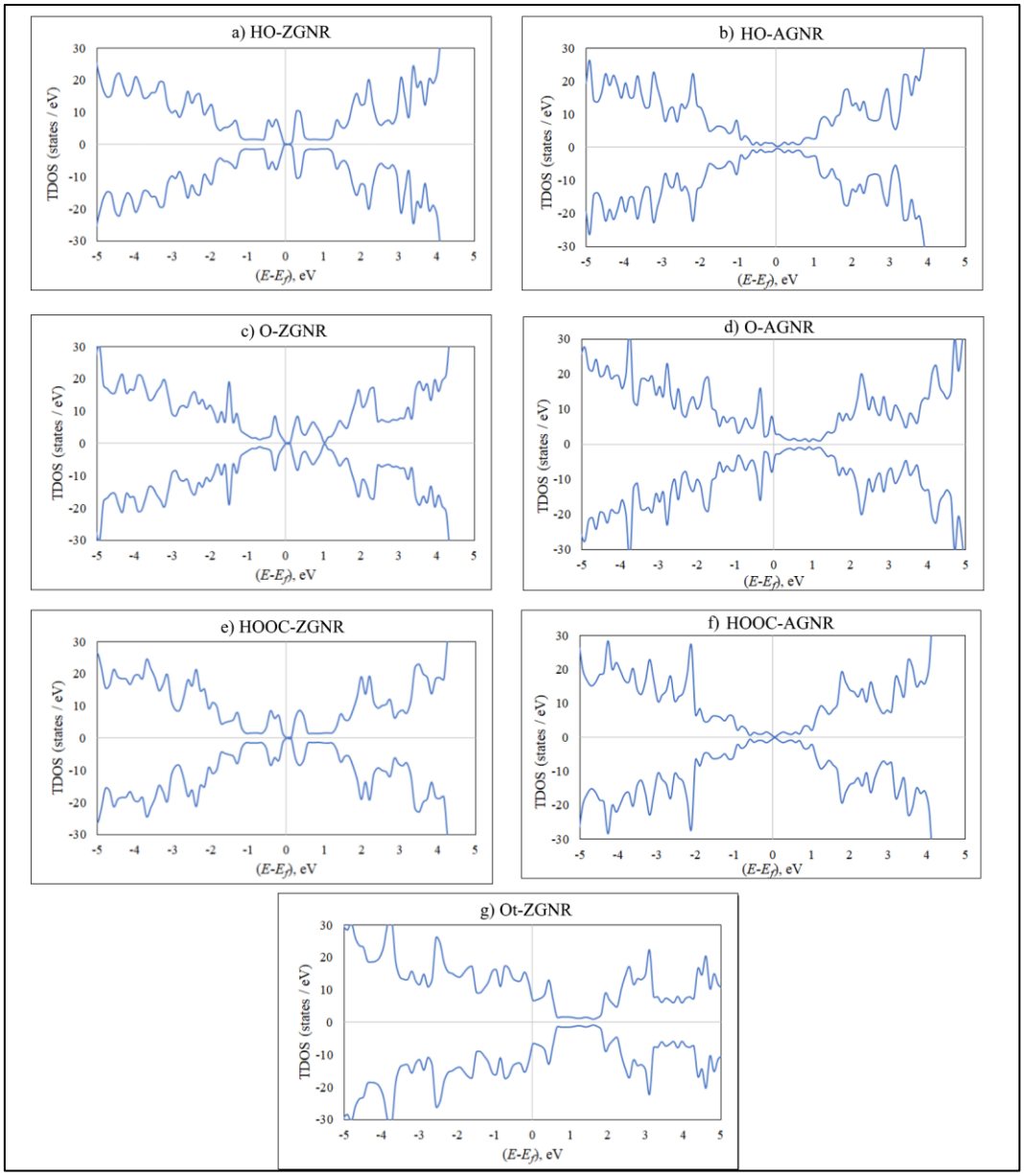

Fig. 5A.6: Total density of states (TDOS) for a) HO-ZGNR, b) HO-AGNR, c) O-ZGNR, d) O-AGNR, e) HOOC-ZGNR, f) HOOC-AGNR, and g) Ot-ZGNR.

The End